



OPTIMIZATION OF OSCILLATING WATER COLUMN WAVE ENERGY CONVERTERS - A NUMERICAL STUDY

Dissertation

submitted to and approved by the

Department of Architecture, Civil Engineering and Environmental Sciences
University of Braunschweig – Institute of Technology

and the

Department of Civil and Environmental Engineering
University of Florence

in candidacy for the degree of a

Doktor-Ingenieur (Dr.-Ing.) /

Dottore di Ricerca in Civil and Environmental Engineering^{*)}

by

Irene Simonetti

27/05/1986

Bagno a Ripoli, Florence, Italy

Submitted on	02/09/2016
Oral examination on	10/11/2016
Professorial advisors	Prof. Lorenzo Cappietti Prof. Hocine Oumeraci

2017

^{*)} Either the German or the Italian form of the title may be used

English Abstract

This PhD research aims at the study of the combined effect of the structure geometry and of the damping applied by a non-linear turbine (i.e., an impulse turbine) on the performance of a fixed Oscillating Water Column (OWC) device for harvesting wave energy. The improved knowledge base regarding the still not well-understood optimal OWC geometry and the optimal turbine damping, specifically for moderate wave climates such as in the Mediterranean Sea, contributes to fill one of the current gaps of knowledge. Moreover, the scale effect induced by neglecting the air compressibility in modelling OWC devices at small-scale is evaluated, and correction factors for the results from small-scale laboratory testing of OWC devices as well as for the results of incompressible numerical models are provided, thus contributing to fill a further recognized knowledge gap. Further, a conceptual model allowing to predict the capture width ratio ε_{owc} of the OWC based on the geometrical parameters (e.g. chamber width and front wall draught), the damping applied by the turbine and the incident wave conditions is proposed. The proposed conceptual model might be applied as a design tool in the process of the OWC device optimization.

The research methodology is based on numerical modelling supported by small-scale laboratory experiments performed by Crema et al. (2016) and further experiments from the literature, which are used to better understand the involved processes and to validate the Computational Fluid Dynamics models. A comparative analysis of the results from the validated CFD codes applied at full-scale (1:1) and three smaller scales (1:25, 1:10 and 1:5) is performed in order to assess the errors induced by neglecting the effect of air compressibility for each scale and to derive the aforementioned correction factors which are valid for the range of considered flow regime in terms of the Mach number ($Ma=0.05-0.15$). Indeed, for the air pressure levels considered in the simulations (up to 350 Pa at model scale 1:50), the effect of neglecting the air compressibility results in an overestimation up to about 15% for the air pressure in the OWC chamber and the subsequent air volume flux, but less than 10% for the capture width ratio ε_{owc} . This overestimation increases with increasing pressure levels.

A parameter study using the incompressible CFD code is performed to extend the range of tested conditions (e.g. geometrical parameters, damping applied by the turbine, incident wave parameters) in the small-scale model of Crema et al. (2016), thus providing a substantially larger dataset for the development a new prediction model to predict the OWC capture width ratio ε_{owc} for incompressible flow conditions. The application of the derived correction factor to the dataset to account for air compressibility effects provides the final dataset for the development of the new conceptual model for compressible flow conditions. Though the new prediction models are based on multiple regression analysis (MRA), the physical processes as observed in the numerical parameter study are implicitly accounted for by imposing on the MRA predetermined functional relationships between *input parameters* and *output parameters*.

German Abstract

In dieser Dissertation wird die kombinierte Auswirkung der Strukturgeometrie und der, durch eine nichtlineare Turbine (z.B. Gleichdruckturbine), aufgebrachten Dämpfung im Hinblick auf die Leistungsfähigkeit einer Wellenenergieanlage untersucht. Der hier betrachtete Prozess der Energieerzeugung basiert auf einer fest installierten, oszillierenden Wassersäule (*Oscillating Water Column*, OWC). Fortgeschrittenes Grundwissens erlaubt sowohl Fragestellungen bezüglich der idealen OWC-Geometrie als auch nach einer optimalen Turbinendämpfung neu zu betrachten. Dies ist insbesondere für moderate Seegangsverhältnisse, wie im Mittelmeer zu beobachten, von Bedeutung und trägt dazu bei gegenwärtige Wissenslücken zu schließen.

Darüber hinaus werden Maßstabeffekte, welche durch die Vernachlässigung der Luftkompressibilität bei der kleinmaßstäblichen Modellierung von OWC-Anlagen induziert werden, ausgewertet. Des Weiteren werden Korrekturfaktoren festgelegt, welche sowohl auf Labortestergebnisse von OWC-Anlagen im Kleinmaßstab als auch auf die Ergebnisse inkompressibler, numerischer Modelle angewendet werden können. Somit kann eine weitere, anerkannte Wissenslücke geschlossen werden. Außerdem wird ein Konzeptmodell vorgestellt, welches die Bestimmung des Einlauf-Breiten-Verhältnisses der OWC (*capture width ratio*, ϵ_{owc}) auf Grundlager geometrischer Parameter (z.B. Kammerbreite und vordere Wandtiefe) ermöglicht. Das vorgeschlagene Konzeptmodell könnte als Design-Tool zur OWC-Anlagenoptimierung verwendet werden.

Die Forschungsmethodik basiert auf numerischer Modellierung, unterstützt durch die kleinmaßstäblichen Laborversuche von Crema et al. (2016) und weiteren, der Fachliteratur entnommenen Experimenten. Diese dienen einer besseren Verständlichkeit der beteiligten Prozesse und gewährleisten die Validierung der Computational Fluid Dynamics (CFD) Modelle. Zur Beurteilung der Fehler, welche infolge der Vernachlässigung der Luftkompressibilität (für jede Skala) entstehen, sowie der bereits erwähnten Korrekturfaktoren (Gültigkeit für den betrachteten Bereich der Durchflussregelung in Bezug auf Mach-Zahlbereich von 0,05 bis 0,15) wird eine vergleichende Ergebnisanalyse der validierten CFD-Codes sowohl vollskalig (1:1) als auch kleinskalig (1:25, 1:10 und 1:5) durchgeführt. Die, in den Simulationen, berücksichtigten Luftdruckniveaus (bis zu 350 Pa im Modellmaßstab von 1:50) in Verbindung mit einer Vernachlässigung der Luftkompressibilität führen zu einer Überschätzung des Luftdrucks in der OWC-Kammer und des nachfolgenden Volumenstroms von bis zu 15%. Die Überschätzung des Einlauf-Breiten-Verhältnis beträgt lediglich 10%. Diese Überschätzung nimmt mit steigendem Druckniveau zu.

Anhand des inkompressiblen CFD-Codes und dem kleinmaßstäblichen Modell von Crema et al. (2016) wird eine Parameterstudie durchgeführt, welche das Spektrum applizierter Bedingungen (z.B. geometrische Parameter, Wellenparameter und Turbinendämpfung) ausdehnt. So wird ein wesentlich größerer Datensatz zur

Entwicklung eines neuen Vorhersagemodells (OWC-Einlauf-Breiten-Verhältnis ε_{owc} für inkompressible Strömungsbedingungen) geschaffen.

Die Anwendung des abgeleiteten Korrekturfaktors auf den Datensatz zur Berücksichtigung von Luftkompressibilitätseffekten liefert den endgültigen Datensatz für die Entwicklung des neuen Konzeptmodells für komprimierbare Strömungsbedingungen. Obwohl die neuen Vorhersagemodelle auf einer multiplen Regressionsanalyse (MRA) basieren, werden die, in der numerischen Parameterstudie beobachteten physikalischen Prozesse, implizit berücksichtigt, indem sie der MRA vorgegebene, funktionale Beziehungen zwischen Eingangsparametern und Ausgangsparametern auferlegen.

Acknowledgments

This PhD research was conducted thanks to a PhD scholarship given by the University of Florence (Italy), which is greatly acknowledged.

I would like to express my special gratitude to Prof. Dr. Ing Hocine Oumeraci, Prof. Dr. Ing Lorenzo Cappietti, Prof. Dr. Ing Hermann Matthies and Prof. Dr. Ing Giampaolo Manfrida for allowing me to conduct the PhD study under their supervision and for encouraging my research with their valuable suggestions. I would also like to thank Dr. Ing Hisham El Safti for his guidance and assistance during my stay in Braunschweig, and my colleague Ilaria Crema for providing the laboratory data used to validate the numerical model.

A special thanks to my colleagues and friends of the international doctorate course, with whom I shared all the best and worst feelings during these three and half years. I will always be grateful for the privilege of having them in my life.

Contents

List of Figures.....	iv
List of Tables.....	ix
List of Notations.....	xi
Chapter 1 - Introduction	1
1.1. Motivation and Problem statement.....	1
1.2. Objectives.....	3
1.3. Methodology.....	3
Chapter 2 - Current knowledge and models for OWC Devices	5
2.1. Hydrodynamics of the OWC and potential flow models.....	6
2.1.1. Rigid piston model.....	8
2.1.2. Uniform pressure distribution model.....	10
2.1.3. Time domain, frequency domain and stochastic analysis for the OWC.....	11
2.1.4. Analytical/numerical approaches for the determination of hydrodynamic coefficients.....	12
2.2. Computational Fluid Dynamics modelling for OWC.....	14
2.3. Thermodynamics of the OWC and air compressibility.....	16
2.4. OWC-air turbine interaction.....	18
2.5. Index for evaluating the OWC performance.....	21
2.6. Summary and implications.....	22
2.6.1. Specification of objectives.....	24
2.6.2. Specification of methodology.....	25
Chapter 3 - Analytical model of a fixed OWC device in the frequency domain	27
3.1. Description of the rigid piston model.....	27
3.1.1. OWC hydrodynamics and aerodynamics.....	28
3.1.2. Stochastic approach to OWC capture width ratio.....	31
3.2. Model results.....	32
3.2.1. Model results for regular waves.....	33
3.2.2. Model results of a fixed OWC device: OWC capture width ratio.....	36
3.3. Summary and implications.....	38
Chapter 4 - Numerical Wave Tank in OpenFOAM®	40
4.1. Theoretical background.....	40
4.1.1. Two-phase incompressible VOF solver.....	40
4.1.2. Wave generation and absorption.....	42
4.2. Set-up of the Numerical Wave Tank and sensitivity analysis.....	44

Contents

4.2.1. Numerical Wave Tank set-up	44
4.2.2. Sensitivity analysis and grid independence tests.....	48
4.3. Numerical Wave Tank validation with laboratory data.....	52
4.4. Summary and implications	55
Chapter 5 - Optimization of OWC geometry and turbine induced damping:	
Parameter study	50
5.1. Sequential optimization approach.....	56
5.2. Set-up of the incompressible model of the OWC.....	60
5.2.1. OWC geometry discretization and mesh generation	60
5.2.2. Numerical set-up of the OWC model.....	63
5.3. Validation of the incompressible CFD model of the OWC with small-scale laboratory tests.....	64
5.4. Parameter study of the OWC device using the validated incompressible CFD model.....	68
5.4.1. Tested OWC geometries, turbine induced damping and reference wave climate	68
5.4.2. OWC capture width ratio	71
5.4.3. Effect of the turbine induced damping on the OWC capture width ratio	72
5.4.4. Effect of the front wall draught on the OWC capture width ratio.....	78
5.4.5. Effect of the chamber width on the OWC capture width ratio	80
5.5. Summary and implications	82
Chapter 6 - Evaluation of air compressibility effects on OWC system dynamics	85
6.1. Theoretical background of the compressible multiphase solver	86
6.2. Implementation of “compressibleInterFoam” into “waves2Foam”.....	88
6.3. Benchmark tests for the validation of the compressible solver	89
6.3.1. Gravity-induced liquid piston in a tube (1D case).....	89
6.3.2. Gravity-induced liquid piston in a tank (2D case).....	90
6.3.2. Air water shock tube	92
6.4. Numerical set-up of the compressible model for the OWC.....	93
6.5. Compressible simulations of the small-scale OWC model	94
6.6. Evaluation of scale effects due to air compressibility in the OWC system	98
6.6.1. Discretization of the prototype OWC scaled up from the 1:50 OWC model....	98
6.6.2. Preliminary tests with the prototype OWC.....	99
6.6.3. Air compressibility effects and proposed correction factors	101
6.6.4. Evaluation of scale effects related to air compressibility at different scales ...	109
6.7. Summary and implications	113
Chapter 7 - Conceptual Multiple Regression Model (MRM) for the prediction of the OWC performance	115
7.1. Incompressible model formulation and validation	115

Contents

7.1.1. Dimensional analysis.....	116
7.1.2. Proposed conceptual Multi Regression Model.....	117
7.1.3. Conceptual model validation.....	121
7.2. Application of the correction factors for air compressibility: compressible MRM.....	124
7.3. Example application of the MRM for site-specific optimization of the OWC.....	126
7.4. Summary and discussion.....	131
Chapter 8 - Concluding remarks and Outlooks.....	133
8.1. General summary of the thesis	133
8.2. Summary and discussion of key results	134
8.3. Outlooks.....	137
References	139

List of Figures

Figure 1-1: Working principle of a shoreline OWC equipped with a Wells turbine (a), from Li & Yu (2012); schematization of the energy conversion chain for OWC devices (b).....	2
Figure 2-1: Current potential flow modelling approaches and solution techniques for OWC devices.....	5
Figure 2-2: Definition sketch for the 2D potential flow formulation of the interaction between the OWC and incident waves (modified from Şentürk & Özdamar 2012).	6
Figure 2-3: Rigid piston model schematization (a), modified from Falcão & Henriques (2016); forces acting on the rigid piston (b).	9
Figure 2-4: OWC device in the uniform pressure distribution model (a), adapted from Falcão & Henriques (2016); basic concepts of the model (air volume flux q_{owc} and pressure p_{owc}) (b).	10
Figure 2-5: Wells turbine (a), from Takao & Setoguchi (2012); rotor of a biradial turbine (b) and whole biradial turbine (c), from Falcão et al. (2013).....	19
Figure 2-6: Parameters affecting the damping and the efficiency of a Wells turbine (modified from Curran et al. 1997).	20
Figure 2-7: Methodology adopted in the PhD thesis.	25
Figure 3-1: Fixed cylindrical OWC device considered in the rigid piston model.	28
Figure 3-2: Absolute values of air pressure oscillation amplitude P_{owc} computed with the rigid piston model for regular waves with height $H=1$ m and for turbine rotation speed $N_T=100$ rad/s (a) and $N_T=200$ rad/s (b).....	34
Figure 3-3: Absolute values of the OWC surface displacement amplitude H_{owc} computed with the rigid piston model for regular waves with height $H=1$ m and for turbine rotation speed $N_T=100$ rad/s (a) and $N_T=200$ rad/s (b).	34
Figure 3-4: Absolute values of the oscillation amplitude air volume flux Q_{owc} computed with the rigid piston model for regular waves with height $H=1$ m and for turbine rotation speed $N_T=100$ rad/s (a) and $N_T=200$ rad/s (b).	35
Figure 3-5: Capture width ratio ϵ_{owc} versus front wall draught D in different sea states (significant wave height $H_s=1-4.5$ m and significant wave period $T_e=5-13$ s) for OWC geometries with radius $r=5$ m and turbine rotational speed $N_T=100$ rad/s. Rigid piston model with stochastic approach results.	37
Figure 3-6: Capture width ratio ϵ_{owc} versus OWC radius r in different sea states (significant wave height $H_s=1-4.5$ m and significant wave period $T_e=5-13$ s) for OWC geometries with front wall draught $D=10$ m and turbine speed $N_T=100$ rad/s. Rigid piston model with stochastic approach results.	38
Figure 3-7: Capture width ratio ϵ_{owc} versus turbine rotational speed N_T in different sea states (significant wave height $H_s=1-4.5$ m and significant wave period $T_e=5-13$ s) for OWC geometries with front wall draught $D=10$ m and radius $r=5$ m. Rigid piston model with stochastic approach results.	38
Figure 4-1: Sketch of the inlet and outlet relaxation zone and relaxation function α_R in the waves2Foam wave generation approach (from Jacobsen et al., 2012).....	43
Figure 4-2: Definition of the boundaries of the Numerical Wave Tank (NWT).	44
Figure 4-3: Sketch of the mesh parameters considered for the sensitivity analysis on the Numerical Wave Tank (NWT), and wave gauges (WGs) location in the NWT.....	48

List of Figures

Figure 4-4: Time series of relative water surface elevation η/H_{targ} at gauge WG1 (distance 3λ from the inlet) in the free NWT for different resolution of the free surface zone mesh (H/cells and λ/cells). Results for regular wave height $H_{\text{targ}}=0.04\text{m}$ and period $T_{\text{targ}}=1\text{s}$	50
Figure 4-5: Time series of relative water surface elevation η/H_{targ} at gauge WG1 (distance 3λ from the inlet) in the free NWT for different mesh Aspect Ratio AR. Results for regular wave height $H_{\text{targ}}=0.04\text{m}$ and period $T_{\text{targ}}=1\text{s}$	50
Figure 4-6: Time series of relative water surface elevation η/H_{targ} at gauge WG1 (distance 3λ from the inlet) in the free NWT for different ratio of cell length in refined to that in unrefined zone (BK _{SF}). Results for regular wave height $H_{\text{targ}}=0.04\text{m}$ and period $T_{\text{targ}}=1\text{s}$	51
Figure 4-7: Sketch of the simulation domain for the numerical wave flumes with waves2Foam generation (a) and piston wave maker generation (b).	53
Figure 4-8: Comparison between laboratory data and numerical results (generated with waves2Foam and piston wave maker approach) for water surface elevation η at wave gauge WG5 (located 9 m away from wave generation) for a regular wave with $H=6.3$ cm and $T=1.1$ s.	54
Figure 4-9: Comparison between laboratory (Lupieri et al. 2015) and numerical (piston wave maker generation) time series of water surface elevation η for a focusing wave at wave gauge WG5 (located 9 m away from wave generation).	54
Figure 5-1: Flow chart of the sequential optimization approach.	57
Figure 5-2: Capture width ratio ε_{owc} obtained from laboratory tests (Crema et al., 2016) for fixed wave parameters ($H=0.04\text{m}$ and $T=1\text{s}$), water depth $h=0.5\text{m}$ and different OWC geometries (chamber width W , front wall draught D and top cover vent area V).	58
Figure 5-3: Capture width ratio ε_{owc} obtained from laboratory tests (Crema et al., 2016) for fixed OWC front wall draught ($D=0.09\text{m}$) and different chamber width W , top cover vent area V , and wave parameters (wave height H and period T) for fixed water depth $h=0.5\text{m}$	59
Figure 5-4: Work flow of the OWC device geometry discretization and mesh generation procedure.	61
Figure 5-5: Definition of the NWT dimensions and position of the OWC model in the NWT.	61
Figure 5-6: Overview of the mesh in the computational domain and refinement mesh region (top), close up of the mesh around the OWC structure (bottom).	62
Figure 5-7: Definition of the boundaries of the Numerical Wave Tank (NWT) with the OWC device.	63
Figure 5-8: Time series of relative pressure p_{owc} in the OWC air chamber, comparison between laboratory data and CFD incompressible model.	66
Figure 5-9: Time series of vertical component of the air velocity U_y , in the OWC top cover pipe, comparison between laboratory data and CFD incompressible model.	66
Figure 5-10: Time series of water level η_{owc} in the OWC chamber, comparison between laboratory data and CFD incompressible model.	66
Figure 5-11: Scatter plot between laboratory (Crema et al., 2016) and numerical data for the period average values of air chamber pressure oscillation amplitude, Δp_{owc} , maximum air velocity, $U_{y_{\text{max}}}$ and water level oscillation $\Delta \eta_{\text{owc}}$. Data refers to laboratory scale (1:50 with Froude similarity).	67
Figure 5-12: Quadratic relations between air volume flux q_{owc} and air chamber pressure p_{owc} obtained for nine values of the top cover orifice V_d considered in the CFD parameter study (see Table 5-8).	70

List of Figures

Figure 5-13: 2D cross-section of vertical component of the air velocity U_y in the OWC chamber, water surface elevation (top) and water velocity U_{water} (bottom) at different times during the wave period T .	71
Figure 5-14: Relative pressure oscillation amplitude Δp_{owc} (a) and water surface displacement $\Delta \eta_{\text{owc}}$ (b) at the centre of the OWC chamber, maximum air volume flux q_{owc}^+ in the top cover pipe (c) versus applied damping K . Results for relative water depth $kh=2.07$, relative wave height $H/h=0.08$ ($H=0.04\text{m}$).	73
Figure 5-15: Capture width ratio ϵ_{owc} versus turbine damping K . Results for relative water depth $kh=1.76$, relative wave height $H/h=0.08$ ($h=0.5\text{m}$) and different OWC geometries (W and D).	74
Figure 5-16: Capture width ratio ϵ_{owc} versus turbine damping K . Results for relative water depth $kh=2.07$, relative wave height $H/h=0.08$ ($h=0.5\text{m}$) and different OWC geometries (W and D).	74
Figure 5-17: Capture width ratio ϵ_{owc} versus turbine damping K . Results for relative water depth $kh=2.51$, relative wave height $H/h=0.08$ ($h=0.5\text{m}$) and different OWC geometries (W and D).	75
Figure 5-18: Capture width ratio ϵ_{owc} versus non-dimensional damping $KBW/\rho_a^{1/2}$. Results for relative OWC chamber thickness $W/\lambda = 0.09-0.21$, relative front wall draught $D/H=2.25$, $W=19\text{ m}$ (a) and $W=0.21\text{ m}$ (b), relative wave height $H/h=0.08$ ($h=0.5\text{m}$) and relative water depth $kh=1.53-3.15$.	77
Figure 5-19: Optimal relative applied damping $KBW/\rho_a^{1/2}$ versus relative water depth kh for different OWC geometries (W/λ and D/H), for relative wave height $H/h=0.08$ ($h=0.5\text{m}$).	77
Figure 5-20: Capture width ratio ϵ_{owc} versus dimensionless water depth kh for different relative front wall draughts D/H , relative chamber thickness W/λ and relative applied damping $KBW/\rho_a^{1/2}=100$ (a), 70 (b), 55 (c), 42 (d). Results for relative wave height $H/h=0.08$ ($h=0.5\text{m}$).	79
Figure 5-21: Capture width ratio ϵ_{owc} versus relative front wall draughts D/H , for relative water depth $kh=2.07$ and 3.15 and different values of the applied damping K . Results for relative wave height $H/h=0.08-0.06$ ($h=0.5\text{m}$).	80
Figure 5-22: Capture width ratio ϵ_{owc} versus relative chamber width W/λ for different values of the applied relative damping $KBW/\rho_a^{1/2}$ (20-170). Results for relative wave height $H/h=0.08$ (water depth $h=0.5\text{m}$) and relative front wall draught $D/H=2.25$.	81
Figure 6-1: Flow chart summarizing the main tasks and results presented in Chapter 6.	86
Figure 6-2: 1D benchmark case (left) and time series of pressure at the bottom centre of the piston (right), comparison between values numerically simulated by compressibleWaveFoam in this study.	90
Figure 6-3: 2D benchmark case (left) and time series of absolute pressure at the wave gauge located at the tank bottom centre (right), comparison between values numerically simulated by compressibleWaveFoam in this study and data available in literature.	91
Figure 6-4: Volume fraction of air and water ($\alpha = \text{water/air}$) in the 2D benchmark case at different time steps after the first impact of the water column on the bottom: $t=0.65\text{s}$, 0.85s , $t=0.95\text{s}$ and $t=1.15\text{s}$. Results obtained with compressibleWaveFoam in this study.	91
Figure 6-5: Air water shock tube benchmarking case and fluid properties (pressure p and density ρ).	92
Figure 6-6: Comparison of the analytical solution (Plumerault et al. 2012) and the numerical simulation obtained with compressibleWaveFoam in this study for the problem of an air-water shock tube at time $5.5137 \cdot 10^{-4}\text{ s}$.	92

List of Figures

Figure 6-7: Time series of relative pressure p_{owc} in the OWC air chamber, comparison between experimental data (Crema et al, 2016) and CFD simulations (compressible and incompressible).....	96
Figure 6-8: Time series of vertical component of the air velocity, U_y , in the OWC top cover pipe, comparison between experimental data (Crema et al, 2016) and CFD simulations (compressible and incompressible).....	96
Figure 6-9: Time series of water level η_{owc} in the OWC chamber, comparison between experimental data (Crema et al, 2016) and CFD simulations (compressible and incompressible).....	96
Figure 6-10: Scatter plot between laboratory and numerical data (obtained with the compressible and the incompressible CFD models) of Δp_{owc} , $U_{y_{max}}$ and $\Delta \eta_{owc}$ at laboratory scale 1:50.	97
Figure 6-11: Comparison of wave propagation in the NWT without OWC at scales 1:50 and 1:1 using incompressible and compressible CFD models (results at scale 1:50 up-scaled according to Froude similarity). Wave gauge located at 3.5λ (λ =incident wavelength) from the NWT inlet.....	100
Figure 6-12: Comparison between p_{owc} (a), η_{owc} (b) and q_{owc} (c) at scales 1:50 and 1:1, obtained by using incompressible and compressible CFD models.	101
Figure 6-13: Correction factor $CF_{\Delta p_{1:50}}$ for the air chamber pressure oscillation amplitude Δp_{owc} (obtained from OWC model scale 1:50 and scaled up to 1:1 according to Froude similarity) versus non-dimensional pressure parameter Γ	103
Figure 6-14: Correction factor $CF_{p^+_{1:50}}$ for the air chamber relative pressure during the exhalation phase, p^+_{owc} (obtained from OWC model scale 1:50 and scaled up to 1:1 according to Froude similarity) versus non-dimensional pressure parameter Γ	103
Figure 6-15: Correction factor $CF_{p^-_{1:50}}$ for the air chamber relative pressure during the inhalation phase, p^-_{owc} (obtained from OWC model scale 1:50 and scaled up to 1:1 according to Froude similarity) versus non-dimensional pressure parameter Γ	104
Figure 6-16: Correction factor $CF_{\Delta q_{1:50}}$ for the volume air flow oscillation amplitude Δq_{owc} (obtained from OWC model scale 1:50 and scaled up to 1:1 according to Froude similarity) versus non-dimensional pressure parameter Γ	105
Figure 6-17: Correction factor $CF_{q^+_{1:50}}$ for the volume air flow during the exhalation phase, q^+_{owc} (obtained from OWC model scale 1:50 and scaled up to 1:1 according to Froude similarity) versus non-dimensional pressure parameter Γ	106
Figure 6-18: Correction factor $CF_{q^-_{1:50}}$ for the volume air flow during the inhalation phase, q^-_{owc} (obtained from OWC model scale 1:50 and scaled up to 1:1 according to Froude similarity) versus non-dimensional pressure parameter Γ	106
Figure 6-19: Correction factor $CF_{\epsilon_{1:50}}$ for the average capture width ratio ϵ_{owc} (obtained from OWC model scale 1:50 and scaled up to 1:1 according to Froude similarity) versus non-dimensional pressure parameter Γ	107
Figure 6-20: Scatter plot between the period average amplitude of water surface elevation $\Delta \eta_{owc}$ simulated with the compressible CFD model at scale 1:50 (scaled up to 1:1 according to Froude similarity) and at scale 1:1.	108
Figure 6-21: Correction factor $CF_{\Delta p}$ for the period average air chamber pressure oscillation amplitude Δp_{owc} (obtained from OWC model scales 1:50, 1:25, 1:10, 1:5 and scaled up to 1:1 according to Froude similarity) versus non-dimensional pressure parameter Γ	110
Figure 6-22: Correction factor $CF_{\Delta q}$ for the period average air volume air flux oscillation amplitude Δq_{owc} (obtained from OWC model scale 1:50, 1:25, 1:10, 1:5 and scaled up to 1:1 according to Froude similarity) versus non-dimensional pressure parameter Γ	110
Figure 6-23: Correction factor $CF_{\epsilon_{owc}}$ for the period average capture width ratio ϵ_{owc} (obtained from OWC model scales 1:50, 1:25, 1:10, 1:5 and scaled up to 1:1 according to Froude similarity) versus non-dimensional pressure parameter Γ	111

List of Figures

Figure 7-1: Iterative non-linear regression procedure used to determine the numerical coefficient of the incompressible MRM.118

Figure 7-2: Global fit of the results of CFD simulations (symbols) to the proposed incompressible MRM (continuous line) for the prediction of the OWC efficiency ϵ_{owc} .119

Figure 7-3: Values of the functions $a(h^*)$, $b(h^*)$, $c(h^*)$, $d(h^*)$ of the incompressible MRM versus the dimensionless water depth h^*119

Figure 7-4: OWC pneumatic efficiency ϵ_{owc} versus turbine damping K (at model scale 1:50) for different OWC geometries and wave conditions in the dataset used for the MRM formulation. Comparison between results of CFD simulations (symbols) and incompressible MRM prediction (continuous lines).121

Figure 7-5: OWC pneumatic efficiency ϵ_{owc} versus turbine damping K (at model scale 1:50) for different OWC geometries and wave conditions in the validation dataset of the MRM. Comparison between results of CFD simulations (symbols) and incompressible MRM prediction (continuous lines).....122

Figure 7-6: Scatter plot between the incompressible MRM prediction and measured data (obtained from laboratory experiments by Crema et al. 2016, and CFD simulations) of ϵ_{owc}123

Figure 7-7: Scatter plot between incompressible MRM prediction and measured data (obtained from laboratory experiments by Crema et al. 2016 and incompressible CFD simulations) for different ranges of the non-dimensional parameters W^* , D^* and h^*123

Figure 7-8: Procedure for the application of the proposed correction factors for air compressibility and for the formulation of the compressible MRM.125

Figure 7-9: Comparison of the fit of the results of CFD simulations (incompressible and corrected with correction factor for air compressibility) and the proposed incompressible and compressible MRM for the prediction of the OWC efficiency ϵ_{owc}125

Figure 7-10: Characterization of the wave resource in terms of significant wave height H_s and wave energy period T_e for the reference installation site (Central Tuscany, water depth $h=25$ m) in terms of total annual energy per meter of wave front AE (data from Vannucchi, 2012).127

Figure 7-11: Scatter plot of the OWC capture width ratio ϵ_{owc} obtained with the compressible MRM for the example application of Case A: wave height $H=2.5$ m, period $T=6$ s, water depth $h=25$ m, damping $K=0.6-1.4 \text{ kg}^{1/2}\text{m}^{-7/2}$, chamber width $W=7.5-11.5$ m and draught $D=3.5$ m (a) and 4.1 m (b).....129

Figure 7-12: Scatter plot of the average OWC capture width ratio ϵ_{owc} obtained with the compressible MRM for the example application of Case B: wave heights $H=1.5-3$ m, periods $T=6-8$ s, water depth $h=25$ m, damping $K=0.6-1.4 \text{ kg}^{1/2}\text{m}^{-7/2}$, chamber width $W=7.5-11.5$ m and draught $D=3.5$ m (a) and 4.1 m (b).....130

Figure 8-1: Non-dimensional parameters of the new MRM and overall structure of the model.137

List of Tables

Table 2-1: Summary of most common modelling approaches for the hydrodynamic modelling of OWC device.....	23
Table 3-1: Parameters of the <i>rigid piston model</i> in the frequency domain: OWC geometry parameters, turbine parameters and wave parameters.	33
Table 3-2: Maximum values of relative air pressure P_{owc} , water levels H_{owc} and air volume flux Q_{owc} obtained with the rigid piston model of the OWC, for $D=10$ m, $r=7$ m and different turbine rotation speed N_T . The results are obtained for regular waves with height $H=3$ m and period $T=8$ s ($\omega=0.78$ rad/s).....	36
Table 3-3: Sea states for the calculation of the average OWC capture width ratio ϵ_{owc} by means of the <i>rigid piston model</i> (significant wave height H_s , energy period T_e , average wave energy per unit of wave crest Π_{wave}).	36
Table 4-1: Boundary conditions for the Numerical Wave Tank (NWT) for velocity u , pressure p , VOF volume phase fraction α	45
Table 4-2: Set of numerical schemes used for the free Numerical Wave Tank (NWT) simulations.....	46
Table 4-3: Set of linear solvers used for the numerical free Numerical Wave Tank (NWT) simulations for velocity u , pressure p , VOF volume phase fraction α , sub-grid scale turbulent kinetic energy k_{SGS}	47
Table 4-4: Time step control parameters adopted in the free NWT simulations.....	47
Table 4-5: Environmental properties used in the Numerical Wave Tank (NWT) simulations.	48
Table 4-6: Mesh parameters: cells per wave height ($H/cells$), cells per wave length ($\lambda/cells$) cells aspect ratio (AR), ratio of cell length in refined zone to that in unrefined zone (BK _{SF}), relative error on the wave height (E_H) and on the wave period (E_T). Average values recorded at gauge WG1 (3λ from the wave generating boundary).....	49
Table 4-7: Simulated cases for testing the sensibility of the free NWT to the inlet/outlet relaxation zone length ($\delta X_{IN}/\delta X_{OUT}$) and reflection coefficient K_r for the target wave..	51
Table 4-8: Maximum relative error in the fully developed wave train on surface displacement η (η_{NRMSE}) and on the wave height H (E_H) and period (E_T). Comparison between laboratory data and waves2Foam generation/piston wave maker generation at wave gauges WG3, WG4 and WG5, for the regular wave $H=0.063$ m, $T=1.1$ s.....	53
Table 5-1: OWC geometrical parameters tested in the laboratory (Crema et al., 2016), incident wave height H and period T and water depth h (values for model scale 1:50).	57
Table 5-2: Time step control parameters adopted for the 3D model of the OWC in the NWT.	64
Table 5-3: Determination coefficient R^2 and NRMSE between the incompressible CFD model of the OWC and laboratory data for relative air chamber pressure, p_{owc} , vertical component of the air velocity, U_y and water levels η_{owc}	65
Table 5-4: Characteristics of tested incident wave height H , wave period T and relative water depth kh (fixed water depth $h=0.5$ m).	69
Table 5-5: Geometrical parameters of the simulated OWC device and water depth (scale 1:50).	69

List of Tables

Table 5-6: Values of the top cover orifice diameter V_d used in the parameter study and corresponding values of the damping coefficient K	70
Table 6-1: Determination coefficient R^2 and NRMSE for comparison of results of the incompressible and compressible CFD simulations with data from laboratory tests. Results for for relative air chamber pressure, p_{owc} , vertical component of the air velocity, U_y and water levels η_{owc}	95
Table 6-2: Froude scale ratios for geometric, dynamic and kinematic similarity between model and prototype.....	98
Table 6-3: Geometrical parameters of the OWC device simulated at scale 1:50 and at prototype scale.....	99
Table 6-4: Characteristics of tested incident wave heights H and periods T in a constant water depth ($h=25m$ at scale 1:1 and $h=0.5m$ at scale 1:50) selected for the scale effects study.	99
Table 6-5: Summary of the proposed correction factors for air compressibility for Δp_{owc} , Δq_{owc} and ϵ_{owc}	108
Table 6-6: Summary of the proposed correction factors CF for air compressibility for Δp_{owc} , Δq_{owc} and ϵ_{owc} at model scales 1:50, 1:25, 1:10 and 1:5.	112
Table 6-7: Maximum air velocities in the OWC chamber (for $0.4 < \Gamma < 1$) in the numerical simulations at model scales 1:50, 1:25, 1:10 and 1:5, and values of Mach number Ma (for the reference speed of sound in the air 340 m/s).....	112
Table 7-1: Structure of the functions defining the proposed incompressible MRM.....	120
Table 7-2: Structure of the functions defining the proposed compressible MRM.....	126
Table 7-3: Wave cases selected for the example application of the MRM in case B (wave height H , wave period T , annual energy AE_n , fraction of the total annual energy in the reference installation site AE_n/AE_{tot}).	128
Table 8-1: Summary of the proposed correction factors (CF) for the pressure oscillation amplitude in the OWC air chamber Δp_{owc} , the volume air flow oscillation amplitude Δq_{owc} the capture width ratio ϵ_{owc} for model scale 1:50.	135

List of Notations

Roman notation

AR	aspect ratio of the computational cells [-]
B	length of the OWC perpendicular to wave propagation direction [m]
BK_{SF}	scale factor between the mesh in the free surface zone and the unrefined mesh [-]
Br	OWC radiation damping [Ns/m]
c	speed of sound [m/s]
CF	correction factor [-]
Co	Courant number [-]
C_p	fluid heat capacity at constant pressure [J/(kgK)]
C_v	fluid heat capacity at constant volume [J/(kgK)]
D	OWC front wall draught [m]
D^*	dimensionless OWC front wall draught [-]
D_T	air turbine diameter [m]
F	source term in Navier-Stokes equations
Fc	OWC freeboard [m]
f_e	excitation force on the OWC in the rigid piston model [N]
f_{hstat}	hydrostatic force on the OWC in the rigid piston model [N]
f_p	applied force due to the OWC air chamber pressure in the rigid piston model [N]
Fr	Froude number [-]
f_{rad}	radiation force on the OWC in the rigid piston model [N]
G	OWC back wall length [m]
g	gravitational acceleration [m/s ²]
g^*	dimensionless gravitational acceleration [-]
h	water depth [m]
H	incident wave height [m]
h^*	dimensionless water depth [-]
h_e	fluid specific enthalpy [J/kg]
H_f	heat of fusion [J/kg]
H_{owc}	complex amplitude of the free surface displacement the OWC chamber [m]
Hs	significant wave height [m]
I	identity tensor
i	fluid specific internal energy [J/kg]
k	wavenumber of the incident wave [1/m]
K	quadratic turbine damping coefficient [kg ^{1/2} m ^{-7/2}]
K^*	dimensionless turbine damping [-]
K_e	fluid kinetic energy [J]
K_{opt}	optimal damping K for a given OWC geometry [kg ^{1/2} m ^{-7/2}]

List of Notations

K_r	wave reflection coefficient [-]
k_{SGS}	sub grid scale turbulent kinetic energy [J/kg]
K_T	linear proportionality constant between pressure head ψ and flow rate [-]
k_t	fluid turbulent kinetic energy [J/kg]
m	mass air flow in the OWC chamber [kg/s]
m_a	OWC added mass [-]
Ma	Mach number [-]
m_w	mass of the water column inside the OWC [kg]
N	length scale ratio [-]
N_T	air turbine rotational speed [rad/s]
p	fluid pressure [Pa]
P_{owc}	complex amplitude of the relative air pressure in the OWC chamber [Pa]
p_{owc}	instantaneous value of the relative air pressure in the OWC chamber [Pa]
p_{owc}^-	period average value of the minimum p_{owc} during inhalation [Pa]
p_{owc}^+	period average value of the maximum p_{owc} during exhalation [Pa]
q	energy flux vector of the fluid [J/m ²]
q_e	excitation air volume flux in the OWC chamber [m ³ /s]
q_{owc}	instantaneous value of volume airflow through the OWC top cover pipe [m ³ /s]
Q_{owc}	complex amplitude of the volume air flux OWC chamber [m ³ /s]
q_{owc}^-	period average value of the minimum q_{owc} during inhalation [m ³ /s]
q_{owc}^+	period average value of the maximum q_{owc} during exhalation [m ³ /s]
q_r	radiation air volume flux in the OWC chamber [m ³ /s]
R	ideal gas constant [J/(kgK)]
r	cylindrical OWC radius [m]
R^2	determination coefficient [-]
S	area of the OWC horizontal cross section [m ²]
S_η	energy density spectrum [m ² /Hz]
t	time [s]
T	incident wave period [s]
T_e	energy period of irregular waves [s]
T_f	fluid temperature [K]
T_{owc}	average OWC inner oscillation period [s]
T_{test}	length of the analysis windows [s]
u	fluid velocity vector [m/s]
u_r	artificial interface velocity vector in VOF method [m/s]
U_{water}	water velocity magnitude [m/s]
U_y	vertical component of air velocity in the OWC top cover pipe [m/s]
$U_{y,max}$	maximum value of the OWC air velocity (referred to T_{owc}) [m/s]
V	ratio of the top cover vent diameter and the OWC top cover area [%]
V_{air}	air volume in the OWC air chamber [m ³]
V_d	OWC top cover vent diameter [m]

List of Notations

W	width of the OWC chamber in wave propagation direction [m]
W^*	dimensionless OWC chamber width in wave propagation direction [-]

Greek notation

α	volume phase fraction in VOF method [-]
α_R	relaxation function in <code>waves2Foam</code> [-]
β	peak-enhancement function of JONSWAP spectrum [-]
Γ	non-dimensional pressure parameter [-]
Γ_h	excitation force amplitude per unit incident wave amplitude [N/m]
γ	specific weight of the water [kg/(m ² s ²)]
γ_j	JONSWAP spectrum peak width [-]
ΔE	wave annual energy in a reference installation site [MWh/m]
$\Delta \eta_{owc}$	period average amplitude of the water surface oscillation in the OWC [m]
Δp_{owc}	period average pressure oscillation amplitude in the OWC chamber [Pa]
Δq_{owc}	period average flowrate oscillation amplitude in the OWC air chamber [m ³ /s]
Δt	time step [s]
Δx	mesh size [m]
δ	specific heat ratio $\delta = C_p/C_v$ [-]
δX_{IN}	length of the inlet relaxation zone [m]
δX_{OUT}	length of the outlet relaxation zone [m]
ε_{owc}	OWC capture width ratio [-]
ζ	diffusion field for dynamic mesh motion [-]
η	water surface elevation of the incident wave [m]
η_{NRMSE}	Normalized Root Mean Square Error (NRMSE) on η [%]
η_{OWC}	water level at the centre of the OWC chamber [m]
\varkappa	local curvature at the fluids interface [-]
λ	incident wave length [m]
λ_1, λ_2	damping parameters for Δt adjustment [-]
μ	fluid dynamic viscosity [kg/(sm)]
μ_a	air dynamic viscosity [kg/(sm)]
μ_l	laminar dynamic viscosity [kg/(sm)]
μ_{SGS}	sub grid scale dynamic viscosity [kg/(sm)]
μ_w	water dynamic viscosity [kg/(sm)]
ν	point velocity vector for dynamic mesh motion [m/s]
ν_a	air kinematic viscosity [m ² /s]
ν_w	water kinematic viscosity [m ² /s]
ξ	linear air turbine dimensionless flow rate coefficient [-]
Π_{owc}	period average pneumatic power absorbed by the OWC [W]
Π_{wave}	period averaged incident wave power per unit width [W/m]
ρ	fluid density [kg/m ³]
ρ_a	air density [kg/m ³]

List of Notations

ρ_w	water density [kg/m ³]
ρ_w^*	dimensionless water density [-]
σ	surface tension coefficient [N/m]
σ_a, σ_b	JONSWAP spectrum peak-enhancement factors [-]
σ_η^2	variance of the Gaussian probability density function of η [-]
σ_η	standard deviation of the Gaussian probability density function of η [-]
τ	viscous stress tensor [kN/m ²]
φ	velocity potential in linear wave theory [m ² /s]
φ^D	diffraction component of velocity potential [m ² /s]
φ^R	radiation component of velocity potential [m ² /s]
φ^S	scattering component of velocity potential [m ² /s]
χ_R	relaxation coefficient in <code>waves2Foam</code> [-]
ψ	linear air turbine dimensionless pressure head coefficient [-]
ψ_e	fluid thermal conductivity [(Wm)/K]
ω	incident wave frequency [rad/s]
Ω_i	volume of the computational cell in the FVM [m ³]

Abbreviations

CFD	Computational Fluid Dynamics
MRM	Multiple Regression Model
NRMSE	Normalized Root Mean Square Error
NWT	Numerical Wave Tank
OWC	Oscillating Water Column
PTO	Power Take Off
SWL	Still Water Level
CFS	Continuum Surface Force
WEC	Wave Energy Converter
BEM	Boundary Element Method
FEM	Finite Element Method
FVM	Finite Volume Method
CSF	Continuum Surface Force method
SGS	Sub Grid Scale
TVD	Total Variation Diminishing discretization scheme

CHAPTER 1

Introduction

1.1. Motivation and Problem statement

Wave energy is, among the renewable energy sources, the one with the highest energy density. The total annual energy transferred from the wind to the ocean is quantified in about 0.17 W/m^2 (Wang & Huang 2004). The wave energy globally reaching the coastline is estimated at 32000 TWh/yr (Mork et al. 2010). Within this framework, the running out of traditional energy sources is enhancing the interest in wave energy conversion technologies.

At present, the exploitation of wave energy is quite limited, and this is probably due to specific difficulties related to the strongly stochastic character of the resource itself. Wave energy is characterized, in fact, by irregularity in wave amplitude, phase and direction: it is difficult to obtain good performance of a device over the entire range of incident wave frequencies (Falcão 2010). A large variety of concepts have been proposed in the field of wave energy converter (WEC) devices (Falcão 2010). The variety of the existing concepts is a strong indicator of the relatively early development stage of wave energy conversion. Despite the large number of proposed WEC technologies, in fact, none of them has, up to date, reached the commercial stage. Even for the simplest and more consolidated concepts, there is still a general uncertainty about the most appropriate and efficient design, and research at a fundamental level is still needed to increase the confidence of the industry towards the best solutions.

The Oscillating Water Column (OWC) is one of the few WEC concepts to have reached the development stage of full size prototype, e.g. the LIMPET experimental plant in Islay island, Scotland (Boake et al. 2002), the Mutriku power plant in Spain (Torre-Enciso et al. 2009), the Pico power plant, in Portugal (Sarmiento et al. 2006), the REWEC3 experimental plant, in Italy (Arena et al. 2013). The OWC success is probably due to its simplicity, both structural and mechanical, i.e. it has a limited number of moving components. In its basic form, the device consists in a partially submerged caisson whose upper part forms an air chamber (Fig 1-1, a). The immersed part of the device is open to the effect of the wave motion, which alternatively compresses and depressurizes the air column in the chamber. The self-rectifying turbine (e.g. Wells turbines or impulse turbines) generally performs the transformation of the oscillatory motion of the air column in a unidirectional rotational motion.

The energy conversion chain for an OWC device consists in the following steps (Fig 1-1, b):

- (i) Transformation of the energy of the incident wave in kinetic energy of the oscillating water column (*hydraulic efficiency*).
- (ii) Transformation of the kinetic energy of the oscillating column of water in pressure and kinetic energy of the reciprocating airflow (*pneumatic efficiency*);
- (iii) Transformation of the pressure and kinetic energy of the reciprocating airflow in mechanical energy in the air turbine (*mechanical efficiency*);
- (iv) Transformation of mechanical energy to electrical energy by means of an electrical generator and complementary electrical equipment (*electrical efficiency*).

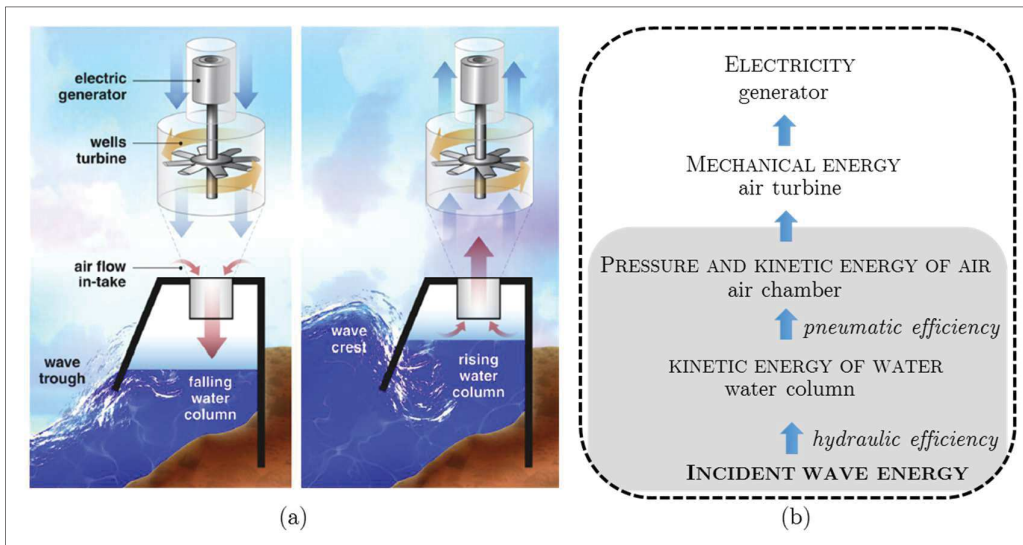


Figure 1-1: Working principle of a shoreline OWC equipped with a Wells turbine (a), from Li & Yu (2012); schematization of the energy conversion chain for OWC devices (b).

The optimization of the design the OWC device in terms of maximizing the wave energy extraction, represents one of the essential steps in order to consolidate the development of the technology towards the commercial stage. Furthermore, most of the previous studies on OWCs refers to the installation in highly energetic sea states (e.g., Oceanic wave climate), while there is limited knowledge about the optimal design for moderate wave climates (e.g. the Mediterranean sea). Research at fundamental level is therefore needed.

Laboratory experiments using small-scale models can be used to assess the performance of different design alternatives for OWC devices. Laboratory testing, however, is highly time consuming, requires the accessibility of expensive equipment and has the disadvantage of allowing to test only a limited range of OWC geometries. Thus, the set of parameters to be varied in the laboratory experiments is necessarily restricted. Moreover, experimental studies on OWCs have proven difficult to perform. In order to accurately reproduce both the hydrodynamics and the thermodynamics of the device, different model scales may be required for the submerged part of the device

and for the air chamber (Falcão & Henriques 2014). These considerations underline why numerical modelling is important and valuable for the development of OWC devices, particularly in combination with laboratory experiments to calibrate and validate the implemented numerical models. Therefore, the synergy between physical and numerical modelling is fundamental.

Although the OWC has been among the first WEC concept to be developed, numerical modelling of such devices started much later and the advance is less than that in the numerical modelling of oscillating body WEC. Indeed, in contrast to the later, the modelling of OWCs could not completely take advantage of the widely available knowledge and advances in the field of ship-hydrodynamics (Cruz 2009). Moreover, in the numerical modelling of OWCs, some specific issues has to be taken into account, including: (i) possible non-linearity of the incident wave-field; (ii) vortex formation and turbulent flows in both water and air; (iii) air compressibility effects taking place in the OWC air chamber. The development of an accurate numerical model for the optimization of OWC design is, therefore, not a trivial task.

1.2. Objectives

The tentative objectives of the PhD thesis, which will be specified more precisely at the end of *Chapter 2*, are summarised as follows:

- (i) Elaboration of a knowledge base on the optimization of the geometry of fixed detached OWC device in moderate wave climate (based on numerical modelling approaches able to take into account all the relevant hydrodynamic and thermodynamic processes involved in the interaction of the incident waves with the OWC and the air in the chamber), thus contributing to consolidate the technology by filling the current gaps of knowledge.
- (ii) Development of a conceptual model allowing to predict the pneumatic efficiency of the OWC device given as input the OWC geometry and the incident wave parameters. The model might be applied as a simple design-supporting tool, avoiding the use of more demanding computational tools in the optimization process of OWC devices.

1.3. Methodology

The tentative methodology, which will be specified in more details at the end of *Chapter 2*, is summarised below.

First, the current knowledge on the modelling approaches for OWC devices is reviewed and analysed, in order to identify specific modelling issues and to select the most appropriate modelling approach for a reliable prediction of the device dynamics and its power output.

Next, a simplified modelling approach is applied to perform a brief preliminary evaluation of the effect of different design parameters on the performance of the OWC

device and to obtain a preliminary characterization of the range of values of the involved variables to be used for the set-up of OWC models and their instrumentation in the laboratory¹.

A more accurate numerical model of the OWC, based on techniques selected using the results of the review of the current knowledge, is later implemented and validated with laboratory experiments. The validated numerical model is applied for an extensive parameter study of the possible performance to be achieved with different OWC geometries in the framework of the device installation in a Mediterranean wave climate. The results of the numerical parameter study are, finally, analysed in order to develop a conceptual model, based on dimensional analysis and Multiple Regression Analysis (MRA), to predict the OWC pneumatic conversion efficiency once given as inputs the device geometry and the incident waves.

¹ The laboratory tests on the OWC device are carried out by I. Crema (Crema et al. 2015; Crema et al. 2016).

CHAPTER 2

Current knowledge and models for OWC Devices

The aim of *this chapter* is to review and analyse the current knowledge and the models on OWC devices, in order to identify the gaps of knowledge, the specific issues to be considered in modelling the OWC device, and consequently to select the most appropriate modelling approach. The tentative objectives and methodologies introduced in *Chapter 1* will be specified more precisely at the end of this chapter.

The formulation describing the OWC hydrodynamics in potential flow theory is first presented (Fig. 2-1), since the major research efforts in the field of OWC modelling focussed on hydrodynamics, i.e. on resolving diffraction and radiation problems around the structure. Within the framework of potential flow theory, the interaction between incident waves and OWCs has mainly been modelled using two approaches: (i) the *rigid piston model* and (ii) the *uniform pressure distribution model* (*section 2.1.1* and *2.1.2*). Depending on the modelling purpose, the models can be solved in the time domain or in the frequency domain (*section 2.1.3*). In both types of potential flow models, the OWC hydrodynamic coefficients must be known. These coefficients can be obtained analytically or numerically. An overview of the application of the aforementioned methods for OWC devices, with their strengths and limitations, is given (*section 2.1.4*).

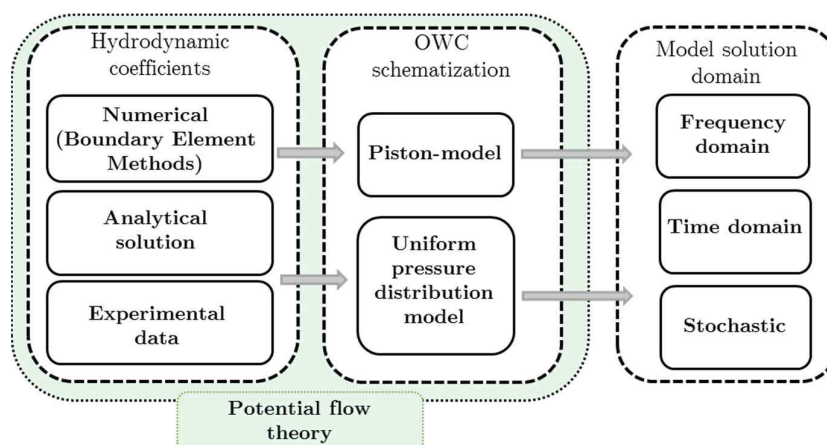


Figure 2-1: Current potential flow modelling approaches and solution techniques for OWC devices.

For a proper characterization of real fluid effects in the OWC system, Computational Fluid Dynamics (CFD) modelling is needed. A review of the main studies based on this approach is performed (*section 2.2*). Currently less investigated and crucial aspects of the OWC system dynamics, namely the thermodynamics of the air chamber and the interaction between the OWC structure and the air turbine, are later presented (*section 2.3* and *section 2.4*).

2.1. Hydrodynamics of the OWC and potential flow models

Since most of the approaches adopted to model the OWC hydrodynamics are based on potential flow, it might be useful to introduce first the specific formulation of the OWC hydrodynamics within the potential flow framework. In linear water-wave theory², the hydrodynamic problem of wave energy absorption by OWC device (or, more in general, by devices whose working principle is based on oscillating bodies) can be regarded as a combination of (i) the radiation problem and (ii) the diffraction problem (Evans 1982; Falcão 2002). The radiation problem concerns the wave field generated by the oscillations of the body or, in the case of a fixed (i.e., not floating) OWC, by the oscillation of the water column generated by the time-varying air pressure inside the chamber. The radiated wave may be produced in absence of incident waves if a time-varying air pressure is supplied to the inner surface of the OWC (Falnes, 2007). The radiation problem for two-dimensional, cylindrical OWC has been analytically formulated and solved by Sarmento & Falcão 1985.

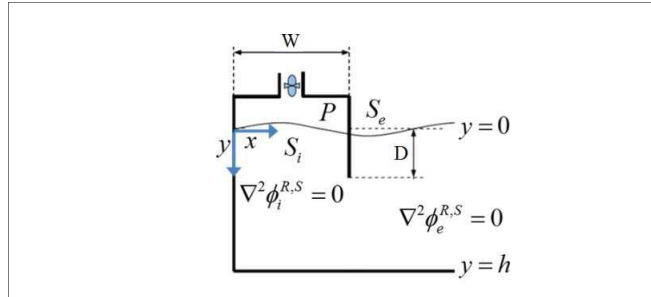


Figure 2-2: Definition sketch for the 2D potential flow formulation of the interaction between the OWC and incident waves (modified from Şentürk & Özdamar 2012).

Under the assumptions of linear wave theory, in the case of a two-dimensional OWC with Cartesian co-ordinates (Figure 2-2), considering a fluid domain bounded by $0 < y < h$ and $0 < x < \infty$, the two-dimensional flow can be expressed in terms of a velocity potential $\Phi(x, y, t)$ (Evans & Porter 1995). The velocity potential Φ satisfies Laplace equation:

² In linear wave theory, the considered disturbances are so small that, in the equation of motion, they can be regarded quantities whose products are negligible. Surface tension is neglected, the fluid is considered a perfect fluid (i.e. viscosity and other dissipative effects are neglected), compressibility is negligible too, so water density can be considered as constant.

$$\nabla^2 \Phi = \frac{\partial^2 \Phi}{\partial x^2} + \frac{\partial^2 \Phi}{\partial y^2} = 0 \quad \text{in the fluid} \quad (2.1)$$

$$\frac{\partial \Phi}{\partial n} = 0 \quad \text{on all solid boundaries} \quad (2.2)$$

If the motion is simple time-harmonic with angular frequency ω , the problem parameters can be written, in complex notation, as time-independent quantities:

$$\Phi(x, y, t) = \text{Re} \{ \phi(x, y) e^{-i\omega t} \} \quad (2.3)$$

$$H(x, t) = \text{Re} \{ \eta(x) e^{-i\omega t} \} \quad (2.4)$$

$$P_{owc}(t) = \text{Re} \{ p_{owc} e^{-i\omega t} \} \quad (2.5)$$

where H is the free surface elevation function, P_{owc} is the relative pressure inside the OWC chamber. Denoting the internal and the external free surfaces respectively by $S_i = \{x, y: y=0, 0 < x < W\}$ and $S_e = \{x, y: y=0, W < x < \infty\}$, where W is the OWC chamber width in wave propagation direction, the linearized free-surface condition is

$$\frac{\partial \Phi}{\partial t} - gH = \begin{cases} P_{owc}(t)/\rho_w, & (x, y) \in S_i \\ 0, & (x, y) \in S_e \end{cases} \quad (2.6)$$

where ρ_w is the water density.

Defining $L_b = \{x, y: x=W, 0 \leq y \leq D\}$ as the surface of the front barrier of the OWC (Fig. 2-2), and $L_g = \{x, y: x=W, h < y \leq D\}$ as the surface of gap under the front barrier, the problem and the boundary conditions can be expressed in terms of the velocity potential ϕ as follows:

$$\nabla^2 \Phi = 0 \quad \text{in the fluid} \quad (2.7)$$

$$\frac{\partial \phi}{\partial y} = 0 \quad \text{on } y=h \quad (2.8)$$

$$\frac{\partial \phi}{\partial x} = 0 \quad \text{on } x=0 \quad (2.9)$$

$$\frac{\partial \phi}{\partial x} = 0 \quad \text{for } (x, y) \in L_b \quad (2.10)$$

$$k\phi + \frac{\partial \phi}{\partial y} = \begin{cases} -i\omega p_{owc}/\rho_w g, & (x, y) \in S_i \\ 0, & (x, y) \in S_e \end{cases} \quad (2.11)$$

where ϕ and $\partial \phi / \partial x$ are continuous for $(x, y) \in L_g$. Equation 2.11 represents the combined free surface boundary condition, where k is the wave number, which, for gravity waves on uniform water depth h , is expressed as $\omega^2 = gk \tanh(kh)$.

The velocity potential ϕ can be decomposed into a radiation and a scattering part as (Evans 1982):

$$\phi = \phi^S - \frac{i\omega p_{owc}}{\rho_w g} \phi^R \quad (2.12)$$

where ϕ^S is the solution of the scattering problem (i.e. related to the incoming wave and without considering a pressure difference on the internal free surface) and satisfies

equations 2.7-2.11 once imposing $p_{owc}=0$ in Eq. 2.11. ϕ^R is the radiated potential, which is the solution of the radiation problem due to the imposed pressure on the internal free surface S_i in absence of incoming waves. The radiated potential ϕ^R is defined by Eqs. 2.7-2.11, with Eq. 2.11 replaced by:

$$k\phi^R + \frac{\partial\phi^R}{\partial y} = \begin{cases} 1, & \text{on } S_i \\ 0, & \text{on } S_e \end{cases} \quad (2.13)$$

Using linear superposition, the solution of the scattering problem can be further decomposed into two parts:

$$\phi^S = \phi^I + \phi^D \quad (2.14)$$

where ϕ^I is the incident wave and ϕ^D the diffracted waves propagating away from the structure. The solution to the boundary-value problem specified above can be used to describe the flow around the OWC structure. Within the framework of potential theory, the interaction between the OWC and the incoming waves is usually modelled with two different approaches:

- (i) *Rigid piston model* is the earliest approach, and considers the OWC free surface as a rigid weightless rigid piston moving only in heave (*section 2.1.1*);
- (ii) *Uniform pressure distribution model* is a later and more accurate approach, which allows for deformations of the OWC inner free surface (*section 2.1.2*).

2.1.1. Rigid piston model

In the earlier studies, the hydrodynamics of the OWC device was modelled by replacing the internal free surface of the device with a weightless rigid piston moving only in heave (Robinson 1982; Watts et al. 1985; Maeda et al. 1985). Using the same approach, Evans (1978 and 1981) and Ma (1995) introduced a vertical velocity of the rigid plate when the structure is subject to incoming waves, giving a more realistic representation of the interior of an OWC device. These earlier studies concluded that the rigid piston approximation might provide satisfactory results if the dimensions of the OWC in wave direction are small compared with the wavelength of the incoming waves (i.e., when sloshing phenomena in the OWC chamber are not supposed to appear).

Brendmo et al. (1996) and Lopes et al. (2009), included the modelling of viscous loss in the rigid piston model, introducing a constant loss resistance representative of viscous friction. In the framework of control strategies development and testing, a similar approach to model a floating OWC device was adopted by Nunes et al. (2011).

More recently, the *rigid piston model* was adopted by Gouaud et al. (2010) and by Karami et al. (2012) to assess the efficiency of a fixed, bottom standing OWC. Falcão et al. (2012), Sykes et al. (2011) and Gomes et al. (2012) applied the rigid piston model to perform the hydrodynamic analysis aimed at the optimization of a floating OWC device. In these recent studies, a comparison of model results and data from laboratory tests showed significantly high correlation coefficients, confirming that the *rigid piston model* is an adequate tool OWC performance evaluation, under the

aforementioned assumption of limited chamber dimensions compared to the reference incident wave length. However, the deformation of the free surface inside the OWC chamber is ignored, thus resulting in a non-uniform pressure distribution that may be unrealistic, since the air pressure in the OWC chamber is approximately uniform in space (Falcão et al. 2012). The *rigid piston model* (Fig. 2-3) has its origin in the theories developed in the mid-1970s about the interaction between floating bodies and waves (Wehausen, 1971), therefore it is based on the concepts of body velocities and forces. In the model, the OWC has a single degree of freedom, which is heave. The rigid piston has the same mass and the same displaced volume as the fluid that it approximates and has its own hydrodynamics coefficients (i.e. added mass, radiation damping and excitation forces).

The forces acting on the heaving plate are (Fig. 2-3, b):

- (i) Excitation forces due to the incident wave f_e ;
- (ii) Hydrodynamic forces f_{rad} due to the radiated waves induced by the motion of the plate (expressed in terms of frequency dependent added mass m_a and radiation damping coefficient B_r);
- (iii) Hydrostatic forces, f_{hstat} , due to hydrostatic pressure of the incident wave;
- (iv) Applied force f_P due to the pressure difference across the PTO system (i.e. the air turbine), which produces an oscillating air pressure on the top face of the rigid plate.

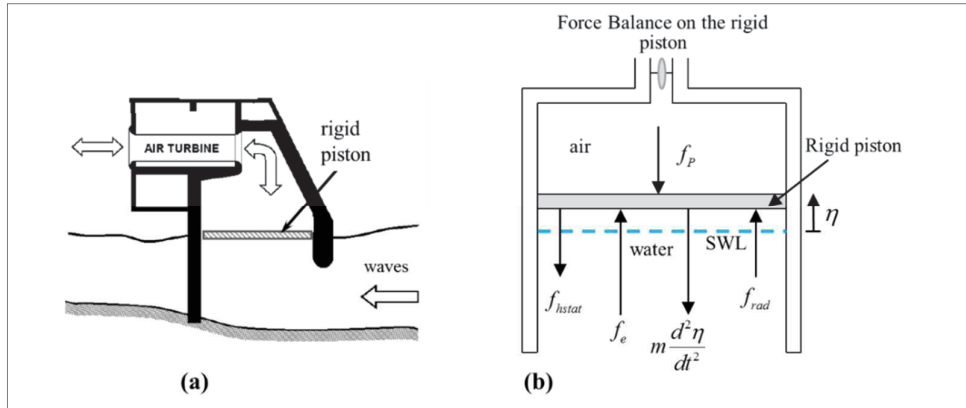


Figure 2-3: *Rigid piston model* schematization (a), modified from Falcão & Henriques (2016); forces acting on the rigid piston (b).

A force balance on the rigid plate leads to the dynamic equation of motion, a linear second order differential equation. The hydrodynamic coefficients m_a and B_r are real-valued functions of the frequency and can be regarded as properties of the structure. Indeed, it could be shown they are (apart from the dependence on the frequency) purely dependent on the geometry of OWC and on the water depth (Ricci, 2012). The explicit expression of the hydrodynamic coefficients m_a and B_r as function of the radiation potential Φ^R is the following (Ricci, 2012):

$$m_a = \rho_w \left(\iint_{S_b} \text{Re} [\Phi^R] n_z \cdot ds \right) \quad (2.15)$$

$$B_r = i\rho_w\omega \left(\text{Im} \iint_{S_b} [\Phi^R] n_z \cdot ds \right) \quad (2.16)$$

where S_b is the wetted surface of the OWC and n_z denotes the normal direction to the surface.

2.1.2. Uniform pressure distribution model

The *uniform pressure distribution model* allows for the distortion of the inner free surface of the OWC device, and its use is not restricted to large values of the ratio between the wave length and the OWC chamber dimensions. The model is applicable also at higher frequencies (i.e. lower wavelengths), since it does not assume any specific shape of the interior free surface.

The OWC device is efficient when working in a piston-like mode, i.e. when sloshing motions of the free water surface of the column, which are inefficient in terms of energy production, are avoided (Falnes, 2002). Using a model capable of predicting the sloshing motion is, therefore, useful to monitor the device's behaviour. The uniform pressure distribution model, unlike the rigid piston model, is suitable for this purpose. The model was proposed for the first time by (Falcão & Sarmento 1980), where a two-dimensional OWC was considered. The uniform pressure distribution model was generalized to fixed OWC with arbitrary geometries by Evans (1982). Later, the model was extended to floating OWC device in Falnes & McIver (1985).

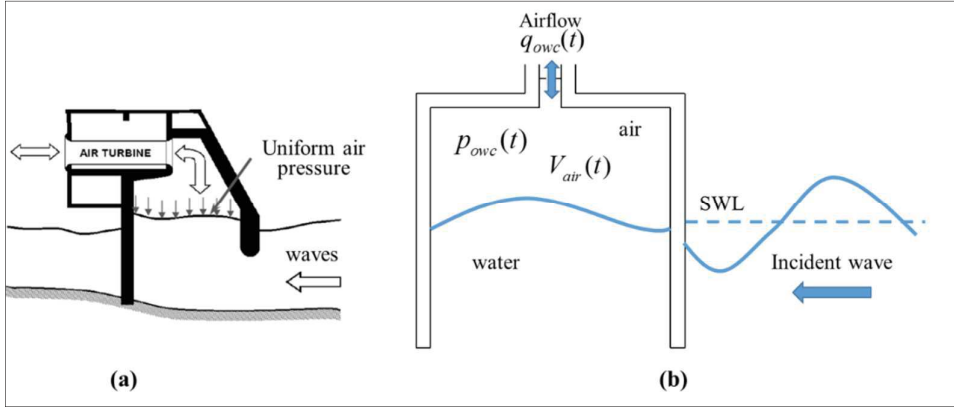


Figure 2-4: OWC device in the *uniform pressure distribution model* (a), adapted from Falcão & Henriques (2016); basic concepts of the model (air volume flux q_{owc} and pressure p_{owc}) (b).

In the uniform pressure distribution model, the concepts of body velocity and forces, adopted in the rigid piston model and, are replaced by those of air volume flux and air pressure (Fig. 2-4). A uniform pressure distribution on the free surface inside the OWC chamber is considered. Considering the instantaneous air volume inside the air chamber, $V_{air}(t)$, the air volume flux displaced by the motion of the free surface inside the OWC chamber, $q_{owc}(t)$, can be expressed as

$$q_{owc}(t) = -\frac{dV_{air}}{dt} \quad (2.17)$$

$q(t)$ can be decomposed in a radiation flowrate, q_r (i.e. the flowrate induced by the oscillating pressure p_{owc} in the chamber in absence of incident waves), and an excitation flowrate, q_e (i.e. the flowrate induced by the incident wave), as

$$q_{owc}(t) = q_r(t) + q_e(t) \quad (2.18)$$

Using the complex amplitude notation (i.e. indicating with Q_r , Q_e and P_{owc} the complex amplitudes of q_r , q_e and p_{owc} respectively), and under the assumption of linear wave theory (implying proportionality between the radiated flow rate and the radiated pressure, eventually with some phase difference), we may write:

$$Q_r = -(R_c + iR_s) P_{owc} \quad (2.19)$$

$$Q_e = \left(\frac{1}{a_t - i\beta_t} + R_c + iR_s \right) P_{owc} \quad (2.20)$$

where R_s and R_c are hydrodynamic coefficient named, respectively, *radiation conductance* and *radiation susceptance*, depending on the OWC geometry and on the frequency of the incident wave (Falnes, 2002), and a_t and β_t are the absolute flow velocity angle and the relative flow velocity angle, which are constitutive characteristics of the used air turbine.

2.1.3. Time domain, frequency domain and stochastic analysis for the OWC

The *rigid piston model* and *uniform pressure distribution model* can be solved in the time domain or in the frequency domain. When the hydrodynamic model assumes the incident waves to be monochromatic and the PTO system to be linear, the model can be solved in frequency domain. Regarding the PTO linearity, the condition is approximately satisfied if the OWC is equipped with a Wells turbine (Gato & Falcão 1984; Falcão & Justino 1999).

The frequency domain approach can be extended to consider irregular waves by means of linear superposition once a spectral distribution is provided.

When non-linear effects are significant, time domain solutions need to be implemented (Ricci et al. 2008). Non-linearity may be introduced in the system as a consequence of:

- (i) the air chamber thermodynamics, i.e. due to air compressibility spring like effects which may rise when large pressure oscillations take place in the OWC chamber (Falcão & Justino 1999; Lovas et al. 2010).
- (ii) the PTO system, which may be characterized by a non-linear behaviour (i.e. a non-linear relation between the relative pressure in the chamber and the induced air volume flow through the PTO). In contrast to Wells turbines, for air turbines of impulse type, the pressure-versus-flow rate relation is almost quadratic (Setoguchi et al. 2001).
- (iii) minor and major losses of the unsteady flow taking place in water (i.e. due to turbulence and vortex formation near the OWC front wall) or in the air flow (Cruz 2009).

- (iv) control strategies concerning the regulation of the air flow through the turbine by means of control valves (Falcão & Justino 1999).

The non-linear effects accounted for in the time domain models are typically associated to convolution integrals (usually referred to as memory functions), which take into account the effects that persist after the end of the motion, as in the Cummins equations in ship hydrodynamics. The radiation force f_{rad} in the *rigid piston model* and the radiation flow rate q_r in the *uniform pressure distribution model* can be expressed by convolution integrals as shown by Falcão & Justino (1995). Though computationally heavier, time domain analysis yields a time dependent performance. Time series of variables such as rotational speed of the turbine or the OWC power output are important to study phenomena like power oscillations induced by wave grouping or to develop control strategies for the OWC-PTO system (Lee et al. 1996; Brito-Melo et al. 2001).

When average values (i.e. the average OWC power output) are the variables of interest, stochastic analysis can be applied. The capability of predicting the average power output in a given sea state may be sufficient in preliminary stages of an OWC device design. Stochastic analysis have been often used to evaluate the average power output of an OWC when the aforementioned linear assumptions were considered acceptable (Falcão & Rodrigues 2002; Falcão 2002a; Falcão 2004; Camporeale & Filianoti 2007; Filianoti & Camporeale 2008). The stochastic approach has the advantage to reduce significantly the computational effort. The application of the stochastic modelling to OWC devices is based on the hypothesis that the dynamic behaviour of the system can be modelled by a set of linear differential equations and that input to the system, the sea surface elevation, has a Gaussian probability density function. Under these hypotheses, the theory of the random processes of the linear systems implies that the outputs of the system have a Gaussian distribution.

2.1.4. Approaches for the determination of hydrodynamic coefficients

In both the aforementioned hydrodynamic models for the OWC (the *rigid piston model* and the *uniform pressure distribution model*), the OWC hydrodynamic coefficients for the specific OWC geometry considered, which are frequency dependent, are required. These coefficients can be obtained analytically (determining velocity potential by solving diffraction and radiation problems for the OWC) or numerically.

Analytical solutions for Laplace equation, available only for simple geometries, e.g. cylindrical axisymmetric OWC with negligible wall thickness, are generally based on *eigenfunction expansion* or *matched eigenfunction expansions* methods (Yeung 1981). The *eigenfunction expansion* method is applied when the geometry of the problem allows the separation of Laplace equation and of the boundary conditions in different variables, reducing the problem to a system of Ordinary Differential Equations (ODE). The method was applied to model a two-dimensional OWC with thin vertical walls (Evans & Porter 1995), a cylindrical OWC with thin walls (Evans & Porter 1997), a two-dimensional floating OWC (Suzuki et al. 2005), a cylindrical OWC integrated in

a breakwater (Martins-Rivas & Mei 2009) and located on a coastal corner (Lovas et al. 2010). *Matched eigenfunction expansions* methods are applied for those problems in which it is impossible to expand the velocity potential in a single sum of eigenfunctions, and the solution of the problem is obtained by dividing the domain in different regions and defining an eigenfunction in each of them. *Matched eigenfunction expansions* were used by Şentürk & Özdamar (2012) to model the hydrodynamics of a fixed, two-dimensional device with a gap on the front wall, by Mavrakos & Konispoliatis (2012), to model a floating axisymmetric OWC, and by (Rezanejad et al. 2015) to model a dual-chamber OWC.

The aforementioned analytical methods are applicable only to relatively simple geometries, i.e. those whose boundary surfaces can be described by a section of a coordinate surface. Therefore, for more complex geometries, numerical solutions of the potential theory formulated OWC-wave interaction problem have to be found. This is generally done with Finite Element Methods (FEM) or Boundary Element Methods (BEM) (Yeung 1982). FEM applications to OWC hydrodynamic modelling are limited. Nader et al. (2012) developed a FEM model based on linear wave theory to study scattered waves for a single OWC and for an array of OWCs. They obtained results in agreement with previous analytical models. BEMs are usually preferred for the purpose of OWC modelling, since they require only boundary meshes, while FEMs need complete volume discretization, thus increasing the computational effort. The first application of a BEM code to the problem of an OWC was presented by Lee et al. (1996). Later, both linear (Brito-Melo et al. 2001; Delauré & Lewis 2003) and non-linear (Clément 1997; Josset & Clément 2007) BEM approaches have been applied to OWC modelling. Time domain BEM models were found to be feasible for capturing the fully nonlinear interaction between waves and the OWC structure, except for breaking-waves, overtopping and viscous flow separation. It has to be underlined that, as reported in Delauré & Lewis (2003), BEM applications are subject to specific difficulties when modelling enclosed domains, e.g. the chamber of an OWC, where the discontinuity between internal and external sources may induce relevant numerical errors, especially near resonance conditions.

Potential flow modelling of the OWC is widely used in the literature, by applying different concepts (*rigid piston model* and *uniform pressure distribution model*) to represent the OWC and different analytical/numerical techniques to determine the device hydrodynamic coefficients. At an early stage of an OWC device development, a *rigid piston model solved* in the frequency domain, associated with the use of BEM to compute the hydrodynamic coefficients, could be useful to perform a relatively quick and computationally inexpensive assessment of the performance of the considered design alternatives, even if non-linear effects are disregarded by such approaches. A *uniform pressure distribution model*, solved in the time domain and associated with BEM for the calculation of the hydrodynamic coefficients, would be feasible for capturing the nonlinear interaction between waves and the OWC device, except the effects associated with wave breaking, overtopping and viscous flow separation as well as with turbulence in water and air flows. The use of BEM

methods has, however, some inherent limitations when modelling enclosed domains, e.g. the chamber of an OWC, where the discontinuity between internal and external sources may induce relevant numerical errors, in particular near the resonant frequency.

2.2. Computational Fluid Dynamics modelling for OWC

All the models mentioned in the previous sections are based on potential flow theory. Important non-linear effects which may take place in OWC device functioning are not accounted for in this modelling approach, namely:

- (i) Effects due to wave breaking;
- (ii) Effects due to the fluid viscosity, turbulence and vortex shedding which may take place in proximity of the OWC front wall;
- (iii) Effects due to the air turbulence taking place during air mixing in the air chamber in the *inhalation phase* and the *exhalation phase* (see section 2.3).

In order to obtain a proper characterization of the aforementioned effects, a fully viscous solution method based on Navier-Stokes equations has to be implemented, by employing Computational Fluid Dynamics (CFD) techniques. While CFD modelling is an established option for the simulation of the PTO component of the OWC device, i.e. the air turbine (Torresi et al. 2004; Torresi et al. 2008; Torresi et al. 2009), the application of CFD techniques for the OWC hydrodynamic optimization is less applied compared to BEM or analytical modelling techniques. This is probably due to the high computational efforts associated with CFD modelling approaches: a CFD simulation of both the OWC hydrodynamics and aerodynamics (i.e. the thermodynamic processes in the air chamber) was not computationally affordable until recent years.

El Marjani et al. (2008) applied a computational fluid dynamics (CFD) technique to perform a numerical modelling of the air chamber of an OWC device, equipped with a radial impulse turbine, using the commercial CFD code FLUENT[®]. In that study, only the OWC air chamber and the air turbine were modelled, using a sinusoidal moving boundary to represent the free surface inside the OWC chamber. The hydrodynamic problem of the interaction between the submerged part of the device and the incident wave was, therefore, not considered. In the same framework, i.e. the study of the characteristics of the air-flow through the turbine, Paixão Conde & Gato (2008) performed a CFD study of the air-flow in a typical pneumatic chamber geometry of an OWC equipped with two vertical-axis air turbines. The computations of the airflow field were made using the commercial code FLUENT[®], and the reciprocating bidirectional airflow was imposed by prescribing a velocity inlet boundary condition.

The first CFD applications including both the hydrodynamics and aerodynamics of the OWC device, i.e. simulating both the air and the water by using a multiphase model, are in the studies of Senturk & Ozdamar (2011) and Zhang et al. (2012). Senturk & Ozdamar (2011) used the FLUENT[®] code to simulate the interaction

between regular waves and a two-dimensional cylindrical OWC with walls of negligible thickness, under the assumptions of viscous, incompressible and unsteady flow. The Volume of Fluid (VOF, Hirt & Nichols, 1981) method was used for the free surface tracking. The results were validated through the comparison with a simplified theoretical model (Hiramoto 1978), based on the theory of a compressible airflow and neglecting viscous losses. Comparing the results from the two models, a substantial agreement was found concerning the water elevation inside the OWC chamber, while up to 30% relative error (overestimation) was experienced for the air velocity through the chamber exit duct. The authors concluded that further CFD analysis should include compressibility effects.

Zhang et al. (2012) realized a two-phase incompressible Numerical Wave Tank (NWT) based on a level-set immersed boundary method (Cottet & Maitre 2004) to simulate a two-dimensional OWC, reporting a slight over-prediction of the device hydrodynamic efficiency compared with the small-scale experimental data by Morris-Thomas et al. (2007).

Recently, the open source CFD code OpenFOAM® was used by Iturrioz et al. (2013, 2014 and 2015) to simulate a fixed detached (i.e. not bottom standing) OWC device with a two-dimensional and a three-dimensional model. The model solves the three-dimensional Reynolds Averaged Navier–Stokes (RANS) equations for two incompressible phases using the VOF method for the free surface tracking. The model, once validated against experimental data from small scale tests, was used to analyse the hydrodynamics and aerodynamics in the OWC chamber, confirming the differences between *inhalation phase* and *exhalation phase* predicted by previous theoretical models (see *section 2.3*).

Kamath et al. (2015) used the open-source CFD code (REEF3D®) to study the interaction between a two-dimensional bottom standing OWC device and regular waves under the assumption of incompressible fluids. The results are also validated against the experimental results of Morris-Thomas et al. (2007) assuming a linear PTO (reproduced in the CFD model by a porous media); a significant effect of the applied damping on the device performance was found.

López et al. (2014 and 2016) used a two-dimensional commercial CFD model (Star-CCM+®) to study the performance of a bottom standing OWC device under regular and irregular waves and for different values of the applied turbine damping. The model solves the RANS equations with a standard $k-\varepsilon$ turbulence closure and was validated against laboratory experiments. The sensitivity of the OWC performance to the applied damping was evaluated for relatively large wave periods ($T=8-13$ s). As a result, differences up to 46% in the annual energy output of the OWC depending on the applied damping level were obtained.

Very recently, Elhanafi et al. (2016a, 2016b, 2016c) used an incompressible 2D RANS-based model (Star-CCM+®) to study the impact of the applied damping and of the asymmetry between the front and back wall of the OWC on the device performance, stressing again that the applied damping is a crucial parameter in the

OWC performance, and an increase in the device performance can be achieved by adopting asymmetric back and front walls.

Despite the growing research efforts on the subject and of the proven capability of CFD modelling to accurately reproduce the dynamics of OWC systems, up to date an extensive and combined study of the effect of the OWC geometry, the turbine damping and the incident wave conditions aimed at the optimization of the device has not yet been performed.

Advanced CFD techniques are needed to fully capture the non-linear interaction between waves and the device (i.e. viscous flow separation, turbulence and wave breaking) and to properly take into account the most relevant hydrodynamic and thermodynamic processes involved in the interaction between waves, OWC and air in the chamber. Quite recently, CFD models of the OWC have been implemented, however such models were not used to systematically study the combined effect of the OWC geometry and of the damping applied by the turbine on the OWC device performance. Moreover, up-to-date, no compressible CFD models have been used to simulate the OWC.

2.3. Thermodynamics of the OWC and air compressibility

Most of the efforts in the field of OWC modelling focus on the system hydrodynamics. The aerodynamic domain (i.e. the air chamber and the ducts connecting the air chamber with the air turbine), coupled with the hydrodynamic domain through the radiation problem and free surface dynamics, is usually modelled using mass conservation principles and based on the assumption of isentropic air compression/decompression in the OWC chamber. The thermodynamic processes in the OWC air chamber may indeed significantly affect the OWC system dynamics.

The air chamber volume above the water level is subject to an oscillating relative pressure. Consequently, the air density also varies in time according to some pressure-density relation. In OWC devices at prototype scale, the thermodynamic effects related to air compressibility may be crucial for the system dynamics, since a relatively large volume of the air chamber is needed to prevent the water from reaching the turbine in the most energetic sea states (Martins-Rivas & Mei 2009; Sheng, Thiebaut, et al. 2013; Falcão & Henriques 2014).

The spring-like effect of air compressibility in OWC devices was theoretically modelled for the first time by Sarmiento & Falcão (1985) and by Jefferys & Whittaker (1986), under the assumption of isentropic compression and decompression in the OWC chamber (i.e., an isentropic relation is assumed between the air density and pressure). If the losses in the flow due to viscous effects were negligible, the process would be reversible, therefore isentropic. The assumption of isentropic processes was also adopted in later studies (Perdigão & Sarmiento 2003; Sheng, Alcorn, et al. 2013).

More refined theoretical models, in which the viscous losses in the air turbine induce variation in the airflow entropy, were developed and applied by Falcão & Justino

(1999). The theoretical analysis was performed under the assumption of adiabatic processes in the OWC chamber. The adiabatic assumption is justified, since the expected temperature oscillations in the air chamber are relatively small, and their time scale (of the order of the wave period with 5-10 seconds) is too short to significantly affect the heat transfer through the OWC walls and through the air-water interface (Falcão & Justino 1999; Falcão & Henriques 2014). In the theoretical study of Falcão & Justino (1999), significant differences are found between the *inhalation phase* ($p_{owc} < 0$) and the *exhalation phase* ($p_{owc} > 0$). During the *inhalation phase*, the air in the OWC chamber is de-pressurised, and its density and temperature are lower than those of the atmosphere. When the air at atmospheric conditions is inhaled in, a highly turbulent mixing process occurs inside the air chamber while the airflow with specific entropy higher than that of the atmosphere enters the OWC. During the *exhalation phase*, the air in the OWC chamber remains approximately isentropic, while a complex mixing process takes place outside of the air chamber.

Based on the ideal gas assumption, a polytropic relationship between p_{owc} and the air chamber density ρ_a was proposed by Falcão & Henriques (2014), as:

$$\frac{p_{owc} + p_{atm}}{\rho_a^\theta} = \frac{p_{atm}}{\rho_{atm}^\theta} \quad (2.21)$$

where p_{atm} and ρ_{atm} are the atmospheric air pressure and density, respectively, and θ is a polytropic exponent related to the average efficiency of the air turbine.

The relevance of the thermodynamic effects associated with air compressibility for OWCs systems poses additional issues when physical modelling of such a device is performed. In fact, to fully respect dynamic similarity between model and prototype, the scale ratio for the volume of the air chamber should not necessarily correspond to the scale ratio for the submerged part of the converter N (Falcão & Henriques 2014). If the same scale ratio is adopted, the exact dynamic similarity of air compressibility spring-like effects would require the atmospheric pressure during the experimental testing to be much smaller than the atmospheric pressure at prototype scale. This would be hardly feasible in most of the available testing facilities.

Consequently, for the more realistic case with the atmospheric pressure being the same at both scales, it is necessary to use a volume of the air chamber larger than that would result from Froude scaling. This result was underlined for the first time in the theoretical works of Sarmiento & Falcão (1985) and Jefferys & Whittaker (1986), and was confirmed later in other papers (Sarmiento 1993; Weber 2007).

One possible way of achieving the required volume scale factor for the OWC air chamber in the laboratory would be to connect the air chamber to a rigid reservoir of appropriate volume (Falcão & Henriques 2014), but this might pose the following problems: (i) the connection between the reservoir and the air chamber may introduce additional forces and moments on the system; (ii) the dynamic of the system may be severely affected, particularly for the case of floating OWCs; (iii) for small scale physical models, the additional volume of the reservoir may be so large that it might become practically non-feasible.

The effect of air compressibility on the performance of an OWC device was also theoretically analysed by Thakker et al. (2003), under the hypothesis of isentropic compression/decompression processes. A 5-8% reduction in the device conversion efficiency was found as a consequence of the compressibility of the flow. Sheng et al. (2013), conducted an experimental study considering the airflow through an orifice connected to a chamber pressurized and depressurized by the motion of a piston. In their work, a power loss due to air compressibility of about 2% was found for a relative pressure in the chamber of about 2.2 kPa. Very recently, Elhanafi et al. (2017) applied a compressible CFD model to evaluate air compressibility effects for a fixed, detached OWC, finding a reduction up to 12% of the maximum device efficiency due to air compressibility near resonance conditions. Furthermore, the air compressibility effects, in terms of discrepancies between results at different model scales, showed a dependence on the turbine damping and the incident wave height.

It is worth to note that, at present, the effect of air compressibility was only assessed on a restricted set of reference cases, and a systematic CFD study of this phenomenon has not been performed.

It is recognised that air compressibility may have a relevant role in the system dynamics in OWC devices at prototype scale. Moreover, in small scale laboratory tests, an appropriate simulation of the thermodynamic effects associated with air compressibility in the OWC chamber is difficult.

In fact, to fully respect dynamic similarity between model and prototype, the scale ratio for the volume of the air chamber should not necessarily correspond to the scale ratio for the submerged part of the converter. Hence, a volume of the air chamber larger than the one resulting from Froude scaling would be needed. Moreover, a systematic evaluation of the error induced by neglecting air compressibility in modelling OWC devices has not yet been performed, underling an important gap of knowledge.

2.4. OWC-air turbine interaction

The air turbine is the element in the conversion chain in which the major energy losses occur (Falcão 2004). In fact, OWC air turbines operate in more demanding conditions than turbines for conventional applications (i.e. under nearly steady flows): the air flow is reciprocating, random and variable on several time scales (from wave to wave to seasonal variations).

The time-average efficiency of an air turbine in an OWC is substantially lower (ca. by 20-30%) than that of a conventional turbine, and it hardly exceeds about 50–60% (Takao & Setoguchi 2012). Most self-rectifying air turbines developed and tested for OWC devices are axial flow machines of two basic types:

- (i) Wells turbines, (Raghunathan et al. 1982);
- (ii) Self-rectifying impulse turbine (Setoguchi et al. 2001).

The Wells turbine (Fig. 2-5, a), with several design configurations, is the most common type used for OWC prototypes and has thus been addressed by a large number of aerodynamic studies on geometry optimization and performance evaluations (Gato & Falcão 1988; Gato et al. 1991; Brito-Melo et al. 2002; Setoguchi et al. 2003; Torresi et al. 2008; Shaaban & Abdel Hafiz 2012).

The main limitations of the Wells turbine are: (i) the large efficiency drop when the flow rate exceeds the stall-free limit; (ii) the small range of flow rates over which the turbine operates with relatively high efficiency; (iii) the high operational speed and the associated high noise generation. In numerical or physical modelling of OWC devices, an important characteristic of the Wells turbine is the linear relation between the air flowrate and the pressure head, as mentioned in the section 2.1.3.

The axial and radial flow impulse turbine exhibits a smoother efficiency curve, whose peak, however, hardly exceeds about 50%, unless variable geometry (with its higher mechanical complexity) is used, which has had so far limited applications (Takao et al. 2000). A new type of radial-flow self-rectifying turbine (Fig. 2-5, b and c), the so called biradial turbine, was recently proposed by Falcão et al. (2013a and 2013b). The model testing results (Falcão et al. 2013b) for this turbine showed a peak efficiency of over 80% and a mean efficiency in random waves greater than 70%.

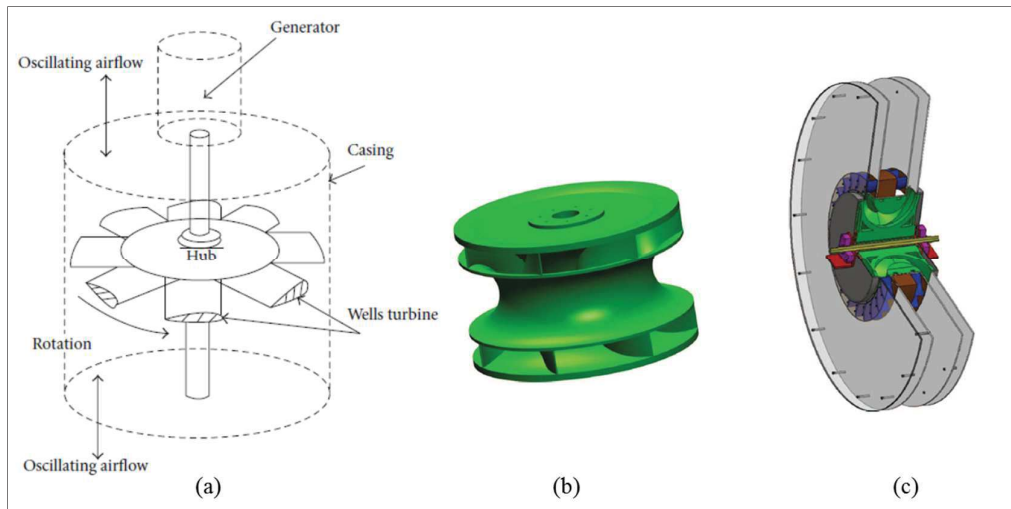


Figure 2-5: Wells turbine (a), from Takao & Setoguchi (2012); rotor of a biradial turbine (b) and whole biradial turbine (c), from Falcão et al. (2013).

The bi-radial turbine appears to be operatively suitable over a much wider flowrate range compared to the Wells turbine, and to have better self-starting characteristics. Since the concept is new, however, large scale testing still needs to be performed, and research at a fundamental level is required to optimize the turbine characteristics.

For impulse turbines (i.e. including bi-radial turbine), the relation between the air flowrate and the pressure head is almost quadratic. Moreover, the behaviour of different turbine types should be considered when planning the testing of an OWC model, in order to accurately reproduce the overall system behaviour (e.g., in physical

scale model on OWC, linear PTO might be represented by porous membranes, while non-linear PTO effects are best reproduced using orifice of variable ratio).

It should be underlined that the overall performance of an OWC depends upon the efficient energy absorption of the OWC chamber itself, namely on the fraction of the incident wave energy the device can convert into pneumatic energy (*pneumatic efficiency*), as well as on the *turbine efficiency*.

The pneumatic efficiency of the OWC chamber is, in turn, a function of the pressure difference across the turbine (i.e., of the applied turbine damping). To ensure an optimal plant performance, the turbine should:

- (i) Maximize the conversion of pneumatic power over the flow rates range produced by the OWC;
- (ii) Apply the optimal damping level in order to maximize the conversion of wave energy to pneumatic energy.

The optimal damping level is a function of the OWC device geometry and of the incident wave characteristics, mainly the incident wave frequency, as shown in the theoretical study of Curran et al. (1997) and the laboratory study of Thiruvenkatasamy & Neelamani (1997). These results were confirmed also by more recent studies based both on potential flow modelling (Falcão et al. 2012; Falcão et al. 2014) and on CFD modelling (Luo et al. 2014; Kamath et al. 2015; Lopez et al. 2016). Curran et al. (1997) showed that far from the resonance condition, the applied damping should be higher than the optimal damping at resonance condition, since higher damping values lead to an increased frequency bandwidth over which the OWC device exhibits a relatively high performance.

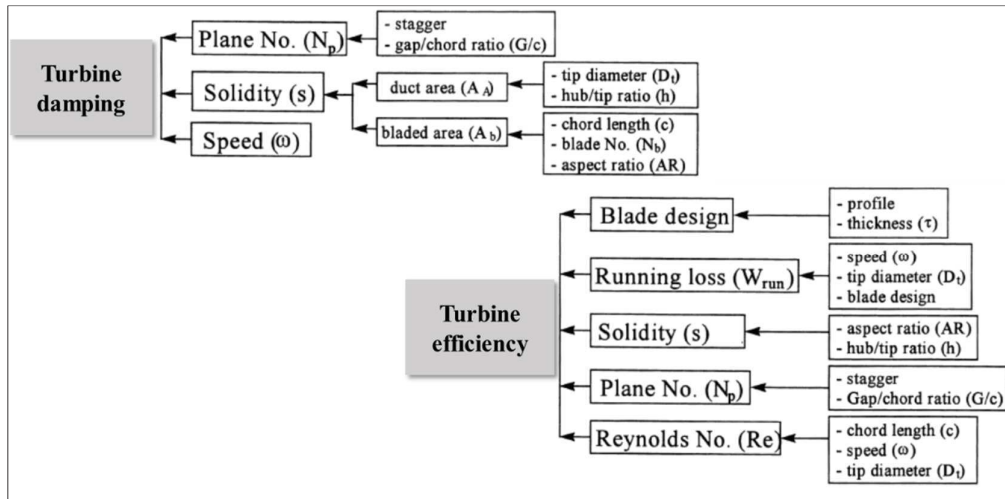


Figure 2-6: Parameters affecting the damping and the efficiency of a Wells turbine (modified from Curran et al. 1997).

The efficiency of the turbine is a function of different design parameters of the turbine itself, and of its working conditions, which, in turns, also affect the damping applied by the turbine (Fig. 2-6). Once a characterization of the optimal damping to

be applied on the OWC chamber is obtained, the turbine should be specifically designed to induce the optimal damping while preserving a relatively high efficiency. An accurate characterization of the wave climate in the location chosen for the OWC power plant is therefore needed in order to properly match the turbine with the OWC chamber.

For the study or the development of an OWC system, it can be concluded that the OWC geometry and the air turbine should be considered together, since they are effectively coupled; i.e. the turbine characteristics (in particular the turbine damping) should be considered as design parameters to be optimized in order to properly define the best OWC design for a particular wave climate. Moreover, the recently proposed bi-radial impulse turbine (Falcão et al. 2013b), show higher values of peak efficiency (over 80%) when compared to Wells turbines. This kind of turbine, characterized by a quadratic relation between pressure drop and volume air flow, might therefore be considered in the study of an OWC system aimed at the overall performance optimization.

2.5. Index for evaluating the OWC performance

In the context of evaluating the OWC device performance in terms of wave energy extraction capability, the performance measure greatly vary from one source to another (Pecher 2012).

In order to allow a consistent comparison between the hydraulic and pneumatic wave energy conversion performance of different OWC device, as well as to more generally compare with the performance of other Wave Energy Converter (WEC) concepts, Babarit (2015) recently proposed to adopt, as a common performance measure, the capture width ratio of the device, defined as:

$$\varepsilon_{owc} = \frac{\Pi_{owc}}{\Pi_{wave} \cdot B} \quad (2.22)$$

where Π_{owc} is the power absorbed by the OWC device, Π_{wave} is the incident wave power and B is a characteristic length of the device (generally, the chamber length transversal to wave propagation direction for OWCs).

The capture width ratio ε_{owc} , also referred to in the literature as non-dimensional performance (Pecher 2012), or efficiency (Evans & Porter 1995, Morris-Thomas et al. 2007; Zhang et al. 2012, Kamath et al. 2015) directly reflects the fraction of the far field available wave power that is adsorbed by the device, and therefore allows to account for both the hydraulic and the pneumatic conversion efficiency of the device (Fig. 1-1).

Despite the different way the capture width ratio is referred to in the literature, far field incident wave conditions are generally used as reference for computing the incident wave power. This is a common practice when considering the wave energy

extraction performance of OWCs (Evans & Porter 1995; Falcão 2004; Morris-Thomas et al. 2007; Zhang et al. 2012, Falcão et al. 2012, Carballo & Iglesias 2012). In this way, the local perturbation of the flow induced by the presence of the device, which is actually (for a fixed wave condition) a specific characteristic of the device itself, is directly accounted for in the index used to evaluate the performance, thus allowing a more consistent comparison between the performance of different OWC design alternatives.

In order to adopt a performance index allowing, from one side, to comparatively evaluate the performance (both hydraulic and pneumatic) of different OWC design alternatives properly, and from the other side to consistently compare with different WEC technologies, the capture width ration ε_{owc} should be used.

2.6. Summary and implications

The review and analysis of the current knowledge and models for points out the following specific issues that need to be taken into account in the modelling the behaviour of OWC devices:

- (i) The water flowing past the front lip may induce vortex shedding and hence turbulent flow within the vicinity of the OWC front wall (*turbulence modelling*);
- (ii) The incident wave-field and the pressure oscillation inside the air chamber are likely to be at least weakly nonlinear (*non-linear modelling*);
- (iii) The process of *inhalation* and *exhalation* in the air chamber involve complex and turbulent mixing with the air from the atmosphere (*turbulence modelling*) as well as possible water droplets suspended within the airflow (*two phases modelling*);
- (iv) The thermodynamics effects related to air compressibility may be crucial in the system dynamics at prototype scale. It should be underlined that the current knowledge suggests that compressibility effects are to be taken into account for an appropriate simulation of the device behaviour (*modelling air compressibility*).
- (v) Aiming at the optimization of the device performance, the mutual effect of the damping applied by the air turbine and the OWC chamber geometry has to be considered. It was proven that the optimal damping for the chamber depends on the OWC geometry and on the wave climate. The optimization of the hydraulic chamber alone cannot be reached, and a combined turbine/OWC optimization is therefore needed (*modelling wave-OWC-air chamber-turbine interaction*).

Moreover, site specific optimization is needed, since the wave climate (and particularly the incident wave period) has a key effect on the system performance in terms of conversion efficiency, corresponding to different OWC geometries.

The available numerical modelling approaches to simulate the hydrodynamics of OWC devices can be divided in two main categories (Tab. 2-1):

- (i) Potential flow modelling using different concepts (*rigid piston model* and *uniform pressure distribution model*) to represent the OWC and different analytical/numerical techniques to determine the device hydrodynamic coefficients;
- (ii) Navier Stokes equations solvers (called hereafter *CFD models*).

Table 2-1: Summary of most common modelling approaches for the hydrodynamic modelling of OWC device.

<i>Hydrodynamic model</i>	<i>Modelling method for hydrodynamic coefficients</i>	<i>Wave modelling</i>	<i>Viscous effect modelling</i>
Potential flow theory, including diffraction-radiation theory	Analytical	Linear, regular waves mainly	Possibly taken into account as linear resistance losses (not accurately modelled)
	Linear BEM	Linear, regular and irregular waves (non-breaking waves)	
	Non-linear BEM	Non-linear, regular and irregular waves (non-breaking waves)	Possibly taken into account as resistance losses
Navier Stokes Equations solvers (CFD)	-	Fully non-linear, breaking, non-breaking and broken waves	Complete viscous solution

CFD techniques are needed to fully capture the non-linear interaction between waves and the device (i.e. viscous flow separation, turbulence and wave breaking) and to properly consider the most relevant hydrodynamic and thermodynamic processes involved in the interaction between waves, OWC and air in the chamber, including the turbulent mixing mechanisms associated with air *inhalation* and *exhalation* and *compressibility effects* in the air chamber.

Numerical wave tanks (NWT) using CFD modelling have been applied in recent years to simulate the hydrodynamics and aerodynamics of OWC devices. The suitability of this modelling approach to accurately analyse the OWC dynamics and the effect of different geometries and turbine damping on the performance of the device has been demonstrated in several studies. However, a combined study of the effect of the OWC geometry and of the turbine damping aimed at the optimization of the device has not yet been performed. The importance of this knowledge gap must be

underlined since the combined optimisation of the OWC geometry and the turbine damping proved to be crucial for OWCs optimization.

Site specific dimensioning and optimization of the device was found to be fundamental, site specific studies generally refer to sea states representative of highly energetic wave climates (e.g. Oceanic ones), characterized by higher and longer waves than those of short fetch (or moderate) wave climates such as those in the Mediterranean Sea (Liberti et al. 2013; Vannucchi & Cappiotti 2013). An optimization of OWC devices has not yet been performed for moderate wave climates.

Moreover, a systematic evaluation of the effect of neglecting air compressibility in physical, numerical and analytical modelling of OWC devices is not yet available, so that correction factors to account for this effect have not yet been proposed.

2.6.1. Specification of objectives

Based on the results of the review and analysis of the current knowledge and models, the objectives of the PhD thesis may be specified as follows:

- (i) Systematic study of the combined effect of the geometry and of the damping applied by the turbine on the pneumatic conversion efficiency of a fixed detached OWC device, taking into account all the relevant phenomena in the OWC hydraulics and thermodynamics.
- (ii) Elaboration of a knowledge base to determine the optimal geometrical parameters of OWC devices for the Mediterranean wave climate, considering the device capture width ratio as a performance parameter.
- (iii) Elaboration of a knowledge base to determine the optimal characteristics, in terms of the applied damping of non-linear air turbines (e.g. among other turbines, biradial turbine was found to have the best performance on a wider range of air flowrates). This would allow developing turbines particularly suited for the Mediterranean wave climate, providing a useful tool for the industry sector of wave energy turbines manufacturers and filling a recognized gap of knowledge.
- (iv) Evaluation of the error induced by neglecting the effect of air compressibility in modelling OWC devices, and provision of correction factors for the results of incompressible numerical models and for the results from small-scale laboratory testing of OWC devices. These results will provide useful guidelines for the scientific community in order to control and correct scale effects that generally affect the small-scale experimental modelling.
- (v) Development of a simple conceptual model allowing to predict the pneumatic efficiency of the OWC based on its geometrical parameters, the damping applied by the turbine and the incident wave parameters (wave periods and wave height). The conceptual model might be applied as a

design supporting tool, thus avoiding the use of a more demanding computational tool in the process of the OWC device optimization.

2.6.2. Specification of methodology

The methodology adopted to achieve the aforementioned objectives is schematically summarized in the flowchart in Figure 2-7 and specified as follows.

In *Chapter 3*, a simplified frequency domain *rigid piston model* of the OWC device is first applied in order to perform a relatively quick and computationally inexpensive evaluation of the effect of different design parameters on the performance of the OWC device, thus allowing to select the most relevant device to be further investigated later using advanced numerical modelling. The frequency domain model is also used to get a preliminary characterization of the range of values of the water level, air pressure and air velocity inside the chamber, which might be useful for the set-up of laboratory experiments on the OWC device³.

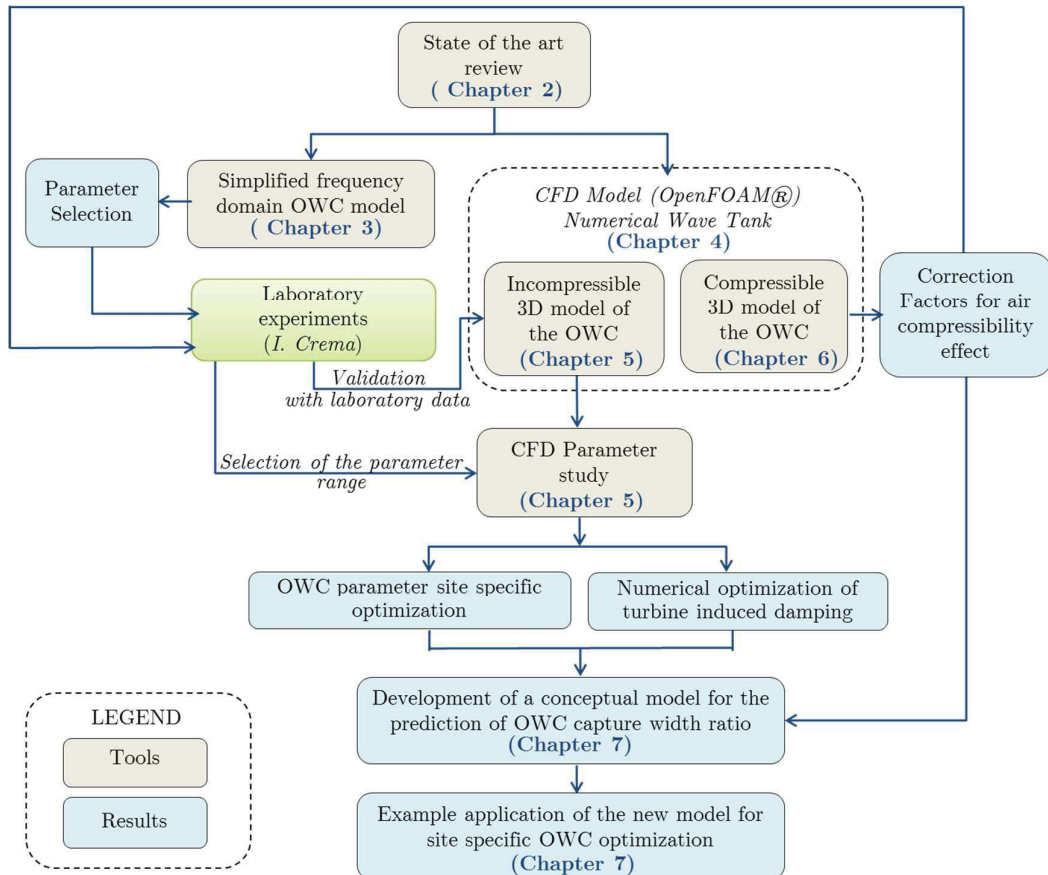


Figure 2-7: Methodology adopted in the *PhD thesis*.

³ The laboratory tests on the OWC device are carried out by I. Crema (Crema et al. 2016).

In *Chapter 4*, a Numerical Wave Tank (NWT) in the open-source CFD code OpenFOAM® is used. Different wave generation approaches are alternatively compared. Wave generation and propagation along the NWT is validated with laboratory data, in order to select the most suitable approach to be used for the simulation of the OWC device.

In *Chapter 5*, a three-dimensional, incompressible model of the OWC device, in OpenFOAM®, is validated with laboratory experiments (Crema et al. 2016) and used to perform a systematic parameter study aimed at the device optimization in moderate wave climates. The effect of the turbine damping is reproduced by using orifice of different aperture in order to reproduce a non-linear damping, representative of impulse turbines. A preliminary analysis of the results of the laboratory experiments is carried out in order to select the the range of the OWC parameters to more extensively explore by means of the CFD model. The numerical model is then applied to enlarge the number of evaluated configurations within that range, thus allowing to refine the selection of the optimal OWC geometry.

In *Chapter 6*, a compressible CFD model is used to simulate the OWC device at different model scales in order to quantify the scale effects related to air compressibility and to determine correction factors for the results of small-scale model tests in the laboratory as well as to those of incompressible numerical simulations.

In *Chapter 7*, a conceptual Multiple Regression Model (MRM) is developed, allowing to predict the OWC capture width ratio given the wave parameters, the geometrical parameters of the OWC device and the turbine damping as input variables. The model, based on dimensional analysis, is formulated by using the results of the CFD parameter study. The new MRM model is then adjusted by applying the correction factors for air compressibility proposed in *Chapter 6*. The relevance of the MRM in in the OWC optimization process is demonstrated by an example application to a selected installation site in the Mediterranean Sea.

CHAPTER 3

Analytical model of a fixed OWC device in the frequency domain

Among the different approaches proposed for OWC modelling (see *Chapter 2*), a simplified and less demanding model (from the point of view of computational time) might be useful in the preliminary stages of a device development. It may help to identify the parameters mostly affecting the OWC capture width ratio, i.e. those parameters to be optimized by means of more advanced numerical simulations or laboratory tests. Moreover, in the planning phase of small-scale model tests, such a simplified model might be used to preliminary specify the variables to be measured (e.g. pressures of the air, water levels in the air chamber) and the appropriate locations of the sensors.

In *this chapter*, an analytical approach, based on the *rigid piston model* of a fixed (i.e. not floating) OWC device, detached from the sea bottom and having a cylindrical shape, is applied in the frequency domain. The model is used in combination with a stochastic approach to deal with irregular waves.

The model enables to preliminary asses the expected range of pressure (up to 20 mbar) and airflow velocity (up to 30 m/s) in the air chamber. The latter are required to set-up laboratory experiments⁴, and for the selection of the relevant design parameters to be considered in a further optimization phase by using CFD modelling (*Chapter 5*).

3.1. Description of the rigid piston model

In the analytical model a cylindrical OWC of radius r and draught D (Fig. 3-1), subject to the action of unidirectional waves in a constant water depth h , is considered. The device is fixed to the sea bottom and the only possible motion mode is the vertical oscillation of the water column (heave motion). The *rigid piston model* is considered, and it is solved in the frequency domain (Robinson 1982; Watts et al. 1985; Nunes et al. 2011; Falcão et al. 2012; Karami et al. 2012; Gomes et al. 2012). The model is based on the hypothesis of incompressible and irrotational flow, and linear wave theory

⁴ The laboratory experiments on the OWC device, at model scale 1:50, are performed by Crema et al., 2016.

is applied. The OWC back wall G is supposed to be long enough (i.e. $G > \lambda/2$, where λ is the incident wave length) to reflect totally (100%) the incident wave. The model is completely linear, so a linear turbine for the PTO of the system is assumed (which is approximately the case if a Wells turbine is adopted).

The limitations of this modelling approach are well known (e.g. completely neglecting non-linear and viscous effects, possibly non-realistic pressure distribution inside the OWC chamber for high values of the ratio of the OWC chamber width in wave propagation direction to the incident wave length λ). However, given the purpose of the model application in the present section (preliminary characterization of the range of the involved variables and relevant parameter selection) the aforementioned limitations are deemed acceptable.

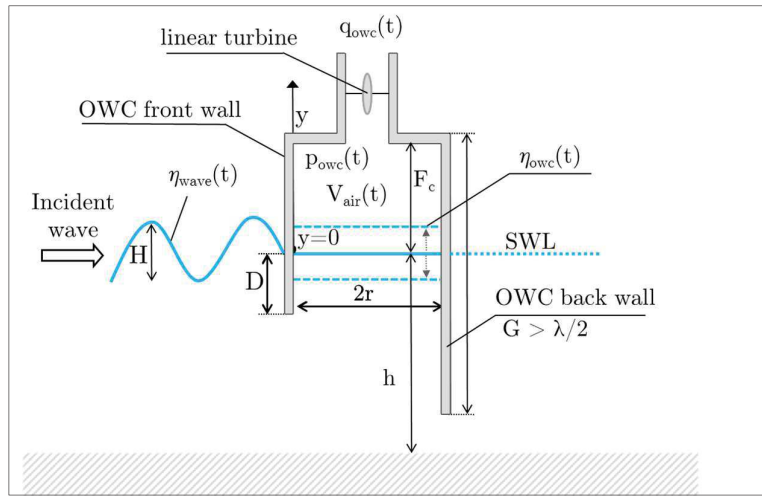


Figure 3-1: Fixed cylindrical OWC device considered in the rigid piston model.

3.1.1. OWC hydrodynamics and aerodynamics

The forces acting on the water column, considered as a rigid piston oscillating in heave, are:

- (i) excitation force, f_e , due to the hydrodynamic pressure caused by the incident wave;
- (ii) hydrostatic force, f_{hstat} , due to the hydrostatic pressure;
- (iii) hydrodynamic force, f_{rad} , due to the radiated wave induced by the pressure oscillation on the inner free surface (Sarmiento & Falcão 1985);
- (iv) force due to the air pressure oscillation in the air chamber, f_p , which is a function of the free surface and of the damping induced by the turbine

$$f_p = f\left(S, turbine \text{ damping}, \frac{d\eta_{owc}}{dt}\right) \quad (3.1)$$

where S is the area of the OWC horizontal cross section and η_{owc} is the vertical displacement of the water surface inside the OWC chamber.

The force balance on the water column is

$$f_e + f_{hstat} + f_{rad} + f_P = m_w \cdot \frac{d^2 \eta_{owc}}{dt^2} \quad (3.2)$$

and the equation of motion for the heaving rigid piston can be written as

$$m_w \cdot \frac{d^2 \eta_{owc}}{dt^2} + S \cdot \rho_w \cdot g \cdot \eta_{owc}(t) + S \cdot p_{owc}(t) = f_e + f_{rad} \quad (3.3)$$

where m_w is the mass of the rigid body, ρ_w is the water density, g is gravitational acceleration, and p_{owc} is the relative air pressure in the OWC chamber.

Within the context of linear wave theory (Airy theory), considering the water surface displacement for a progressive cosine wave

$$\eta = \frac{H}{2} \cos(kx - \omega t) \quad (3.4)$$

the dynamic component of the associated pressure, vertically distributed over the water column, is as follows

$$p_{wave} = \rho_w \cdot g \cdot \eta \cdot \frac{\cosh(k(h+y))}{\cosh(kh)} \quad (3.5)$$

where H is the incident wave height, ω is the wave angular frequency, k is the wave number, obtained solving the linear dispersion relation $\omega^2 = kg \tanh(kh)$ for water depth h .

The excitation force due to the incident wave acting at a water level equal to the OWC front wall draught D may, therefore, be expressed as

$$f_e = 2 \cdot \eta \cdot S \cdot \rho_w \cdot g \cdot \frac{\cosh(k(h-D))}{\cosh(kh)} \quad (3.6)$$

where the assumption of complete reflection of the incident wave on the back wall is made. The radiation force f_{rad} can be expressed in terms of frequency dependent added mass m_a , and radiation damping B_r (Karami et al. 2012).

$$f_{rad}(t) = \left(m_a \frac{d^2 \eta_{owc}}{dt^2} + B_r \frac{d\eta_{owc}}{dt} \right) \quad (3.7)$$

The air in the OWC chamber is modelled as an ideal gas, and the processes of compression and decompression of the air are assumed to be isentropic as in Falcão & Justino (1999). The mass air flow rate through the turbine (assumed positive for the *exhalation phase*) is given by

$$\frac{dm}{dt} = -d(\rho_a V_{air}) / dt \quad (3.8)$$

where ρ_a is air density and V_{air} is the volume of air in the chamber. With the isentropic process assumption, the mass air flow dm/dt can be related to the pressure oscillation inside the OWC air chamber as

$$\frac{dm}{dt} = \rho_a q_{owc} - V_{air}(t) \frac{1}{c^2} \frac{dp_{owc}}{dt} = \rho_a q - (V_0 + \eta_{owc}(t)S) \frac{1}{c^2} \frac{dp_{owc}}{dt} \quad (3.9)$$

where c is the speed of sound in air, V_0 is the air chamber volume in unperturbed conditions, q_{owc} is the volume flow rate. In the hypothesis of small values of $\eta_{owc}(t)S$

compared to the volume V_0 , the term can be neglected in Eq. 3.9, obtaining a linear equation

$$\frac{dm}{dt} = \rho_a q - V_0 \frac{1}{c^2} \frac{dp_{owc}}{dt} \quad (3.10)$$

The effect of the turbine is introduced in the model considering the dimensionless coefficients of flow rate (ξ) and pressure head (Ψ), according to the definitions of Falcão & Justino (1999).

$$\xi = \frac{dm/dt}{\rho N_T D_T^3}; \quad \Psi = \frac{p_{owc}}{\rho N_T^2 D_T^2}; \quad (3.11)$$

where N_T is the turbine rotational speed in radians per unit time, D_T is the turbine diameter and ρ is a reference density, here assumed equal to the atmospheric air density ρ_a . For a linear turbine, $\xi = K_T \Psi$, where K_T is a constant dependent on the turbine geometry, but not on its diameter D_T and rotational speed N_T (Gato & Falcão 1984). In dimensional form, it is possible to write

$$\frac{dm}{dt} = \frac{K_T D_T}{N_T} p_{owc} \quad (3.12)$$

where $K_T D_T / N_T$ gives the dimensional turbine damping. Eq. 3.12 expresses a linear relationship between the mass flow rate dm/dt and the pressure fluctuation inside the OWC air chamber p_{owc} . Eq. 3.10 can, therefore, be written as a linear differential equation

$$\frac{K_T D_T}{N_T} p_{owc} + \frac{V_0}{c^2} \frac{dp_{owc}}{dt} = \rho_a q_{owc} \quad (3.13)$$

Considering the complex representation of the involved parameters and applying Fourier transform, the linear system arising from Eq. 3.3 and Eq. 3.13 may be written in the frequency domain in terms of

$$\left\{ f_e, f_{rad}, p_{owc}, q_{owc}, \eta_{owc}, \frac{d\eta_{owc}}{dt}, \frac{d^2\eta_{owc}}{dt^2} \right\} = \text{Re} \left(\left\{ A_w \Gamma_h, F_{rad}, P_{owc}, Q_{owc}, H_{owc}, i\omega H_{owc}, -i\omega^2 H_{owc} \right\} e^{i\omega t} \right) \quad (3.14)$$

where Γ_h is the excitation force amplitude per unit of incident wave amplitude, and F_{rad} , P_{owc} , Q_{owc} and H_{owc} are the complex amplitudes of radiation force, relative pressure inside the OWC chamber, air volume flow rate and surface displacement, respectively.

The radiation force F_{rad} may be related to the hydrodynamic coefficients m_a and B_r and to H_{owc} as:

$$F_{rad} = \left(-\omega^2 m_a + i\omega B_r \right) H_{owc} \quad (3.15)$$

Introducing the transfer function Λ of the pressure P_{owc} frequency response to the flow rate Q_{owc} from Eq. 3.12, the equation representing the lumped model of the air chamber aerodynamic can be written as

$$P_{owc} = \left(i\omega \frac{V_0}{\rho_a c^2} + \frac{K_T D_T}{\rho_a N_T} \right)^{-1} \cdot Q_{owc} = \Lambda \cdot Q_{owc} \quad (3.16)$$

where $Q_{owc} = -i\omega SH_{owc}$.

The overall linear system describing the OWC dynamic is, therefore

$$\begin{cases} (-\omega^2 (m_w + m_a) + i\omega B_r + \rho_w g S) H_{owc} + S P_{owc} = A_w \Gamma_h \\ P_{owc} = \Lambda Q_{owc} \end{cases} \quad (3.17)$$

3.1.2. Stochastic approach to OWC capture width ratio

In order to preliminary evaluate the effect of different OWC geometrical parameters on the average power output of the device, the frequency domain model is combined with a stochastic approach (Falcão & Rodrigues 2002; Falcão 2002 and 2004), that allows to also account for irregular waves. Considered the aims of the model presented in this section (i.e. to obtain a preliminary characterization of the effect of design parameters on the device capture width ratio, aimed at the selection of the most relevant parameters to be later further investigated by means of CFD modelling) a stochastic approach is judged to be sufficient.

In the stochastic approach, the wave climate is represented by a set of stationary sea states with a given frequency spectrum. Each sea state is supposed to be characterized by a Gaussian probability density function of the surface elevation $f(\eta)$, an assumption widely used in ocean engineering (Sarpkaya & Isaacson 1981; Goda 2010).

$$f(\eta) = \frac{1}{\sqrt{2\pi}\sigma_\eta} \exp\left(-\frac{\eta^2}{2\sigma_\eta^2}\right) \quad (3.18)$$

where σ_η^2 and σ_η denote the variance and the standard deviation of η . The variance is related to the energy density spectrum $S_\eta(\omega)$ by

$$\sigma_\eta^2 = \int_0^\infty S_\eta(\omega) d\omega \quad (3.19)$$

Since the model is completely linear, it is possible to determine the variance of the pressure oscillation in the OWC air chamber as a function of the oscillation amplitude (Falcão & Rodrigues 2002).

$$\sigma_p^2 = \int_0^\infty S_\eta(\omega) |P_{owc}|^2 d\omega \quad (3.20)$$

The instantaneous pneumatic power available to the air turbine can be expressed as

$$\Pi_{owc}^{ist} = \frac{dm/dt}{\rho_a} p_{owc} \quad (3.21)$$

The time averaged value of the pneumatic power available to the OWC, Π_{owc} in a determined sea state can be determined as proposed by Falcão & Rodrigues (2002).

$$\Pi_{owc} = \frac{1}{\varrho_a \sqrt{2\pi} \sigma_p} \int_0^{\infty} \frac{dm}{dt} p_{owc} \exp\left(-\frac{p_{owc}^2}{2\sigma_p^2}\right) dp_{owc} \quad (3.22)$$

In the model application, the JONSWAP spectrum is used (Hasselmann et al. 1973). For JONSWAP wave spectrum, $S_\eta(\omega)$ is given by

$$S_\eta(\omega) = \frac{1}{2\pi} \beta H_s^2 T_e^{-4} \left(\frac{\omega}{2\pi}\right)^{-5} \exp\left(-1.25 \left(T_e \frac{\omega}{2\pi}\right)^{-4}\right) F(\omega) \quad (3.23)$$

where H_s and T_e are respectively the significant wave height and the energy period⁵, β is computed as in Eq. 3.23, and $F(\omega)$ represents the peak enhancement function of JONSWAP spectrum (Eq. 3.25):

$$\beta = (1.094 - 0.01915 \cdot \ln \gamma_j) \frac{0.0624}{0.23 + 0.0336\gamma_j - 0.185(1.9 + \gamma_j)^{-1}} \quad (3.24)$$

$$F(\omega) = \gamma_j \exp\left(-\frac{(\omega - \omega_p)^2}{2\omega_p^2 \sigma}\right) \quad (3.25)$$

where ω_p is the spectrum peak frequency γ_j and σ are the peak width parameter and the peak-enhancement factor for the given site (with $\sigma = \sigma_a$ for $\omega \leq \omega_p$, $\sigma = \sigma_b$ for $\omega > \omega_p$).

3.2. Model results

The freeboard of the device, F_c (i.e. the height of the OWC air chamber above the Still Water Level, SWL) is fixed to a value of 7.5 m. In fact, in OWCs, F_c has to be high enough to prevent the water from reaching the turbine in highly energetic sea states. The value of F_c , therefore, is generally fixed rather based on this consideration than on its effect on the overall device performance (Falcão & Henriques 2016).

The submerged back-wall G is assumed to be long enough to provide complete reflection of the incident wave (i.e. $G > \lambda/2$), thus maximizing the wave energy capture capability. To assess the effect of the other geometrical parameters, the front wall draught D and the radius r are varied in the range 5-15 m and 3-7 m, respectively (Table 3-1).

The turbine proportionality constant between flow coefficient and pressure head, is set to a value $K_T=0.28$, coherently with results of model testing on a Wells turbine carried out by Gomes et al. (2011). A constant turbine diameter $D_T=1.75$ m is used in the simulations. The effect of different turbine damping is evaluated by considering turbine rotational speed N_T varying in the range 100-200 rad/s (Falcão et al. 2014).

A constant water depth $h=50$ m is assumed. The values of the shape parameters for JONSWAP spectrum are chosen according to the data of the R.O.N. (national

⁵ The energy period T_e is used since this spectral period is widely adopted in the field of wave energy converters performance evaluation with the stochastic approach (see Falcão & Rodrigues 2002; Falcão 2004).

Italian sea wave measurement network) for a point in North Sardinia (Corsini et al. 2004).

The hydrodynamic coefficients (added mass m_a and radiation damping B_r) for the considered range of wave frequencies ($\omega=0.2-1.8$ rad/s) have been obtained from the literature on cylindrical shaped OWC devices, and are based on BEM computations (Vannucchi 2012).

Table 3-1: Parameters of the *rigid piston model* in the frequency domain: OWC geometry parameters, turbine parameters and wave parameters.

<i>Parameter</i>	<i>Description</i>	<i>Value</i>	<i>Unit</i>
G	OWC back wall draught	$>\lambda/2$	[m]
D	OWC front wall draught	5-15	[m]
r	OWC radius	3-7	[m]
Fc	OWC freeboard	7.5	[m]
K_T	turbine proportionality flow/pressure constant	0.28	[-]
D_T	turbine diameter	1.75	[m]
N_T	turbine rotational speed	100-200	[rad/s]
p_a	atmospheric pressure	101325	[Pa]
ρ_a	air density	1.25	[kg/m ³]
ρ_w	water density	1025	[kg/m ³]
h	water depth	50	[m]
ω	Incident wave frequency	0.2-1.8	[rad/s]
σ_a	JONSWAP peak-enhancement factor	0.076	[-]
σ_b	JONSWAP peak-enhancement factor	0.089	[-]
γ_J	JONSWAP peak width	1.86	[-]

3.2.1. Model results for regular waves

For monochromatic waves with angular frequency ω in the range 0.2-1.8 rad/s, absolute values of water surface displacement H_{owc} (Fig. 3-2), pressure oscillation amplitude P_{owc} (Fig. 3-3) and volume flow rate Q_{owc} (Fig. 3-4) are obtained for different values of the parameters r , D and N_T .

Considering an incident wave height $H=1$ m, for a fixed value of D and N_T , larger values of r determine an increase of P_{owc} . In the case of $D=10$ m and $N_T=100$ rad/s (Fig. 3-2, a), the maximum P_{owc} rises from approximately 8 kPa to over 11 kPa, when r increases from 3 m to 7 m. Moreover, increasing r results in a decrease of the frequency corresponding to the maximum value of P_{owc} , H_{owc} and Q_{owc} (i.e., the resonance frequency of the device), independently from the value of N_T .

Smaller values of r determine an increase in the OWC inner surface elevation H_{owc} and a shift toward higher frequencies of maximum values of H_{owc} (Fig. 3-3). For the case $r=3$ m, the maximum value of the ratio H_{owc}/H is up to 2.5 for $N_T=100$ rad/s (Fig. 3-3, a) and up to 1.6 for $N_T=200$ rad/s.

For a fixed value of r , varying the parameter D between 5 m and 15 m results in a drop of maximum values of P_{owc} and H_{owc} , per the wave dynamic pressure decrease along the vertical direction. Moreover, the frequency corresponding to the maximum P_{owc} (Fig. 3-2) and to the maximum H_{owc} (Fig. 3-3) decreases with increasing D (i.e. only longer waves have relevant effect on the motion of the inner water column for devices with high front wall draught D).

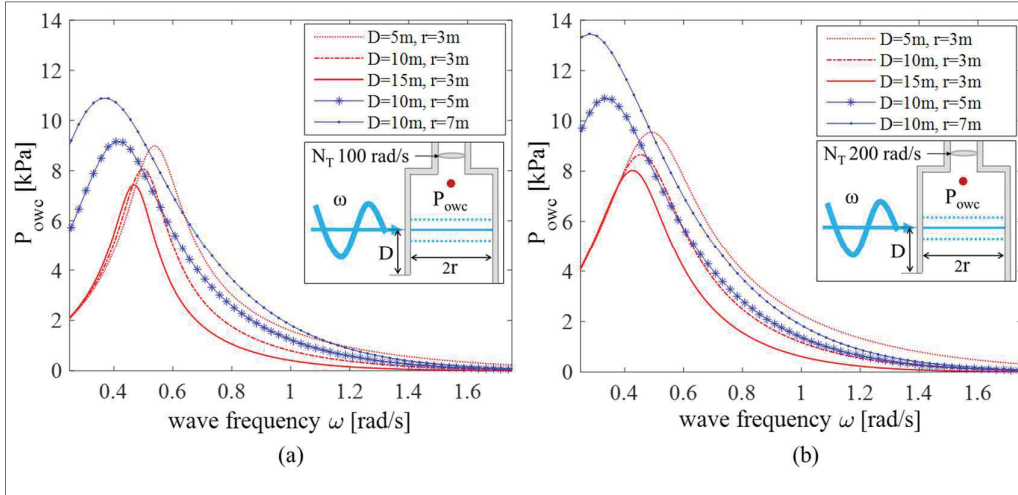


Figure 3-2: Absolute values of air pressure oscillation amplitude P_{owc} computed with the *rigid piston model* for regular waves with height $H=1$ m and for turbine rotation speed $N_T=100$ rad/s (a) and $N_T=200$ rad/s (b).

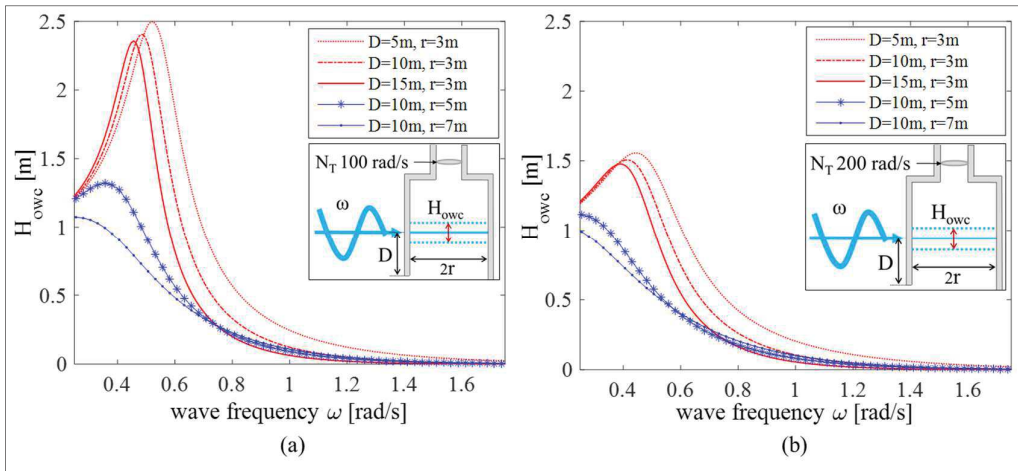


Figure 3-3: Absolute values of the OWC surface displacement amplitude H_{owc} computed with the *rigid piston model* for regular waves with height $H=1$ m and for turbine rotation speed $N_T=100$ rad/s (a) and $N_T=200$ rad/s (b).

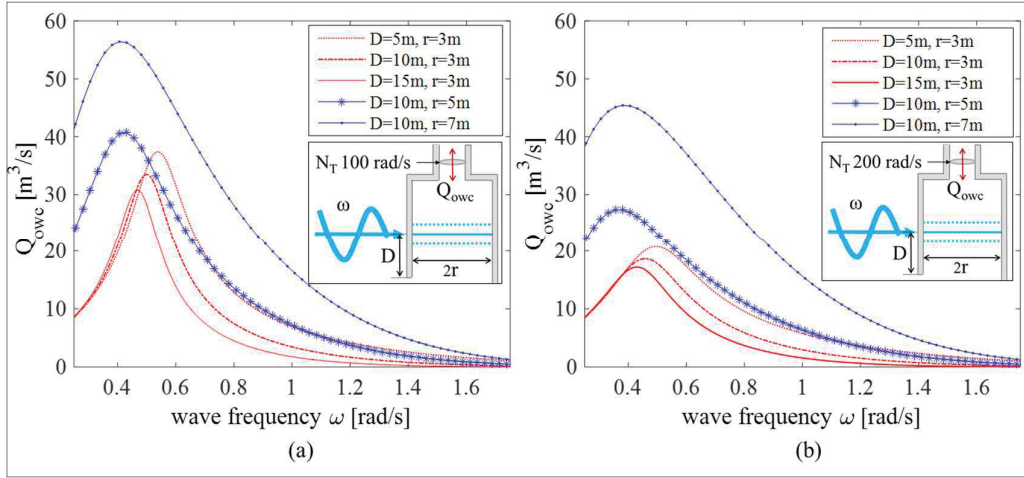


Figure 3-4: Absolute values of the oscillation amplitude air volume flux Q_{owc} computed with the *rigid piston model* for regular waves with height $H=1$ m and for turbine rotation speed $N_T=100$ rad/s (a) and $N_T=200$ rad/s (b).

For both cases $N_T=100$ rad/s and $N_T=200$ rad/s, the maximum value of the air volume flux Q_{owc} (Fig. 3-4) is reached for the OWC geometry $D=10$ m and $r=7$ m. For $N_T=100$ rad/s (Fig. 3-4, a) the maximum is about $57 \text{ m}^3/\text{s}$ (for the incident wave frequency $\omega=0.4$ rad/s), while for $N_T=200$ rad/s (Fig. 3-4, b) the maximum Q_{owc} -value is about $45 \text{ m}^3/\text{s}$ (for $\omega=0.38$ rad/s).

For incident waves with frequency higher than that of resonance, a decreasing tendency in Q_{owc} is observed when increasing the value of the front wall draught D . When ω is lower than the OWC resonance frequency, the effect of D on Q_{owc} appears to be less relevant.

Overall, increasing the turbine rotational speed N_T from 100 to 200 rad/s (hence, increasing the damping applied by the turbine), an increase up to about 30% is observed in P_{owc} , while H_{owc} and Q_{owc} exhibit a decrease of about 40% and 60%, respectively.

The results of the rigid piston model are used to estimate the range of variation of the processes and parameters expected for the planning phase of the laboratory tests with a 1:50 OWC scale model, carried out by Crema et al. (2016). In the laboratory tests, waves with periods T between 5 and 8 seconds, and height H between 2 and 3 m are considered. In the range of the parameters investigated by means of the rigid piston model, the highest values of P_{owc} and Q_{owc} obtained with $D=10$ m, $r=7$ m and with an incident wave with $H=3$ m and $T=8$ s ($\omega=0.78$ rad/s) are $P_{owc}=10.8$ kPa and $Q_{owc}=82 \text{ m}^3/\text{s}$ (Table 3-2).

The maximum values of P_{owc} and Q_{owc} predicted by the rigid piston model (i.e., for scale 1:1) are scaled down to 1:50 according to Froude similarity. In this way, a maximum expected value up to $P_{owc}=20$ mbar for the air pressure in the 1:50 model is predicted. The maximum expected values for the air volume flux in the small scale

model is up to $Q_{owc} = 4.6 \cdot 10^{-3} \text{ m}^3/\text{s}$, and the maximum air velocity is up to 30 m/s ⁶. The measurement range of the pressure sensors and of the hot wire anemometer deployed in the small scale model in the laboratory tests were selected accordingly (Crema et al. 2016).

Table 3-2: Maximum values of relative air pressure P_{owc} , water levels H_{owc} and air volume flux Q_{owc} obtained with the rigid piston model of the OWC, for $D=10 \text{ m}$, $r=7 \text{ m}$ and different turbine rotation speed N_T . The results are obtained for regular waves with height $H=3 \text{ m}$ and period $T=8 \text{ s}$ ($\omega=0.78 \text{ rad/s}$).

N_T [rad/s]	100	200
maximum P_{owc} [kPa]	10.5	10.8
maximum H_{owc} [m]	3.0	2.1
maximum Q_{owc} [m ³ /s]	82.0	78.9

3.2.2. Model results: average OWC capture width ratio for different

To tentatively assess the effect of the OWC design parameters on the device performance in irregular waves, the OWC averaged pneumatic power absorbed by the OWC, Π_{owc} , is determined for 5 different sea states (Table 3-3) by applying the stochastic approach described in *section 3.1.2*.

Table 3-3: Sea states for the calculation of the average OWC capture width ratio ϵ_{owc} by means of the *rigid piston model* (significant wave height H_s , energy period T_e , average wave energy per unit of wave crest Π_{wave}).

Wave condition	H_s [m]	T_e [m]	Π_{wave} [kW/m]
1	1	5	2.39
2	2	7	13.4
3	3	9	38.8
4	4	11	84.5
5	4.5	13	126.3

The OWC averaged capture width ratio, ϵ_{owc} , is computed as

$$\epsilon_{owc} = \frac{\Pi_{owc}}{\Pi_{wave} 2r} \quad (3.26)$$

⁶ In the laboratory tests, the OWC top cover is equipped with circular orifices with different diameter, to reproduce the effect of the turbine damping. The maximum expected value of the air velocity in the small scale OWC model is obtained from the maximum volume air flow preliminary estimated with the frequency domain model, Q_{owcMAX} , by considering the case of OWC equipped with the smallest orifice, with area $A_{min}=1.53 \cdot 10^{-4} \text{ m}^2$. The maximum expected value of the air velocity is therefore Q_{owcMAX}/A_{min} .

where the time averaged value of the pneumatic OWC power, Π_{owc} , is obtained from Eq. 3.22, and the average wave energy per unit of wave crest, Π_{wave} , considering deep water conditions, is expressed as

$$\Pi_{wave} = \frac{1}{64} \frac{g^2}{\pi} \rho H_s^2 T_e \quad (3.27)$$

where H_s is the significant wave height and T_e is the energy period.

Fixing the values of r and N_T , increasing the front wall D results in a decrease of ε_{owc} for all the considered sea states, coherently with the decrease of P_{owc} and Q_{owc} for increasing D observed in *section 3.2.1* (Fig. 3-5). This effect is particularly relevant for the sea states characterized by shorter wave periods: for *Sea state 1* (parameters as defined in Table 3-3), i.e. for significant period $T_e=5$ s, a reduction of ε_{owc} of about 50% is observed when increasing D from 5 to 15 m. For *Sea state 5* ($T_e=13$ s), the variation of ε_{owc} due to changing D is lower than 10% in the range of values considered.

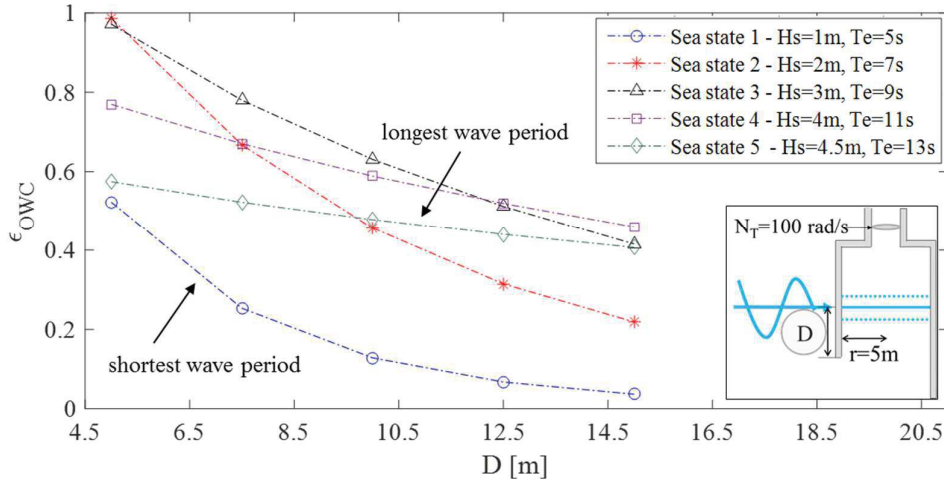


Figure 3-5: Capture width ratio ε_{owc} versus front wall draught D in different sea states (significant wave height $H_s=1-4.5$ m and significant wave period $T_e=5-13$ s) for OWC geometries with radius $r=5$ m and turbine rotational speed $N_T=100$ rad/s. *Rigid piston model* with stochastic approach results.

For the effect of the OWC radius r on ε_{owc} for fixed values of the parameters D and N_T (Fig. 3-6), contrasting tendencies are observed in the different sea states. For *Sea state 1* ($T_e=5$ s) and *Sea state 2* ($T_e=7$ s), smaller r -values result in a moderate increase of ε_{owc} , with maximum variations of 10% in the considered range of parameters. For *Sea state 4* ($T_e=11$ s) and *Sea state 5* ($T_e=13$ s), higher ε_{owc} are found for larger r -values, with a total variation up to 30%.

As far as the damping applied by the turbine is concerned, differences in ε_{owc} - values up to 20% are observed as a consequence of varying N_T in the range 100-200 rad/s (Fig. 3-7).

Overall, it is worth to underline that remarkable differences are found in the OWC device performance (*capture width ratio* ε_{owc}) between different sea states, confirming that the need of site specific optimization is a crucial aspect for this type of device.

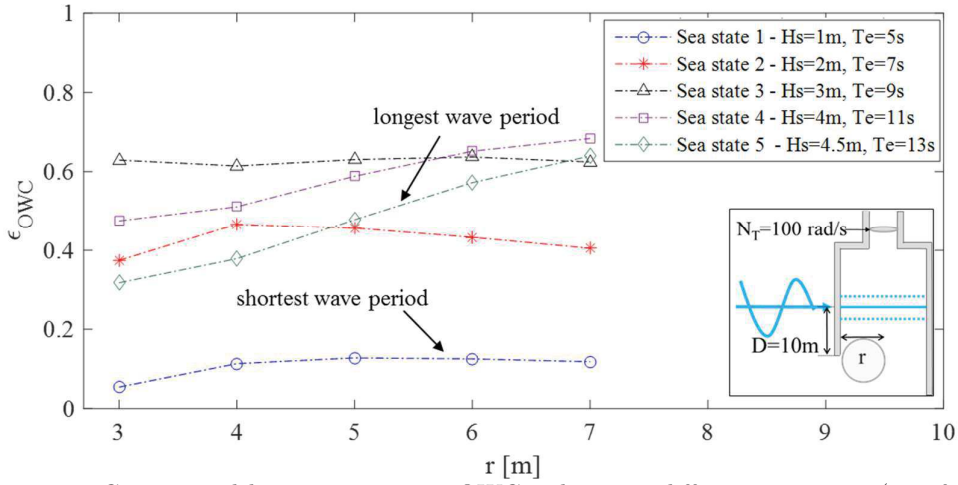


Figure 3-6: Capture width ratio ϵ_{owc} versus OWC radius r in different sea states (significant wave height $H_s=1-4.5$ m and significant wave period $T_e=5-13$ s) for OWC geometries with front wall draught $D=10$ m and turbine speed $N_T=100$ rad/s. *Rigid piston model* with stochastic approach results.

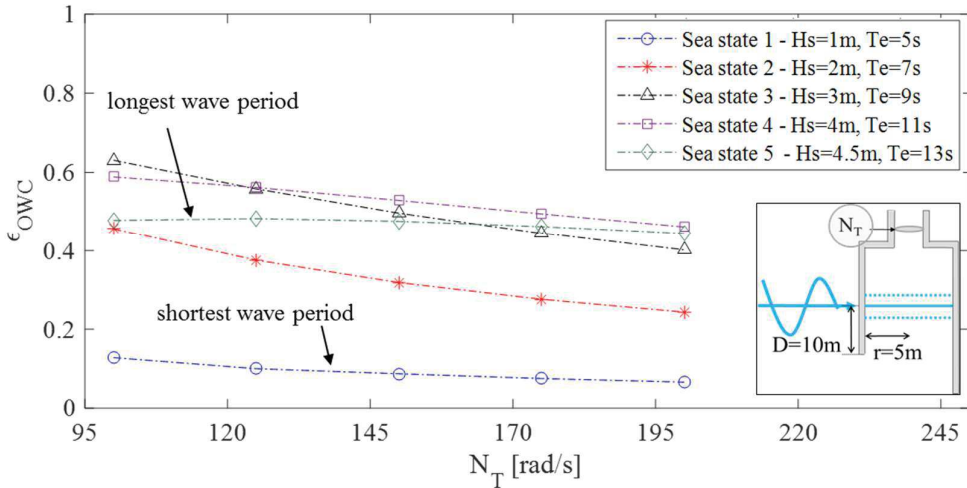


Figure 3-7: Capture width ratio ϵ_{owc} versus turbine rotational speed N_T in different sea states (significant wave height $H_s=1-4.5$ m and significant wave period $T_e=5-13$ s) for OWC geometries with front wall draught $D=10$ m and radius $r=5$ m. *Rigid piston model* with stochastic approach results.

3.3. Summary and implications

A frequency domain *rigid piston model* of a cylindrical OWC (with a stochastic approach to evaluate the average capture width ratio in given sea states) has been successfully applied as a computationally inexpensive to select:

- (i) the most significant parameters in the OWC system dynamics, i.e. the parameters that need to be further optimized by means of physical model testing and more advanced numerical modelling,
- (ii) the expected range of air pressures and air velocities in the device for the set-up of the planned laboratory tests.

The OWC front wall draught D , the chamber radius r and the damping applied by the turbine (varied in the model by considering different rotational speed N_T) are found to significantly affect the OWC device dynamics. Therefore, these parameters will be further investigated by means of a CFD model, in order to appropriately account for all the relevant effects which may take place in the OWC system, including non-linear and viscous effects, turbulence and air compressibility effects.

The *rigid piston model* has allowed to assess the maximum values of the air pressure (20 mbar) and of the air flow velocity (30 m/s) expected in a 1:50 OWC scale model. This was required to appropriately set-up the laboratory experiments performed by Crema et al. (2016).

Remarkable differences are found in the capture width ratio ε_{owc} of the OWC device for different sea states, thus confirming that the site-specific optimization represents a crucial issue for any OWC device.

CHAPTER 4

Numerical Wave Tank in OpenFOAM®

The set-up of a Numerical Wave Tank (NWT) based on a multi-phase (air-water) Computational Fluid Dynamic (CFD) modelling approach is presented in *this chapter*. OpenFOAM® (Open Field Operation and Manipulation), an open source package of C++ libraries and solvers for fluid and solid mechanic problems, is used.

Two different approaches to wave generation are alternatively compared, in order to select the most suitable for the following step of the research, i.e. the simulation of the OWC device (*Chapter 5*). Both generation approaches are validated with laboratory data.

Since an accurate wave generation process is fundamental to obtain accurate results, sensitivity and grid independence tests for wave generation and propagation in the NWT are performed, with particular reference to the mesh resolution.

4.1. Theoretical background

Within the OpenFOAM® framework, the discretization of the governing equation is based on the Finite Volume Method (FVM) with a co-located methodology for unstructured polyhedral meshes with arbitrary grid elements (fluids quantities are stored at control volume centroids). The study is carried out by using the `interFoam` solver, which solves for the incompressible 3D Navier-Stokes equations for a single Eulerian fluid mixture of two immiscible phases (i.e. water and air) by applying the Volume Of Fluid (VOF) method for free the surface tracking.

4.1.1. Two-phase incompressible VOF solver

A complete description of the solution procedure of the of the solver `interFoam` can be found in Rusche (2002) and Deshpande et al. (2012). Only the basic principle are described in this section.

For a Newtonian, incompressible and isothermal fluid, the set of governing equations for the fluid dynamics are the equation of conservation of mass (Eq. 4.1) and momentum (Eq. 4.2) (Navier stokes equations). The conservation equations must account for the surface tension force acting at the fluids interface (Rusche, 2002).

$$\nabla \cdot \mathbf{u} = 0 \quad (4.1)$$

$$\frac{\partial(\rho \mathbf{u})}{\partial t} + \nabla \cdot (\rho \mathbf{u} \mathbf{u}) = -\nabla p + \nabla \cdot \boldsymbol{\tau} + \rho \mathbf{g} + F \quad (4.2)$$

where u is the fluid velocity field, ρ is the fluid density, p is the pressure, $\boldsymbol{\tau}$ is the deviatoric viscous stresses tensor, g is the gravity acceleration, F is the source of momentum due to surface tension, only acting at the interface, t is time.

In `interFoam`, the well-established VOF method (Hirt & Nichols 1981) is used for the free surface tracking. In the domain composed of a liquid (\mathbb{R}_w) and a gas (\mathbb{R}_a) phase regions, the indicator for the phase $I(x, t)$ is expressed as:

$$I(x, t) = \begin{cases} 1 & \text{for } x \in \mathbb{R}_w \text{ at time } t \\ 0 & \text{for } x \in \mathbb{R}_a \text{ at time } t \end{cases} \quad (4.3)$$

Integrating $I(x, t)$ over a computational cell volume Ω_i , the liquid volume fraction a can be expressed as:

$$a(x_i, t) = \frac{1}{|\Omega_i|} \int_{\Omega_i} I(x_i, t) dV \quad (4.4)$$

Since the single fluid Eulerian approach is adopted, the two immiscible fluids are considered as one effective fluid having physical properties resulting from weighted averages based on the liquid volume fraction a . Denoting with ρ_w , μ_w and ρ_a , μ_a the constant density and viscosity values for liquid and gas phase respectively, density and viscosity fields can be expressed as:

$$\rho(x, t) = \rho_w I(x, t) + \rho_a (1 - I(x, t)) \quad (4.5)$$

$$\mu(x, t) = \mu_w I(x, t) + \mu_a (1 - I(x, t)) \quad (4.6)$$

Substituting Eq. 4.5 in Eq. 4.4, and integrating over the cell volume Ω_i is possible to write the transport equation for volume fraction a

$$\frac{\partial a}{\partial t} + \nabla \cdot (\mathbf{u} a) = 0 \quad (4.7)$$

In the classical VOF method (Hirt & Nichols 1981) the transport equation of a (4.7) is solved together with continuity (4.1) and momentum (4.2) equations. The volume phase fraction a is advected by the fluids. For incompressible flows, this is equivalent to a conservation law for the VOF function, and therefore ensures the conservation of mass (Ubbink 1997). The classic VOF approach is modified in `interFoam` (Rusche 2002) in order to improve the boundedness and conservativeness of the volume fraction a , mitigating the typical diffusion effects of the VOF method, which may result in the smearing of the interface sharpness (Tryggvason et al. 2011; Berberović et al. 2009). An interfacial compression flux term, whose derivation is outlined below, is therefore included in the VOF formulation

$$\frac{\partial a}{\partial t} + \nabla \cdot (\mathbf{u} a) + \nabla \cdot (\mathbf{u}_r a(1 - a)) = 0 \quad (4.8)$$

where the term u_r is a velocity field normal to the interface, representing an artificial contribution to the convection of the phase fraction a to prevent it from dispersing.

u_r does not affect the solution outside the interface region. The additional convective term significantly contributes to a higher interface resolution, avoiding the need to employ compressing differencing schemes.

The surface tension force F in momentum equation (Eq. 4.2) is evaluated by using the Continuum Surface Force (CSF) method (Brackbill, 1992). For a two-phase incompressible flow with surface tension coefficient σ and viscosity μ , the surface tension force F , which is only active in the interfacial region, is formulated as

$$F = \sigma \kappa (\nabla a) \quad (4.9)$$

where κ is the local curvature of the interface, obtained from the volume phase fraction α as

$$\kappa = \nabla \cdot (\nabla a / |\nabla a|) \quad (4.10)$$

The pressure-velocity coupling is performed in `interFoam` using the so-called PIMPLE algorithm, which is hybrid in the sense that it consists of two classical algorithms, PISO and SIMPLE, for pressure-velocity coupling (PISO: Pressure Implicit with Splitting of Operators, Issa, 1986 and SIMPLE: Semi-Implicit Method for Pressure-Linked Equations, Patankar & Spalding, 1972).

In the framework of the VOF method, PISO and SIMPLE algorithms are extensively explained by Jasak (1996). The main structure of the PIMPLE algorithm is inherited from the PISO algorithm, but it additionally allows under-relaxation to ensure the equation convergence when bigger time steps are used. The coupled system of algebraic equations resulting from the discretization is solved sequentially. The solution procedure in a transient simulation can be summarized as follow (Ubbink, 1997; Rusche, 2002):

- (i) Variable initialization;
- (ii) Solve the equation of the volume phase fraction a (Eq. 4.8) by using the previous time step volumetric fluxes;
- (iii) Use the new α values together with the constitutive relations to obtain an estimate for the new viscosity μ , density ρ and the face densities;
- (iv) Calculate the interface curvature κ (Eq. 4.10);
- (v) Optionally, assemble and solve the momentum predictor equation (Eq. 4.2);
- (vi) PIMPLE loop iteration until the pre-defined tolerance for pressure-velocity system is reached.

4.1.2. Wave generation and absorption

Two wave generation approaches are preliminary tested and compared:

- (i) Wave generation by prescribing boundary and initial conditions for velocity and water levels according to selected wave theories, performed with the `waves2Foam` toolbox (called hereafter *waves2Foam generation*);
- (ii) Wave generation with a numerical piston wave maker based on dynamic mesh (called hereafter *piston wave maker generation*).

The strength and the drawbacks of two methods in terms of accuracy of reproducing the wave dynamics and computational demands, are evaluated.

Waves2Foam generation

For the wave generation approach based on prescribing boundary and initial condition for velocity and water levels, the **waves2Foam** toolbox (Jacobsen et al. 2012) is used. In **waves2Foam** toolbox a relaxation zones approach for generation/absorption of waves is implemented to the **interFoam** hydrodynamic solver. At the domain inlet, a boundary condition is defined to introduce waves according to different wave theories. Inside the relaxation zones the required wave profile is imposed: computational solutions are replaced with values calculated by weighing predefined analytical and solved ones according to a relaxation function either to generate and/or absorb waves at each time step.

The relaxation function, given by

$$a_R = 1 - \frac{\exp(\chi_R^{relExp}) - 1}{\exp(1) - 1} \quad (4.11)$$

is applied to impose the values of a and u as follow:

$$\Phi = a_R \Phi_{\text{computed}} + (1 - a_R) \Phi_{\text{target}} \quad (4.12)$$

where Φ indicates either a or u , Φ_{target} is the prescribed value at the beginning of the relaxation zone (either for a or u) and χ_R is defined to have $\alpha_R = 1$ at the end of the relaxation zone (Fig. 4-1). In the outlet relaxation zone, a_{target} is determined based on the still water level (SWL).

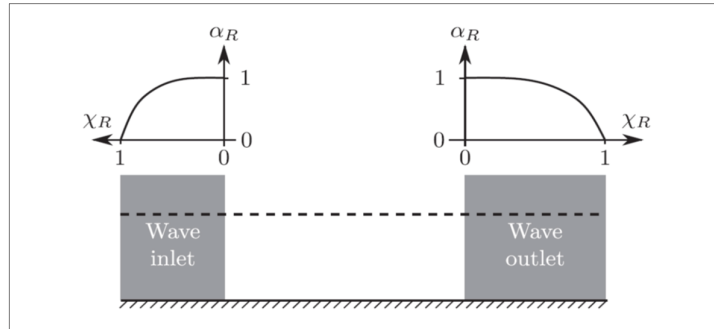


Figure 4-1: Sketch of the inlet and outlet relaxation zone and relaxation function α_R in the *waves2Foam* wave generation approach (from Jacobsen et al., 2012).

Piston wave maker generation

A piston type wave maker is numerically simulated to mimic the way waves are generated in a laboratory facility. The piston type wave maker is simulated imposing a moving wall boundary condition, causing the mesh to change with every time step (i.e. a dynamic mesh is adopted). The time history of positions of the wave maker can be given as an input to impose a prescribed motion to the numerical piston wave-

maker. To accommodate this motion in the framework of OpenFOAM® FVM discretization, Laplace equation (Eq. 4.13) is solved to determine the positions of points in the mesh (Eq. 4.13), based on the prescribed boundary motion (Jasak & Tukovi, 2007 and 2010).

$$\nabla \cdot (\zeta \nabla v) = 0 \quad (4.13)$$

$$x_{new} = x_{old} + v \Delta t \quad (4.14)$$

where ζ is a diffusion field, v is the point velocity used to modify point position, x_{new} and x_{old} are point position after and before mesh motion for time step Δt .

A distance-based diffusivity ζ is applied to Laplace equation (i.e. the diffusivity field is a function of the cell distance from the moving boundary) to calculate the displacement of each point in the computational domain.

For wave absorption, a relaxation zone is placed at to outlet of the domain to damp the reflected wave, i.e. the same concept implemented in `waves2Foam` toolbox for wave absorption is used (Fig. 4-1).

4.2. Set-up of the Numerical Wave Tank and sensitivity analysis

4.2.1. Numerical Wave Tank set-up

The set-up of the Numerical Wave Tank (NWT), in terms of (i) boundary conditions and initial conditions, (ii) turbulence modelling, (iii) numerical schemes, (iv) linear solvers, (v) time step control and (vi) fluid properties are presented in this section.

Boundary conditions and initial conditions

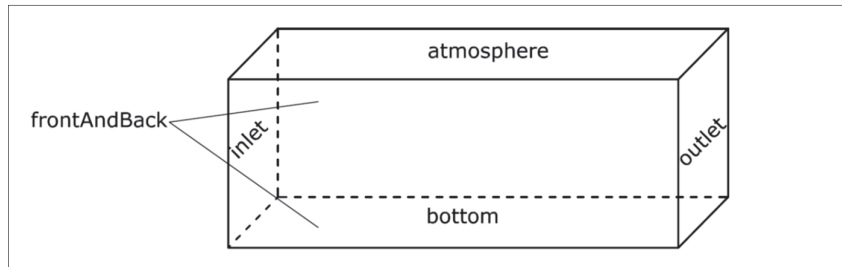


Figure 4-2: Definition of the boundaries of the Numerical Wave Tank (NWT).

Considering the designation of the NWT boundaries defined in Fig. 4-2, the boundary conditions used in the simulations are summarized in Table 4-1, using the OpenFOAM naming convention⁷.

⁷ The *pressureInletOutletVelocity* condition (which is imposed on the atmosphere boundary for the velocity u) applies *zeroGradient* condition on all components, except where there is inflow, in which case a value of zero is applied to the tangential velocity component. The *inletOutlet* condition (applied to a on the atmosphere boundary) implements a *zeroGradient* condition

For both (i) the *waves2Foam generation* and (ii) the *Piston wave maker generation*, no slip conditions are set at the *bottom boundary* of the NWT. The *atmosphere boundary* of the NWT, occupied by the air, is set as a constant pressure boundary (with a relative pressure $p=0$). An open inlet-outlet condition is applied for the velocity u and the volume phase fraction a on the *atmosphere boundary* (for inward pointing velocity vector, a Dirichlet type boundary condition is applied, while for the case of outward pointing velocity vector, a Neumann boundary condition is applied). A *symmetry* condition is specified on the *front boundary* of the NWT, to reduce the size of the computational domain.

For the *waves2Foam generation*, velocity vector u and volume phase fraction a at the domain *inlet boundary* are strongly imposed with a Dirichlet boundary condition, with values given based on an appropriate closed form wave theory. The appropriate wave theory is selected based on the classical graph by Le Méhauté (1976).

For the *Piston wave maker generation*, the time series of the position of the *inlet boundary* is prescribed at every time step (i.e. moving wall boundary condition).

Table 4-1: Boundary conditions for the Numerical Wave Tank (NWT) for velocity u , pressure p , VOF volume phase fraction a .

<i>Boundary</i>	u	p	a
inlet	fixedValue	zeroGradient	fixedValue
outlet	fixedValue	zeroGradient	zeroGradient
bottom	fixedValue	zeroGradient	zeroGradient
atmosphere	pressureInletOutletVelocity	totalPressure	inletOutlet
front	simmetryPlane	simmetryPlane	simmetryPlane
back	fixedValue	zeroGradient	zeroGradient

Turbulence modelling

A Large Eddy Simulation (LES) approach to turbulence is used. The LES applied in this study uses a k-equation eddy-viscosity (**oneEquationEddy** in OpenFOAM®) sub-grid scale closure. In this model, a transport equation for the sub-grid scale (SGS) turbulent kinetic energy k_{SGS} is introduced and solved, to take into account the effects of convection, diffusion, production and destruction on the SGS velocity scale (Villers 2006).

The transport equation solved for k_{SGS} is

$$\frac{\partial(\rho k_{SGS})}{\partial t} + \nabla \cdot (\rho k_{SGS} \mathbf{u}) = \nabla \cdot ((\mu_{SGS} + \mu_l) \nabla k_{SGS}) + 2\mu_{SGS} S_s^2 - \rho \frac{C_\epsilon k_{SGS}^{2/3}}{\Delta} \quad (4.15)$$

where Δ is the spatial filter size (separating the resolved eddies from the SGS ones, which are modelled), $C_\epsilon = 1.048$ is the model constant, S_s is the strain rate tensor magnitude, μ_l is the laminar dynamic viscosity and μ_{SGS} is the SGS dynamic viscosity,

when the velocity vector points out of the domain, with a having a value of 0 when the velocity vector points into the domain.

calculated as

$$\mu_{SGS} = \rho C_{SGS} \Delta \sqrt{k_{SGS}} \quad (4.16)$$

with the constant $C_{SGS} = 0.01$ (Villers 2006). The use for a transport equation for the SGS kinetic energy may allow for coarser mesh compared to a zero equation eddy viscosity model.

Numerical schemes

The discretization schemes for the time derivatives used is a second order scheme, blended with a first order Euler scheme to improve stability. For generic gradient operators, a standard finite volume discretization of Gaussian integration is applied, with a central differencing scheme (i.e. second order accurate, unbounded) for value interpolation from cell centers to cell faces (**Gauss linear** entry in OpenFOAM). Regarding divergence operators, the discretization of the convection term in momentum equation is done with a Total Variation Diminishing (TVD) scheme with a central differencing interpolation scheme bounded by a Sweby limiter (Sweby 1984) (**Gauss linearLimited** entry in OpenFOAM). For the convection term in the transport equation of the phase volume fraction α , Monotone Upwind Schemes for Scalar Conservation Laws (MUSCL, Van Leer 1979) (**Gauss MUSCL** entry in OpenFOAM) interpolation scheme is used, which is a TVD scheme with an high accuracy even in the case of shocks or elevate gradient of the solution. The information required for discretization of Laplacian terms include both the interpolation scheme for diffusion coefficients and a surface normal gradient scheme: a central difference scheme and an explicit non-orthogonal correction schemes are applied respectively (**Gauss linear corrected** entry in OpenFOAM).

Table 4-2: Set of numerical schemes used for the free Numerical Wave Tank (NWT) simulations

<i>Term description</i>	<i>Expression</i>	<i>Scheme</i>
Time derivative	$\frac{\partial}{\partial t}$	blended CrankNicolson/Euler
Gradient	∇	Gauss linear
Divergence	$\nabla \cdot (\rho \mathbf{u})$	Gauss limitedLinear
	$\nabla \cdot (\rho \mathbf{u} \alpha)$	Gauss MUSCL
Laplacian	∇^2	Gauss linear corrected

Linear solvers

A preconditioned conjugate gradient solver (PCG) with a simplified diagonal based incomplete Cholesky (DIC) smoother is used for the pressure equation. The Krylov subspace solver bi-conjugate gradient solver for axisymmetric matrix (PBiCG) is used for u and for α , with a simplified diagonal based incomplete LU preconditioner (DILU). An iterative GaussSaidel iterative smoother is used for k_{SGS} .

Table 4-3: Set of linear solvers used for the numerical free Numerical Wave Tank (NWT) simulations for velocity u , pressure p , VOF volume phase fraction a , sub-grid scale turbulent kinetic energy k_{SGS} .

<i>Variable</i>	<i>Solver</i>
p	PCG, DIC smoother
u	PBiCG, DILU preconditioner
a	PBiCG, DILU preconditioner
k_{SGS}	smoothSolver, smoother GaussSeidel

Time step control

A self-adjusting time step is used, to increase the solution procedure stability. Independently from the use of an explicit scheme for time derivatives discretization, in a transient problem simulation where the coupling terms are evaluated from the previous time step solution, high values of the Courant number could imply abrupt changes in the solution. In this case, convergence could be not guaranteed. Time step is adapted at the beginning of every new time loop based on Courant number Co , defined as:

$$Co = \frac{u\Delta x}{\Delta t} \quad (4.17)$$

where Δx and Δt are the mesh size and the time step, respectively. The maximum acceptable value of Co , and the maximum time step Δt_{max} are set as summarized in Tab. 4-4. In each time step, the maximum local Co is calculated and the Δt for the next time step is evaluated as:

$$\Delta t^{n+1} = \min \left\{ \frac{Co_{max}}{Co^n} \Delta t^n, \left(1 + \lambda_1 \frac{Co_{max}}{Co^n} \right) \Delta t^n, \lambda_2 \Delta t^n, \Delta t_{max} \right\} \quad (4.18)$$

where the damping parameters λ_1 and λ_2 ensure a smooth adjustment of Δt .

Table 4-4: Time step control parameters adopted in the free NWT simulations.

<i>Parameter [unit]</i>	<i>Value</i>
Time step control	Adjustable time step
Co_{max}	0.7
Δt_{max}	T/200

Fluid properties

The values of gravitational acceleration, g , water and air densities (ρ_w and ρ_a , respectively), water and air kinematic viscosity (ν_w and ν_a , respectively) implemented in the NWT simulations are summarized in Table 4-5⁸.

⁸ Environmental (gravity acceleration) and transport properties (kinematic viscosity, density) are defined in specific dictionary (*environmentalProperties* and *transportProperties*) located in the *constant* folder of the simulated case directory.

Table 4-5: Environmental properties used in the Numerical Wave Tank (NWT) simulations.

Parameter – symbol [unit]	Value
Gravitational acceleration - g [m/s ²]	9.81
water density - ρ_w [kg/m ³]	1000
water kinematic viscosity - ν_w [m ² /s]	$1.3 \cdot 10^{-6}$
air density - ρ_a [kg/m ³]	1
air kinematic viscosity - ν_a [m ² /s]	$1.48 \cdot 10^{-5}$

4.2.2. Sensitivity analysis and grid independence tests

Benchmark tests on regular waves propagation in the 3D free Numerical Wave Tank (NWT) are performed. A hexahedral dominant mesh with a refinement zone around the free surface is used to discretize the NWT. The refinement zone thickness is fixed as $2H$, where H is the height of the simulated wave.

The sensitivity analysis, only performed for the *waves2Foam generation* approach, is carried out on the following parameters (as defined in Fig. 4-3):

- (i) Mesh size in the free surface refinement zone, expressed in terms of number of computational cells per wave height (H/cells) and length (λ/cells);
- (ii) Computational cells aspect ratio (AR), defined as the ratio of the computational cell length in the vertical to that in the horizontal direction, i.e. $AR = \Delta Y_{BK} / \Delta X_{BK} = \Delta Y_{FS} / \Delta X_{FS}$;
- (iii) Ratio of the length of the computational cell in the unrefined zone away from the free surface to that in the free surface zone, $BK_{SF} = \Delta X_{BK} / \Delta X_{FS}$;
- (iv) Length of the inlet relaxation zone δX_{IN} and of the outlet relaxation zone, δX_{OUT} .

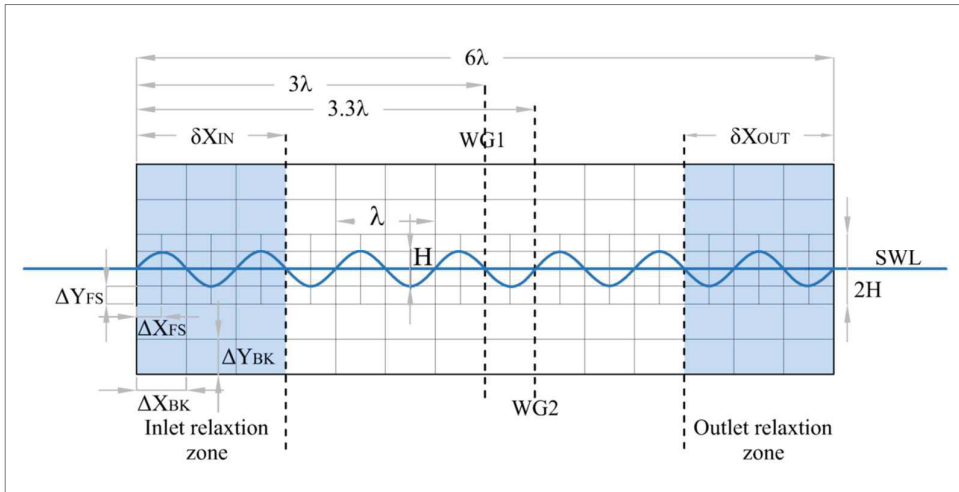


Figure 4-3: Sketch of the mesh parameters considered for the sensitivity analysis on the Numerical Wave Tank (NWT), and wave gauges (WGs) location in the NWT.

In the NWT discretization, a resolution in the transversal direction $\Delta Z = \Delta X$ is used. The wave used for tests has a height $H_{targ} = 0.04$ m, a period $T_{targ} = 1$ s and propagates over a constant water depth $h = 0.5$ m. Stokes second order wave theory is used to prescribe boundary and initial conditions for wave generation (according to Le Méhauté, 1976). The simulation domain has a length equal to 6λ , and it is $20H_{targ}$ high and $10H_{targ}$ wide.

For the sampling of the water level η , two wave gauges, WG1 and WG2, are placed at a distance 3λ and 3.3λ from the wave-generating boundary, respectively (Fig. 4-3). For each simulated case, a total simulation time of $20T$ (T =wave period) is considered.

Zero crossing analysis is applied to determine the average wave height H and wave period T of generated waves.

The relative error on the wave height, E_H , and on the wave period, E_T , are computed as

$$E_H = \frac{H - H_{targ}}{H_{targ}} \quad E_T = \frac{T - T_{targ}}{T_{targ}} \quad (4.19)$$

The effect of the mesh size in the free surface refinement zone is analysed by varying $H/cells$ between 2 and 10, and $\lambda/cells$ between 40 and 240 (parameters as defined in Table 4-6, *testWave1* to *testWave5* and Figure 4-4).

Table 4-6: Mesh parameters: cells per wave height ($H/cells$), cells per wave length ($\lambda/cells$), cells aspect ratio (AR), ratio of cell length in refined zone to that in unrefined zone (BK_{SF}), relative error on the wave height (E_H) and on the wave period (E_T). Average values recorded at gauge WG1 (3λ from the wave generating boundary).

<i>Test</i> (*)	$H/cells$	$\lambda/cells$	AR	BK_{SF}	H [m]	T [s]	E_H [%]	E_T
testWave1	2	40	2	4	0.033	0.996	-21	<1
testWave2	4	80	2	4	0.036	0.996	-9	<1
testWave3	6	120	2	4	0.039	0.998	-2	<1
testWave4	8	160	2	4	0.039	0.999	-1.5	<1
testWave5	10	240	2	4	0.041	0.998	1.5	<1
testWave6	6	60	4	4	0.034	0.998	-14	<1
testWave7	6	240	1	4	0.039	1.000	-2	<1
testWave8	6	120	2	2	0.040	1.000	1	<1
testWave9	6	120	2	8	0.038	1.000	-6	<1

(*) A constant value of the inlet/outlet relaxation zone length, $\delta X_{IN} = \delta X_{OUT} = \lambda$, is used.

Results for regular wave height $H_{targ} = 0.04$ m and period $T_{targ} = 1$ s.

For fixed $AR = 2$, $BK_{SF} = 4$, and $\delta X_{IN} = \delta X_{OUT} = \lambda$, relevant diffusive error are found with $H/cells = 2$ and $H/cells = 4$, with values of E_H up to about 20%. Increasing the mesh resolution to $H/cells = 6$ (*testWave3*), E_H reduces to about 2%, and no remarkable differences are observed when further increasing $H/cells$ (*testWave4* and *tesWave5*).

The phase error (expressed in terms of E_T) is lower than 1% for all the considered cases. Therefore, mesh independence may be considered achieved for discretization refinements in the free surface zone higher or equal to $H/cells = 6$, with $AR = 2$.

Fixing the number of cells per wave height in the free surface zone ($H/cells=6$), and assuming $BK_{SF}=4$ and $\delta X_{IN}=\delta X_{OUT}=\lambda$, the relative error on H_{targ} , E_H , is ca. 2% with $AR=1$ (*testWave7*) and $AR=2$ (*testWave3*), while it increases up to 14% for $AR=8$ (*testWave6*), as depicted in Figure 4-5.

The number of computational cells used to discretize the wave length, $\lambda/cells$, is therefore a relevant parameter, and an AR greater than 4 implies noticeable diffusive errors. No phase errors (E_T) are observed instead, even for the higher AR .

The effect of the ratio of cell length in the refined to that in the unrefined zone (BK_{SF}) is analyzed for values varying from 2 to 8 (Tab. 4-6 and Fig. 4-6). With fixed values of the mesh parameters in the free surface refinement zone ($H/cells=6$ and $AR=2$), E_H is lower than 2% for $BK_{SF}=1$ (*testWave8*) and $BK_{SF}=4$ (*testWave3*). Increasing the mesh size away from the free surface, i.e. for $BK_{SF}=8$ (*testWave9*), E_H increases to ca. 6%.

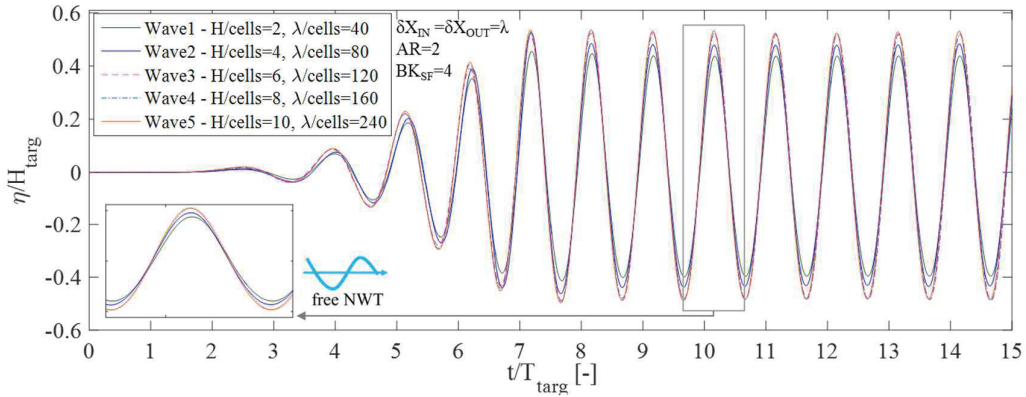


Figure 4-4: Time series of relative water surface elevation η/H_{targ} at gauge WG1 (distance 3λ from the inlet) in the free NWT for different resolution of the free surface zone mesh ($H/cells$ and $\lambda/cells$). Results for regular wave height $H_{targ}=0.04m$ and period $T_{targ}=1s$.

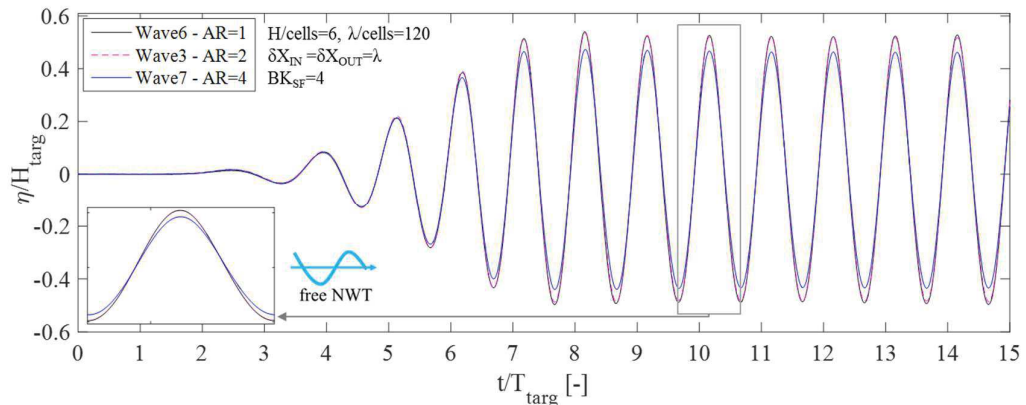


Figure 4-5: Time series of relative water surface elevation η/H_{targ} at gauge WG1 (distance 3λ from the inlet) in the free NWT for different mesh Aspect Ratio AR . Results for regular wave height $H_{targ}=0.04m$ and period $T_{targ}=1s$.

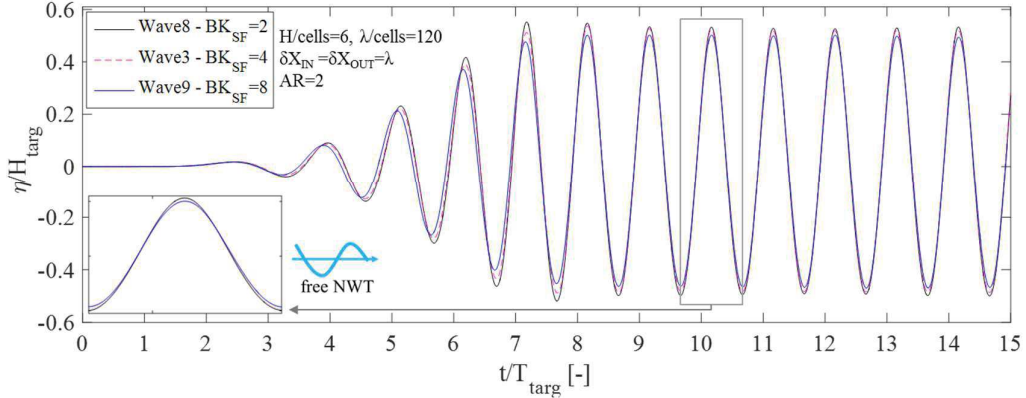


Figure 4-6: Time series of relative water surface elevation η/H_{targ} at gauge WG1 (distance 3λ from the inlet) in the free NWT for different ratio of cell length in refined to that in unrefined zone (BK_{SF}). Results for regular wave height $H_{targ}=0.04\text{m}$ and period $T_{targ}=1\text{s}$.

To evaluate the effect of the relaxation zone parameters, i.e. the minimum length required to achieve satisfactory absorption of the reflected wave on the *inlet* and *outlet* boundaries, additional simulations are performed by varying relaxation zones length, δX_{IN} and δX_{OUT} , in the range 0.3λ - 1.6λ (Tab. 4-7).

The time series of surface elevation recorded at the two wave gauges WG1 and WG2 (Fig. 4-3) are used in order to determine the reflection coefficient K_r by applying the method of Goda & Suzuki (1976).

Values of K_r lower than 10% are found for all the tested relaxation zone length (Table 4-7). In particular, for $\delta X_{IN}=\delta X_{OUT}=0.3\lambda$, K_r is ca. 8.4%, while values lower than 5% are obtained when the relaxation zones length is greater than λ .

Table 4-7: Simulated cases for testing the sensibility of the free NWT to the inlet/outlet relaxation zone length ($\delta X_{IN}/\delta X_{OUT}$) and reflection coefficient K_r for the target wave.

<i>Test</i> (*)	δX_{IN}	δX_{OUT}	K_r [%]
testWave10	0.3λ	0.3λ	8.4
testWave11	0.6λ	0.6λ	6.2
testWave3	λ	λ	3.7
testWave12	1.3λ	1.3λ	3.1
testWave13	1.6λ	1.6λ	3.2

(*) Constant values $H/\text{cells}=6$, $\lambda/\text{cells}=120$, $AR=2$ and $BK_{SF}=4$ are used.

Summarizing, from the sensitivity analysis performed on the *free NWT*, the following main conclusions might be drawn:

- (i) Mesh independence may be considered as achieved for a refinement in the free surface zone equal to 6 H/cells , with $AR=2$, since no significant increases in the accuracy are observed when further increasing H/cells .
- (ii) The aspect ratio AR , i.e. the ratio of the cell length in vertical direction to that in horizontal direction, was found to significantly affect the accuracy of

the NWT in reproducing the target wave height H_{targ} . For values of $AR=8$, a diffusive error E_H of ca. 14% is observed, even when the adopted value of $H/cells$ is sufficiently high.

- (iii) Adopting a sufficient mesh resolution in the free surface zone (i.e. at least 6 $H/cells$, with $AR=2$), values of the ratio of cell length in the refined and the unrefined zone, BK_{SF} higher than 4 determine a diffusive error E_H of ca. 6%.
- (iv) Lengths of the inlet and outlet relaxation zone (δX_{IN} , δX_{OUT}) equal or greater than the incident wave length λ allows to achieve wave reflection coefficient K_r lower than 5%.

4.3. Numerical Wave Tank validation with laboratory data

The two wave generation approaches (*waves2Foam generation* and *piston wave maker generation*) are tested by comparing wave propagation along the *free NWT* with data from laboratory experiments. A reference monochromatic wave having height $H=6.3$ cm and period $T=1.1$ s on a 0.5 m water depth h is used to perform the comparison. The simulation domain has a length of 15 m (Fig. 4-7). The length of the inlet and outlet relaxation zones is $\delta X_{IN}=\delta X_{OUT}=2$ m for wave generation/absorption with *waves2Foam generation*. For the *piston wave maker generation*, an outlet relaxation zone ($\delta X_{OUT}=2$ m) is used for wave absorption (hence, the length of the relaxation zones is approximately 1.12λ).

The mesh resolution in the free surface zone is $H/cells=6$ and $\lambda/cells=120$, with aspect ratio $AR=2$ and $BK_{SF}=4$. These values are chosen based on with the results of the sensitivity analysis on mesh parameters performed in *section 4.2.2*. The simulation time is $20T$.

For the *waves2Foam generation*, a Stokes second order wave theory boundary condition is used. For the *piston wave maker generation*, the time history of positions of the moving boundary recorded in the laboratory test is used as an input, in order to prescribe exactly the same motion the physical and the numerical wave makers.

Three wave gauges (WGs) are placed along the wave flume to obtain time series of free surface displacement η (positions as in Figure 4-7).

The relative error between simulated and laboratory data is calculated for H and T at the different WGs (as in Eq. 4.19). Moreover, the Normalized Root Mean Square Error (*NRMSE*) on η was computed as:

$$\eta_{NRMSE} = \frac{1}{(\eta_{max} - \eta_{min})} \sqrt{\left(\frac{1}{N} \sum_{i=1}^N (\eta_i - \eta_{Ni})^2 \right)} \quad (4.20)$$

where η_i are the experimental data, η_{Ni} are the corresponding numerically simulated data, η_{max} and η_{min} are the maximum and minimum values of the data from the laboratory test.

For the fully developed wave train (i.e. for after ~ 5 wave periods T from the moment of the first wave arrival at the WG, Fig. 4-8), a good agreement was found

for the considered WGs for both *waves2Foam* and *piston wave maker generation* approaches, with maximum errors on η , η_{NRMSE} , and on H , E_H , lower than 10% (Tab. 4-8) and maximum relative error on T lower than 1%.

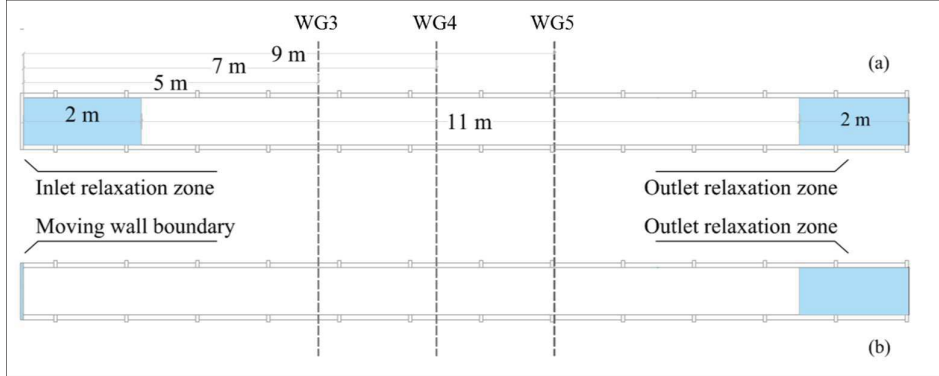


Figure 4-7: Sketch of the simulation domain for the numerical wave flumes with *waves2Foam* generation (a) and *piston wave maker generation* (b).

Table 4-8: Maximum relative error in the fully developed wave train on surface displacement η (η_{NRMSE}) and on the wave height H (E_H) and period (E_T). Comparison between laboratory data and *waves2Foam* generation/*piston wave maker generation* at wave gauges WG3, WG4 and WG5, for the regular wave $H=0.063\text{m}$, $T=1.1\text{s}$.

Wave Gauge	Wave generation approach					
	<i>wave2Foam</i> generation			<i>Piston wave maker</i> generation		
	η_{NRMSE}	E_H	E_T	η_{NRMSE}	E_H	E_T
WG3	6%	5%	<1%	4%	4%	<1%
WG4	9%	7%	<1%	7%	5%	<1%
WG5	9%	7%	<1%	8%	6%	<1%

The accuracy of η simulation with the piston wave maker is $\sim 2\%$ higher than the one obtained with *waves2Foam* generation. In the not fully developed wave field, however, remarkable differences in η are noticed for the *waves2Foam* generation case (Fig. 4-8): the first free surface displacement happens about two wave periods earlier than the first wave arrival for experimental and piston wave maker generation, and the surface profile develops faster. This effect, due to the specific initial paddle displacement of the wave maker, does not produce remarkable differences in the fully developed wave train (Fig. 4-8).

The computational time needed to complete a 30 s simulation on a single 2.3 GHz processor is about 2 hours for the *waves2Foam* generation, while about 6 hours are necessary for the piston wave maker generation. The higher computational time is related to the dynamic mesh motion resolution.

The *piston wave maker generation* is also tested for irregular and highly non-linear wave simulations e.g. the phase-focused wave in (Fig. 4-9). In this case, the numerical computation follows laboratory experiments carried out by Lupieri et al. (2015), by prescribing the time series of displacement of the numerical wave maker used in the

laboratory to generate the phase-focused wave. Also for this application, the performance of the *piston wave maker generation* are fairly good, with a maximum experimental/numerical relative error never higher than 10%. For such cases, the use of the *piston wave maker generation* would allow a precise simulation of the wave tested in the laboratory, thus giving better consistence to comparison between numerical and laboratory results.

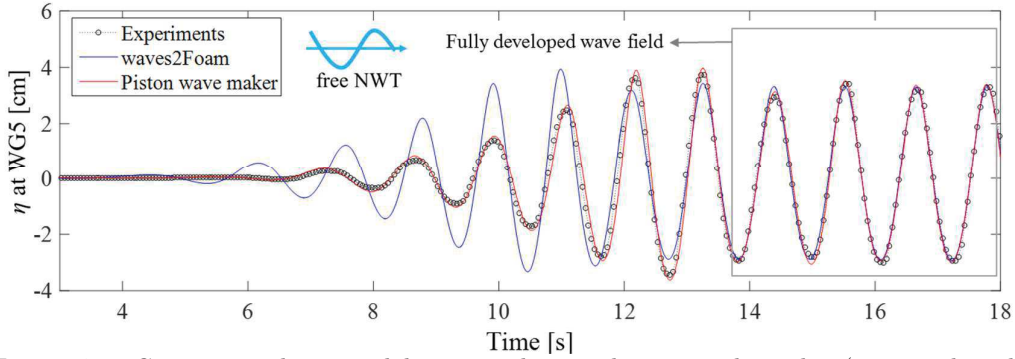


Figure 4-8: Comparison between laboratory data and numerical results (generated with *waves2Foam* and *piston wave maker approach*) for water surface elevation η at wave gauge WG5 (located 9 m away from wave generation) for a regular wave with $H=6.3$ cm and $T= 1.1$ s.

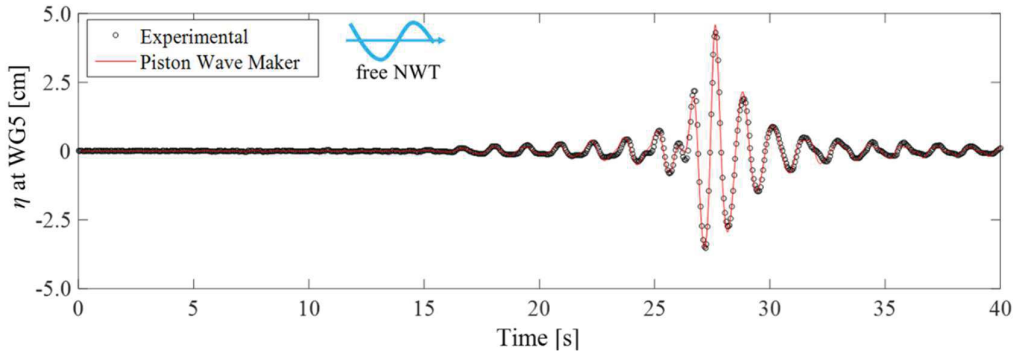


Figure 4-9: Comparison between laboratory (Lupieri et al. 2015) and numerical (*piston wave maker generation*) time series of water surface elevation η for a focusing wave at wave gauge WG5 (located 9 m away from wave generation).

Two wave generation approaches are alternatively compared: *waves2Foam generation* and *piston wave maker generation*. Both approaches are found to be appropriate in reproducing laboratory data for the water surface displacement η of regular waves for the completely developed wave train (relative errors lower than 10%). The *waves2Foam generation*, however, allows a significant reduction of the computational demands (up to ca. 60%), since it avoids the computational time related to the dynamic mesh motion solution.

4.4. Summary and implications

The set-up of a 3D Numerical Wave Tank (NWT), based on Computational Fluid Dynamic (CFD) modelling and developed within the OpenFOAM® framework is presented in this chapter.

Two wave generation approaches are compared: *waves2Foam generation* and *piston wave maker generation*.

Sensitivity tests on the mesh parameters (cells per wave height, H/cells , cells per wave length, and λ/cells , cells aspect ratio, AR , ratio of cell length in refined zone to that in unrefined zone, BK_{SF}) and on the length of the inlet/outlet relaxation zones are performed. The following main conclusion can be drawn:

- (i) Mesh independence may be considered as achieved for a refinement in the free surface zone characterized by of $H/\text{cells}=6$, with $AR=2$ and $BK_{SF}\leq 4$, since no increases in accuracy are observed when adopting a finer mesh. By using these mesh parameters, a relative diffusive error lower than 5% is found.
- (ii) For lengths of the inlet/outlet relaxation zone equal or greater than the incident wave length λ , wave reflection coefficient lower than 5% are obtained.

These results are considered for an accurate simulation of wave generation and propagation processes in the following step of the research, i.e. the three-dimensional model of the OWC device in the NWT (*Chapter 5*).

For both the tested approaches (*waves2Foam generation* and *piston wave maker generation*) wave generation and propagation along the *free NWT* is validated against laboratory data, with the following main results:

- (i) For regular waves, both approaches are found to be fairly good in reproducing experimental measured water surface displacement for the completely developed wave train (i.e. relative errors lower than 10% are found)
- (ii) The *waves2Foam generation* approach, however, allows a significant reduction of the computational demands (up to ca. 60%).

The *waves2Foam generation* approach is, therefore, selected as the wave generation method to be used for the 3D model of the OWC device (*Chapter 5*).

CHAPTER 5

Optimization of OWC geometry and turbine damping: Parameter Study

A three-dimensional, incompressible model of the OWC device in the OpenFOAM® framework is used to perform a systematic parameter study aimed at the device optimization in moderate wave climates. The incompressible CFD model uses the multiphase solver `interFoam`. The wave generation and absorption in the Numerical Wave Tank (NWT) are performed by using the *waves2Foam generation* approach (Jacobsen et al. 2012), discussed in *Chapter 4*.

A preliminary analysis of the results of the laboratory tests by Crema et al. (2016) is carried out in order to select the range of OWC parameters to be more extensively investigated with the CFD model, i.e. the set of OWC geometries leading to the higher capture width ratio (*section 5.1*).

The OWC geometry discretization and the numerical set-up of the CFD model are presented, and the model is validated with data from laboratory tests (*section 5.2* and *section 5.3*).

The parameter study with the validated CFD model aims at providing a knowledge base for the device optimization in a moderate wave climate. Particular attention is given to the effect of the turbine damping, and to the selection of the optimal turbine-OWC chamber coupling (*section 5.4*).

The analysis of the results of the CFD parameter study provides, together with the correction factors for air compressibility delivered in *Chapter 6*, the knowledge base for the development of a conceptual model to be used in the process of OWC design optimization in a moderate wave climate (*Chapter 7*).

5.1. Sequential optimization approach

The starting point for the numerical optimization are the results of the laboratory tests performed by Crema et al., 2016: the range of the OWC parameters to more extensively explore by means of the CFD model is chosen based on the geometries which resulted in higher capture width ratio from the laboratory tests (Fig. 5-1). The numerical model is, therefore, used to enlarge the number of evaluated configurations in the selected range of parameters, allowing a more precise identification of the

conditions leading to the maximum device performance. Indeed, this allows to achieve a high resolution in the exploration of the parameter range around the sub-optimal geometries, without excessively increasing the required number of CFD simulations that are computationally demanding.

The results of the CFD parameter study provide the knowledge base to develop a conceptual model for the prediction of the device capture width ratio, specifically conceived as a tool to be used in the process of OWC design optimization in a moderate wave climate (*Chapter 7*).

The OWC geometries tested in the laboratory and the wave conditions considered are summarized in Table 5-1. The methodology adopted to estimate the OWC capture width ratio, ε_{owc} , from the data collected in the laboratory tests is described in Crema et al., 2015.

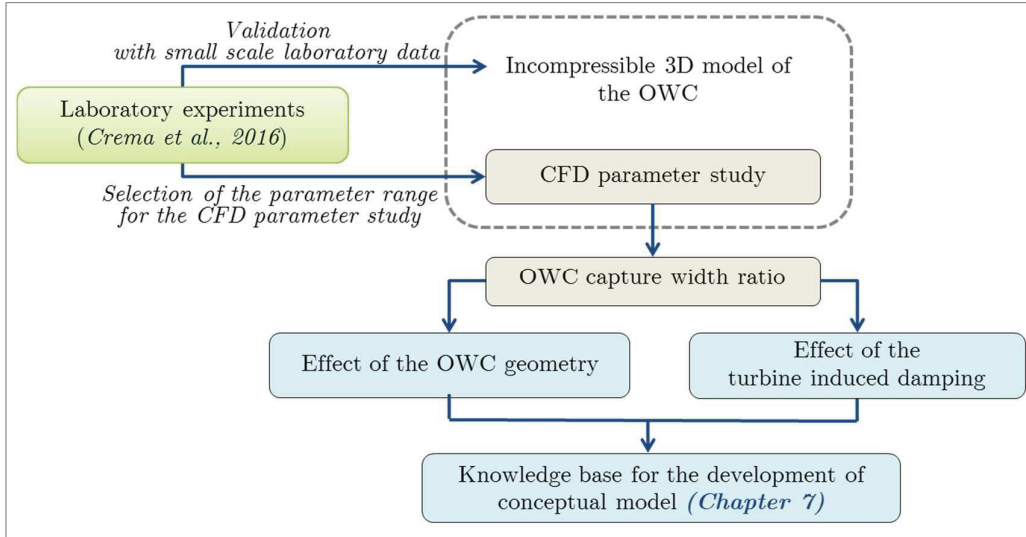
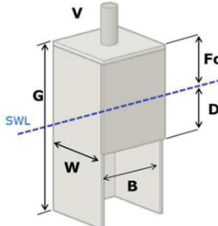


Figure 5-1: Flow chart of the sequential optimization approach.

Table 5-1: OWC geometrical parameters tested in the laboratory (Crema et al., 2016), incident wave height H and period T and water depth h (values for model scale 1:50).

	Front wall draught D [m]	Chamber width W [m]	Top cover vent area
	D1=0.09	W1=0.09	V1=0.5% of top cover
	D2=0.18	W2=0.19	V2=1% of top cover
	D3=0.29	W3=0.29	V3=2% of top cover

	Fixed OWC parameters: $F_c=0.15$ m, $G=0.45$ m Wave conditions and water depth: $H=0.04$ m, $T=0.8/1.0/1.4$ s, $h=0.5$ m
---	--

The highest ε_{owc} -values in the experimental tests are obtained for the following OWC geometries (parameters W , D and V defined in Table 5-1): $W2D1V2$ (0.19m, 0.09m, 1%) and $W2D1V3$ (0.19m, 0.09m, 2%). $\varepsilon_{owc}=0.73$ is reached for the incident wave with $H=0.04$ m and $T=1$ s. For fixed values of W and V , lower ε_{owc} -values are

obtained when increasing the front wall draught D (Fig 5-2). In the configurations with the highest D ($D3=0.29\text{m}$, $D3/H=7.25$), $\varepsilon_{owc}<0.2$ for all tested wave conditions is obtained. For a given value of the front wall draught D and of the top cover orifice aperture V , ε_{owc} is always lower for $W1$ ($W1/\lambda=0.03-0.09$) than for $W2$ ($W2/\lambda=0.07-0.19$) and $W3$ ($W3/\lambda=0.11-0.29$).

For wave periods $T<1$ s (i.e. $W2/\lambda=0.12-0.19$, and $W3/\lambda=0.19-0.29$, Fig. 5.3), the OWC geometries with chamber width $W2$ have ε_{owc} about 10% higher than those with chamber $W3$. On the other hand, for OWC geometries with chamber $W3$, a slightly higher (10% -15%) ε_{owc} -value is obtained for wave period $T=1.4$ s (in this case, $W3/\lambda=0.11$, while $W1/\lambda=0.03$ and $W2/\lambda=0.07$, Fig. 5-3).

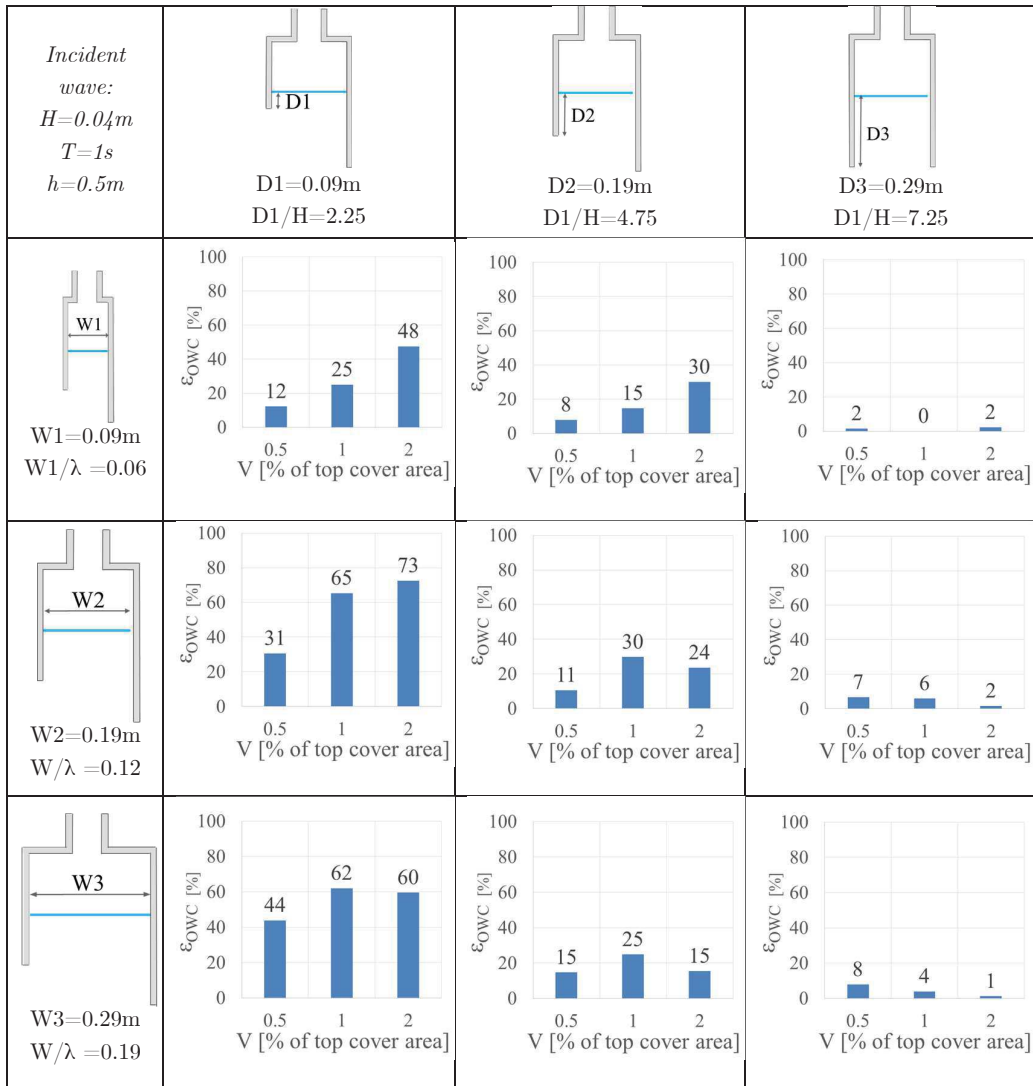


Figure 5-2: Capture width ratio ε_{owc} obtained from laboratory tests (Crema et al., 2016) for fixed wave parameters ($H=0.04\text{m}$ and $T=1\text{s}$), water depth $h=0.5\text{m}$ and different OWC geometries (chamber width W , front wall draught D and top cover vent area V).

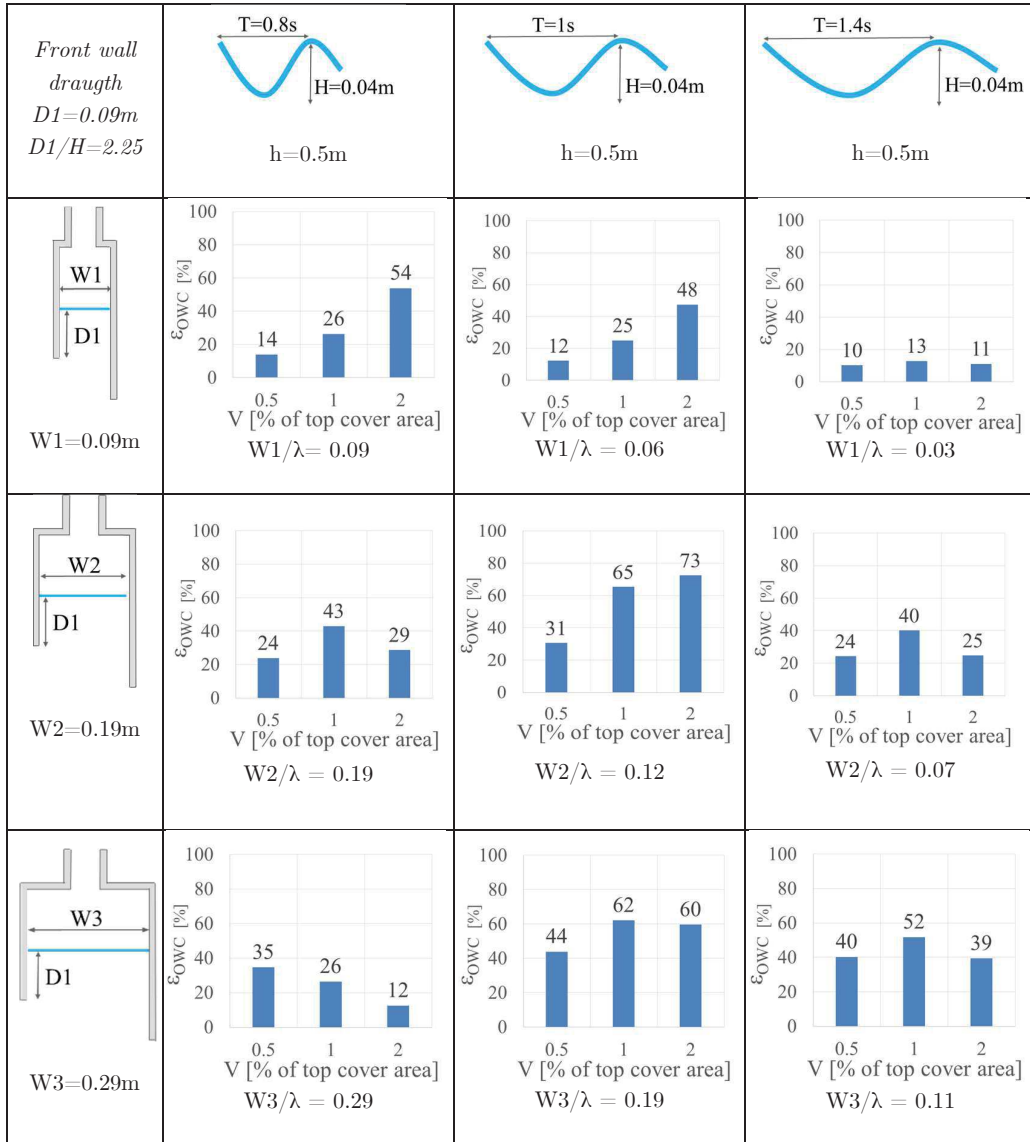


Figure 5-3: Capture width ratio ϵ_{OWC} obtained from laboratory tests (Crema et al., 2016) for fixed OWC front wall draught ($D=0.09m$) and different chamber width W , top cover vent area V , and wave parameters (wave height H and period T) for fixed water depth $h=0.5m$.

Laboratory tests provide a preliminary indication that the optimal design conditions are within the following range of parameters:

- (i) relative chamber width $W/\lambda = 0.07-0.19$,
- (ii) relative front wall draught $D/H \sim 2.25$ and
- (iii) relative vent area $V=1\%-2\%$.

However, the tests did not allow to identify precisely the optimal OWC geometry, since only a limited number of geometries were tested.

Based on these considerations, the range of the design parameters to be more deeply investigated by means of the CFD model, to more accurately individuate the optimal geometry, is selected. In particular, more values around the chamber width $W2$

($W2/\lambda=0.19-0.07$), around the front wall draft $D1$ ($D1/H=2.25$), and vent area between 1% and 2% of the top cover are explored with the numerical model.

The results of the laboratory tests by Crema et al. (2016) provide the basis for the selection of the range of the parameters for the OWC geometry to be further explored by means of the CFD model. Laboratory tests provide a preliminary indication that higher capture width ratio are obtained for relative chamber width $W/\lambda=0.07-0.19$, relative front wall draught $D/H=2.25$ and relative vent area $V=1\%-2\%$. Since only a limited number of OWC geometries were tested in the laboratory, a clear selection of the optimal geometry is not possible. Therefore, the range of OWC parameters to be further explored at a higher resolution by CFD simulations is selected around the geometries resulting in the higher capture width ratios in the laboratory tests.

5.2. Set-up of the incompressible model of the OWC

The theoretical framework of the multiphase solver `interFoam`, which is used for the incompressible simulation of the OWC device, and the wave generation and absorption method for the NWT, the *waves2Foam generation* approach, were presented in *Chapter 4 (section 4.1)*. The numerical discretization of the OWC device geometry and set-up of the model in terms of (i) boundary conditions, (ii) turbulence modelling, (iii) numerical schemes, (iv) linear solvers, (v) time step control and (vi) fluid properties are presented in *this section*.

5.2.1. OWC geometry discretization and mesh generation

A set of different tools, some of which are not part of the OpenFOAM® suite, are used for the discretization of the OWC geometry and for the computational mesh generation (Fig. 5-4).

As a first step, a 3D model of the OWC geometry is generated as a STereoLithography (STL) file. For this purpose, the open source three-dimensional finite element mesh generator Gmsh® (Geuzaine, 2009) is used. In Gmsh®, a 3D geometry can be created based on the code own scripting language, it is therefore possible to define the OWC geometry in a parametric way. This feature is particularly useful in *this PhD research*, since a parameter study on the OWC geometry is performed (*section 5.4*).

Once the STL file of the single OWC geometry is created, the software Paraview® is used to assemble multiple chambers and/or to modify the STL coordinates to locate the OWC in a specific position in the NWT. The computational mesh is created by using the mesh generation utilities `blockMesh` and `snappyHexMesh` of OpenFOAM®. The `blockMesh` utility is used to create a fully structured hexahedral mesh over the entire computational domain (named hereafter background mesh).

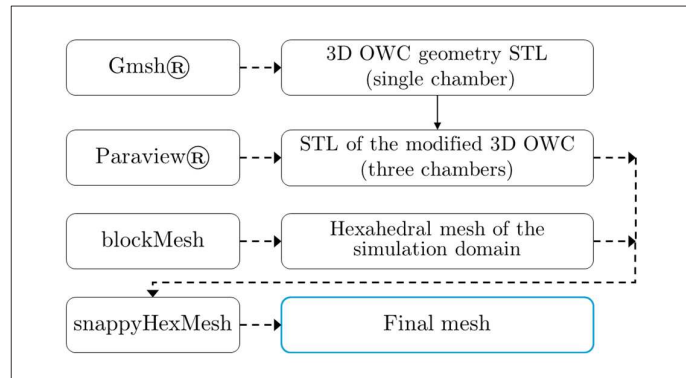


Figure 5-4: Work flow of the OWC device geometry discretization and mesh generation procedure.

Once the background mesh is created, the mesh refinement in the free surface zone and the inclusion of the OWC geometry inside the background mesh are performed using `snappyHexMesh`.

Starting from the background mesh, `snappyHexMesh` performs the following basic steps: (i) refinement of the mesh in specified regions and around specified surfaces by means of an iterative splitting procedure; (ii) adjustment of the mesh on the provided 3D geometry by projecting the mesh boundary cuts created in the refinement process on the surface geometry; (iii) addition of the specific number of layers to the selected patches.

The computational domain has a total length in wave propagation direction of 4.5λ (where λ is the length of the incident wave), a height of approximately 1 m and a width of 0.8 m. Since a symmetry condition is applied, the effective width implemented in the computational domain is reduced to 0.4 m. The OWC model is placed at a distance equal to ca. 2.5λ from the end of the inlet relaxation zone (Fig. 5-5).

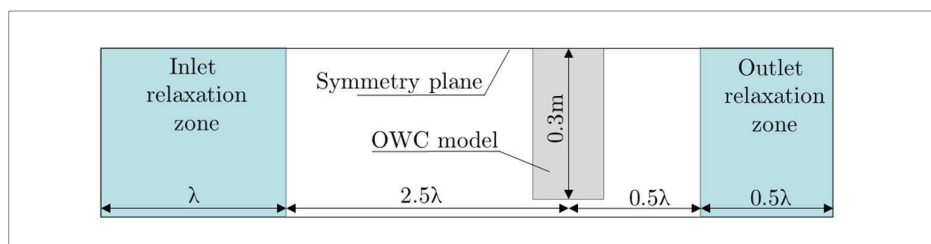


Figure 5-5: Definition of the NWT dimensions and position of the OWC model in the NWT.

In the NWT the mesh is refined around the free surface zone (*free surface mesh region*, Fig. 5-6), based on the characteristics of the incident wave (wave height H and wave length λ), in order to achieve the resolution determined in the grid independence tests performed in *Chapter 4*:

- (i) Number of cells per wave height, $H/cells=6$ and cells aspect ratio $AR=2$;
- (ii) Ratio of the length of the computational cells in the unrefined zone to that in

- the refined free surface zone, BK_{SF} , equal to 4 (see definition sketch in figure 4-3);
- (iii) Length of the inlet and outlet relaxation zone, δX_{IN} and δX_{OUT} , equal to λ and 0.5λ , respectively (Fig. 5-5).

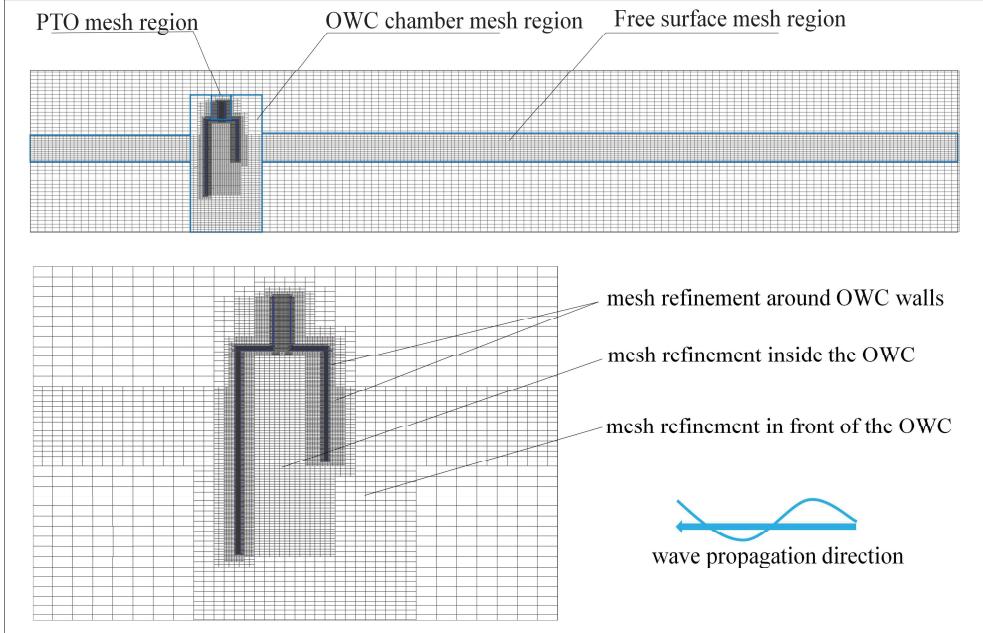


Figure 5-6: Overview of the mesh in the computational domain and refinement mesh region (top), close up of the mesh around the OWC structure (bottom).

In addition to the refinement in the *free surface mesh region*, the computational mesh is specifically refined in other regions (Fig. 5-6): around the OWC structure (*OWC chamber mesh region*), around the OWC top cover vent and pipe (*PTO mesh region*).

In the *OWC chamber mesh region*, the mesh in front of the OWC is refined, by halving the length of the computational cells with respect to the *free surface mesh region*, starting from a distance from the front OWC wall equal to approximately W (Fig. 5-6). In this region, the mesh is progressively further refined around the OWC walls. The length of the cells near the OWC walls is ca. 1.5 mm (corresponding to ca. $W/130$).

In the *PTO mesh region*, the mesh is further refined to properly discretize the circular geometry, in order to have a resolution of about $V_d/\text{cells}=20$, where V_d is the diameter of the circular vent.

Furthermore, 10 prism layers, with expansion factor 1.3, are placed around the OWC walls, to obtain a first cell height equivalent to $y^+\sim 1$ in the submerged region near the OWC walls. The resulting mesh has a size of approximately 2.500.000-3.000.000 cells (depending on the considered λ and on the dimensions of the OWC chamber). The mesh is hexahedral dominant, the maximum value of the mesh non-

orthogonality is around 53, the average non-orthogonality value is about 10.7 and the maximum mesh skewness is about 2.4.

5.2.2. Numerical set-up of the OWC model

Boundary conditions and initial conditions

Considering the boundaries of the NWT with the OWC device as defined in Fig. 5-7, the boundary conditions applied to the NWT were already presented in *Chapter 4 (section 4.2.1)*. As a brief reminder, no slip conditions are set at the bottom of the numerical wave flume and at the OWC structure walls.

The *atmosphere boundary* of the NWT, occupied by the air, is set as a constant pressure boundary. The velocity u and the volume phase fraction a at the *inlet boundary* are strongly imposed by a Dirichlet boundary condition, with values given according to a selected wave theory (see *section 4.2.1* for further details).

Turbulence modelling

As for the case of the *free NWT* of the OWC, a Large Eddy Simulation (LES) approach to turbulence modelling is used. The LES applied in this study uses a k -equation eddy-viscosity closure, which solves a transport equation for the sub-grid scale (SGS) turbulent kinetic energy k_{SGS} (Villers 2006). Further details can be found in *section 4.2.1*.

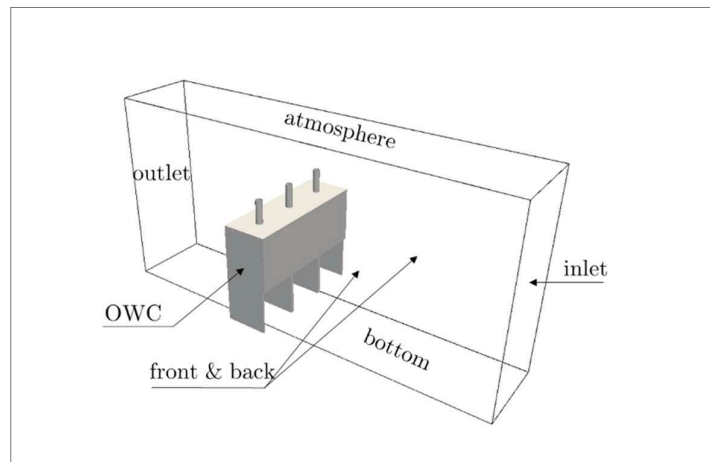


Figure 5-7: Definition of the boundaries of the Numerical Wave Tank (NWT) with the OWC device.

Numerical schemes

The set of numerical schemes applied for the temporal and spatial discretization of governing equations (Eqs. 4.1, 4.2 and 4.8) for the 3D model of the OWC in the NWT can be found in *section 4.2.1* and Table 4-2.

Linear solvers

The set of linear solvers used for the solution of the discretized algebraic system of equations used in the 3D model of the OWC in the NWT are the same adopted for the simulations with the *free NWT* (see *section 4.2.1.* and Table 4-3).

Time step control

In order to increase the solution procedure stability, a self-adjusting time step is used. Time step is adapted at the beginning of every new time loop according to Courant number Co , defined as in Eqs. 4.17 and 4.18. The maximum acceptable value of Co , and the maximum time step Δt_{max} are set as summarized in Tab. 5-2.

Table 5-2: Time step control parameters adopted for the 3D model of the OWC in the NWT.

<i>Parameter [unit]</i>	<i>Value</i>
Time step control	Adjustable time step
Co_{max}	0.6
Δt_{max}	T/200

Environmental and transport properties

The values of gravity acceleration, g , water and air densities (ρ_w and ρ_a , respectively), water and air kinematic viscosity (ν_w and ν_a , respectively) applied for the simulations 3D model of the OWC in the NWT are summarized in Table 4-5.

5.3. Validation of the incompressible CFD model of the OWC with small-scale laboratory tests

The incompressible CFD model of the OWC is validated with data from the laboratory experiments of Crema et al. (2016).

A set of 16 simulations, referred to different OWC geometrical configurations (different draught of the front wall D , different chamber width in wave propagation direction W and different diameter of the top cover pipe V) are tested.

The regular waves used for the validation are the same tested in the laboratory experiments, i.e. are characterized by wave height $H=0.04$ m and periods T ranging from 0.8 s to 1.4 s.

The simulation time is set to around $20T$. The inner OWC surface elevation (η_{owc}) and the relative air pressure (p_{owc}) are sampled at the chamber centre, the vertical component of the velocity of the incoming/outgoing air flux U_y is sampled at the centre of the top cover pipe.

The time series of air pressure p_{owc} (Fig. 5-8), U_y (Fig. 5-9) and surface elevation η_{owc} (Fig. 5-10) in the chamber are compared with laboratory data by means of the determination coefficient R^2 and the Normalized Root Mean Square Error ($NRMSE$).

$$R^2 = \sum_{i=1}^N \left(\frac{x_i - \bar{x}}{\sigma_x} \right) \left(\frac{y_i - \bar{y}}{\sigma_y} \right) \quad (5.1)$$

$$NRMSE = \frac{1}{(x_{\max} - x_{\min})} \sqrt{\left(\frac{1}{N} \sum_{i=1}^N (x_i - y_i)^2 \right)} \quad (5.2)$$

where x_i are the experimental data, y_i are the corresponding numerical data, \bar{x} and \bar{y} are the arithmetic means of the physical and numerical datasets, σ_x and σ_y are the standard deviations of the physical and numerical datasets, x_{\max} and x_{\min} are the maximum and minimum values of the data from the laboratory test.

Overall, the value of the determination coefficient R^2 over the complete validation dataset is higher than 0.93 for all the considered parameters (η_{owc} , p_{owc} and U_y), with an average value of about 0.97 for U_y and 0.98 for η_{owc} and p_{owc} .

The $NRMSE$ over the validation dataset is lower than 16% for all the parameters, with an average value of about 8% (Table 5-3).

Considering values referred to the average OWC inner oscillation period (T_{owc}), i.e. period average values, the maximum value of the air velocity Uy_{max} , the amplitude of the inner water level oscillation $\Delta\eta_{owc}$ and the amplitude of the air chamber pressure oscillations Δp_{owc} have a determination coefficient R^2 with the experimental data of about 0.98 (Fig. 5-11).

Moreover, the good agreement between the laboratory data and the results from the incompressible CFD model persists over the entire range of values of the reference parameters, i.e. no systematic differences are found between the capability of the incompressible CFD model to accurately simulate the OWC system dynamics between low and high values of Δp_{owc} , Uy_{max} and $\Delta\eta_{owc}$.

Table 5-3: Determination coefficient R^2 and $NRMSE$ between the incompressible CFD model of the OWC and laboratory data for relative air chamber pressure, p_{owc} , vertical component of the air velocity, U_y and water levels η_{owc} .

	R^2		$NRMSE$ [%]	
	<i>average</i>	<i>minimum</i>	<i>average</i>	<i>maximum</i>
P_{owc}	0.98	0.94	9.2	15.1
U_y	0.97	0.93	8.2	15.9
η_{owc}	0.98	0.94	8.1	15.6

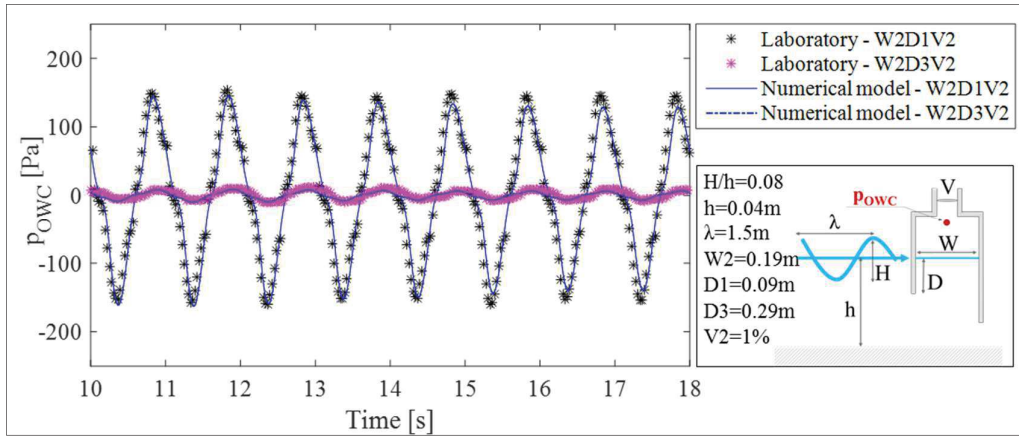


Figure 5-8: Time series of relative pressure p_{owc} in the OWC air chamber, comparison between laboratory data and CFD incompressible model.

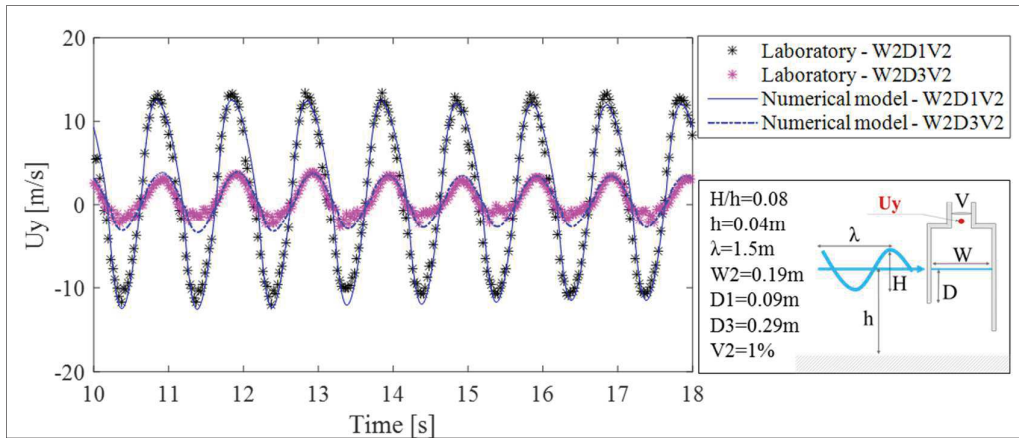


Figure 5-9: Time series of vertical component of the air velocity U_y , in the OWC top cover pipe, comparison between laboratory data and CFD incompressible model.

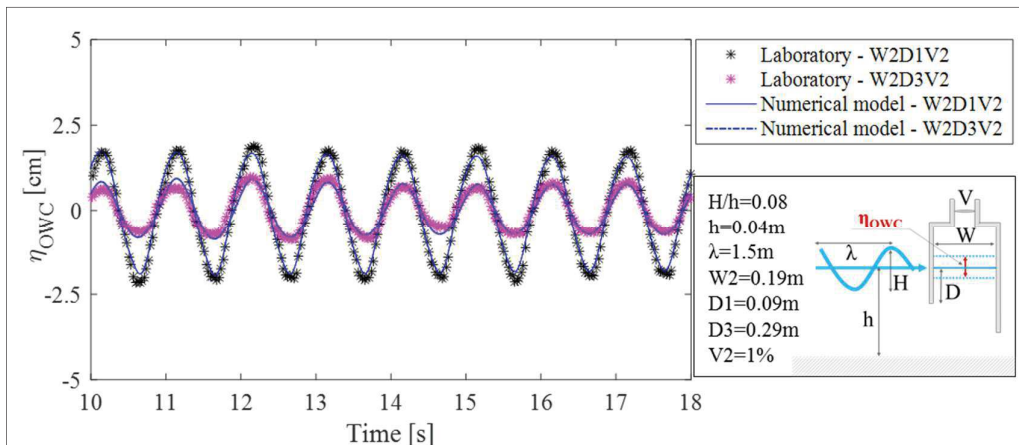


Figure 5-10: Time series of water level η_{owc} in the OWC chamber, comparison between laboratory data and CFD incompressible model.

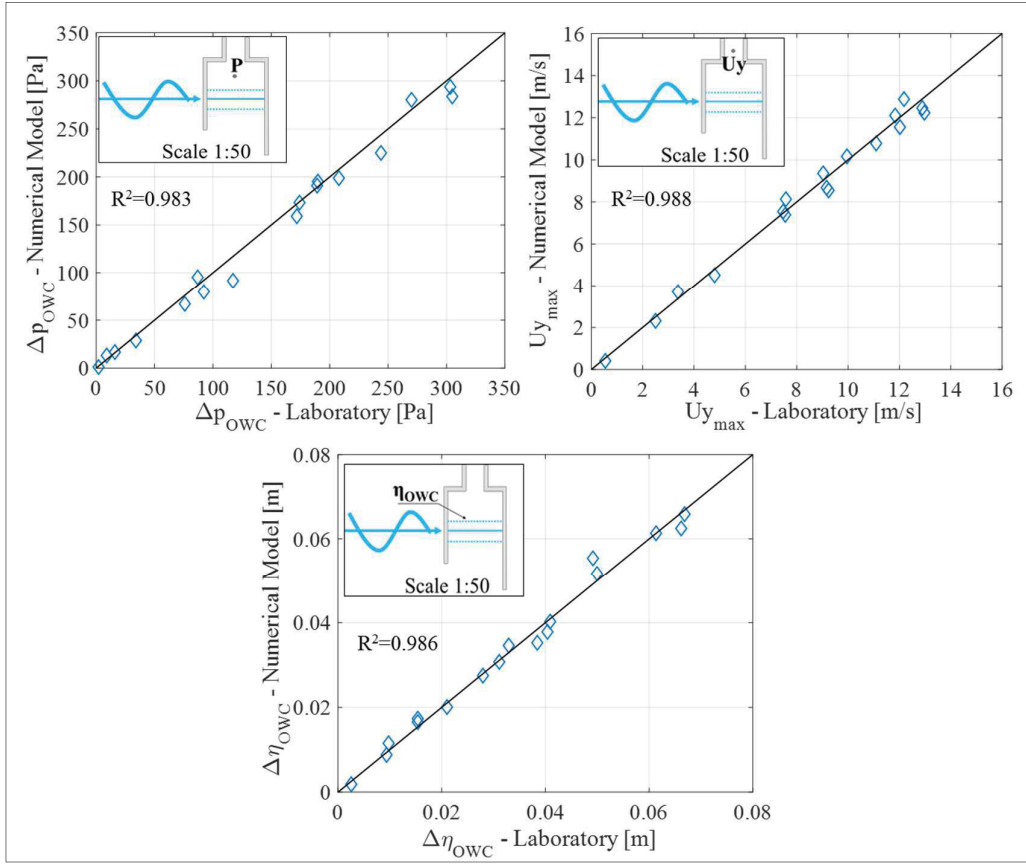


Figure 5-11: Scatter plot between laboratory (Crema et al., 2016) and numerical data for the period average values of air chamber pressure oscillation amplitude, Δp_{owc} , maximum air velocity, $U_{y_{max}}$ and water level oscillation $\Delta \eta_{owc}$. Data refers to laboratory scale (1:50 with Froude similarity).

The incompressible CFD model of the OWC device shows a satisfactory agreement with small-scale laboratory tests from Crema et al. (2016) for both instantaneous and values averaged over the wave period (for relative air pressure, water level and air velocity). The maximum value of the *NRMSE* is about 16% and the minimum R^2 -value is no lower than 0.93.

The relatively good agreement of the results from the incompressible CFD model with those from the small-scale model tests in the laboratory indicates that the air compressibility effects, which may significantly affect the OWC dynamics at full scale, might not be reproduced in the small-scale model tests. Therefore, the evaluation of the error induced by neglecting the effect of air compressibility, and provision of correction factors is crucial. The latter will be provided in *Chapter 6* by the simulations using a compressible CFD model.

5.4. Parameter study of the OWC device using the validated incompressible CFD model

The incompressible CFD model of the OWC device, once validated with experimental data, is used to perform an extensive parameter study aimed at providing a knowledge base to select an optimal OWC geometry (chamber width W and draught D) and an optimal damping that should be applied by the turbine to achieve the maximum wave energy conversion.

Even if it is recognized that the air compressibility may affect the OWC device capture width ratio (*see section 2.3*), the use of the incompressible CFD model to perform a parameter study is justified as follows:

- (i) It allows a better comparison with small scale laboratory data, such as those of Crema et al., 2016, where air compressibility effects might not be reproduced;
- (ii) The methodological approach adopted in to deal with air compressibility in *this PhD research* is based on the provision of correction factors (*see Chapter 6*). The proposed correction factors could be generally applied to small scale laboratory tests on OWC models, therefore extending the impact of the results beyond the specific contest of the *present research*.
- (iii) It would be hardly feasible to perform an extensive parameter study by using a compressible CFD model, given the high computational demands of the compressible model (*see section 6.6*).

It is worth to mention that the parameter study conducted by means of the incompressible CFD model, although being adequate to reproduce the OWC system dynamics at small scale, might be not fully appropriate to characterize the physical phenomena taking place in the OWC at prototype scale. Such phenomena might, in fact, substantially differ from those taking place at small scale, due to air compressibility. This issue should be further investigated in future studies.

In this section, the results of the parameter study are presented, and the sensitivity of the OWC device capture width ratio to the considered parameters is assessed, in order to provide a knowledge base to guide the formulation of a conceptual model based on dimensional analysis, which is presented in *Chapter 7*.

5.4.1. Tested OWC geometries, turbine induced damping and reference wave climate

The parameter study is performed on the OWC device at the same model scale 1:50, as for the laboratory tests carried out by Crema et al. (2016). The tested device is, therefore, composed of three adjacent, identical, OWC chambers, fixed and detached from the NWT bottom. The device is asymmetric in the front and back walls (with a fixed back wall length $B=0.45\text{cm}$, and variable front wall length). The parameters varied in the CFD simulations are: the incident wave parameters (Table

5-4), the OWC front wall draught D , the chamber width W , the top cover vent diameter V (Table 5-5).

In particular, three values of D , three values of W , nine values of V and five values of the incident wave period T are combined and tested to simulate different OWC geometries. Overall, a total number of 220 CFD simulations are performed.

Recalling one of the specific objective of *this PhD research*, i.e. to provide a knowledge base for choosing the optimal OWC geometry parameters for the Mediterranean wave climate, the considered incident waves are those associated with the highest annual energy in the Mediterranean Sea. Therefore, waves with periods between 6 and 8 seconds and heights between 2 and 3 meters at prototype scale are considered (Vannucchi & Cappietti 2013).

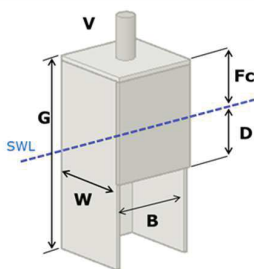
Considering the aforementioned values of the reference wave height, values of the front wall draught D lower than 2.5 m (corresponding to $D < 0.05$ m at model scale 1:50 with Froude similarity) are not investigated, since D should be selected to limit the occurrence of inlet broaching. Broaching phenomenon occurs when the water level falls below the level of the front wall draught, and air at atmospheric conditions directly penetrates the OWC air chamber. Broaching phenomenon is undesirable since it causes loss in the extracted power due to sudden pressure changes in the OWC chamber.

Table 5-4: Characteristics of tested incident wave height H , wave period T and relative water depth kh (fixed water depth $h=0.5$ m).

<i>wave code</i>	H [m]	T [s]	kh
H01	0.04	0.8	3.15
H02	0.04	0.9	2.51
H03	0.04	1.0	2.07
H04	0.04	1.1	1.76
H05	0.04	1.2	1.53
H06(**)	0.04	1.4	1.22
H07	0.03	1	2.07
H08	0.05	1	2.07

(**) only tested in the laboratory (Crema et al., 2016)

Table 5-5: Geometrical parameters of the simulated OWC device and water depth (scale 1:50).

	<i>parameter</i>	[unit]	<i>value</i>
	Chamber width W	[m]	0.17 - 0.19 - 0.21
	Front wall draught D	[m]	0.07 - 0.09 - 0.11
	Top cover vent diameter V_d	[m]	0.022-0.038 (**)
	Back wall length G (*)	[m]	0.45
	Chamber length B (*)	[m]	0.2
	Chamber freeboard F_c (*)	[m]	0.15
	Water depth h (*)	[m]	0.5

(*) Fixed parameters, i.e. parameters that are not varied during in the numerical simulations

(**) Nine values of V_d are considered, from 0.022 m to 0.038 m with a step of 0.002 m.

Turbine induced damping

In the numerical simulations, as well as in the laboratory tests by Crema et al. (2016), the effect of the turbine on the OWC system is reproduced by using orifices of different diameters located on the chamber top cover, in order to simulate the effect of a non-linear power take off (PTO) system. The use of this technique to reproduce non-linear PTO (i.e. representative of turbines of impulse type) was previously applied in Sarmiento, 1992; Sheng et al., 2012; Zhang et al., 2012; Iturrioz et al., 2014.

By using orifices, the relation between q_{owc} and p_{owc} is almost quadratic, with a constant value of the damping coefficient K , is defined as (Pereiras et al. 2015):

$$K = \sqrt{p_{owc}} / q_{owc} \quad (5.3)$$

This assumption was checked with the results of the CFD model, calculating the value of K from the instantaneous values of q_{owc} and p_{owc} for each of the considered orifice diameters (Table 5-6). Values of K in the range $1125 \text{ kg}^{1/2}\text{m}^{-7/2} - 4150 \text{ kg}^{1/2}\text{m}^{-7/2}$ are obtained, and the quadratic air flow-pressure relation is confirmed, with values of the determination coefficient R^2 for the parabolic fit higher than 0.98 for the tested orifices (Fig. 5-13)

Table 5-6: Values of the top cover orifice diameter V_d used in the parameter study and corresponding values of the damping coefficient K .

Orifice diameter V_d [mm]	Damping K [$\text{kg}^{1/2}\text{m}^{-7/2}$]
22	4150
24	3260
26	2680
28	2235
30	1925
32	1650
34	1480
36	1350
38	1125

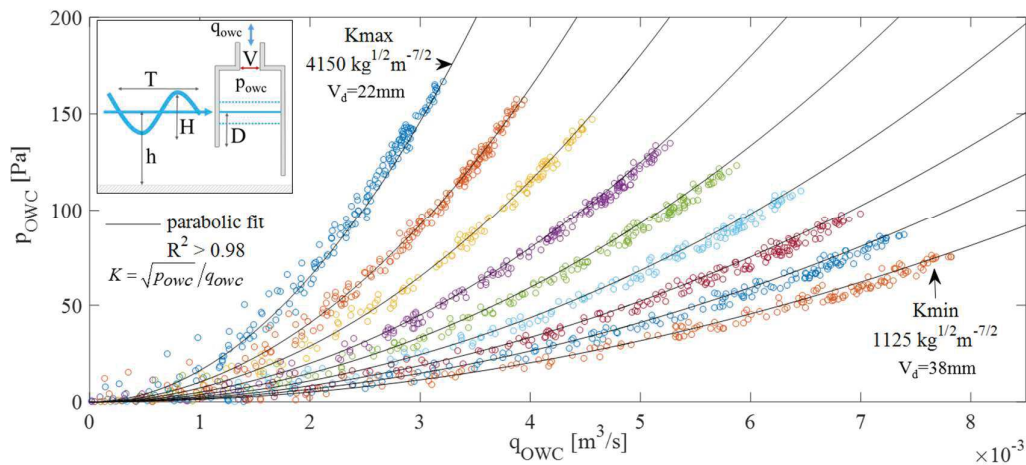


Figure 5-12: Quadratic relations between air volume flux q_{owc} and air chamber pressure p_{owc} obtained for nine values of the top cover orifice V_d considered in the CFD parameter study (see Table 5-8).

5.4.2. OWC capture width ratio

For each simulated case, a total simulation time of $20 \cdot T$ (T =wave period) is considered. This choice is made in order to have at least 10 fully developed oscillation periods inside the OWC chamber. Time series of water level at the centre of the OWC chamber, η_{owc} , relative pressure at the centre of the OWC air chamber, p_{owc} , air velocity Uy and air volume flux q_{owc} at the centre of the top cover piper are collected (Figure 5-13).

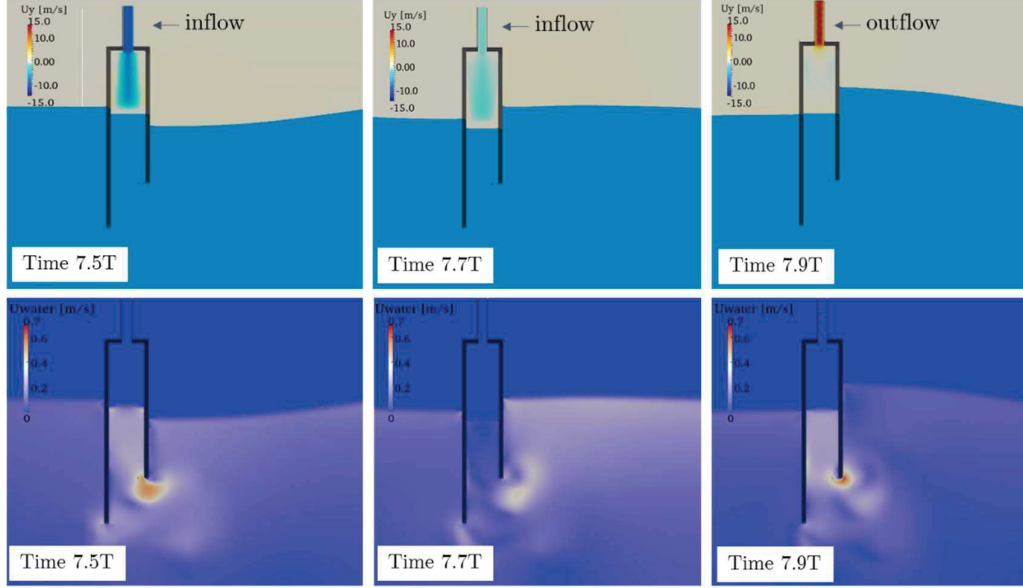


Figure 5-13: 2D cross-section of vertical component of the air velocity Uy in the OWC chamber, water surface elevation (top) and water velocity U_{water} (bottom) at different times during the wave period T .

The capture width ratio of the OWC device, ε_{owc} , is computed as the ratio between the period averaged pneumatic power absorbed by the OWC and the period averaged incident wave power.

Considering incident waves with characteristics corresponding to Stokes second order wave theory, the period averaged incident wave power per unit width [W/m], for generic a water depth h , is expressed as

$$\Pi_{wave} = \frac{1}{16} \rho g H^2 \frac{\omega}{k} \left(1 + \frac{2kh}{\sinh(2kh)} \right) \left(1 + \frac{9}{64} \frac{H^2}{k^4 h^6} \right) \quad (5.4)$$

where ρ_w is the water density, ω is wave frequency and k is the wave number, g is gravitational acceleration. The mean pneumatic power Π_{owc} [W] absorbed by the OWC, is estimated by integrating over the total length of the analysis windows⁹, T_{test} , the product of air pressure p_{owc} in the chamber and air volume flux q_{owc} (Sarmento 1993):

⁹ The analysis widows is chosen in order to consider the fully developed oscillations inside the OWC chamber.

$$\Pi_{owc} = \frac{1}{T_{test}} \int_1^{T_{test}} p_{owc} \cdot q_{owc} dt \quad (5.5)$$

Given the OWC device chamber length perpendicular to the wave propagation direction, assumed at a constant value $B=0.2$ m in this study (Table 5-6), ε_{owc} is computed as:

$$\varepsilon_{owc} = \frac{\Pi_{owc}}{\Pi_{wave} B} \quad (5.6)$$

It should be underlined that, throughout this study, the incident wave conditions in Eq. 5.4 are obtained from specific CFD simulations, performed in the NWT without the OWC device (free NWT) and based on the surface elevation η recorded by a wave gauge located at the OWC device position (3.5λ from the inlet boundary, see Fig. 5-5).

Therefore, far field incident wave conditions are used as reference for computing the capture with ratio ε_{owc} . This is a common practice when considering the wave energy extraction performance of OWCs (see section 2.5). The reflection coefficients Kr of each tested OWC device would be needed to exactly quantify the effect of the device on perturbation of the near field, i.e. obtaining an index strictly defying the OWC efficiency. However, the capture with ratio ε_{owc} is preferred as a reference performance index, since it allows to directly include the local perturbation of the flow induced by the presence of the device, which is (for a fixed wave condition) a specific characteristic of the device itself. This method, therefore, allows for a more consistent comparison of the performance of different OWC device (see section 2.5).

5.4.3. Effect of the turbine induced damping on the OWC capture width ratio

From the results of the CFD parameter study performed on the OWC model, a relevant effect of the applied damping K on both the OWC hydrodynamics and its capture width ratio ε_{owc} , as described by Eq. 5.6, is found.

For a fixed value of the incident wave height H and period T , increasing K results in the increase of the period average value of the relative pressure oscillation amplitude in the air chamber, Δp_{owc} (Fig. 5-14, a). In the range of the numerically tested damping values K , for relative wave height $H/h=0.08$ ($H=0.04$ m) and dimensionless water depth $kh=2.07$, Δp_{owc} is in the range 120-150 Pa for the smallest damping $K=1125$ $\text{kg}^{1/2}\text{m}^{-7/2}$ and in the range 250-300 Pa for the highest damping $K=4150$ $\text{kg}^{1/2}\text{m}^{-7/2}$ (Fig. 5-14, a). It is worth to note that the rate of increase of Δp_{owc} with K is progressively smaller, and would tend to zero in the case of an infinite damping (i.e., a closed OWC chamber, where no water oscillation n_{owc} would take place). The observed variation in the value of Δp_{owc} for the same K are due to the effect of the OWC geometry parameters (W and D).

For the aforementioned incident wave condition ($H=0.04$ m & $kh=2.07$), the period average water surface displacement in the OWC chamber, $\Delta \eta_{owc}$, decreases from about 0.09-0.07 m to about 0.03-0.05 m when increasing the K from 1125 $\text{kg}^{1/2}\text{m}^{-7/2}$ to 4150 $\text{kg}^{1/2}\text{m}^{-7/2}$ (Fig. 5-14, b). The period average value of the maximum air volume flux in

the *exhalation phase* (outflow), q^+_{owc} , instead, decreases from around $7.5 \cdot 10^{-3} \text{ m}^3/\text{s}$ to around $2.5 \cdot 10^{-3} \text{ m}^3/\text{s}$ (Fig. 5-14, c).

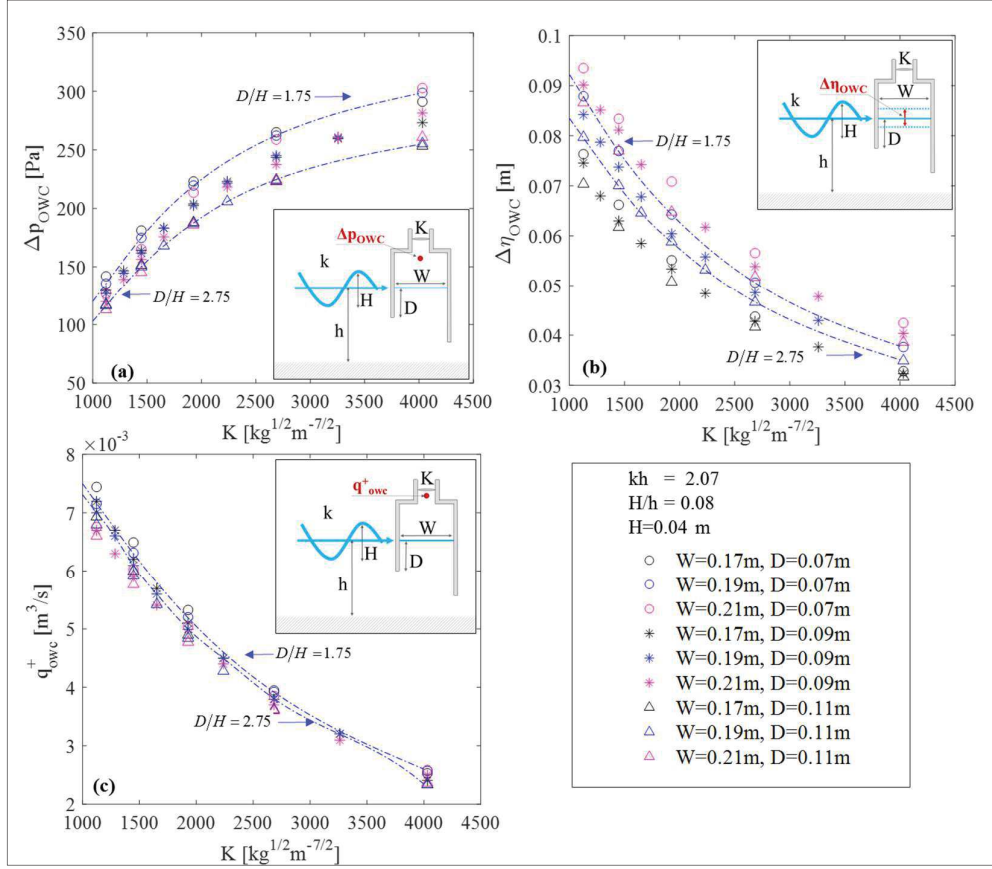


Figure 5-14: Relative pressure oscillation amplitude Δp_{owc} (a) and water surface displacement $\Delta \eta_{owc}$ (b) at the centre of the OWC chamber, maximum air volume flux q^+_{owc} in the top cover pipe (c) versus applied damping K . Results for relative water depth $kh=2.07$, relative wave height $H/h=0.08$ ($H=0.04\text{m}$).

Regarding the capture width ratio ε_{owc} , fixing the geometrical parameters of the OWC (W and D) and the incident wave parameters, the effect of the damping results in a variation of ε_{owc} up to 0.3 for the range of damping K ($=1125\text{-}4150 \text{ kg}^{1/2}\text{m}^{-7/2}$) considered (Fig. 5-15, Fig. 5-16 and Fig. 5.17).

It is worth to note that for each geometry of the OWC chamber (W and D) and for each wave condition (H and kh), a unique optimal value of the PTO damping K_{opt} can be identified, i.e. the value allowing to obtain the maximum ε_{owc} . On both sides of K_{opt} , ε_{owc} decreases, with an evident asymmetry: for $K < K_{opt}$ the rate of decrease of ε_{owc} is higher than for $K > K_{opt}$. This trend is generally valid, despite of the values of W , D , and kh (Fig. 5-15: $kh=1.76$, Fig. 5-16: $kh=2.07$, and Fig. 5.17: $kh=2.51$).

Therefore, *underdamping* ($K < K_{opt}$) reduces the performance of the OWC device to a greater extent with respect to *overdamping* ($K > K_{opt}$). This result is consistent with the previous numerical results by Lopez et al. 2014 (obtained for an OWC system by using an orifice as PTO simulator, as in the *this research*). It can be explained

considering, from one side, the progressively lower rate of increase of Δp_{owc} observed for increasing K (see Fig. 5-14, a), and from the other side, the quadratic relation between p_{owc} and q_{owc} (Eq. 5.3), whose product defines the OWC adsorbed power (Eq. 5.5).

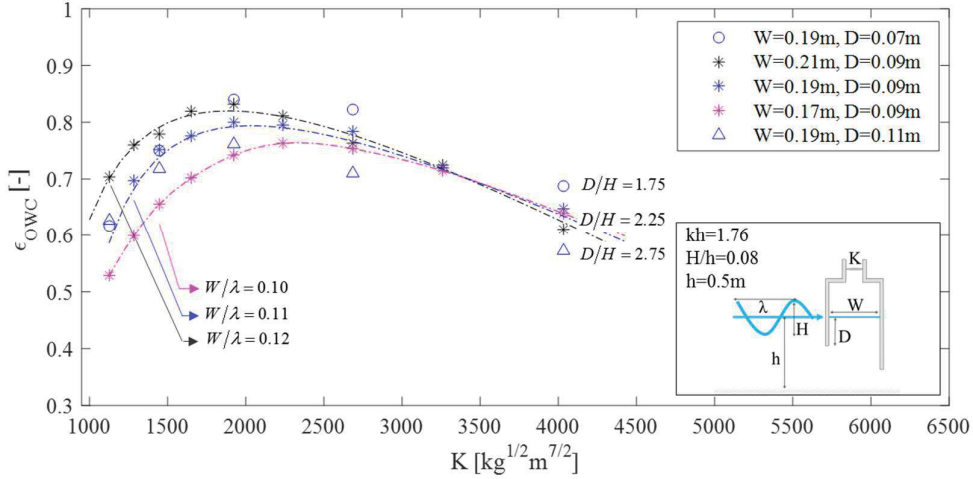


Figure 5-15: Capture width ratio ϵ_{owc} versus turbine damping K . Results for relative water depth $kh=1.76$, relative wave height $H/h=0.08$ ($h=0.5\text{m}$) and different OWC geometries (W and D).

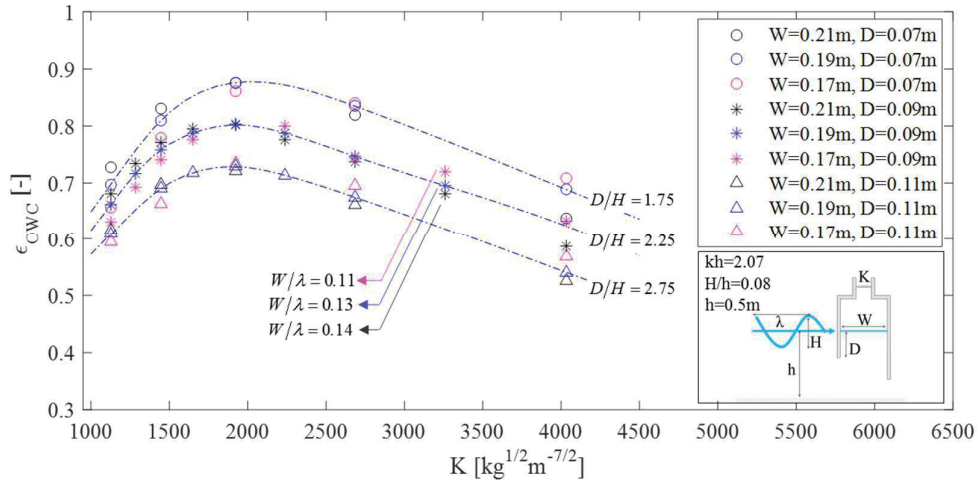


Figure 5-16: Capture width ratio ϵ_{owc} versus turbine damping K . Results for relative water depth $kh=2.07$, relative wave height $H/h=0.08$ ($h=0.5\text{m}$) and different OWC geometries (W and D).

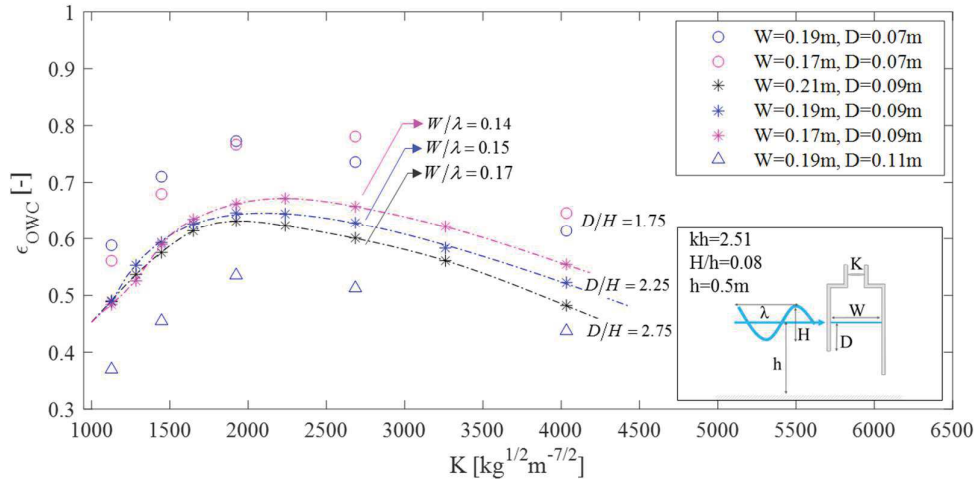


Figure 5-17: Capture width ratio ε_{owc} versus turbine damping K . Results for relative water depth $kh=2.51$, relative wave height $H/h=0.08$ ($h=0.5\text{m}$) and different OWC geometries (W and D).

The effect of damping K on ε_{owc} is, however, strongly dependent on both the chamber geometry (mainly on the chamber thickness W) and the relative water depth kh (i.e. the incident wave length λ for a fixed value of the water depth h). The following observations can be made:

- For relative water depth $kh=1.76$ (Fig. 5-15), a shift towards higher values of the optimal turbine damping K_{opt} can be clearly noticed when decreasing the chamber width W from 0.21 m ($W/\lambda=0.12$, and $K_{opt}\sim 1900 \text{ Kg}^{1/2}\text{m}^{-7/2}$) to 0.17 m ($W/\lambda\sim 0.10$ and $K_{opt}\sim 2200 \text{ Kg}^{1/2}\text{m}^{-7/2}$).
- For the relative water depth $kh=2.07$ (Fig. 5-16), the effect of the chamber width W on K_{opt} is less evident, and values of $K_{opt}\sim 2000 \text{ Kg}^{1/2}\text{m}^{-7/2}$ are found.
- For the relative water depth $kh=2.51$ (Fig. 5-17) a shift towards higher values of the optimal turbine damping K_{opt} when decreasing the chamber width W is, again, evident: for $W=0.21$ m ($W/\lambda=0.17$) $K_{opt}\sim 1900 \text{ Kg}^{1/2}\text{m}^{-7/2}$, for $W=0.17$ m ($W/\lambda=0.14$) $K_{opt}\sim 2200 \text{ Kg}^{1/2}\text{m}^{-7/2}$.

These results could be interpreted by considering that the relative water depth $kh=2.07$ (i.e. incident wave frequency 1 Hz) corresponds to near resonance conditions for the tested values of the front wall draught ($D=0.07\text{-}0.11$ m), as resulting from both laboratory tests by Crema et al. 2016 and the incompressible CFD simulations (Simonetti et al. 2015). For $D=0.09$ m, a value of the resonance frequency of ca. 1 Hz is predicted by the laboratory experiments of Crema et al. 2016 and confirmed by the incompressible CFD simulations, while for $D=0.07$ m and $D=0.11$ m, values only slightly different (~ 0.97 Hz and ~ 1.02 Hz, respectively) are determined by using the CFD model¹⁰. Therefore, near resonance, the value of the optimal damping K_{opt} is

¹⁰ The specific procedure adopted for determining the OWC resonance frequency from the CFD simulations, by means of *decay tests*, is illustrated in Simonetti et al. 2015.

relatively insensitive to the OWC geometry (D and W), while *off resonance* increasing values of K_{opt} are found for decreasing chamber width W . This result is, indeed, expected, and could be theoretically demonstrated by using the analogy of a *mass-spring-damper* systems for the OWC (see Curran et al. 1997).

Moreover, for a given OWC geometry, i.e. fixing relative chamber width W/λ and relative front wall draught D/H , the value of the optimal applied damping K_{opt} (expressed hereafter in terms of the relative damping parameter $KBW/\rho_a^{1/2}$, where B is the chamber length perpendicular to wave propagation direction, W is the chamber width and $\rho_a=1 \text{ kg/m}^3$ is the density of the air) strongly depends on the incident wave conditions, expressed in terms of relative water depth kh (Fig. 5-18). In particular, K_{opt} varies nonlinearly with kh (Fig. 5-19). Increasing kh from ca. 1.53 to 3.15 K_{opt} first tends to decrease (showing minimum values $K_{opt}\sim 75$ at $kh=2.07$ for all the tested geometries). Further increasing kh , K_{opt} tends to increase again.

Overall, for all the tested geometries and relative water depths ($kh=1.53-3.15$), the optimum relative damping K_{opt} is contained in the range 70-110. An interpretation of this effect could be given recalling that the relative water depth $kh=2.07$ (i.e., incident wave frequency 1 Hz at laboratory scale 1:50) corresponds to near resonance conditions for the tested values of the front wall draught ($D=0.07-0.11 \text{ m}$). The optimal applied damping K_{opt} assumes, therefore, a minimum value around the OWC resonance frequency and increases when the excitation frequency does not coincide with that of resonance (*off resonance conditions*).

This result is consistent with the theoretical results by Curran et al. 1997 and Stappenbelt & Cooper 2010, and with the more recent numerical and experimental results by Lopez et al. 2016. A clear theoretical demonstration, based on a simplified *mass-spring-damper* model of the OWC device, is provided by Curran et al. (1997).

A simple explanation of the basic physical phenomena involved can be provided in the framework of linear wave theory, in which, briefly recalling (see *section 2.1*), the wave field is considered as a superposition of the diffraction wave field and the radiation problem (i.e. the wave field generated by the oscillating air pressure in the air chamber, see *section 2.1*).

Theoretically, the maximum absorption of the energy of the incident wave would occur if the reflected wave (*diffraction problem*) was cancelled out by the radiation wave (*radiation problem*) (Falnes & McIver 1985; Falnes 2002). This condition would require the air pressure fluctuation to be in phase with the diffraction flow¹¹. It was also theoretically shown that at resonance, this condition would be automatically satisfied (Falnes 2002). Based on these considerations, the well-known theory of *mass-spring-damper* systems could provide a physical explanation to the observed phenomena: *off resonance* higher values of applied damping allow to reduce the phase-difference between the air pressure fluctuation and the diffraction flow, thus resulting in higher values capture width ratio.

¹¹ This concept is, indeed, at the base of the development of control strategies for OWC systems based on *phase control* (see Strati et al. 2016, Freeman et al. 2014, Falcão 2002).

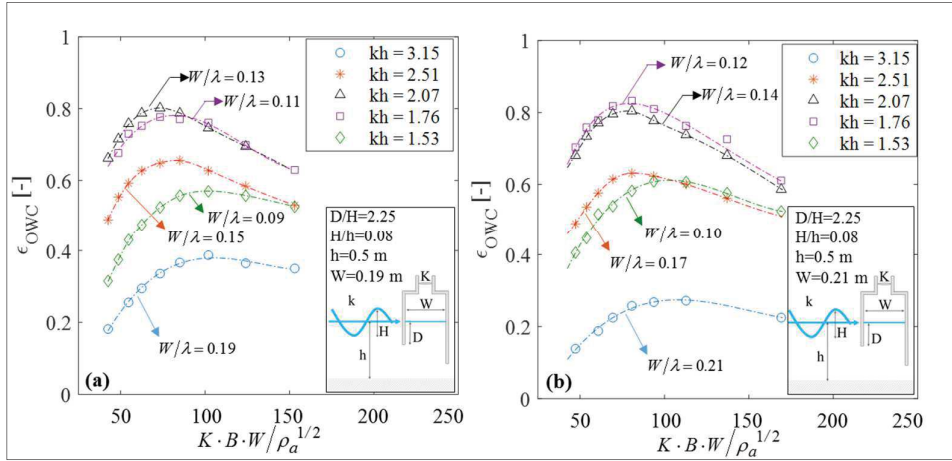


Figure 5-18: Capture width ratio ϵ_{owc} versus non-dimensional damping $KBW/\rho_a^{1/2}$. Results for relative OWC chamber thickness $W/\lambda = 0.09-0.21$, relative front wall draught $D/H=2.25$, $W=19$ m (a) and $W=0.21$ m (b), relative wave height $H/h=0.08$ ($h=0.5$ m) and relative water depth $kh=1.53-3.15$.

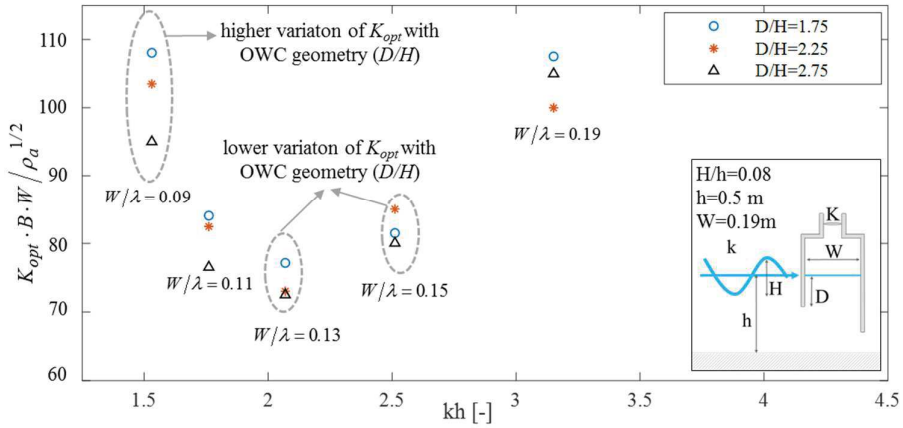


Figure 5-19: Optimal relative applied damping $KBW/\rho_a^{1/2}$ versus relative water depth kh for different OWC geometries (W/λ and D/H), for relative wave height $H/h=0.08$ ($h=0.5$ m).

For each geometry of the OWC chamber described by relative chamber width W/λ and relative front wall draught D/H , a unique value (K_{opt}) of the applied damping K allowing to maximize the capture width ratio ϵ_{owc} exists.

The following main conclusion can be drawn:

- (i) For fixed OWC geometry (W/λ and D/H) and fixed wave conditions, a higher rate of decrease of ϵ_{owc} is observed for $K < K_{opt}$ (*underdamping*). Therefore, *underdamping* reduces the device performance to a greater extent than *overdamping* ($K > K_{opt}$).
- (ii) For a fixed wave condition (kh), the optimal damping K_{opt} decreases when increasing the relative chamber width W/λ .

- (iii) For fixed OWC geometry (W/λ and D/H), the value of the optimal damping K_{opt} is a non-linear function of the relative water depth kh . K_{opt} has the minimum value around the OWC resonance frequency, and increases *off resonance*. For relative water depth $kh=1.5-3.15$, the optimal value of the relative damping $KBW/\rho_a^{1/2}$ varies between 70 and 110.
- (iv) For variations of the relative damping in the range of $KBW/\rho_a^{1/2}=20-170$, the damping K has a crucial effect on ε_{owc} , with variations up to 0.3 in the device capture width ratio ε_{owc} for a given OWC geometry and given incident wave conditions.

5.4.4. Effect of the front wall draught on the OWC capture width ratio

The front wall draught D remarkably affects the OWC capture width ratio ε_{owc} , affecting the OWC system performance by a combination of the following phenomena:

- (i) Increasing D affects the resonance frequency of the OWC device, causing a shift toward higher frequency (i.e. resonance at lower values of kh). This tendency was confirmed by the results of both laboratory tests from Crema et al. (2016) and numerical simulations (Simonetti et al, 2015). It is worth to remark that in the range of D tested with the incompressible CFD model ($D=0.07-0.11$ m, $D/H=1.75-3.6$), the estimated resonance frequency of the OWC is ca. 1 Hz ($kh\sim 2.07$).
- (ii) Increasing D , for fixed incident wave conditions (H and kh), decreases the wave-induced pressure acting on the OWC. The wave-induced pressure decreases for increasing elevation y beneath SWL as described by Eq. 3.5.

For $D/H=1.75-3.6$, a general trend towards higher ε_{owc} is found for decreasing values of the relative draught D , physically interpreted as an effect of the reduced wave induced pressure.

The effect of the relative front wall draught D/H on ε_{owc} strongly depends on kh (Fig. 5-20). In particular, for fixed values of the water depth $h=0.5$ m, relative wave height $H/h=0.008$ and chamber width $W=0.19$ m, higher variations of ε_{owc} with changing D/H are observed for higher values of kh (i.e. for shorter waves):

- For $KBW/\rho_a^{1/2}=100$ it is shown in (Fig. 5-20,a) that decreasing the relative draught from $D/H=1.75$ to $D/H=2.75$ leads to an increase of ε_{owc} from about 0.2 to about 0.6 for $kh=3.15$. For $kh<2.07$, instead the same decrease of D/H results in an increase of ε_{owc} lower than 0.2. The maximum $\varepsilon_{owc}=0.83$ is reached for $kh\sim 2.07$ and $D/H=1.75$.
- For $KBW/\rho_a^{1/2}=70$ (Fig. 5-20,b), decreasing the relative draught from $D/H=1.75$ to $D/H=2.75$ leads to an increase of ε_{owc} from about 0.15 to about 0.4 for $W/\lambda=0.14$ and $kh=3.15$. As for the previous case ($KBW/\rho_a^{1/2}=100$, Fig. 5-20,a), lower rate of decrease of ε_{owc} with D/H are observed when decreasing the relative water depth kh ($kh<2.07$). It is worth to note that for $KBW/\rho_a^{1/2}=70$, the maximum $\varepsilon_{owc}=0.87$ (reached for $kh\sim 2.07$ and $D/H=1.75$) is higher than that observed for $KBW/\rho_a^{1/2}=70$ ($\varepsilon_{owc}=0.83$, Fig. 5-20,a). This confirms that

near resonance, the optimal damping is located around $KBW/\rho_a^{1/2}=70-80$, as observed in *section 5.4.4*, Fig.5-19.

- For $KBW/\rho_a^{1/2}=55$ (Fig. 5-20,c), the rate of decrease of ϵ_{owc} with D/H is further reduced ($\Delta\epsilon_{owc} < 0.1$ when $kh < 2.07$).
- For $KBW/\rho_a^{1/2}=42$ (Fig. 5-20,d), the lower rate of decrease of ϵ_{owc} with D/H for $kh < 2.07$, observed for the previous cases, is confirmed. Moreover, the OWC chamber is strongly underdamped ($K < K_{opt}$) and lower values of the maximum $\epsilon_{owc}=0.70$ (reached for $kh \sim 2.07$ and $D/H=1.75$) are found, confirming that *underdamping* greatly penalizes the OWC performance (see *section 5.4.4*).

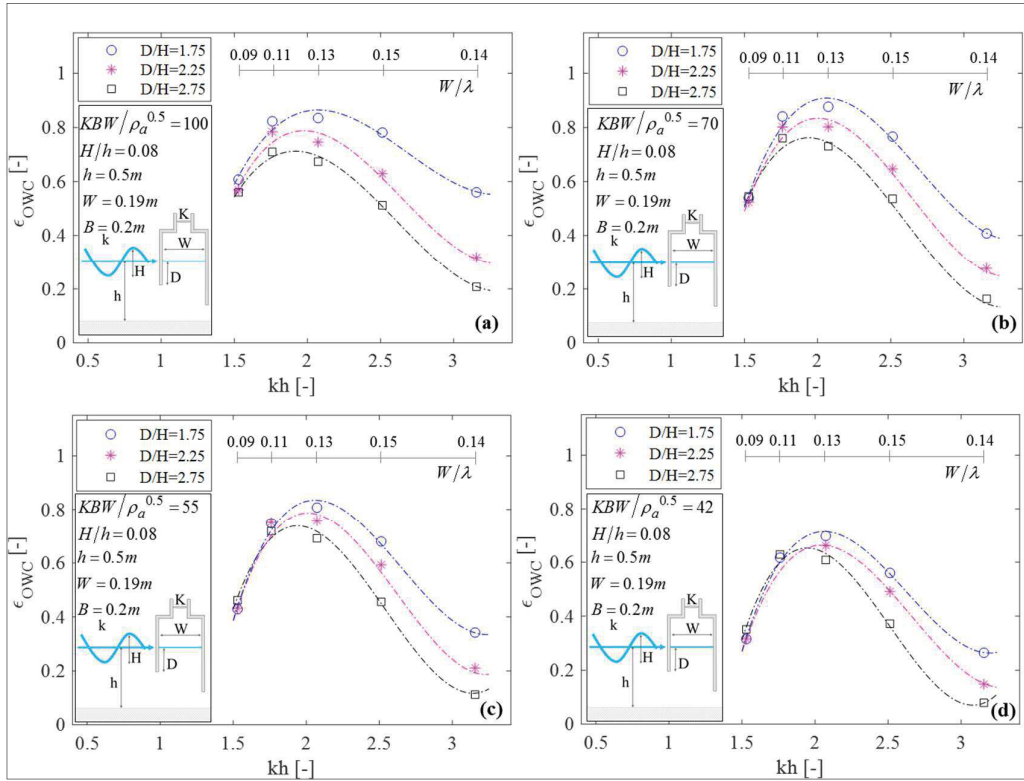


Figure 5-20: Capture width ratio ϵ_{owc} versus dimensionless water depth kh for different relative front wall draughts D/H , relative chamber thickness W/λ and relative applied damping $KBW/\rho_a^{1/2}=100$ (a), 70 (b), 55 (c), 42 (d). Results for relative wave height $H/h=0.08$ ($h=0.5m$).

By explicitly considering the effect of the relative front wall draught D/H on the OWC capture width ratio ϵ_{owc} (Fig. 5.21), the aforementioned differences in the system response at different relative water depth kh are clearly illustrated.

For smaller relative water depth $kh < 2.07$, an almost linear decrease of ϵ_{owc} with increasing D/H is found (with a slight increase of the rate of variation $\Delta\epsilon_{owc}/\Delta(D/H)$ for higher values of the applied damping).

For larger relative water depth $kh > 2.07$, the capture width ratio ϵ_{owc} decreases almost exponentially with increasing D/H . This result, which was also observed in the laboratory tests of Morris-Thomas et al. (2007), can be physically interpreted as a

consequence of the dependency of the vertical distribution of the wave-induced pressure on the wave length λ . For shorter waves (i.e. higher kh values), the higher gradient of the vertical distribution of the wave-induced pressure corresponds to higher rate of decrease $\Delta\epsilon_{owc}/\Delta(D/H)$.

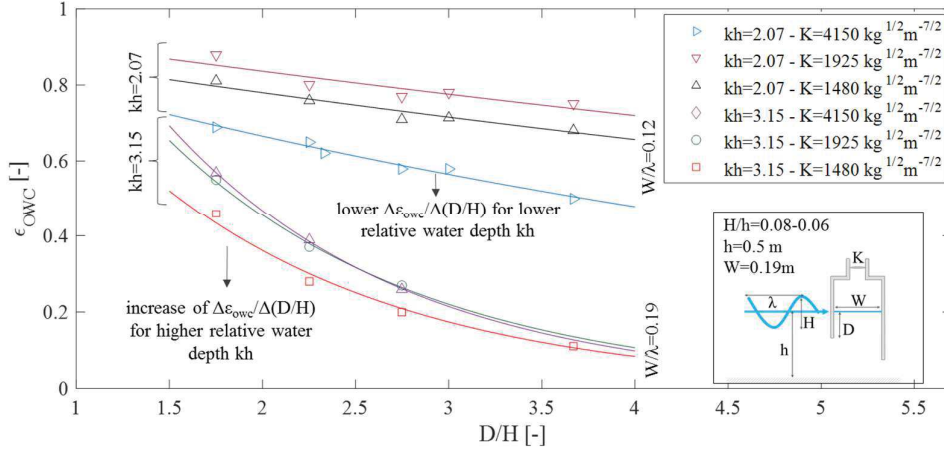


Figure 5-21: Capture width ratio ϵ_{owc} versus relative front wall draughts D/H , for relative water depth $kh=2.07$ and 3.15 and different values of the applied damping K . Results for relative wave height $H/h=0.08-0.06$ ($h=0.5\text{m}$).

The relative front wall draught D/H affects both the wave-induced pressure acting on the OWC and the resonance frequency of the OWC device, which are both determinant for the capture width ratio ϵ_{owc} .

It can generally be observed that, for a fixed relative water depth kh , increasing D/H from 1.75 to 2.75 may result in a decrease of ϵ_{owc} by up to 0.4 as a consequence of the decrease of the wave-induced pressure with increasing depth y below SWL. Moreover, remarkable differences in the effect of D on ϵ_{owc} are observed for different values of the relative water depth kh , which might be physically related to the difference in the vertical distribution of the wave-induced pressure under progressive waves for different length kh . An approximately linear rate of decrease of ϵ_{owc} with increasing D/H is found for $kh < 2.07$, while for $kh > 2.07$ the rate of decrease tends to become exponential ($kh=2.07$ located around optimal value, i.e. around the resonance frequency of the OWC device for $D=0.09-0.11$ m).

5.4.5. Effect of the chamber width on the OWC capture width ratio

Regarding the effect of the chamber width W on the capture width ratio ϵ_{owc} , in the range $D/H=1.75-2.75$, an optimum value of the relative chamber width W/λ exists (Fig. 5-22). Increasing W/λ from 0.08 to 0.12 may result in an increase of ϵ_{owc} up to 0.2, confirming that W/λ represents one of the governing parameters for the optimization of the device design.

For the wide range of the applied relative damping $KBW/\rho a^{1/2}=20-170$, the highest OWC capture width ratio ϵ_{owc} is obtained for $W/\lambda = 0.12$ (for $D/H=2.25$, $h=0.5$ and

$H/h=0.08$). On both sides of $W/\lambda=0.12$ ϵ_{owc} decreases following an approximately quadratic trend, even if asymmetry is observed in the rate of decrease of ϵ_{owc} for $W/\lambda<0.12$ and $W/\lambda>0.12$.

As shown in Fig. 5-22, for a fixed relative front wall draught $D/H=2.25$, the effect of relative chamber width W/λ on the capture width ratio ϵ_{owc} shows a strong dependence on the relative water depth kh (i.e. on the incident wave length λ since the water depth is kept constant with $h=0.5\text{m}$).

In particular, as aforementioned, ϵ_{owc} decreases at different rates at both sides of the optimal value $W/\lambda=0.12$: for $W/\lambda<0.12$ (i.e. for longer waves), the decrease rate is higher than for $W/\lambda>0.12$ (i.e. for shorter waves). This may be physically interpreted by considering that for lower kh -values (i.e. for longer waves), the incident waves propagate with a larger velocity, possibly inducing a more pronounced flow separation at the submerged end of the OWC front wall. The higher flow separation and vortex losses near the front wall end for lower kh -values may, therefore, explain the higher decrease rate of ϵ_{owc} for $W/\lambda<0.12$. Higher intensity of flow separation and turbulence for lower relative depths kh were also observed in the laboratory experiments by Morrison & Greated (1992) and Morris-Thomas et al. (2007).

The observed optimal value of $W/\lambda=0.12$ allows to better understand the results presented in section 5.4.3. For fixed $D/H=2.25$, $H/h=0.08$, $h=0.5\text{m}$ and $kh=1.76$ (Fig. 5-15), the maximum ϵ_{owc} -value is higher for the chamber width $W=0.21\text{ m}$ ($W/\lambda=0.12$, $\epsilon_{owc}\sim 0.83$) than for $W=0.17\text{ m}$ ($W/\lambda=0.10$, $\epsilon_{owc}\sim 0.75$), while for $kh=2.51$, (Fig. 5.17) the maximum ϵ_{owc} is higher for the chamber width $W=0.17\text{ m}$ ($W/\lambda=0.14$, $\epsilon_{owc}\sim 0.67$) than for $W=0.21\text{ m}$ ($W/\lambda=0.17$, $\epsilon_{owc}\sim 0.73$). This trend could be now explained, considering the aforementioned optimal value of $W/\lambda=0.12$, and the asymmetric rate of decrease of W/λ observed on both sides of the optimum.

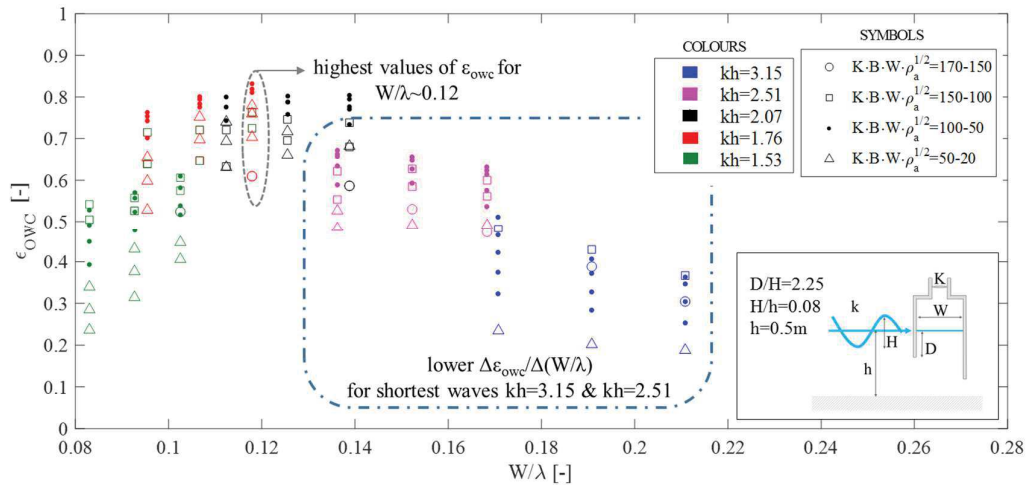


Figure 5-22: Capture width ratio ϵ_{owc} versus relative chamber width W/λ for different values of the applied relative damping $KBW/\rho a^{1/2}$ (20-170). Results for relative wave height $H/h=0.08$ (water depth $h=0.5\text{m}$) and relative front wall draught $D/H=2.25$.

In the tested range of relative OWC front wall draught, D/H ($=1.75-3.6$) and relative damping $KBW/\rho a^{1/2}$ ($=20-170$), the highest values of the OWC capture width ratio ε_{owc} are obtained for values of the relative chamber width W/λ of about 0.12. The decreasing rate for $W/\lambda < 0.12$ is slightly higher than for $W/\lambda > 0.12$. Increasing W/λ from 0.08 to 0.12 may result in an increase of ε_{owc} up to 20%, confirming that W/λ represents one of the governing parameters for the optimization of the device design.

The effect of relative chamber width W/λ on the capture width ratio ε_{owc} shows a strong dependence on the relative water depth kh which might be physically related to the higher energy loss induced by flow separation at the front wall for lower values of kh . Moreover, a strong correlation between W/λ and the applied damping K is found: the value of the optimal damping K_{opt} increases when decreasing W/λ .

5.5. Summary and implications

Laboratory tests from Crema et al. (2016) show that higher pneumatic conversion efficiencies are obtained for relative chamber width within the range of $W/\lambda = 0.07-0.19$, values of the relative front wall draught around $D/H \sim 2.25$ and vent areas (to simulate turbine damping) between 1% and 2% of the top cover area. Since only a limited number of OWC geometry alternatives were tested in the laboratory, the optimal OWC geometry in terms of capture width ratio ε_{owc} could not be precisely identified. Therefore, an incompressible CFD model is used to extend the range of tested conditions within and around the aforementioned range by using a higher resolution in the parameter variation, thus allowing to better identify the conditions maximising ε_{owc} .

The CFD modelling results shows a satisfactory agreement with the small scale laboratory tests, with maximum *NRMSE*-values of about 15% and minimum determination coefficient $R^2 = 0.93$. This relatively good agreement indicates that compressibility effects are not reproduced in the small-scale model tests. Therefore, the evaluation of the error induced by neglecting the effect of air compressibility, and provision of correction factors, as performed in *Chapter 6*, is crucial.

Considering the best performing OWC geometry and wave conditions obtained from the laboratory tests ($\varepsilon_{owc} = 0.73$ for relative chamber width $W/\lambda = 0.12$, relative front wall draught $D/H = 2.25$, relative vent area $V = 2\%$, for regular wave height $H = 0.04$ m and period $T = 1$ s in a constant water depth $h = 0.5$ m), the CFD parameter study allowed to achieve a higher capture width ratio ($\varepsilon_{owc} = 0.87$) for $W/\lambda = 0.12$, $D/H = 1.75$ and $KBW/p_a^{1/2} = 70$, $H = 0.04$ m $T = 1$ s and $h = 0.5$ m.

The maximum value of ε_{owc} obtained in this study is consistent with the laboratory tests of Morris-Thomas et al., 2007 ($\varepsilon_{owc} \sim 0.8$) and the numerical (CFD) results by Zhang et al., 2012 ($\varepsilon_{owc} \sim 0.85$), both referred to bottom-standing OWCs. The recent laboratory tests of He et al., 2016, performed on a fixed, detached, symmetric OWC showed, instead, significantly lower value of the maximum ε_{owc} (~ 0.4). The asymmetry of the OWC device considered in *this PhD research* (with fixed relative back wall

length $B/h=0.6$), indeed specifically conceived to minimize the transmitted wave (Crema et al. 2015), might therefore allow to substantially increase the device performance. This result is also confirmed in the recent studies of Elhanafi et al. (2016c), who found that an asymmetric increase of the back wall draught could determine an increase of the ε_{owc} -value from ~ 0.30 to ~ 0.68 .

It is worth to note that for the moderate wave climate considered in *this PhD research*, resonance with waves contributing to a great fraction of the total annual energy in the reference installation site (i.e. $H=2\text{m}$ and $T=7\text{s}$ at scale 1:1, see Vannucchi & Cappietti, 2013) can be achieved with relatively small values of the front wall draught D ($D=4.5\text{ m}$ at scale 1:1).

From the results of the parameter study, the following main conclusions might be drawn:

- (i) A value of the turbine damping K_{opt} allowing to maximize the OWC capture width ratio ε_{owc} can univocally be determined for a given OWC geometry (i.e. fixing the values of front wall draught D and chamber width W) and for a given relative water depth kh . Moreover, *underdamping* ($K < K_{opt}$) reduces the device performance much more than *overdamping* ($K > K_{opt}$). The optimal value of damping K_{opt} is strongly dependent on both the chamber width W (K_{opt} increases when W decreases) and the relative water depth kh (assuming minimum value around resonance conditions, increasing *off resonance*), even if the effect of the latter is much higher.
- (ii) The front wall draught D has a fundamental effect on the capture width ratio ε_{owc} , since it affects both the resonance frequency of the device and wave-induced pressure acting on the OWC. In the tested range of D/H ($=1.75\text{-}3.75$) and kh ($=1.53\text{-}3.15$) it can generally be observed that increasing D results in a decrease of the capture width ratio ε_{owc} . Moreover, remarkable differences in the effect of D on ε_{owc} are observed for different values of the relative water depth kh .
- (iii) The relative OWC chamber width W/λ crucially affects the capture width ratio ε_{owc} . In the tested range of D/H ($=1.75\text{-}3.75$) and kh ($=1.53\text{-}3.15$) higher ε_{owc} -values are obtained for $W/\lambda \sim 0.12$, and an approximately quadratic decreasing trend is found for both higher and lower values W/λ . The decreasing rate for $W/\lambda < 0.12$ is slightly higher than for $W/\lambda > 0.12$.
- (iv) A strong mutual interaction is found between all the parameters considered. This overall finding, therefore, confirmed that an optimization of the OWC device in terms of capture width ratio ε_{owc} , can be achieved only through a combined consideration of the design parameters.

The results of the parameter study using the incompressible CFD model provides a fundamental knowledge base, and substantially extends the dataset generated in the small-scale laboratory tests (Crema et al., 2016). This knowledge base will be used, after the evaluation of air compressibility effects and the correction of the overall dataset to account for air compressibility (as determined in *Chapter 6*), for the

development of a conceptual model for the prediction of the device capture width ratio (*Chapter 7*).

The methodological choice of performing the parameter study by using the incompressible CFD model is, justified since: (i) it allows a more consistent comparison with the small scale laboratory data of Crema et al. 2016; (ii) it allows to develop a knowledge base on the reference conditions at small scale (in terms of air chamber pressure and air velocity) which is fundamental for the subsequent provision of correction factors; (iii) it would be practically not feasible to perform such an extensive parameters study with a compressible CFD model, which is remarkably more computationally demanding. The methodological approach adopted in *this research*, is seemingly adequate to reproduce the processes in the OWC at laboratory scale and for the provision of a knowledge base to develop a conceptual model of the OWC performance (*Chapter 7*). Among the limitation of this approach, it should be mentioned that the parameter study conducted by means of the incompressible CFD model might be not fully representative of physical phenomena taking place in the OWC at prototype scale, which might substantially differ due to air compressibility. This aspect should be studied in deep in future research.

CHAPTER 6

Evaluation of air compressibility effects on OWC system dynamics

It is recognized that air compressibility may have a relevant role in the system dynamics in OWC devices at prototype scale, since large volumes of the air chamber are needed to prevent green water from reaching the turbine. Moreover, in small-scale laboratory tests, an appropriate simulation of the thermodynamic effects associated with air compressibility in the OWC chamber is difficult. In fact, to completely fulfil dynamic similarity between model and prototype, the scale ratio for the volume of the air chamber should not necessarily correspond to the scale ratio for the submerged part of the converter. Hence, a volume of the air chamber larger than the one resulting from Froude scaling would be needed to reproduce in compressibility effects in a small scale model of an OWC device (*see section 2.3*).

Chapter 6 presents the evaluation of the error induced by neglecting the effect of air compressibility in modelling OWC devices, and provision of correction factors for the results from incompressible numerical models and from small-scale laboratory testing of OWC devices. A compressible CFD model is used to simulate the OWC device at different model scales (1:50, 1:25, 1:10, 1:5 and 1:1). For this purpose, the standard compressible VOF solver of OpenFOAM® (`compressibleInterFoam`) is implemented into the wave generation framework `waves2Foam` (*section 6.2*).

Before using the compressible model to simulate the OWC device at prototype scale, a benchmarking of the compressible solver is performed to ensure its suitability to properly reproduce compressible effects (*section 6.3*).

The compressible code is then used to simulate the OWC device at laboratory scale (1:50). The calculated results are in good agreement with both the experimental data and the results of the incompressible OWC model in *Chapter 5*, confirming that compressibility effects are not well reproduced in the small-scale model tests (*section 6.5*). A preliminary comparative analysis of results obtained with the incompressible CFD model at scale 1:50 and 1:1 is performed (*section 6.6.2*), to verify whether effects not related to air compressibility affect the up-scaling of the problem. Finally, the compressible model is applied to simulate the OWC device at prototype scale. The effect of neglecting air compressibility is analysed and correction factors to take into account air compressibility effects are proposed (*section 6.6.3*).

The task which have been performed and the main results which have been achieved in *Chapter 6* are schematically summarized in Figure 6-1.

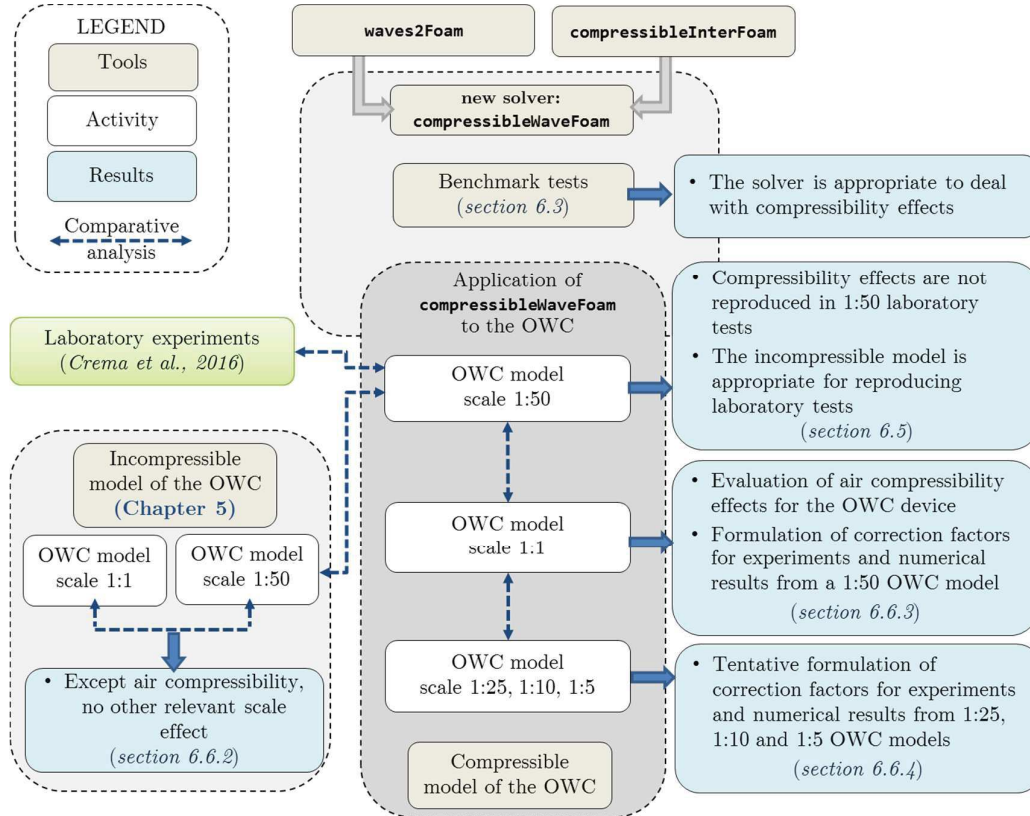


Figure 6-1: Flow chart summarizing the main tasks and results presented in *Chapter 6*.

6.1. Theoretical background of the compressible multiphase solver

The study is based on the `compressibleInterFoam` solver. The CFD solver can describe low Mach number flows of two compressible, non-isothermal immiscible fluids using a VOF interface capturing approach. The governing equations for the two-phase flow are solved using a Eulerian fluid mixture approach, i.e. momentum and other fluid properties are of the two fluid mixture, and properties vary according to the volume fraction of each phase (phase fraction, a).

The `compressibleInterFoam` is a pressure-based solver, i.e. it adopts pressure as the primary variable. In the *pressure-based approach*, finite variations of pressure take place, regardless the value of *Mach number* Ma (Webster et al. 2004), hence the problems of density-based methods in the low *Mach number* regime are avoided. *Density-based solver*, in fact, may fail to appropriately reproduce the incompressible flow governing equations for *Mach number* $Ma \ll 0.3$ (Guillard & Viozat 1999; Murrone & Guillard 2008; Roller & Munz 2000). In the subsonic regime, the magnitude of the flow velocity is small compared to the speed of the acoustic wave, and the resulting discretized system is stiff and exhibits slow convergence due to the dominance

of convection terms. The effect of the system stiffness on the convergence of the solution affects both explicit and implicit schemes.

This aspect is particularly important for the application of the compressible solver to the OWC case, since the expected maximum Ma , even at prototype scale, is generally around 0.3¹². Hence, the expected flow regime is, at maximum, weakly compressible.

A brief introduction to the theoretical background and the formulation of the solver `compressibleInterFoam` is given hereafter.

The governing equations for fluid dynamics describe mass conservation (Eq. 6.1), momentum conservation (Eq. 6.2) and energy conservation (Eq. 6.3), together with an *equation of state*, relating the fluid density ρ to its pressure p and temperature T_f .

$$\nabla \cdot (\rho u) + \frac{\partial \rho}{\partial t} = 0 \quad (6.1)$$

$$\frac{\partial \rho u}{\partial t} + \nabla \cdot (\rho u u) = -\nabla p + \nabla \cdot \tau + \rho g + F \quad (6.2)$$

where u is the fluid velocity vector, τ the viscous stress tensor, g the gravity acceleration, p the pressure and t the time, and F is the source of momentum due to surface tension (see *section 4.1.1*).

The energy conservation equation is solved along with the mass and momentum conservation equations. The energy conservation equation, which may generally be expressed either in the form of (i) specific enthalpy h_e , (ii) specific internal energy i , or (iii) temperature T_f , is formulated in `compressibleInterFoam` in terms fluid temperature T_f (Eq. 6.3).

$$\frac{\partial (\rho C_p T_f)}{\partial t} + \nabla \cdot (\rho C_p T_f u) = \nabla \cdot (\Psi_e \nabla T_f) + S_T \quad (6.3)$$

where C_p is the fluid specific heat, ψ_e is the fluid thermal conductivity and S_T is the source term in energy equation.

The constitutive relation for τ is:

$$\tau = \mu \left[\nabla u + (\nabla u)^T \right] + \frac{2}{3} \mu (\nabla \cdot u) I \quad (6.4)$$

where μ is the fluid dynamic viscosity, I is the identity tensor.

For an ideal gas, the *equation of state* is:

$$p = \rho R T_f \quad (6.5)$$

where R is the ideal gas constant.

For water, which is nearly incompressible in the range of pressure here considered, a simplified equation of state is used (as proposed in Cole, 1948):

¹² The maximum value of *Mach number* Ma inside the OWC air chamber at prototype scale can be preliminary evaluated by considering the maximum value of air velocity obtained in the parameter study at scale 1:50 (documented in *Chapter 5*), $Uy \sim 15$ m/s. Scaling up to scale 1:1 this maximum velocity by applying Froude similarity (Tab. 6-4), and considering a reference speed of sound in the air 340 m/s, maximum values of Ma of about 0.3 would be estimated.

$$\varrho = \frac{1}{R_w T} p + \varrho_0 \quad (6.6)$$

where ϱ_0 is the reference water density at $T=0$ °C, and R_w ($=3000$ J/kgK) is a constant which allows to set the appropriate value of the speed of sound in the liquid as:

$$c = \sqrt{\delta R_w T} \quad (6.7)$$

where $\delta=C_p/C_v$ is the specific heat ratio.

The basic principles of the VOF approach, which is used by `compressibleInterFoam`, are described in *section 4.1.1*. The pressure-velocity coupling is performed in `compressibleInterFoam` using the PIMPLE algorithm (see *section 4.1.1*). In the specific case of a transient compressible simulation, the non-linear effects of the velocity could be more significant due to the fluid compressibility. The momentum equation is therefore located in the outer PIMPLE loop, and recalculated as many times as the specified number of iterations for the PIMPLE loop. In the implementation of the solver `compressibleInterFoam`, also the energy equation is located in the outer PIMPLE loop.

Concerning the modifications needed to momentum equation and to the pressure-velocity coupling algorithm to deal with density variations in compressible flows, as implemented in `compressibleInterFoam` starting from version 2.3.0 of OpenFOAM®[®], the following reference might be consulted: Moukalled et al., 2016.

6.2. Implementation of `compressibleInterFoam` into `waves2Foam`

As mentioned in *Chapter 4* and *Chapter 5*, the *waves2Foam generation approach* is used in this PhD study. which is based on the library `waves2Foam` (Jacobsen et al. 2012). The working principles of the *waves2Foam generation approach* and its validation are described in *Chapter 4*. As a brief reminder, the standard `waves2Foam` toolbox is coupled with the incompressible VOF scheme of OpenFOAM®[®] (`interFoam`).

In order to combine the capability of the *waves2Foam generation approach* with the need to solve for compressible flow, `compressibleInterFoam` is implemented into the library `waves2Foam`, adding to it the relaxation zone approach to generate/adsorb waves and a set of pre/post processing utilities (e.g. to set the initial conditions in the computational domain, `setWaveFields`; to compute the relevant parameters for the selected wave theory, `setWaveParameters`; to create wave gauges and probes, `waveGaugeNProbes`). Some comments to the modifications made to `compressibleInterFoam` in this PhD study to obtain the new solver named `compressibleWaveFoam`, and how these modifications affect the code, are briefly given hereafter.

The following line is added in the header of `compressibleWaveFoam.C`:

```
#include "relaxationZone.H"
```

This includes the `relaxationZone` class, the general relaxation zone interface which is the base class for `relaxationSchemes`. In `relaxationZone.H`, `relaxationScheme.H` is

included. It declares `relaxationSchemes` class, an abstract base class for the generation of different relaxation schemes by means of `waveProperties` dictionary lookup. There are abstract base classes for allowing run time selection of both relaxation parameters and wave theory to be used.

Inside the `main` section in `compressibleWaveFoam.C`, the following line has to be included:

```
#include "readWaveProperties.H"
```

which reads the species wave properties and the relaxation zone parameters in the dictionary `system/waveProperties`.

Adding before the PIMPLE loop inside `compressibleWaveFoam.C`

```
relaxing.correct();
```

explicit relaxation is performed before the solution of momentum equation.

6.3. Benchmark tests for the validation of the compressible solver

In order to evaluate the capability of the numerical solver to deal with air compressibility, `compressibleWaveFoam` is applied to a set of benchmark cases. The selected benchmark are used in the literature as reference cases to assess the performance of numerical methods for air-water systems in which air compressibility is relevant. In particular, since the topic of air compressibility bias in small scale model testing was extensively investigated within the Sloskel Joint Industry Project (Braeunig et al. 2009; Brosset & Dias 2009; Bogaert et al. 2009), the selected benchmarks presented in *section 6.3.1* and *section 6.3.2* are chosen among the reference cases used in this project.

6.3.1. Gravity-induced liquid piston in a tube (1D case)

The first considered benchmark consists in a 1D closed tube, with a total length of 15 m, filled with an 8 m water column surrounded by two air pockets, one at the top and the other at the bottom of the tube (Fig. 6-2). Given the dimension of the geometry, and the consequent high value of the air pressure reached in the compression phase, this benchmark might be considered as representative of prototype scale conditions for a one-dimensional model. This benchmark case, which is very close to the classical Bagnold problem (Bagnold 1939), was proposed as a reference case for the Sloskel project (Dias & Brosset 2010), and its wide application for benchmarking purposes is well-documented (Bredmose et al. 2009; Braeunig et al. 2009; Guilcher et al. 2009; Ma et al. 2014).

Friction effects are ignored, and the initial density of air is set to $\rho=1 \text{ kg/m}^3$, while the density of water is $\rho=1000 \text{ kg/m}^3$. At the beginning, the velocity of both air and water is zero and the air pressure is equal to 1 bar everywhere in the computational domain. Then, the water column starts falling due to gravity effects, compressing the air in the lower pocket. The water decelerates while the pressure in the lower pocket

increases, until the water velocity reduces to zero. At that point, the air pocket starts to expand pushing the water column upwards.

To discretize the case, 300 cells equally spaced were distributed along the vertical tube, and the time series of pressure was recorded at the bottom of the tube. The discretization schemes are second order accurate in both time and space. A time step Δt equal to 10^{-3} s is used, and the vertical dimension of the computational cells is 0.05m. The results, in terms of both peak pressure inside the lower air pocket and its time of occurrence, are in good agreement with data from the literature (e.g. Guilcher et al. 2009).

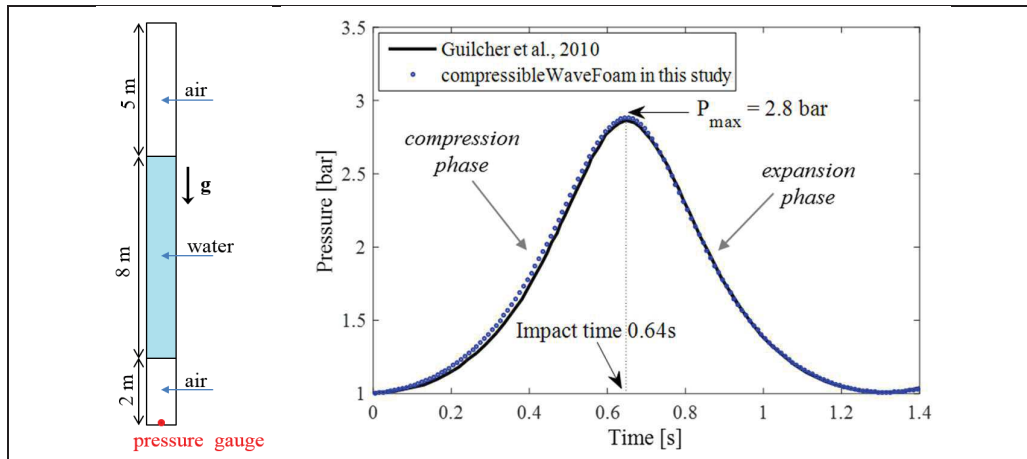


Figure 6-2: 1D benchmark case (left) and time series of pressure at the bottom centre of the piston (right), comparison between values numerically simulated by `compressibleWaveFoam` in this study.

6.3.2. Gravity-induced liquid piston in a tank (2D case)

The second test case considered is an extension to 2D of the gravity induced liquid piston case: it consists in the gravity fall of a rectangular water column in a closed tank (Fig. 6-3). Also this benchmark has such big dimensions to be considered as representative of prototype scale for a two-dimensional model.

The case has been widely used as a further benchmark for numerical codes (Braeunig et al. 2009; Guilcher et al. 2009; Bogaert et al. 2009; Ma et al. 2014). In the 2D tank, the water ($\rho_w = 1000 \text{ kg/m}^3$) is surrounded by air ($\rho_a = 1 \text{ kg/m}^3$), the velocity field is initially set to zero, and the initial pressure in the air phase is equal to 1 bar. Under gravity, the water column drops and impacts the bottom after about 0.65s. The pressure peak at the time of impact has a maximum value at the centre of the tank (Ma et al, 2014), where a small amount of air is trapped between the water column and the tank bottom, and undergoes compression and expansion (Fig. 6-4). Therefore, a pressure probe is set at this location to record the pressure time history. The computational mesh used for the simulation with `compressibleWaveFoam` has 400 cells in horizontal direction and 300 cells in vertical direction. The discretization schemes are second order accurate in both time and space. A time step Δt equal to

10^{-3} s is used, and the size of the computational cells is 0.05 m, in both vertical and horizontal directions.

A satisfactory agreement between the calculated results and the data from the literature is achieved in terms of both peak pressure at the time of the first impact of the water column on the bottom and its time of occurrence $t=0.65$ s (Fig. 6-3). A slightly lower peak pressure is obtained with respect to the results of Ma et al. (2014) (ca. 31 bar against ca. 34 bar). This might be due to the higher number of cells in vertical direction (1400) used by Ma et al.

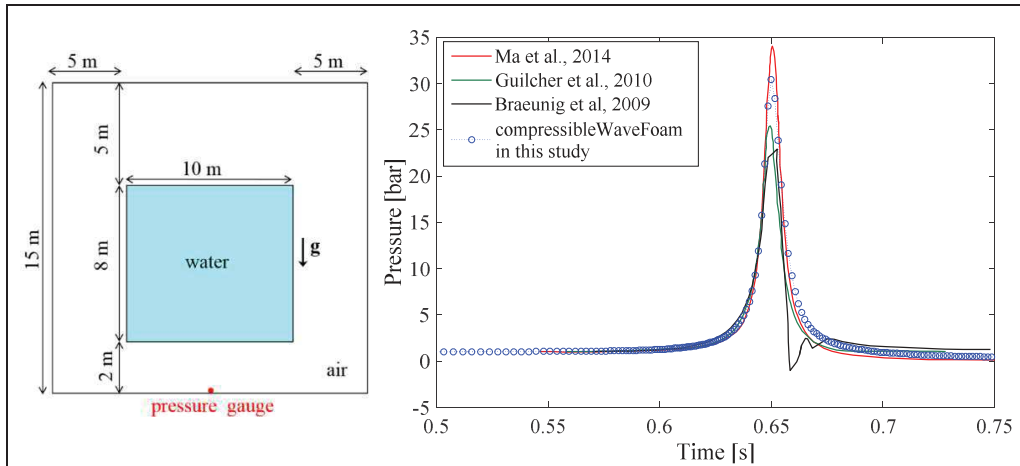


Figure 6-3: 2D benchmark case (left) and time series of absolute pressure at the wave gauge located at the tank bottom centre (right), comparison between values numerically simulated by `compressibleWaveFoam` in this study and data available in literature.

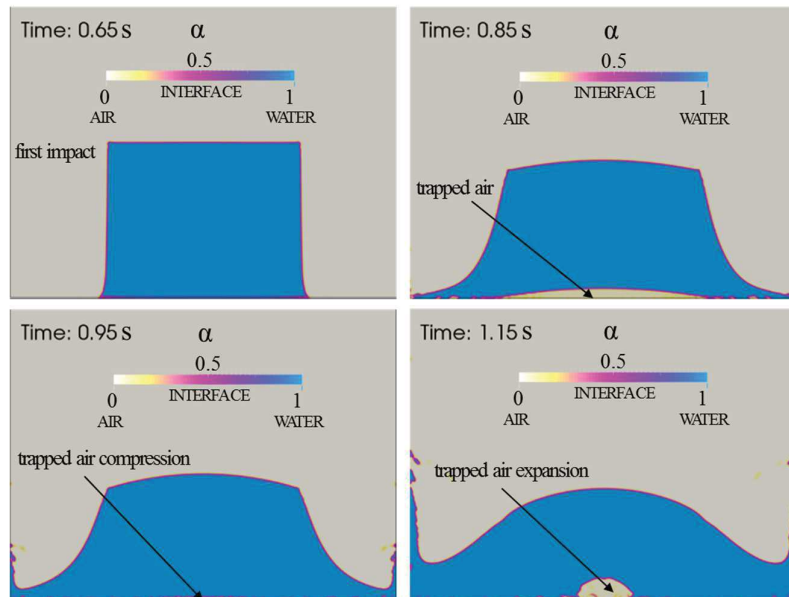


Figure 6-4: Volume fraction of air and water ($\alpha = \text{water/air}$) in the 2D benchmark case at different time steps after the first impact of the water column on the bottom: $t=0.65$ s, 0.85 s, $t=0.95$ s and $t=1.15$ s. Results obtained with `compressibleWaveFoam` in this study.

6.3.2. Air water shock tube

In several studies (e.g. Bullock et al. 2007; Peregrine et al. 2005), it is reported that shock waves may occur in the region of the aerated water after the impact of a wave on a wall. In a more general framework it is, therefore, appropriate to assess the capability of a compressible numerical model to deal with shock waves propagation.

A classical shock tube problem involving air and water mixture is tested (Fig. 6-5): a one-dimensional tube divided by a membrane into two inner parts. The left part is filled with a fluid at high pressure, and the right part with another fluid at low pressure, then the membrane is removed.

The domain is discretized distributing 1000 equally spaced cells along the tube. The computation time step is set to 10^{-8} s, and second order accurate schemes for time and space discretization are adopted.

The numerical results are compared with analytical results (Plumerault et al. 2012). The location of the rarefaction wave (Fig. 6-6) is well predicted, i.e. the model is able to reproduce the velocity of propagation of the shock.

Some non-physical spurious oscillations are observed near the contact discontinuity. Spurious oscillations are, however, a typical behaviour of numerical codes for this kind of application, which results from numerical discretization.

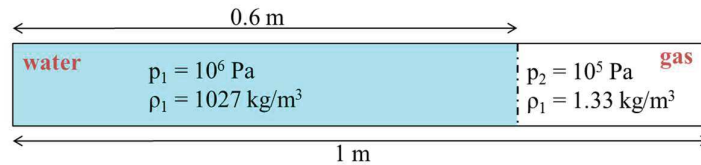


Figure 6-5: Air water shock tube benchmarking case and fluid properties (pressure p and density ρ).

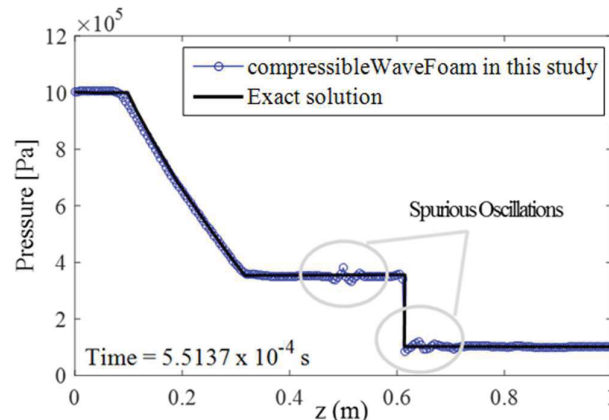


Figure 6-6: Comparison of the analytical solution (Plumerault et al. 2012) and the numerical simulation obtained with `compressibleWaveFoam` in this study for the problem of an air-water shock tube at time $5.5137 \cdot 10^{-4}$ s.

Benchmarking is fundamental in the present study, since data at prototype scale (1:1) for the OWC device are not available.

Benchmark tests, widely used in literature to assess the performance of compressible air-water models, are performed in this study using the new solver `compressibleWaveFoam` to ensure its capability to reproduce properly compressible effects. In particular, the benchmarks in *section 6.3.1* and *6.3.2* might be considered as representative of prototype scale (in terms of compression levels) for one-dimensional and two-dimensional models respectively. The results show that the performance of the code is fairly in good agreement with available data from the literature, hence demonstrating the capability of the solver to cope with compressible two-phase flows.

Besides the good performance of the solver on the selected benchmarks, it is worth to note that a validation of the OWC compressible model with full-scale data on a completely equivalent OWC system, would still be required to demonstrate the accuracy of the results obtained from the compressible OWC simulation at scale 1:1 (see *section 6.6*).

6.4. Numerical set-up of the compressible model for the OWC

Boundary conditions and initial conditions

Considering the designation of the boundaries of the NWT with the OWC device defined in Fig. 5-7, the boundary condition applied to the NWT for velocity u , pressure p , VOF volume phase fraction a are the same used for the incompressible CFD simulations in *section 5.2.2*. Additionally, in the compressible simulations, boundary and initial conditions are needed for the fluid temperature T_f . An value of 293 K is imposed for T_f at the inlet boundary with a Dirichlet boundary condition.

Turbulence modelling

As for the case of the incompressible CFD model of the OWC (*chapter 5*), a Large Eddy Simulation (LES) approach to turbulence modelling is used. The Large Eddy Simulation (LES) applied in this study uses a k-equation eddy-viscosity closure, which solves a transport equation for the sub-grid scale (SGS) turbulent kinetic energy k_{SGS} (Villers 2006). Details on the model can be found in *section 4.2.1*. The use of such a model for LES of compressible flows is well documented in Martín et al. 2000 and Chai & Mahesh 2010.

Numerical schemes, linear solvers and time step

The discretization schemes for the time derivatives used is a second order scheme, blended with a first order Euler scheme to improve stability. The discretization of the convection terms is done with second order schemes, In particular, convection terms in momentum equation are discretized with a total variation diminishing (TVD)

scheme with a central differencing interpolation scheme bounded by a Sweby limiter (Sweby 1984). For the convection term in the transport equation of the volume phase fraction a , Monotone Upwind Schemes for Scalar Conservation Laws (MUSCL, Van Leer 1979) interpolation scheme is used, which is a TVD scheme with an high accuracy level even in the case of shocks or elevate gradient of the solution. For generic gradient operators, second order accurate discretization schemes are applied.

Regarding the linear solvers, a preconditioned conjugate gradient solver (PCG) is used for the pressure equation. The Krylov subspace solver bi-conjugate gradient solver for axisymmetric matrix (PBiCG) is used for u and for a , with a simplified diagonal based incomplete LU preconditioner (DILU). An iterative GaussSaidel iterative smoother is used for k_{SGS} and T_f .

An adaptive time step is used, determined based on the maximum Courant number $Co=0.6$, based on Eqs. 4.17 and 4.18.

6.5. Compressible simulations of the small-scale OWC model

The compressible CFD code is used to simulate the flow processes in the OWC device at laboratory scale (1:50). The aims of this step is to verify whether there are systematic differences between the compressible and the incompressible model results when simulating the OWC device at laboratory scale 1:50. This is done to confirm that the incompressible model, as found in *Chapter 5*, is capable to properly reproduce the laboratory experiments at such small scales where the air compressibility effects are negligibly small.

The simulations at small-scale, i.e. in a context where Ma is supposed to be low ($\ll 0.3$)¹³, are particularly important to also ensure the suitability of the compressible CFD model to provide an accurate approximation of the incompressible equations for low *Mach number* flows. In fact, compressible schemes may become inefficient and suffer severe instability for low-*Mach number* flow regimes (Roller & Munz 2000).

A set of 16 simulations with different OWC geometrical configurations (different draught of the front wall D , different length of the chamber in wave propagation direction W , different diameter of the top cover pipe V_d) are tested. The regular wave trains tested are characterized by wave height $H=0.04$ m and periods T ranging from 0.8 s to 1.4 s. The simulation time is set to $20T$ (in order to observe at least 10 completely developed oscillation periods inside the OWC chamber, see *Fig. 6-11*). The inner OWC surface elevation (η_{owc}) and air pressure (p_{owc}) are sampled at the chamber centre, the vertical component of the velocity of the incoming/outgoing air flux, U_y , is sampled at the centre of the top cover pipe.

The time series of p_{owc} (*Fig. 6-7*), U_y (*Fig. 6-8*) and η_{owc} (*Fig. 6-9*) are compared with

¹³ The maximum values of *Mach number* Ma inside the OWC air chamber at small scale can be evaluated by considering the maximum values of air velocity obtained in the parameter study documented in *Chapter 5*, $U_y \sim 15$ m/s. Considering a reference speed of sound in the air 340 m/s, maximum values of Ma of about 0.05 are estimated.

experimental data by means of the determination coefficient R^2 and the Normalized Root Mean Square error ($NRMSE$), defined as in Eq. 5.1 and Eq. 5.2, respectively.

For the compressible OWC model, the value of the determination coefficient R^2 with laboratory data by Crema et al. (2016) is higher than 0.93 for all the considered parameters (η_{owc} , p_{owc} and U_y), with an average value of about 0.98 for p_{owc} and η_{owc} , and 0.97 for U_y (Table 6-1).

The $NRMSE$ over the validation dataset is lower than 18% for all the parameters, with an average value of about 9% (Table 6-1). A slightly higher value of the $NRMSE$ (around 17.5%) is found on p_{owc} in the compressible CFD simulations respect to the incompressible CFD simulations (where the $NRMSE$ on p_{owc} is ca. 15%).

This could be a consequence of the spurious oscillations that can be observed in the compressible model for values of p_{owc} close to zero (Fig. 6-7). These spurious oscillations could be an index of the instability of the compressible code for very low *Mach numbers* as reported in the literature (e.g. Roller & Munz 2000). Values of p_{owc} close to zero, in fact, occurs when U_y is approximately zero (hence when $Ma \approx 0$). The observed instability is, however, moderate and does not compromise the efficiency of the compressible model.

Table 6-1: Determination coefficient R^2 and $NRMSE$ for comparison of results of the incompressible and compressible CFD simulations with data from laboratory tests. Results for for relative air chamber pressure, p_{owc} , vertical component of the air velocity, U_y and water levels η_{owc} .

		R^2		$NRMSE$ [%]	
		average	minimum	average	maximum
Incompressible model	p_{owc}	0.98	0.94	9.2	15.1
	U_y	0.97	0.93	8.2	15.9
	η_{owc}	0.98	0.94	8.1	15.6
Compressible model	p_{owc}	0.98	0.93	10.0	17.5
	U_y	0.97	0.93	8.5	16.3
	η_{owc}	0.98	0.94	8.4	15.3

The relatively good agreement between the physical model data and the results from both compressible and incompressible CFD models persists over the entire range of values of the reference parameters. Considering values referred to the average OWC inner oscillation period (T_{owc}), called hereafter period average values, the maximum value of the air velocity $U_{y_{max}}$, the amplitude of the inner water level oscillation $\Delta\eta_{owc}$ and the amplitude of the air chamber pressure oscillations Δp_{owc} have a determination coefficient R^2 with the experimental data of about 0.98, for both compressible and incompressible CFD models (Fig. 6-10).

No relevant or systematic differences are found between the performance of the compressible and incompressible models in simulating the OWC device at scale 1:50. This is valid when considering both the instantaneous values and period average values.

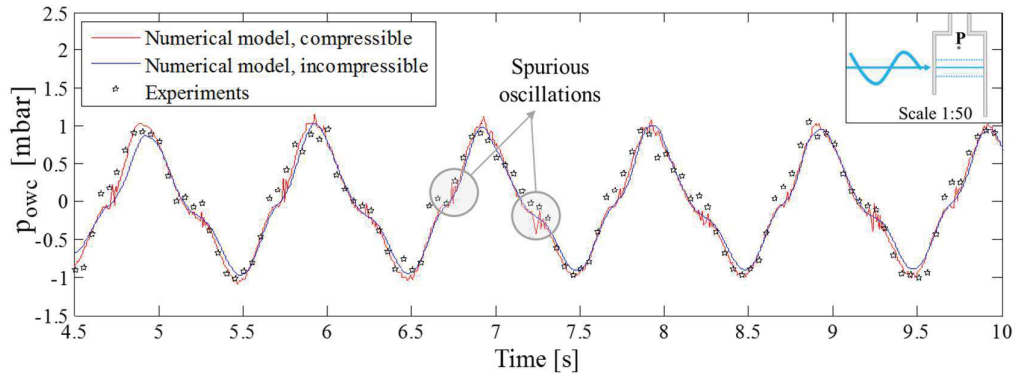


Figure 6-7: Time series of relative pressure p_{owc} in the OWC air chamber, comparison between experimental data (Crema et al, 2016) and CFD simulations (compressible and incompressible).

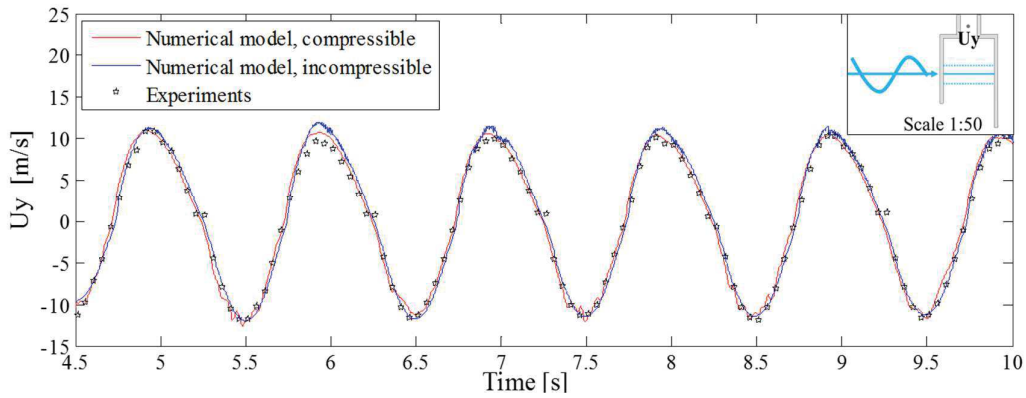


Figure 6-8: Time series of vertical component of the air velocity, U_y , in the OWC top cover pipe, comparison between experimental data (Crema et al, 2016) and CFD simulations (compressible and incompressible).

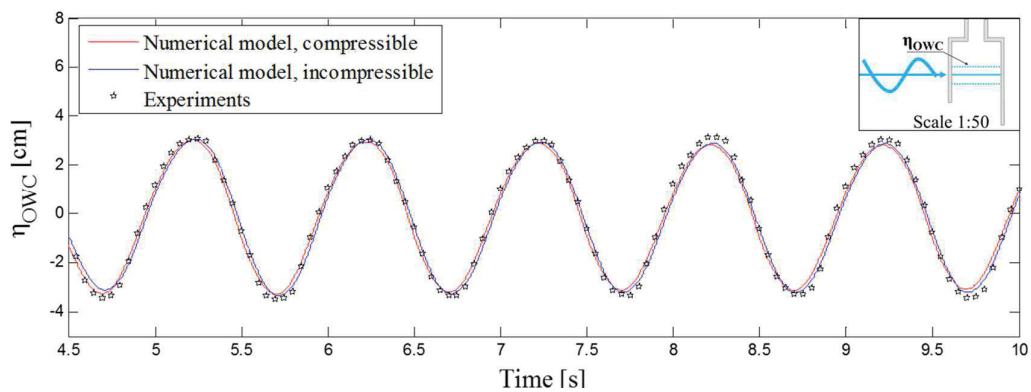


Figure 6-9: Time series of water level η_{owc} in the OWC chamber, comparison between experimental data (Crema et al, 2016) and CFD simulations (compressible and incompressible).

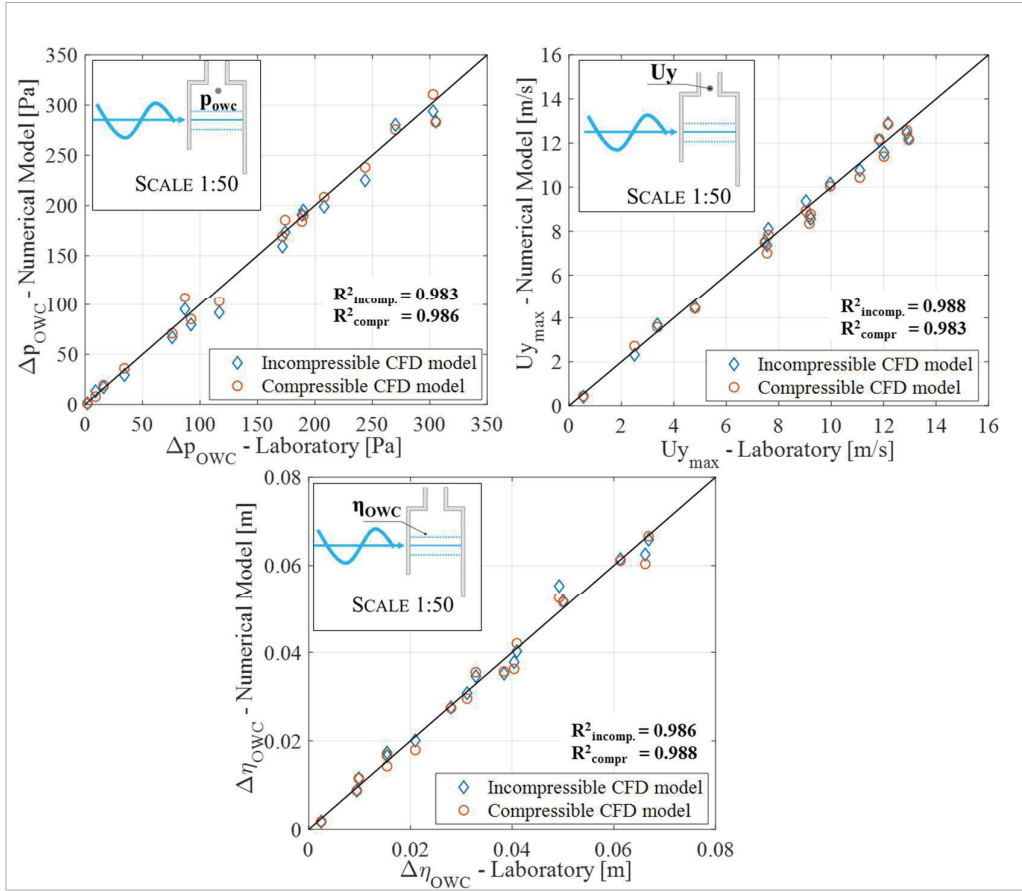


Figure 6-10: Scatter plot between laboratory and numerical data (obtained with the compressible and the incompressible CFD models) of Δp_{owc} , $U_{y_{max}}$ and $\Delta \eta_{owc}$ at laboratory scale 1:50.

The good agreement found between laboratory data and CFD results using the compressible solver at laboratory scale 1:50 has the following implications:

- (i) An incompressible CFD code can properly reproduce small-scale OWC model tests such as those by Crema et al, 2016, therefore confirming that compressibility effects are not reproduced in such small-scale OWC model tests. Hence, the simulation of the OWC device at prototype scale with the compressible solver (see *section 6.6*) is necessary in order to quantify the scale effects due to air compressibility, and to derive correction factors for laboratory tests (see *chapter 7*).
- (iii) The compressible model is also appropriate for reproducing the flow in the incompressible regime ($Ma \ll 0.3$), except from moderate spurious oscillations observed in the time series of p_{owc} . The spurious oscillations are limited and do not compromise the applicability of the compressible code to simulate the flow dynamics inside an OWC.

6.6. Evaluation of scale effects due to air compressibility in the OWC system

The compressible model is used to simulate the OWC device at prototype scale. Results of the simulations at prototype scale are compared with those of the small-scale model, in order to evaluate the importance of air compressibility effects on the system dynamics, and to provide correction factors to be applied to small-scale model results, as well as to numerical results from incompressible CFD models.

The simulations with the compressible model at prototype scale are highly computation demanding, therefore the work documented in this section was performed by accessing the computational resources of CINECA, the largest High Performance Computing centre in Italy (<http://www.cineca.it/en>). The used system architecture is an IBM neXtScale model, with 516 nodes, 16 cores/node and 2.40 GHz Intel Haswell processors (2 per node). The needed computational time for a single run (i.e. 20 wave periods T) on the aforementioned architecture is about 600 CPU hours.

6.6.1. Discretization of the prototype OWC scaled up from the 1:50 OWC model

Considering the simulations at the laboratory scale 1:50 performed in accordance with Froude similarity, the OWC device geometry and the characteristics of the incident waves are up-scaled to prototype scale by considering the scale ratios reported in Table 6-2.

Table 6-2: Froude scale ratios for geometric, dynamic and kinematic similarity between model and prototype.

<i>Parameter</i>	<i>Dimension</i>	<i>Froude scale ratio</i>
Length	[L]	N
Volume	[L ³]	N ³
Time	[T]	N ^{1/2}
Velocity	[LT ⁻¹]	N ^{1/2}
Volume Flux	[L ³ T ⁻¹]	N ^{5/2}
Mass	[M]	N
Pressure	[ML ⁻¹ T ⁻²]	N
Power	[ML ² T ⁻³]	N ^{7/2}

To ensure a consistent comparison between the simulation results at different scales, the following ratios, which are based on the characteristics of the incident wave according to previously (see also *Chapter 4*) performed mesh independence tests, are kept constant in the discretization of the NWT (see definition sketch in Fig. 5-5):

- (i) Number of cells per wave height H (corresponding to approximately 6 in the refinement zone around the free surface)
- (ii) Number of cells per wave length λ (corresponding to approximately 78 in the

- refinement zone around the free surface)
- (iii) Length of the inlet and outlet relaxation zone, equal to λ and 0.5λ respectively.
 - (iv) Distance from the end of the inlet relaxation zone and the position of the OWC model in the NWT (approximately 2.5λ).

The adopted discretization schemes and solvers of the algebraic system of governing equations are the same used for the simulations at small scale (see *section 5.2.2*).

In order to consider a wider range of pressure oscillation amplitudes Δp_{owc} inside the OWC than the range tested in the laboratory, different top cover vent diameters, chamber width W (Table 6-3) and incident wave heights ($H=1.2-2.8$ m with $T=7.07$ s and 8.48 s at prototype scale, Table 6-4) were tested. A total number of 21 simulations at prototype scale were performed, and compared with the results of corresponding simulation at laboratory scale 1:50.

Table 6-3: Geometrical parameters of the OWC device simulated at scale 1:50 and at prototype scale.

	<i>parameter</i>	[unit]	<i>scale 1:50</i>	<i>scale 1:1</i>
	Chamber length B	[m]	0.2	10
	Front wall draught D	[m]	0.07	3.5
	Chamber width W	[m]	0.17-0.21	8.5-10.5
	Back wall length G	[m]	0.45	22.5
	Top cover vent diameter V	[m]	0.022-0.038 ^(*)	1.1-1.9
	water depth h	[m]	0.5	25

(*) Nine values of the top cover vent diameter, ranging from 0.022 to 0.038 m (corresponding to 1.1 and 1.9 m at prototype scale) with a step of 2 mm (corresponding to 10 cm at prototype scale)

Table 6-4: Characteristics of tested incident wave heights H and periods T in a constant water depth ($h=25$ m at scale 1:1 and $h=0.5$ m at scale 1:50) selected for the scale effects study.

<i>wave code</i>	<i>scale 1:50</i>		<i>scale 1:1</i>	
	H [m]	T [s]	H [m]	T[s]
H09	0.024	1.00	1.20	7.07
H010	0.030	1.00	1.50	7.07
H011	0.034	1.00	1.70	7.07
H012	0.043	1.00	2.15	7.07
H013	0.050	1.20	2.50	8.48
H014	0.056	1.20	2.80	8.48

6.6.2. Preliminary tests with the prototype OWC

In order to exclude relevant numerical effects due to discretization, which may be misleading in interpreting the results, and to exclude possible scale effects due to phenomena different from air compressibility, the following preliminary tests are performed:

- (i) Comparison of wave propagation in the NWT without the OWC model (called

hereafter *free NWT*), obtained with the incompressible model at scale 1:50, the incompressible model at scale 1:1 and the compressible model at scale 1:1.

- (ii) Comparison of numerical results for the OWC model obtained with the incompressible model at scale 1:50 and the incompressible model at scale 1:1, in order to evaluate if, excluding air compressibility effects, other scale effects affect the up-scaling of the model.

For the wave propagation in the *free NWT*, the 6 regular wave tests in Table 6-4 are performed. Time series of the surface elevation η_{owc} are recorded at a wave gauge located 3.5λ m away from the NWT inlet. *NRMSE* and determination coefficient R^2 (as defined in Eq. 5.1 and Eq. 5.2) are used as indices to compare η_{owc} time series obtained from the models.

The 1:50 model data are up-scaled by applying Froude similarity (Tab. 6-2). No relevant differences were found in the fully developed wave field (which takes place after around $7T$, Fig. 6-11), with an average value of *NRMSE* of around 3% and an average R^2 of around 0.99. Therefore, the incident wave propagation is not affected by the up scaling of the NWT.

The comparison of the OWC model results between the simulations at scale 1:50 and at scale 1:1 by using the incompressible model is performed for a set of 21 cases. The relative pressure in the chamber, p_{owc} (Fig. 6-12,a) has an average *NRMSE* lower than 3% in the completely developed flow field (after about $7T$ from the simulation beginning) and an average R^2 of about 0.99. Similar values are obtained for η_{owc} (Fig. 6-12,b) and for the volumetric airflow rate¹⁴ in/out from the OWC chamber, q_{owc} (Fig. 6-12,c). Except the possible effects due to air compressibility, therefore, no other scale effect is identified.

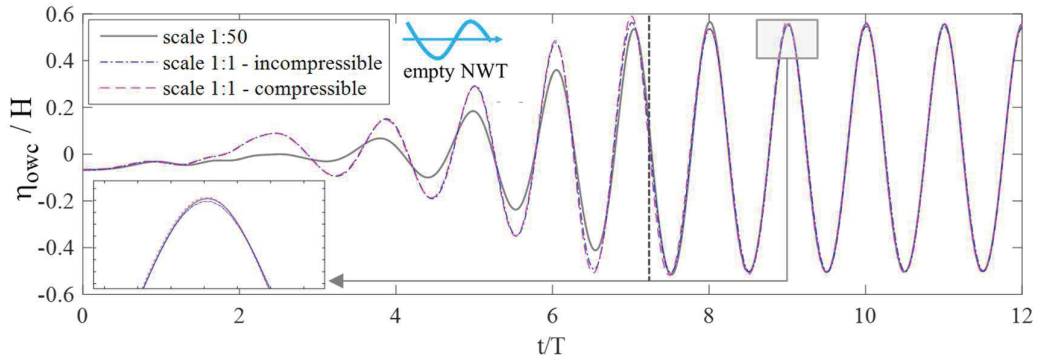


Figure 6-11: Comparison of wave propagation in the NWT without OWC at scales 1:50 and 1:1 using incompressible and compressible CFD models (results at scale 1:50 up-scaled according to Froude similarity). Wave gauge located at 3.5λ (λ =incident wavelength) from the NWT inlet.

¹⁴ In the numerical model, the airflow rate q_{owc} is directly computed, for each time step, from the cumulative value of the fluxes at the cell faces across a cross-section of the top cover pipe.

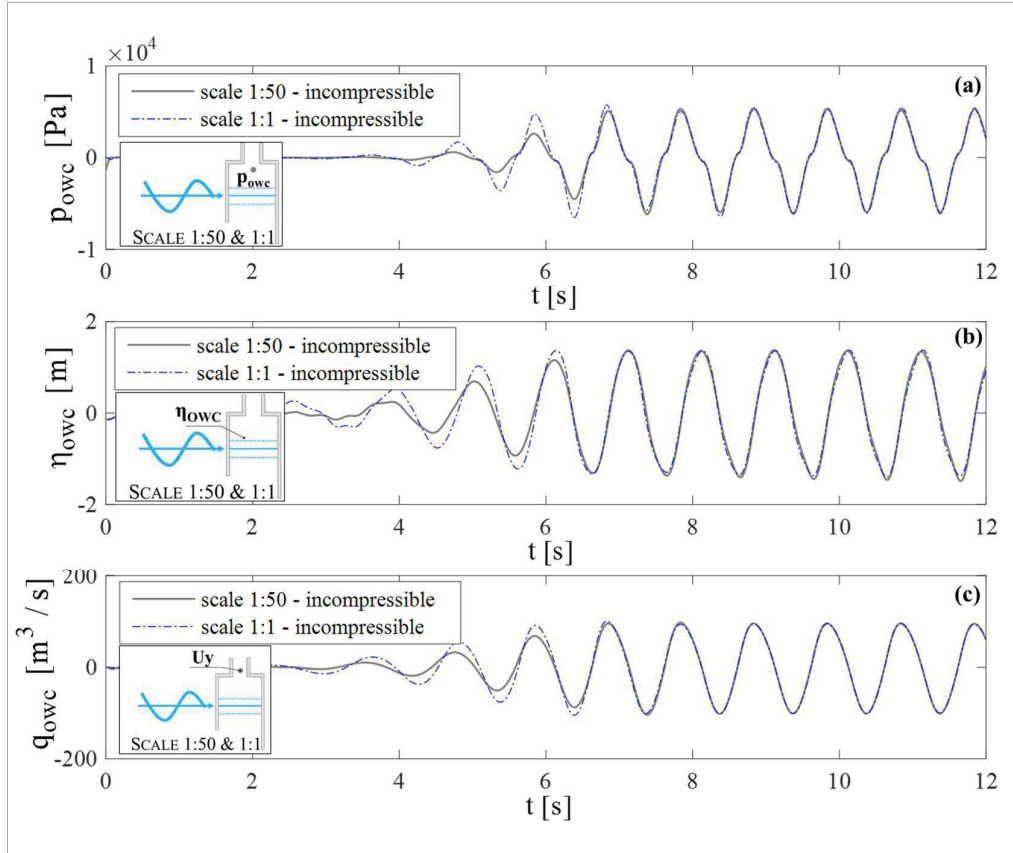


Figure 6-12: Comparison between p_{owc} (a), η_{owc} (b) and q_{owc} (c) at scales 1:50 and 1:1, obtained by using incompressible and compressible CFD models.

The comparative analysis of the results obtained by using the incompressible CFD model at scale 1:50 and those obtained at scale 1:1 shows a relatively good agreement, for both the wave propagation in the *free NWT* and the simulation of the OWC device. Therefore, excluding air compressibility, all other effects due to phenomena that do not scale with Froude similarity (which might be misleading in the interpretation of the following results on scale effect induced by air compressibility) can be neglected.

6.6.3. Air compressibility effects and proposed correction factors

The effect of air compressibility is evaluated by means of a comparative analysis of the results obtained from the compressible CFD model at scale 1:50 and at scale 1:1

The effect of air compressibility is assessed on those parameters that are relevant in the evaluation of the OWC device performance, i.e. water surface elevation η_{owc} inside the OWC, pressure inside the chamber p_{owc} , the air flow rate q_{owc} , the pneumatic

power output Π_{owc} or, equivalently the OWC capture width ratio¹⁵ ε_{owc} . Power output Π_{owc} and capture width ratio ε_{owc} are estimated by using Eqs. 5.4 and 5.5, respectively. Since ε_{owc} is a more explicit index than Π_{owc} to evaluate the device performance, the effect of air compressibility will be presented hereafter in terms of ε_{owc} , without consideration of Π_{owc} .

For each of the aforementioned parameter χ (ε_{owc} , η_{owc} , p_{owc} and q_{owc}) a correction factor CF is defined as the ratio between the value of χ in the 1:50 scale model (Froude scaled to scale 1:1 by applying the ratios in Table 6-2) and the value of χ in the simulations at prototype scale, as in:

$$CF_{\chi 1:50} = \chi_{1:50} / \chi_{1:1} \quad (6.8)$$

To consider the effect of air compressibility on the system dynamics as a function of both the pressure variation inside the OWC air chamber and the characteristic of the incident wave (T and H), the correction factor CF is expressed as a function of the non-dimensional pressure parameter Γ , defined as:

$$\Gamma = \Delta p_{owc 1:50} / \left(\gamma H \frac{\cosh k(h-D)}{\cosh(kh)} \right) \quad (6.9)$$

where $\Delta p_{owc 1:50}$ is the period average value of the pressure oscillation amplitude in the OWC chamber as simulated in the 1:50 scale model and scaled up to 1:1 according to Froude similarity (Table 6-2), $\gamma = \rho g$ is the water specific weight, k is the wave number of the incident wave, h is the water depth and D is the OWC front wall draught. The denominator in Eq. 6.9 represents the maximum wave-induced pressure at a depth $y = -D$ (according to *Airy wave theory*). Since, for a given wave number k , a given OWC geometry and turbine applied damping, the air volume variation in the OWC chamber during a wave cycle is related to the incident wave height H , Γ allows to also implicitly account for the air volume variation during compression/decompression.

a) Effect of the air compressibility on pressure in the air chamber p_{owc}

As far as p_{owc} is concerned, the period average value of pressure oscillation amplitude Δp_{owc} inside the OWC air chamber is found to be relevantly affected by the air compressibility (Fig. 6-13). The maximum difference between Δp_{owc} in the simulations at scale 1:50 (where air compressibility is not reproduced) and those at scale 1:1, expressed in terms of correction factor $CF_{\Delta p 1:50}$, is about 1.15 (for $\Gamma = 1$).

For decreasing values of the non-dimensional pressure parameter Γ , lower $CF_{\Delta p 1:50}$ -values would result, and $CF_{\Delta p 1:50}$ tends to 1 (i.e. results from scale 1:50 tend to converge to that at prototype scale) when Γ tends to zero. For $\Gamma \sim 0.4$, $CF_{\Delta p 1:50}$ -values close to 1.02 would result, meaning that air compressibility has a negligible effect on the OWC system dynamics for low values of the dimensionless pressure parameter Γ . The relation between $CF_{\Delta p 1:50}$ and Γ is approximately quadratic (Fig.

¹⁵ The power of the incident wave is not modified by the air compressibility phenomena taking place in the OWC air chamber, therefore any variation of Π_{owc} due to air compressibility produce an equivalent variation in the overall device capture width ratio ε_{owc} .

6-13), with a relatively high value of the determination coefficient for the fitting ($R^2=0.96$). Differences in the system response to air compressibility are observed between the *exhalation* (outflow) and the *inhalation* (inflow) phases. During exhalation, the airflow is driven out of the chamber, and the pressure in the OWC chamber is higher than the atmospheric pressure (i.e. $p_{owc}>0$). During *inhalation*, the pressure in the OWC chamber is lower than the atmospheric pressure (i.e. $p_{owc}<0$) and the airflow is driven towards the depressurized chamber.

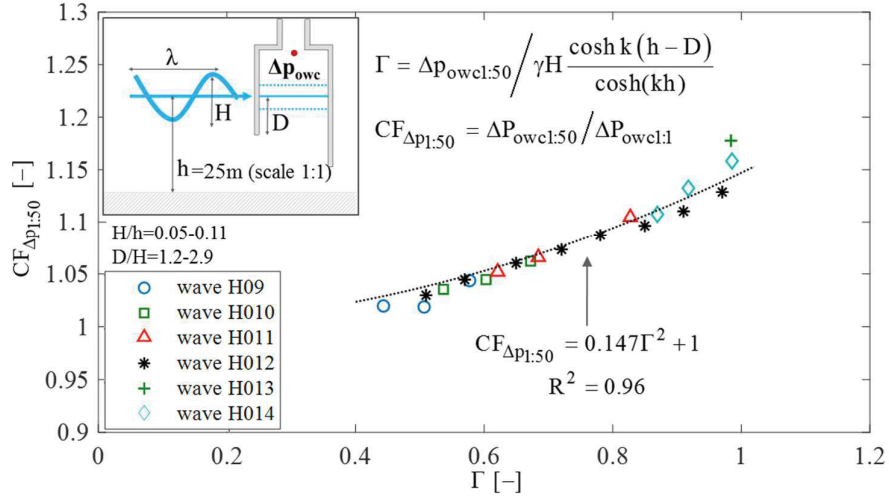


Figure 6-13: Correction factor $CF_{\Delta p_{1:50}}$ for the air chamber pressure oscillation amplitude Δp_{owc} (obtained from OWC model scale 1:50 and scaled up to 1:1 according to Froude similarity) versus non-dimensional pressure parameter Γ .

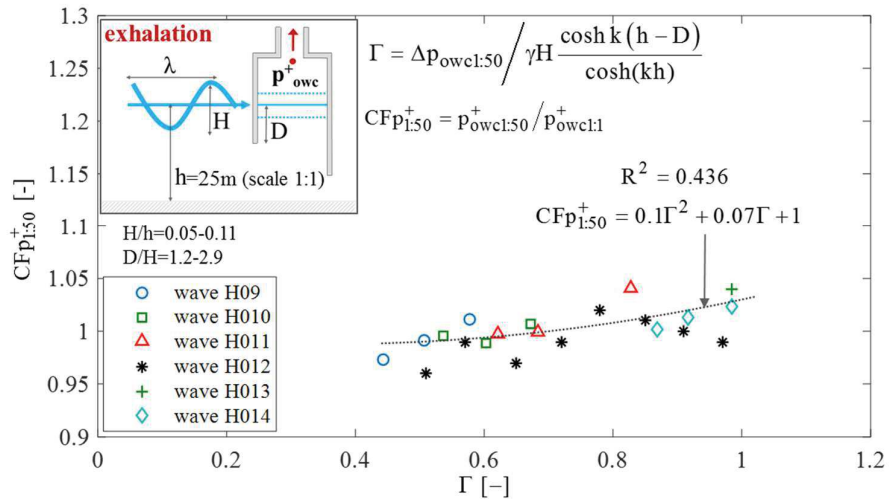


Figure 6-14: Correction factor $CF_{p^+_{1:50}}$ for the air chamber relative pressure during the exhalation phase, p^+_{owc} (obtained from OWC model scale 1:50 and scaled up to 1:1 according to Froude similarity) versus non-dimensional pressure parameter Γ .

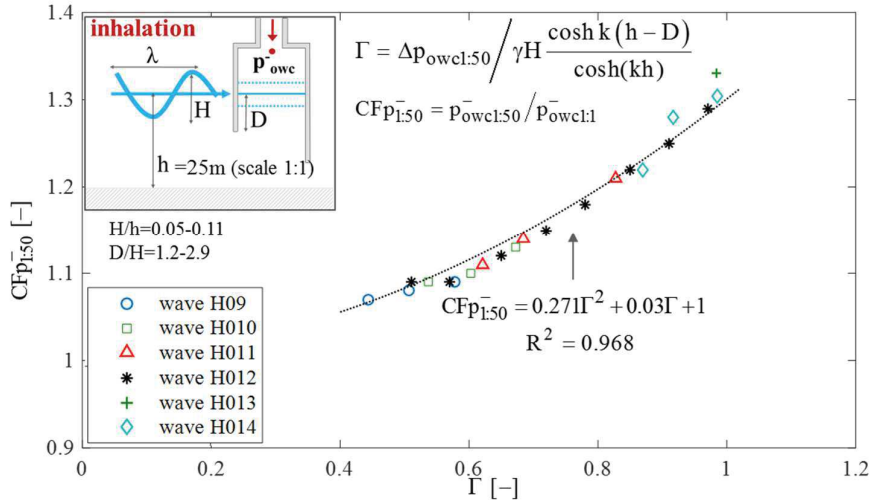


Figure 6-15: Correction factor $CFp_{1:50}$ for the air chamber relative pressure during the inhalation phase, p_{owc} (obtained from OWC model scale 1:50 and scaled up to 1:1 according to Froude similarity) versus non-dimensional pressure parameter Γ .

In the *exhalation phase*, the average value of the maximum pressure, denoted as p_{owc}^+ , is less affected by air compressibility, with a maximum value of $CFp_{1:50}^+$ in the investigated range of Γ of about 1.05 (Fig. 6-14).

In the *inhalation phase*, the effect of air compressibility is remarkably higher (Fig. 6-15). The average value of the minimum chamber pressure during depressurization, denoted as p_{owc}^- , shows maximum value of correction factor $CFp_{1:50}^- = 1.3$ in the investigated range of Γ . Also in this case, the relation between $CFp_{1:50}^-$ and Γ is approximately quadratic with a quite high value of the determination coefficient ($R^2 = 0.97$).

Sheng et al. 2013 already observed the different effect of air compressibility between *exhalation* and *inhalation* by means of experimental studies¹⁶. This difference may be explained considering that an asymmetry in the thermodynamic conditions exists between *inhalation* and *exhalation* phases.

During the *exhalation phase*, the thermodynamic conditions inside the chamber are approximately isentropic (as previously observed by Falcão & Justino 1999), and the air, which is progressively compressed by the upward motion of the inner water surface of the OWC, is driven out of the top cover orifice, where it rapidly accelerates due to the sudden decrease of the cross sectional area for the flow at the orifice. In the *exhalation phase*, therefore, the turbulent mixing process between the air at

¹⁶ The experimental studies of Sheng et al. (2013) refers to the airflow through an orifice connected to the atmosphere from one side and, from the other side, to a chamber pressurized and depressurized by the motion of a piston, and have the main aim to investigate the effect of air compressibility on the system dynamics. In this study, relatively small values of the relative chamber pressure were investigated (up to 2000 Pa), while in the present study relative pressure in the OWC chamber up to ca. 9000 Pa are considered.

atmospheric conditions and the pressurized high-speed airflow takes place outside the OWC air chamber.

During the *inhalation phase*, the inflow accelerates through the orifice before entering the air chamber. The mixing process, therefore, takes place inside the OWC chamber. In other words, for a given value of relative pressure oscillation amplitude Δp_{owc} , and a given applied damping K , even if the airflow q_{owc} and the velocity in the top cover pipe are approximately the same in the *inhalation* and the *exhalation* phases, the air velocity inside the chamber is remarkably higher during *inhalation*.

This difference during an exemplarily wave cycle can be clearly visualized in Fig. 5-13 (comparing the air velocity in the air chamber during *inhalation*, time $7.5T$, and those during *exhalation*, time $7.9T$). The higher air velocity inside the chamber during *inhalation* results in a higher value of *Mach number* Ma , explaining the observed difference in the air compressibility effect.

b) Effect of the air compressibility on the airflow rate q_{owc}

Air compressibility also influences the period average value of volume airflow oscillation amplitude Δq_{owc} in/out the OWC air chamber (Fig. 6-16). The maximum difference observed between Δq_{owc} at scale 1:50 and at scale 1:1, expressed in terms of correction factor $CF_{\Delta q_{1:50}}$, is about 1.16.

When decreasing the value of the non-dimensional pressure parameter Γ , air compressibility has a lower effect on q_{owc} , with $CF_{\Delta q_{1:50}} < 1.03$ for $\Gamma < 0.4$.

The relation between $CF_{\Delta q_{1:50}}$ and Γ can be fitted with a second order polynomial (Fig. 6-16), with a value of the determination coefficient R^2 equal to about 0.97.

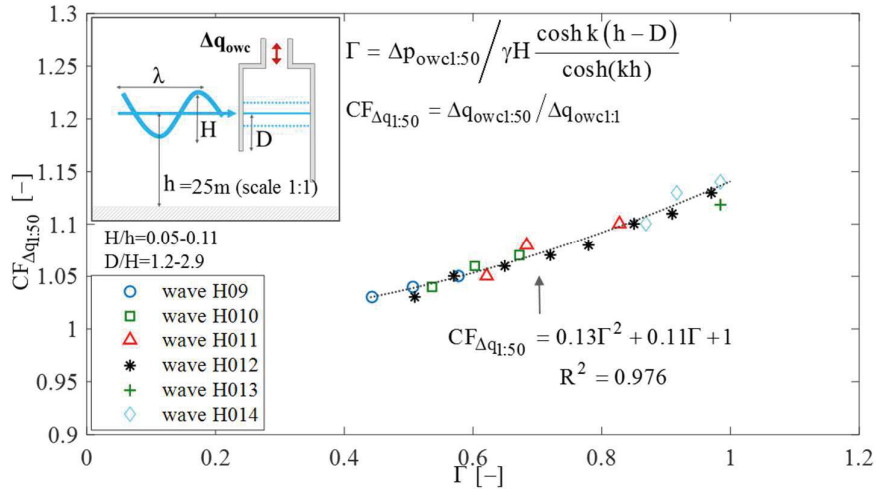


Figure 6-16: Correction factor $CF_{\Delta q_{1:50}}$ for the volume air flow oscillation amplitude Δq_{owc} (obtained from OWC model scale 1:50 and scaled up to 1:1 according to Froude similarity) versus non-dimensional pressure parameter Γ .

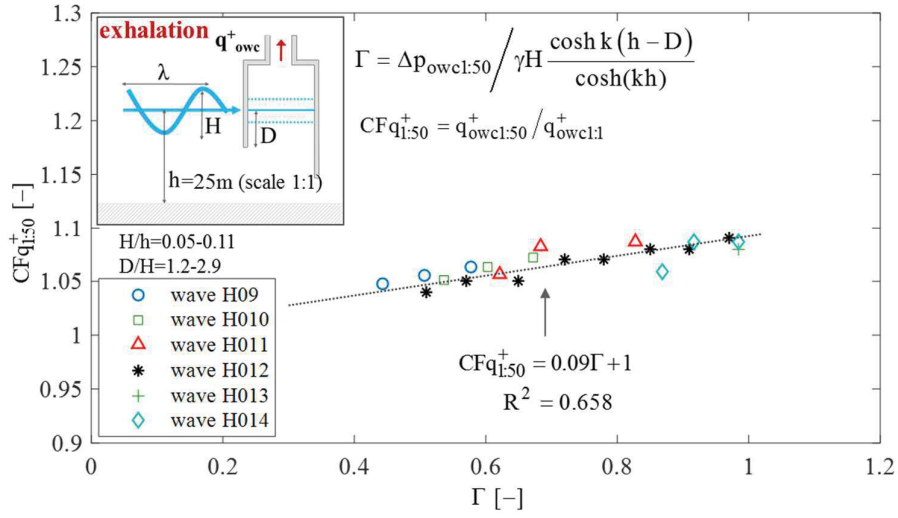


Figure 6-17: Correction factor $CFq_{1:50}^+$ for the volume air flow during the exhalation phase, q_{owc}^+ (obtained from OWC model scale 1:50 and scaled up to 1:1 according to Froude similarity) versus non-dimensional pressure parameter Γ .

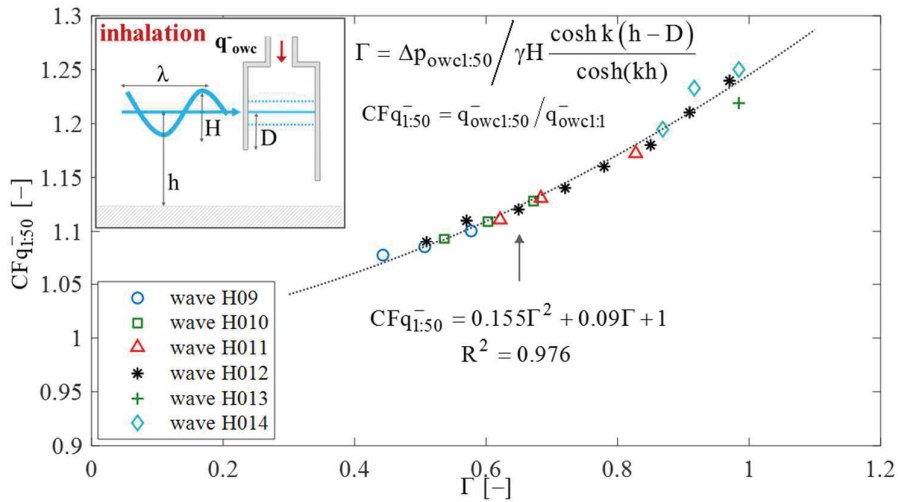


Figure 6-18: Correction factor $CFq_{1:50}^-$ for the volume air flow during the inhalation phase, q_{owc}^- (obtained from OWC model scale 1:50 and scaled up to 1:1 according to Froude similarity) versus non-dimensional pressure parameter Γ .

Also for q_{owc} , differences in the effect of air compressibility between the *exhalation* and the *inhalation* phases are observed. This effect may be related to the asymmetry in the thermodynamic conditions between inhalation and exhalation phases, as aforementioned.

In the *exhalation phase*, the average value of the maximum airflow q_{owc} directed out of the chamber, denoted as q_{owc}^+ , is less affected by air compressibility, with a maximum $CFq_{1:50}^+ = 1.1$ in the investigated range of Γ (Fig. 6-17).

In the *inhalation phase*, as observed for p_{owc} , the effect of air compressibility on q_{owc} is higher. In the considered range of Γ , the period average value of the maximum airflow directed towards the OWC chamber, q_{owc} , has a maximum $CF_{q_{1:50}}=1.25$ (Fig. 6-18). The relation between $CF_{q_{1:50}}$ and Γ is can be fitted with a quadratic function, with determination coefficient $R^2=0.97$.

c) Effect of the air compressibility on capture width ratio ε_{owc}

The air compressibility effect results in a power loss as compared to the incompressible case. This loss can be evaluated in terms of the correction factor $CF_{\varepsilon_{1:50}}$ (Fig. 6-19) that applies to the period average OWC capture width ratio ε_{owc} .

In the investigated range of Γ , the maximum value of $CF_{\varepsilon_{1:50}}$ is about 1.09. Assessing the capture width ratio ε_{owc} by using an incompressible CFD model or laboratory tests at a small-scale is conservative, i.e. for a model scale such as that used by Crema et al (2016) this might result in an overestimation of ε_{owc} by up to 10% for higher pressure conditions in the air chamber up to $\Gamma=1$.

The relation between $CF_{\varepsilon_{1:50}}$ and Γ can be fitted with a parabolic function with a value of $R^2=0.87$ (Fig. 6-19). The effect of air compressibility on the period average value of the capture with ratio ε_{owc} is smaller than that on the period average pressure amplitude Δp_{owc} and air volume flux Δq_{owc} . This might be explained by the fact that part of the input power is stored in the compressible air when the air in the chamber is pressurized or depressurised. When the pressure in the air chamber diminishes from its peak, the stored power might be released, hence reducing the observed air compressibility effect on ε_{owc} . A similar interpretation was previously given by Sheng et al. (2013).

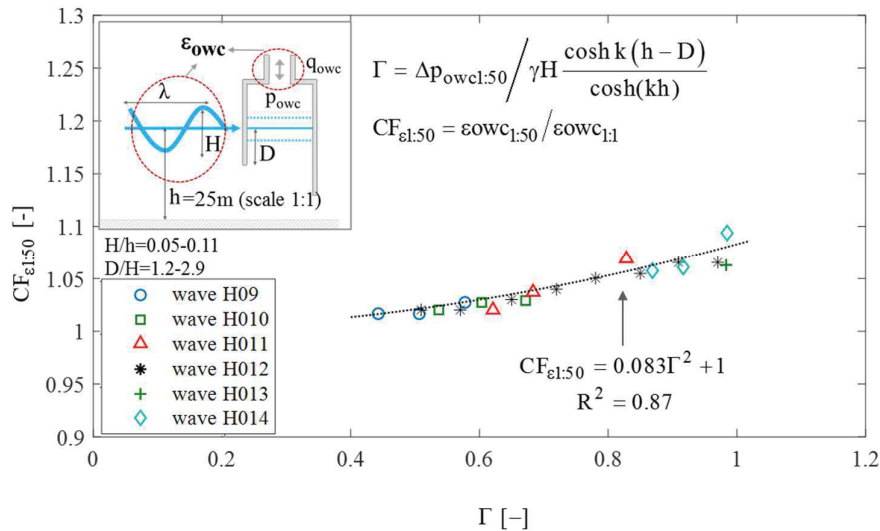


Figure 6-19: Correction factor $CF_{\varepsilon_{1:50}}$ for the average capture width ratio ε_{owc} (obtained from OWC model scale 1:50 and scaled up to 1:1 according to Froude similarity) versus non-dimensional pressure parameter Γ .

d) Effect of the air compressibility on water surface elevation η_{owc}

Only small differences in the period average amplitude of the water surface elevation inside the OWC, $\Delta\eta_{owc}$ ($NRMSE < 0.05$ and determination coefficient $R^2 = 0.98$) are found between the results of the simulations at scale 1:50 and scale 1:1 (Fig. 6-20).

This implies that air compressibility only affects the thermodynamics of the air chamber with much less effects on the hydrodynamics inside the OWC.

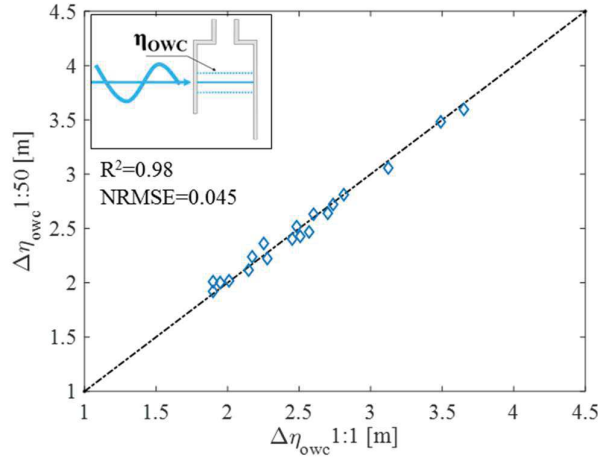


Figure 6-20: Scatter plot between the period average amplitude of water surface elevation $\Delta\eta_{owc}$ simulated with the compressible CFD model at scale 1:50 (scaled up to 1:1 according to Froude similarity) and at scale 1:1.

The proposed correction factors on Δp_{owc} , Δq_{owc} and ε_{owc} are summarized in Table 6-5. It is worth to note that when the non-dimensional pressure parameter Γ goes to zero, i.e. when the relative pressure inside the OWC chamber goes to zero, all the proposed correction factors tends to the value 1, meaning that no differences in the OWC system dynamics would occur in such conditions for the effect of air compressibility.

Table 6-5: Summary of the proposed correction factors for air compressibility for Δp_{owc} , Δq_{owc} and ε_{owc} .

<i>parameter</i>	$CF_{1:50}$	R^2
Δp_{owc}	$0.147\Gamma^2 + 1$	0.95
Δq_{owc}	$0.13\Gamma^2 + 0.11\Gamma + 1$	0.97
ε_{owc}	$0.083\Gamma^2 + 1$	0.87

$$\Gamma = \Delta p_{owc1:50} / \left(\gamma H \frac{\cosh k(h-D)}{\cosh(kh)} \right)$$

$$CF_{\chi^{1:50}} = \chi_{1:50} / \chi_{1:1} \text{ with } \chi = \Delta p_{owc}, \Delta q_{owc} \text{ and } \varepsilon_{owc}$$

The air compressibility scale effect between model scale 1:50 and 1:1 is analysed in terms of the non-dimensional parameter Γ , which accounts for both the level of air compression in the OWC chamber and the incident wave conditions (wave height, wave number and water depth). Correction factors (*CFs*) for the pressure inside the OWC chamber p_{owc} , the air flow rate q_{owc} and the OWC capture width ratio ε_{owc} , obtained experimentally or numerically from a 1:50 OWC model, are proposed (Table 6-5). The effect of neglecting the air compressibility results in an overestimation up to about 15% for the relative air pressure p_{owc} and the air volume flux q_{owc} , but less than 10% for capture width ratio ε_{owc} (in the tested range of $\Gamma=0.4-1.0$). This overestimation increases with increasing Γ , i.e. with increasing level of the pressure in the air chamber, while air compressibility is progressively less relevant for lower pressure levels.

Air compressibility effects are remarkably higher (about 20% on p_{owc} , and q_{owc}) in the *inhalation phase* (airflow from turbine to chamber with $p_{owc}<0$) than in the *exhalation phase* (airflow from chamber to turbine with $p_{owc}>0$). This might be physically related to the higher air velocity inside the OWC air chamber during *inhalation*, resulting in higher values of *Mach number* Ma and thus in more compressible flow conditions.

6.6.4. Evaluation of scale effects related to air compressibility at different scales

In order to obtain more general correction factors for the specific case of OWC device, besides those obtained for model scale 1:50, the compressible model is used to simulate the device at additional model scales 1: N (i.e. $N = 25, 10, 5$). As for the case of scale 1:50 (*section 6.6.3*), the effect of air compressibility is evaluated by comparing results from the different OWC model scales (scaled up to 1:1 according to Froude similarity) with those obtained at prototype scale.

The considered parameters are: (i) the period average air chamber pressure oscillation amplitude Δp_{owc} , (ii) the period average air volume flux Δq_{owc} , (iii) the period average OWC capture width ratio, ε_{owc} .

For each parameter χ , the correction factor CF is computed as the ratio between χ in the 1: N model scale and χ at prototype scale, as:

$$CF_{\chi^{1:N}} = \chi_{1:N} / \chi_{1:1} \quad (6.10)$$

The correction factors CF for Δp_{owc} , Δq_{owc} and ε_{owc} are evaluated as a function of the non-dimensional pressure parameter Γ , generically defined for the scale ratio N as:

$$\Gamma = \Delta p_{owc^{1:N}} / \left(\gamma H \frac{\cosh k(h-D)}{\cosh(kh)} \right) \quad (6.11)$$

where $\Delta p_{owc1:N}$ denotes the value of Δp_{owc} as simulated in the 1: N scale model, scaled up to 1:1 according to Froude similarity (Tab. 6-2).

For each model scale, six simulations were performed, corresponding to the OWC geometrical parameters reported in Table 6-5. The tested incident wave height and period at prototype scale are $H=2.15$ m and $T=7.07$ s (wave code H012 in table 6-4), scaled according to Froude similarity for the smaller scales.

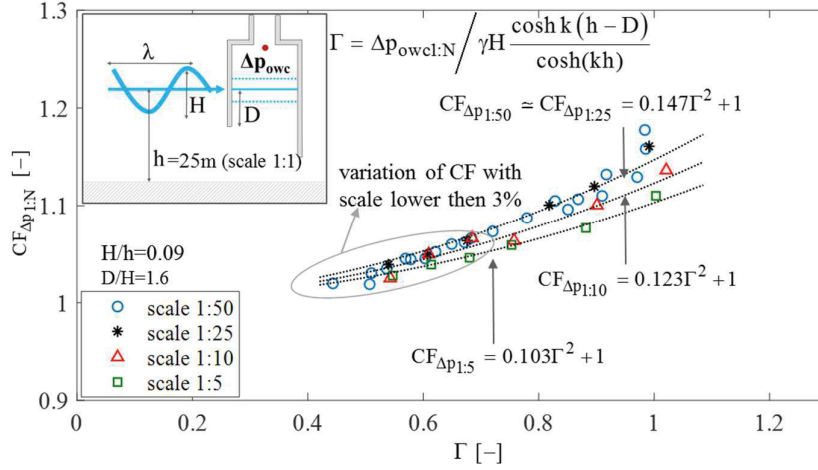


Figure 6-21: Correction factor $CF_{\Delta p}$ for the period average air chamber pressure oscillation amplitude Δp_{owc} (obtained from OWC model scales 1:50, 1:25, 1:10, 1:5 and scaled up to 1:1 according to Froude similarity) versus non-dimensional pressure parameter Γ .

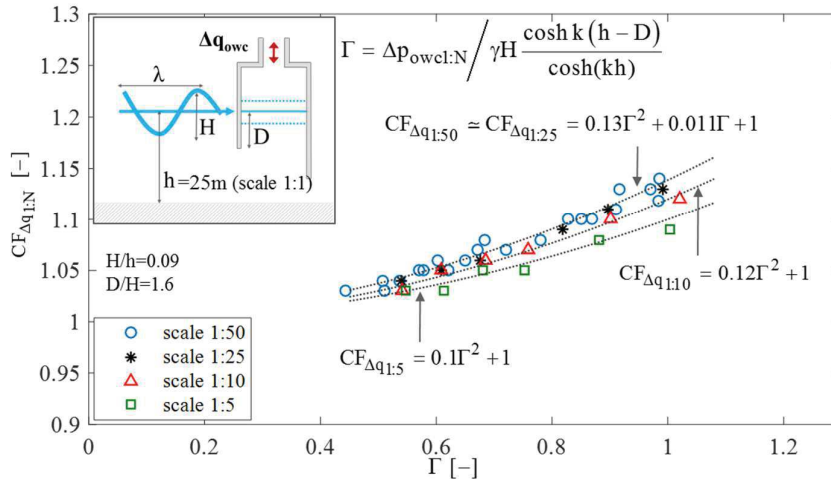


Figure 6-22: Correction factor $CF_{\Delta q}$ for the period average air volume air flux oscillation amplitude Δq_{owc} (obtained from OWC model scale 1:50, 1:25, 1:10, 1:5 and scaled up to 1:1 according to Froude similarity) versus non-dimensional pressure parameter Γ .

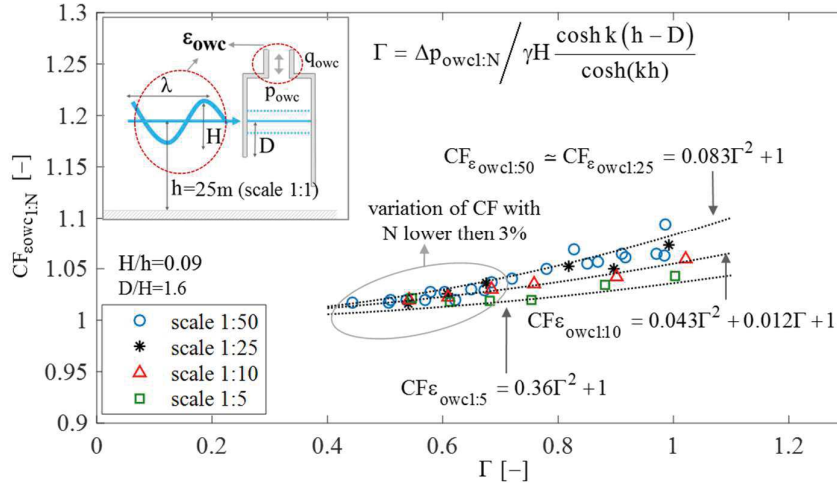


Figure 6-23: Correction factor $CF_{\varepsilon_{owc}}$ for the period average capture width ratio ε_{owc} (obtained from OWC model scales 1:50, 1:25, 1:10, 1:5 and scaled up to 1:1 according to Froude similarity) versus non-dimensional pressure parameter Γ .

For model scale 1:25, no relevant or systematic differences are found in the values of CF as compared to those at model scale 1:50, for the parameters Δp_{owc} (Fig. 6-21), Δq_{owc} (Fig. 6-22) and ε_{owc} (Fig. 6-23). Therefore, for model scale 1:25, the quadratic relations to relate $CF_{\Delta p1:25}$, $CF_{\Delta q1:25}$, $CF_{\varepsilon_{owc1:25}}$ and Γ can be approximated with the same relations proposed for model scale 1:50 (see Table 6-5). This indicates that, in the considered range of $\Gamma=0.45-1.0$, compressible effects are not reproduced in model scale 1:25.

For model scale 1:10 and for $\Gamma < 0.7$, the obtained CF-values are close to those obtained for model scales 1:50 and 1:25 (with a relative difference lower than 3%). A further increase of Γ leads to a moderate decrease of CF for all the considered parameters (Δp_{owc} , Fig. 6-21, Δq_{owc} , Fig. 6-22 and ε_{owc} , Fig. 6-23), hence the scale effect related to air compressibility is moderately reduced when simulating the device at scale 1:10. The maximum difference between results at scale 1:10 and 1:1, expressed in terms of CF, is about 1.15 for Δp_{owc} , 1.10 for Δq_{owc} and only 1.07 for ε_{owc} . By applying regression analysis quadratic relations between $CF_{\Delta p1:10}$, $CF_{\Delta q1:10}$, $CF_{\varepsilon_{owc1:10}}$ and Γ , different from those obtained for model scale 1:50 and 1:25, are tentatively proposed (Tab. 6-6).

For model scale 1:5, a decrease of CF is found with respect to the smaller model scales, with a maximum difference between scale 1:5 and 1:1, expressed in terms of CF, of about 1.13 for Δp_{owc} , 1.07 for Δq_{owc} and 1.05 for ε_{owc} . Quadratic relations between $CF_{\Delta p1:5}$, $CF_{\Delta q1:5}$, $CF_{\varepsilon_{owc1:5}}$ and Γ , different from those obtained for model scales 1:10 and 1:50/1:25, can be tentatively proposed (Tab. 6-6).

The magnitude of scale effects related to air compressibility in model scales 1:50 and 1:25 is nearly the same for the simulated range of Γ . Therefore, at both scales, the airflow in the OWC chamber behaves approximately as incompressible. This is confirmed by considering the values of *Mach number* (Ma) in the OWC air chamber,

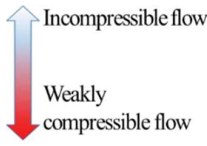
computed as the ratio between the maximum value of the speed of the airflow in the simulations and the speed of sound (Tab. 6-7). For both model scale 1:50 and 1:25, Ma is about 0.05, i.e. the flow behaves as approximately as incompressible. Further increasing the model scale (1:10 and 1:5), Ma increases to 0.1 and 0.15 respectively, i.e. the flow regime moves towards the weakly compressible flow regime, and a moderate decrease of the scale effect related to air compressibility is observed.

The comparative analysis of the results at different model scales shows, therefore, that the magnitude of scale effects related to air compressibility is governed by the values of *Mach number* (Ma) in the OWC air chamber. This suggests that, by adopting Ma as the governing variable and by extending the resolution on both the number of model scales N comparatively analysed and the number of tests performed at each model scale N , it might be possible to obtain a more generic formula to evaluate compressibility scale effects in OWC systems, valid for all scales.

Table 6-6: Summary of the proposed correction factors CF for air compressibility for Δp_{owc} , Δq_{owc} and ε_{owc} at model scales 1:50, 1:25, 1:10 and 1:5.

parameter	$CF_{1:50}$ and $CF_{1:25}$	$CF_{1:10}$	$CF_{1:5}$
Δp_{owc}	$0.147\Gamma^2 + 1$	$0.123\Gamma^2 + 1$	$0.103\Gamma^2 + 1$
Δq_{owc}	$0.13\Gamma^2 + 0.11\Gamma + 1$	$0.12\Gamma^2 + 1$	$0.1\Gamma^2 + 1$
ε_{owc}	$0.083\Gamma^2 + 1$	$0.043\Gamma^2 + 1$	$0.036\Gamma^2 + 1$

Table 6-7: Maximum air velocities in the OWC chamber (for $0.4 < \Gamma < 1$) in the numerical simulations at model scales 1:50, 1:25, 1:10 and 1:5, and values of *Mach number* Ma (for the reference speed of sound in the air 340 m/s).

Model scale	Max. air velocity [m/s]	Mach number Ma	
1:50	15	0.05	
1:25	20	0.06	
1:10	35	0.1	
1:5	50	0.15	
1:1	110	0.3	

The simulations of the OWC device at the model scales 1:25, 1:10 and 1:5 lead to the following remarks:

- (i) The scale effect related to air compressibility is still relevant at model scale 1:5 (i.e. when the maximum value of Ma is ca. 0.15), with a maximum overestimation of the capture width ratio ε_{owc} of about 5% (for $\Gamma=0.4-1.0$).
- (ii) The magnitude of scale effects related to air compressibility is governed by the value of *Mach number* (Ma) in the OWC air chamber (Table 6-7). For model scale 1:50 and 1:25, Ma is about 0.05, i.e. the flow behaves as nearly incompressible.
- (iii) By considering *Mach number* (Ma) as the governing variable it might be possible to obtain a generic formula for air compressibility effects, valid for all model scales N .

6.7. Summary and implications

A compressible CFD model is applied to simulate the hydrodynamics and aerodynamics inside the OWC device at scale 1:1 (prototype) and at smaller scales, in order to quantify scale effects related to air compressibility. For this purpose, the standard compressible VOF solver of OpenFOAM® (`compressibleInterFoam`) was implemented into the wave model `waves2Foam`, resulting in a new solver named `compressibleWaveFoam`.

Benchmark tests are performed on the new solver to ensure its capability to reproduce properly compressible effects. In this respect, a relatively good performance of the code is achieved.

Using both compressible and incompressible CFD solvers to reproduce the OWC device at laboratory scale (1:50), it was shown that the results of both solvers are in good agreement with the laboratory data, thus confirming that compressibility effects are not reproduced in the small-scale model tests. On the other side, the results also confirm that the incompressible code can properly reproduce small-scale laboratory test, so it can be used as a virtual laboratory for simulating hydrodynamic and aerodynamic processes inside OWC devices at smaller scales where the air compressibility effects in the OWC chamber are not significant ($Ma < 0.05$).

A preliminary comparative analysis of the numerical results obtained by using the incompressible model at scale 1:50 and those obtained at scale 1:1 is performed in order to exclude any relevant effects due to discretization and/or other effects associated with factors different from the air compressibility, which might be misleading in the interpretation of the results. For all the considered parameters, the *NRMSE* for the data at scale 1:1 and 1:50 is lower than 3%, and therefore considered as negligible; i.e. except scale effects due to air compressibility, other scale effects can be neglected in up-scaling the model.

Using `compressibleWaveFoam`, a set of 21 simulations of the OWC device at prototype scale are performed. The differences between the results at scale 1:50 and at scale 1:1 are analysed in terms of the non-dimensional parameter Γ , which accounts for both the level of air compression in the OWC chamber and the incident wave period and height. The effect of neglecting the air compressibility results in an over estimation of p_{owc} and q_{owc} (up to about 15% in the tested range of $\Gamma = 0.4 - 1.0$) and ε_{owc} (up to 10%). This effect is more relevant for high value of the pressure in the air chamber, and the results from scale 1:50 tends to converge to those from scale 1:1 when Γ tends to 1. Correction factors for p_{owc} , q_{owc} and ε_{owc} for results obtained experimentally or numerically from a 1:50 OWC model results, are proposed.

The magnitude of the maximum overestimation of ε_{owc} (up to 10%) with respect to the incompressible case, is confirmed in the theoretical studies of Thakker et al. (2003) (where a reduction of ε_{owc} up to 8% was found) and the numerical study of Elhanafi et al. (2017), where a 12% decrease in ε_{owc} was obtained. *This PhD study* extends the previous findings as it reveals that the compressibility effect is strongly correlated to the newly defined non-dimensional pressure parameter Γ and propose a set of empirical

model equations giving correction factors (therefore, providing an operative tool to account for air compressibility effects).

Finally, the OWC device is simulated with the compressible CFD model at additional model scales (1:25, 1:10 and 1:5). The scale effect related to air compressibility is still relevant at model scale 1:5, resulting in a maximum overestimation of the OWC capture width ratio ε_{owc} of about 5% for $\Gamma=1.0$. Tentative correction factors CF based on the non-dimensional pressure parameter Γ are proposed for these smaller model scales.

The main limitations of the work and the need for future research may be outlined as follows:

- (i) Even if benchmarks on `compressibleWaveFoam` proved that the solver can accurately reproduce compressible effects, a validation of the compressible model of the OWC at scale 1:1, on a completely equivalent system from both the dynamic and thermodynamic point of view, is required to confirm the results obtained at scale 1:1.
- (ii) Future research might increase the number of model scales N to be comparatively analysed and the number of tests to be performed at each model scale N , and thus possibly derive a more generic formula to evaluate air compressibility scale effects, valid for all scales, by considering the *Mach number* Ma in the OWC air chamber as the governing variable.
- (iii) In the overall *PhD research*, the air turbine is only introduced as an induced damping. This assumption, widely used in the literature for modelling OWC devices (Sarmiento, 1992; Sheng et al., 2012; Zhang et al., 2012; Iturrioz et al., 2014, Falcão & Henriques 2014), is appropriate to determine the optimal damping, that the air turbine should apply on the OWC chamber, which is one of the main objectives of *this PhD research*. However, regarding the specific aspect of the evaluation of air compressibility effects for the OWC, it should be noted that when an air turbine is used, at prototype scale, significant change in the specific entropy may occur in the flow through the turbine, due to viscous losses (Falcão & Henriques, 2014). The possible impact of this effect on the proposed correction factors should be further investigated in future research. A CFD compressible model which includes the effect of the air turbine in a more accurate way could be applied for this purpose, i.e. substituting the orifice with an actuator disk (Réthoré et al. 2014).
- (iv) The compressible CFD code is appropriate for the simulation of two-phase flows within the limit of separated-phase flows, but not for the simulation of dispersed-phase flows. Hence, a more refined model might be needed for estimating pressure-fields in dispersed-phase flows. This would be the case if breaking-wave impact problems are considered, where air bubbles in the liquid phase may be present during and after the wave impact.

CHAPTER 7

Multiple Regression Model (MRM) for the prediction of the OWC performance

A new Multiple Regression Model (MRM), based on dimensional analysis is proposed. The model predicts the OWC capture width ratio ε_{owc} given the wave conditions, the geometrical parameters of the OWC device and the turbine damping as *input variables*. The results of the incompressible CFD parameter study presented and discussed in *Chapter 5* are used to develop the incompressible model, which is later validated by applying it on an independent set of CFD simulations (i.e. OWC geometries and wave conditions not tested in the parameter study) and on the laboratory tests by Crema et al., 2016.

Once validated, the *incompressible MRM* is corrected by applying the correction factors for air compressibility proposed in *Chapter 6*, resulting in the formulation of a model (the *compressible MRM*) able to predict the OWC capture width ratio ε_{owc} by including compressibility effects.

The relevance of the new model in the OWC optimization process is finally demonstrated by an example application to a selected installation site in the Mediterranean Sea.

7.1. Incompressible model formulation and validation

This section presents the dimensional analysis and the Multi Regression Model (MRM) to predict the OWC conversion efficiency ε_{owc} (the dependent variable) given the following independent variables to be expressed in non-dimensional form:

- (i) incident wave height H and wave number k .
- (ii) geometrical parameters of the OWC: front wall draught D , chamber width W , chamber length transversal to wave propagation direction B ;
- (iii) turbine damping coefficient K .

The dimensional analysis is used to identify the dimensionally independent length scales of the phenomenon and to formulate the dimensionless products as independent parameters (Yalin 1971). A model describing the functional dependence of the OWC efficiency by the dimensionless products is proposed, and the model coefficients are estimated by means of an iterative multiple non-linear regression analysis.

The developed model is proposed as a simple tool to aid in the definition of the optimal OWC design parameters (D , W , B and K) in a site-specific wave field (H and k) during the prototyping phase.

7.1.1. Dimensional analysis

The most significant independent parameters affecting the OWC device pneumatic power output, Π_{owc} , are: the incident wave parameters (H , k and h); the parameters related to the OWC geometry and the applied damping (W , D , B and K); the fluid properties (water density, ρ_w , air density, ρ_a); gravitational acceleration g .

Therefore, Π_{owc} can, be expressed as a function of the aforementioned parameters

$$\Pi_{owc} = f(H, k, h, W, D, K, B, \rho_w, \rho_a, g, \dots) \quad (7.1)$$

The *II-theorem* is applied, in order to formulate dimensionless power products, leading to a reduction of the number of the independent variables in the functional formulation. The dimensionally independent parameters H , T (i.e. k and λ via the dispersion relation) and ρ_a are chosen as phenomenon's length scales (length, time and mass). Π_{owc} can be expressed in dimensionless form by means of the capture width ratio ε_{owc} (as in Eq. 5.5 and Eq. 5.6). The dimensionless products are as follows:

$$(i) \quad \text{relative water depth, } h^* \\ h^* = k \cdot h \quad (7.2)$$

$$(ii) \quad \text{front wall draught, } D^* \\ D^* = D / \left(H \cdot \frac{\cosh k(h-D)}{\cosh(kh)} \right) \quad (7.3)$$

$$(iii) \quad \text{chamber width, } W^* \\ W^* = W / \lambda \quad (7.4)$$

$$(iv) \quad \text{turbine damping, } K^* \\ K^* = K \cdot B \cdot W / \rho_a^{1/2} = K \cdot B \cdot W^* \cdot \lambda / \rho_a^{1/2} \quad (7.5)$$

$$(v) \quad \text{water density, } \rho_w^* \\ \rho_w^* = \rho_w / \rho_a \quad (7.6)$$

$$(vi) \quad \text{gravitational acceleration, } g^* \\ g^* = g \cdot T^2 / H \quad (7.7)$$

The sensitivity of ε_{owc} to the two latter parameters, ρ_w^* and g^* , is assumed to be negligible with respect to the other parameters; it is worth to note that the approximations arising from this hypothesis may be limited due to the small range of variation of ρ_w^* and g^* in practical applications.

The definition of D^* takes into account the effect of the incident wave H and the attenuation of the wave-induced pressure at a depth equal to D below the SWL

(according to Airy theory). The sensitivity study conducted in *section 5.4.4*, in fact, proved that the value of wave-induced pressure acting on the OWC is of paramount importance to determine the OWC system response to variations of D .

The parameter W^* accounts for the relevant effect on the OWC device performance of the relative chamber width, i.e. the ratio of W to the incident wavelength λ , which was found to be a fundamental parameter in the sensitivity study (see *section 5.4.5*).

The parameter K^* is defined to account for the fundamental effect of the chamber width W on the response of the OWC system to variations of the applied damping (see *section 5.4.3* and *section 5.4.5*).

By using the defined dimensionless parameters, ε_{owc} can be expressed as:

$$\varepsilon_{owc} = f(h^*, W^*, D^*, K^*) \quad (7.8)$$

Determining a model for the prediction of ε_{owc} consists, therefore, in determining the structure of the function f in Eq. 7.8, which relates the *output parameter* ε_{owc} to multiple *input parameters*. ε_{owc} is a multivariate function of h^* , W^* , D^* , K^* . A multiple regression model (MRM) is therefore needed for the development of the conceptual model.

7.1.2. Proposed conceptual Multi Regression Model

In the formulation of the Multi Regression Model (MRM), a fixed and predetermined functional structure of the relation between *input parameters* and *output parameters* is considered. The form of the proposed MRM is as follow:

$$\varepsilon_{owc} = \frac{f_1(K^* - d(h^*))}{f_2(D^*) \cdot f_3(W^*) \cdot c(h^*)} \quad (7.9)$$

$$f_2(D^*) = \exp(a(h^*)D^*) \quad (7.10)$$

$$f_3(W^*) = 1 + (W^* - W_{opt}^*)^2 \cdot b(h^*) \quad (7.11)$$

where the predetermined functional structure of $f(K^*-d)$ is imposed in the form of a rational polynomial, and a non-linear least square regression procedure is adopted to determine the numerical coefficients.

The functional structures of $f(D^*)$, $f(W^*)$ are a priori imposed in the MRM model to reflect the observed physical phenomenon: the decrease of the capture width ratio ε_{owc} for increasing values of D^* , and the existence a univocal value maximizing ε_{owc} for W^* . This contribute to overcome one of the drawbacks of the multiple regression analysis technique adopted, i.e. it only assesses the relationship between variables but it does not ensure that the relationship is causal.

A quadratic form is imposed for the functional structure of $f(W^*)$, in order to account for the effect of the relative chamber width W^* observed in *section 5.4.5*. (Fig. 5-22). Increasing the difference between W^* and $W_{opt}^* \sim 0.12$, higher values of $f(W^*)$ are obtained (i.e. lower capture width ratio ε_{owc} are predicted).

Given the fundamental effect of the relative water depth h^* on the response of the OWC system to variations of all the design parameters, a dependence of $f(D^*)$, $f(W^*)$ and $f(K^*)$ on h^* is explicitly introduced via the functions $a(h^*)$, $b(h^*)$, $c(h^*)$ and $d(h^*)$.

These functions take into account different physical effects observed at different h^* , in particular:

- (i) $a(h^*)$ is related to the different effect of D^* on the ϵ_{owc} observed at different h^* (i.e. it accounts for the different resonance conditions in the OWC chamber: when D^* increases, a shift of the OWC resonance frequency towards lower values of h^* takes place, and the decreasing value of $a(h^*)$ for decreasing h^* , see Fig. 7.3, allows to account for such an effect, attenuating the decrease of ϵ_{owc});
- (ii) $b(h^*)$ is related to the different effect of W^* on the ϵ_{owc} observed at different h^* (i.e. it accounts for the asymmetry in the rate of decrease of W^* from the optimal value $W^* \sim 0.12$, possibly due to different intensity of flow separation phenomena at the front wall for different h^* , see section 5.4.5)
- (iii) $c(h^*)$ has a less evident physical meaning, and is directly related to the values of $a(h^*)$ and $b(h^*)$;
- (iv) $d(h^*)$ accounts for the nonlinear variation of the optimal damping value at different h^* , as observed in section 5.4.3.

The numerical coefficients of the rational polynomial $f(K^*-d)$, are, in turns, a function of the values of $a(h^*)$, $b(h^*)$, $c(h^*)$ and $d(h^*)$. Therefore, an iterative non-linear multiple regression process is adopted (Fig. 7-1), to determine the numerical coefficients of the rational polynomial $f(K^*-d)$ and $a(h^*)$, $b(h^*)$, $c(h^*)$ and $d(h^*)$ which maximize the global fit between the conceptual MRM and the simulated data.

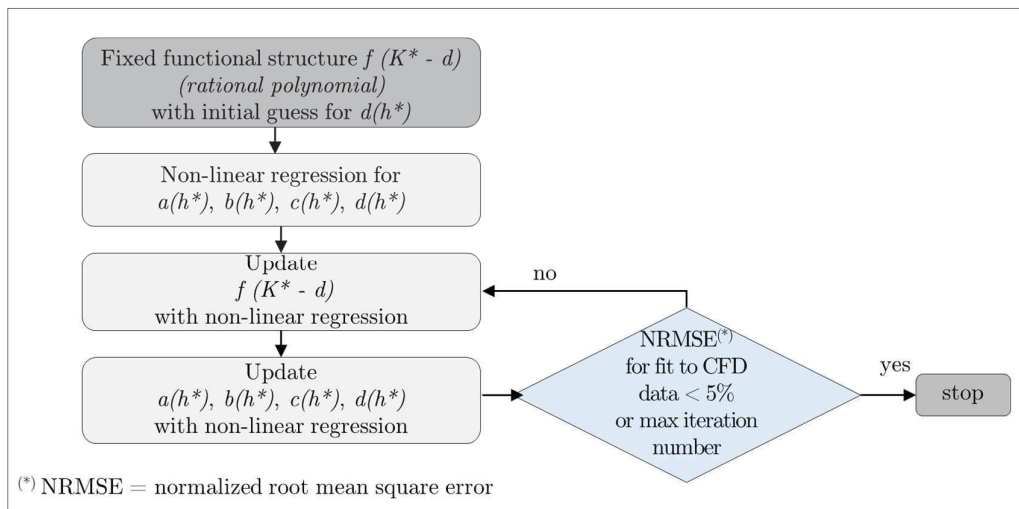


Figure 7-1: Iterative non-linear regression procedure used to determine the numerical coefficient of the incompressible MRM.

The fit of the proposed *MRM* (called hereafter *incompressible MRM*) to all the 220 cases simulated by means of the incompressible CFD model (Fig. 7-2) has a global value of the determination coefficient R^2 of about 0.94, with an average value of the normalized root mean square error (*NRMSE*) of about 2.5%.

The dependence of the functions $a(h^*)$, $b(h^*)$, $c(h^*)$ and $d(h^*)$ on the dimensionless water depth h^* is shown in Fig. 7-3. The functional structure of $f(K^*-d)$, $a(h^*)$, $b(h^*)$, $c(h^*)$ and $d(h^*)$, with the relative numerical coefficients, defining the proposed *incompressible MRM* are summarized in Table 7-1.

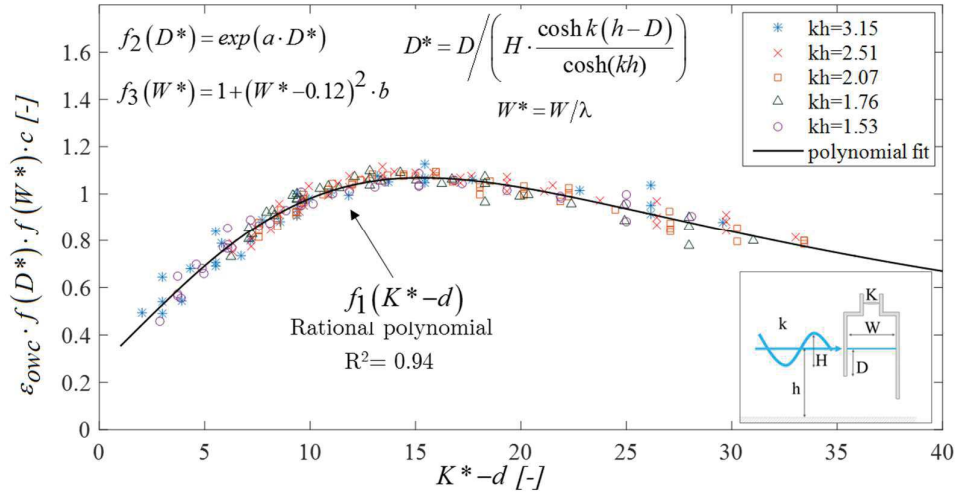


Figure 7-2: Global fit of the results of CFD simulations (symbols) to the proposed *incompressible MRM* (continuous line) for the prediction of the OWC efficiency ϵ_{owc} .

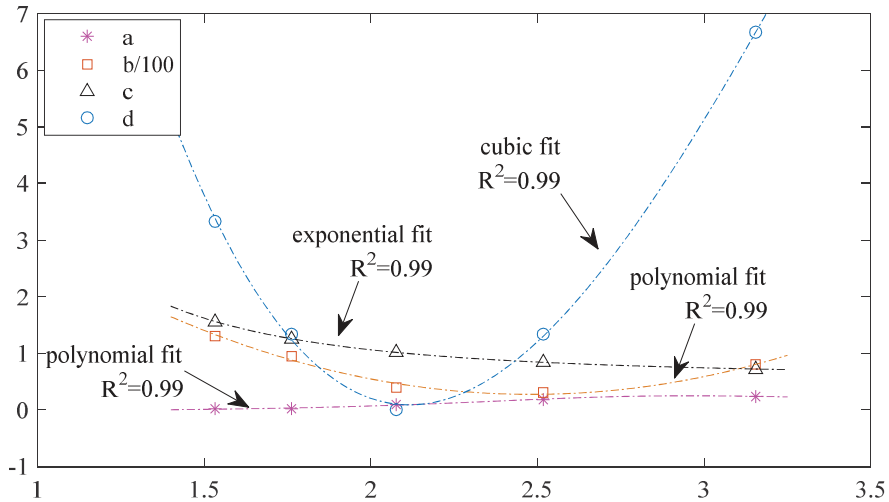


Figure 7-3: Values of the functions $a(h^*)$, $b(h^*)$, $c(h^*)$, $d(h^*)$ of the *incompressible MRM* versus the dimensionless water depth h^* .

It has to be underlined that given the structure of the model (based on multiple regression with fixed functional structures), it is fundamental to obtain very good fit for $a(h^*)$, $b(h^*)$, $c(h^*)$ and $d(h^*)$ ($R^2 > 0.98$), in order to avoid error propagation and to have an overall good accuracy in the prediction of ϵ_{owc} . Therefore, considering the non-linearity of the physical phenomena the model implicitly aims to reproduce, fitting with relatively high order polynomial is required (≤ 3) (Fig. 7.3). This might limit the applicability of the model outside the specific parameter range considered in *this PhD research* ($h^* = 1.5-3.5$, $D^* = 1.8-5$, $W^* = 0.08-0.2$, $K^* = 20-170$).

The choice of giving priority to the model accuracy in the aforementioned parameter range is justified by recalling:

- (i) the main requirement of the proposed MRM, i.e. to be a simple, non-computationally demanding and to account for all relevant phenomena in the OWC dynamics, implicitly including non-linear effects;
- (ii) the preliminary and clear indication, from laboratory tests (Crema et al., 2016), that the optimal design parameters for the OWC are within the range considered in this *PhD research* (see *section 5.1*).
- (iii) being conceived as an optimization tool, the *incompressible MRM* was formulated to have the highest possible accuracy in the parameter range where the highest ϵ_{owc} are expected.

Table 7-1: Structure of the functions defining the proposed *incompressible MRM*

	Functions	Coefficients
f	$f_1(K^* - d) = \frac{(P_1 \cdot (K^* - d) + P_2)}{((K^* - d)^2 + Q_1 \cdot (K^* - d) + Q_2)}$	$P_1 = 144.9$ $P_2 = 39.58$ $Q_1 = -23.06$ $Q_2 = 6300$
a	$a(h^*) = \frac{(P_3 \cdot h^* + P_4)}{(h^{*2} + Q_3 \cdot h^* + Q_4)}$	$P_3 = 0.133$ $P_4 = -0.178$ $Q_3 = -5.378$ $Q_4 = 8.021$
b	$b(h^*) = P_5 \cdot h^{*2} + P_6 \cdot h^* + P_7$	$P_5 = 117.1$ $P_6 = -581.3$ $P_7 = 748.9$
c	$c(h^*) = P_8 h^{*R_9} + P_{10}$	$P_8 = 3.084$ $P_9 = -2.680$ $P_{10} = 0.581$
d	$d(h^*) = P_{11} \cdot h^{*3} + P_{12} \cdot h^{*2} + P_{13} \cdot h^* + P_{14}$	$P_{11} = -6.678$ $P_{12} = 67.61$ $P_{13} = -196.4$ $P_{14} = 176.4$
$Incompressible\ MRM:\ \epsilon_{owc} = \frac{f_1(K^* - d(h^*))}{\exp(a(h^*) \cdot D^*) \cdot (1 + b(h^*) \cdot (W^* - 0.12)^2)} \cdot c(h^*)$		

7.1.3. Incompressible MRM validation

The performance of the proposed *incompressible MRM* in predicting the *output parameter* ε_{owc} as a function of the (*input*) *parameters*, i.e. incident wave (H, k), OWC geometry (W, D, B) and the applied damping (K) is evaluated by applying the model to:

- (i) the data used for the model formulation (Fig. 7-4), i.e. the 220 OWC geometries and wave conditions used in the CFD simulations carried out for the parameter study;
- (ii) an independent set of data, called hereafter the *validation dataset* (Fig. 7-5), i.e. cases not included in the dataset used for the model formulation. For this purpose, 20 additional CFD simulations are performed, considering OWC geometries characterized by combinations of W and D that were not simulated in the parameter study.

The conceptual model is able to predict ε_{owc} with a satisfactory accuracy for both the data used for the model formulation and those in the *validation dataset*. The maximum relative error between the value of ε_{owc} resulting from the simulations and that predicted by the *incompressible MRM* is lower than 15%.

Within the limit of the application in the considered range of dimensionless parameters ($h^*=1.5-3.5$, $D^*=1.8-5$, $W^*=0.08-0.2$, $K^*=20-170$), the model could be applied as a simple tool in the framework of the optimization of OWC device, allowing the selection of the optimal value of the design. Moreover, the good performance of the *incompressible MRM* in reproducing new data in the *validation dataset* proved that, despite the relatively high order of the polynomial used for defining the functional structures, the model is not over fitted.

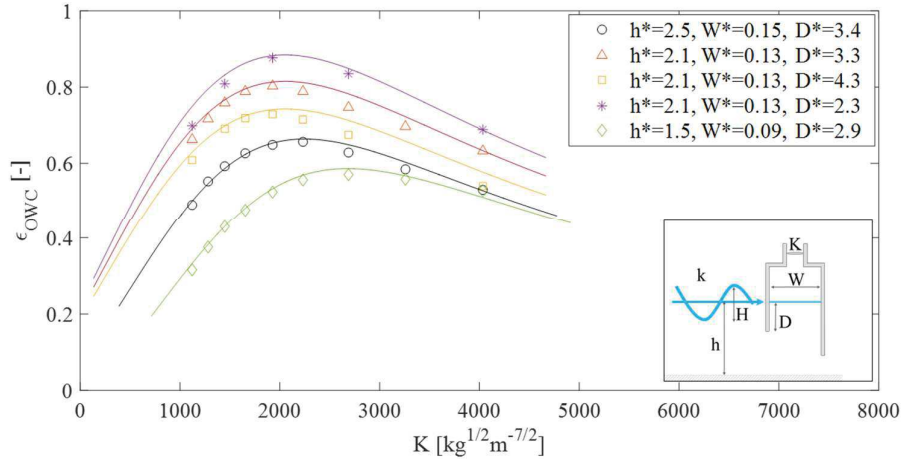


Figure 7-4: OWC pneumatic efficiency ε_{owc} versus turbine damping K (at model scale 1:50) for different OWC geometries and wave conditions in the dataset used for the MRM formulation. Comparison between results of CFD simulations (symbols) and *incompressible MRM* prediction (continuous lines).

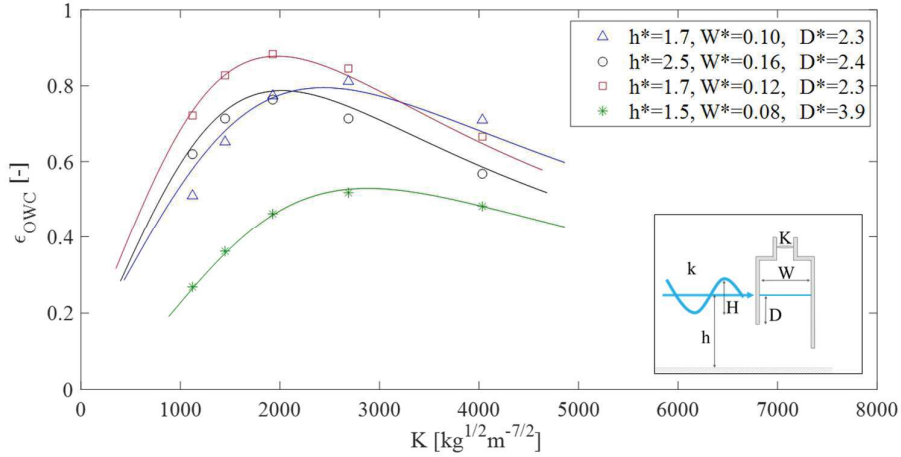


Figure 7-5: OWC pneumatic efficiency ϵ_{owc} versus turbine damping K (at model scale 1:50) for different OWC geometries and wave conditions in the validation dataset of the MRM. Comparison between results of CFD simulations (symbols) and *incompressible MRM* prediction (continuous lines).

In order to further test its performance, the *incompressible MRM* was applied on the same OWC geometries (D and W), damping values (K), wave period (T) and heights (H) tested in the laboratory experiments by Crema et al., 2016. It is worth to stress that the laboratory tests were carried out over a wider range of design parameters than that considered in the CFD parameter study:

- Range of parameters in the laboratory tests by Crema et al. (2016):
 $h^*=1.2-3.5$, $D^*=2.25-40$, $W^*=0.04-0.3$, $K^*=80-800$;
- Range of parameters considered in this research:
 $h^*=1.5-3.5$, $D^*=1.8-5$, $W^*=0.08-0.2$, $K^*=20-170$;

Moreover, laboratory data by Crema et al., 2016, were not directly included in the dataset used for the *incompressible MRM* formulation for the following reasons:

- (i) In order to have independent data to further test the new model, and particularly evaluate its behaviour outside the range of parameters used for its formulation. As aforementioned, in fact, the aim of the new model is to allow the selection of optimal geometries (W , D) and damping values (K), and is therefore reasonable to assume it should be used in the range containing the optimum ($h^*=1.5-3.5$, $D^*=1.8-5$, $W^*=0.08-0.2$, $K^*=20-170$). The evaluation of the model behaviour outside this range is, however, fundamental in order to exclude non-physical behaviours, which may be caused by the multiple-regression approach.
- (ii) Given the wide range of parameters explored in the laboratory tests by Crema et al., and the relatively low number of configurations evaluated in this range (86), laboratory data did not have the required resolution to properly be used in a multiple-regression model without the risk of overfitting it.

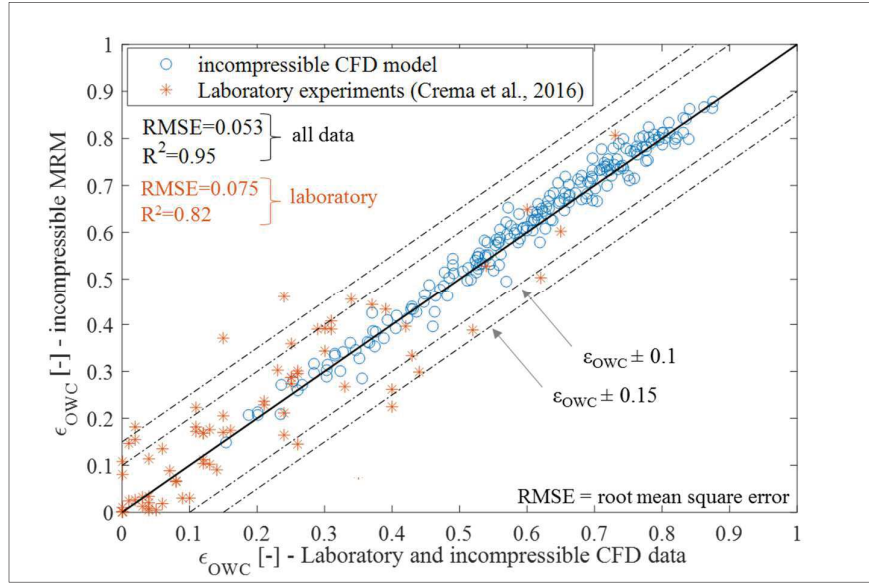


Figure 7-6: Scatter plot between the *incompressible MRM* prediction and measured data (obtained from laboratory experiments by Crema et al. 2016, and CFD simulations) of ϵ_{owc} .

Considering both the results of laboratory experiments by Crema et al. (2016) and those of CFD simulations, an overall value of $R^2=0.95$ is found for the *incompressible MRM* predictions (Fig. 7-6) with a Root Mean Square Error (RMSE) of about 0.053. The maximum absolute error on the predicted value of ϵ_{owc} is about 0.2, and an absolute error lower than 0.15 is observed for about 92% of the available data. Considering only the laboratory data, a determination coefficient $R^2=0.82$ is found for the prediction of the *incompressible MRM*.

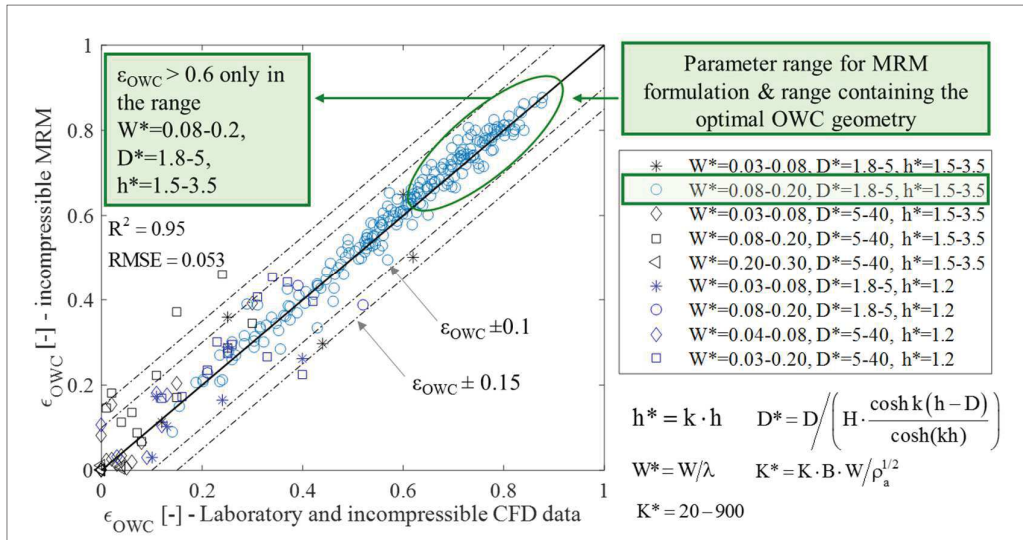


Figure 7-7: Scatter plot between *incompressible MRM* prediction and measured data (obtained from laboratory experiments by Crema et al. 2016 and incompressible CFD simulations) for different ranges of the non-dimensional parameters W^* , D^* and h^* .

Applying the MRM to the relative water depth $h^*=1.2$ (lower than the minimum value investigated in the CFD study, $h^*=1.53$), the agreement between the MRM predictions and the experimental data is still relatively satisfactory, with a maximum error on ε_{owc} of about 0.15, excluding therefore non-physical behaviours of the model when h^* is slightly outside the considered range.

Moreover, the scatter plot for different ranges of the non-dimensional design parameters (Fig. 7-7) also allows to confirm that ε_{owc} -values higher than 0.6 are only found in the range $W^*=0.08-0.2$, $D^*=1.8-5$, $h^*=1.5-3.5$, which is the one considered in this research.

Within this range, the absolute error of the *incompressible MRM* is always lower than 0.1, for both laboratory test and CFD data, confirming that the model can be appropriately used for OWC optimization.

A new model is proposed, which is able to predict the OWC capture width ratio ε_{owc} given the wave parameters (wave height H and period T), the geometrical parameters of the device (chamber width in wave propagation direction, W , front wall draught, D) and the turbine damping (K). Dimensional analysis is applied to define non-dimensional independent parameters: non-dimensional water depth h^* , non-dimensional front wall draught, D^* , non-dimensional chamber width W^* and non-dimensional turbine damping K^* . The structure of the functions of the model is a priori imposed to reflect the physical phenomenon observed in the parameter study (see *Chapter 5*).

The model is at first formulated by multiple regression on the results of the incompressible CFD simulations, in order to be able to verify the model formulation by applying it on both the results of additional incompressible CFD simulations and to the laboratory data by Crema et al. 2016. The performance of the *incompressible MRM* in predicting the OWC capture width ratio ε_{owc} is quite good (absolute error on $\varepsilon_{owc} < 0.1$, $R^2 = 0.95$) in the range of parameters used for the formulation of the model ($h^* = 1.5-3.5$, $D^* = 1.8-5$, $W^* = 0.08-0.2$, $K^* = 20-170$). Even if tentatively applied outside of this range, absolute errors on ε_{owc} lower than 0.2 are found ($R^2 = 0.82$), thus proving the consistency of the model formulation.

7.2. Application of the correction factors for air compressibility: compressible MRM

The effect of air compressibility is introduced in the MRM by applying the correction factors for air compressibility proposed in *Chapter 6* (see Table 6-5) to the results obtained from the incompressible CFD model.

The non-dimensional pressure parameter Γ (Eq. 6-9) is computed for each case, based on the value of the pressure oscillation amplitude Δp_{owc} , the incident wave height H , the wave number k , the water depth h and the front wall draught D . The

correction factor for the OWC capture width ratio, $CF_{\epsilon_{1:50}}$, is evaluated and applied to ϵ_{owc} .

Once the whole dataset is corrected, the iterative non-linear regression procedure used to determine the numerical coefficient of the *incompressible MRM* (Fig. 7-1) is applied, leading to the formulation of a model which includes the air compressibility effect, called hereafter *compressible MRM*.

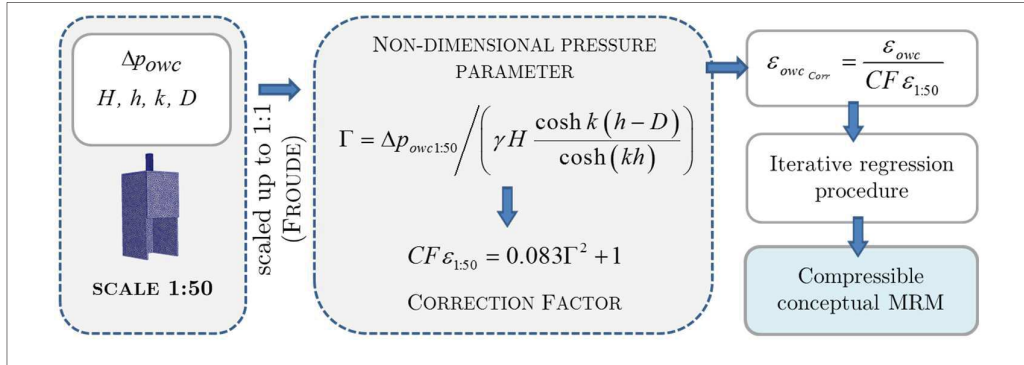


Figure 7-8: Procedure for the application of the proposed correction factors for air compressibility and for the formulation of the *compressible MRM*.

A relatively good agreement between the results of the CFD simulations corrected to account for the air compressibility effect and the prediction of the *compressible MRM* ($R^2=0.93$, Fig. 7-9) is found by using the same structure of the functions adopted in the *incompressible conceptual MRM*. Moreover, the numerical coefficients for the functions are the same as in the *incompressible MRM*, except for those of the rational polynomial $f_{1c}(K^*-d)$ (Table 7-2).

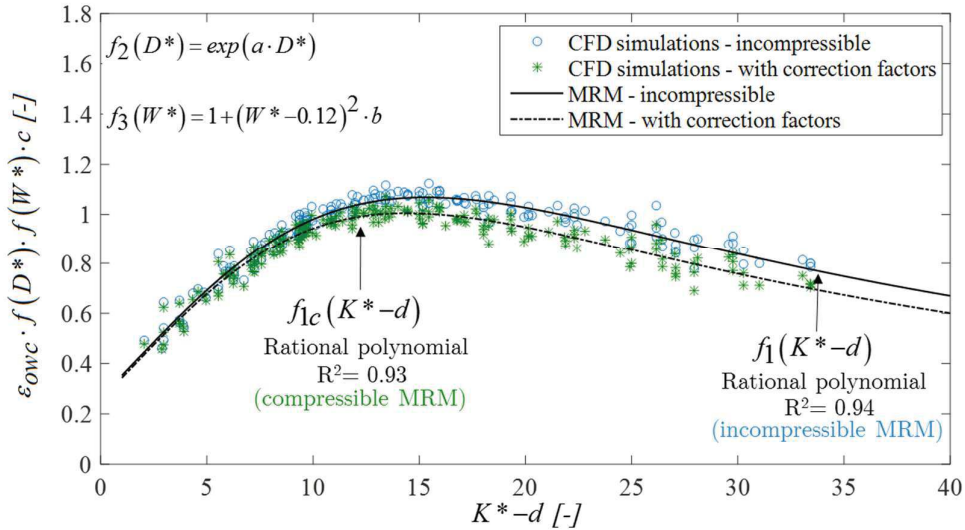


Figure 7-9: Comparison of the fit of the results of CFD simulations (incompressible and corrected with correction factor for air compressibility) and the proposed *incompressible* and *compressible MRM* for the prediction of the OWC efficiency ϵ_{owc} .

Table 7-2: Structure of the functions defining the proposed *compressible MRM*

	<i>Functions</i>	<i>Coefficients</i>
<i>f</i>	$f_1(K^* - d) = \frac{(P_1 \cdot (K^* - d) + P_2)}{((K^* - d)^2 + Q_1 \cdot (K^* - d) + Q_2)}$	P ₁ = 124.8 P ₂ = 34.27 Q ₁ = -29.24 Q ₂ = 5780
<i>a</i>	$a(h^*) = \frac{(P_3 \cdot h^* + P_4)}{(h^{*2} + Q_3 \cdot h^* + Q_4)}$	P ₃ = 0.133 P ₄ = -0.178 Q ₃ = -5.378 Q ₄ = 8.021
<i>b</i>	$b(h^*) = P_5 \cdot h^{*2} + P_6 \cdot h^* + P_7$	P ₅ = 117.1 P ₆ = -581.3 P ₇ = 748.9
<i>c</i>	$c(h^*) = P_8 h^{*P_9} + P_{10}$	P ₈ = 3.084 P ₉ = -2.680 P ₁₀ = 0.581
<i>d</i>	$d(h^*) = P_{11} \cdot h^{*3} + P_{12} \cdot h^{*2} + P_{13} \cdot h^* + P_{14}$	P ₁₁ = -6.678 P ₁₂ = 67.61 P ₁₃ = -196.4 P ₁₄ = 176.4
<i>Incompressible MRM: $\epsilon_{owc} = \frac{f_1(K^* - d(h^*))}{\exp(a(h^*) \cdot D^*) \cdot (1 + b(h^*) \cdot (W^* - 0.12)^2) \cdot c(h^*)}$</i>		

The results of the incompressible CFD simulations are corrected by applying the correction factors obtained in *Chapter 6*. Consequently, a new model, based in multiple regression (denoted as *compressible MRM*) is formulated, allowing to also account for the effect of air compressibility when predicting ϵ_{owc} . The structure of the functions used to formulate the model are unvaried with respect to that of the *incompressible MRM*. Therefore, air compressibility should not significantly affect the selection of the optimal OWC geometry (in terms of chamber width W , front wall draught D and damping K), but only results in a moderate overestimation of the resulting capture width ratio (<10%, see *Chapter 6*).

7.3. Example application of the MRM for site-specific optimization of the OWC

The proposed *compressible MRM* is conceived as a tool to be used in the process of optimization of OWC devices, for the site-specific installation in moderate wave climate. The model, which is not computationally demanding, allows to comparatively evaluate the capture width ratio of a number of design alternatives much higher than using more time demanding CFD simulations and more expensive laboratory tests. The model can, therefore, be efficiently applied for combined optimization of the

considered design parameters, fulfilling one of the objectives of this PhD study (see *section 2.5.1*).

Exemplary applications, based on different optimization criteria, are shown hereafter for the hypothetical case of a site-specific case installation in an area located in Central Tuscany (latitude 4821420, longitude 589519, UTM32 coordinate), on a water depth $h=25\text{m}$ (value at full scale). The site for this exemplary application is characterized by a mean annual wave power of about 2.8 kW/m (Vannucchi, 2012), and total annual energy AE as in Fig. 7-10.

It has to be underlined that the *compressible MRM* is developed taking into account regular waves only. Therefore, the strong assumption of approximating the wave climate in the installation site by means of a set of regular waves having height H and period T corresponding to the significant height H_s and the energy period T_e in the scatter matrix in Fig. 7-10 is made.

The effect of irregular waves on the device efficiency, and in turn on the selection of the optimal OWC geometry should be investigated in future studies.

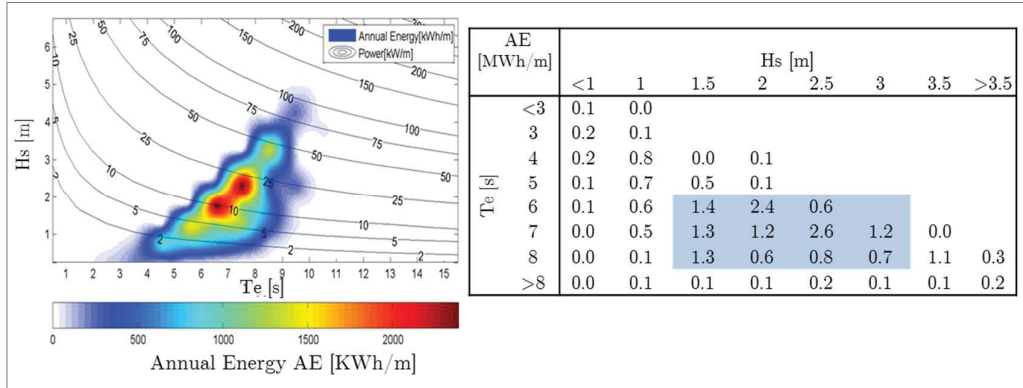


Figure 7-10: Characterization of the wave resource in terms of significant wave height H_s and wave energy period T_e for the reference installation site (Central Tuscany, water depth $h=25\text{m}$) in terms of total annual energy per meter of wave front AE (data from Vannucchi, 2012).

Two optimization criteria are exemplarily applied:

- (i) *Case A*: Combined optimization of the geometry parameters (W and D) and the applied damping (K) for the wave associated to the highest annual energy in the installation site (i.e., wave height $H=2.5\text{m}$ and period $T=7\text{s}$, with total annual energy $AE=2.6\text{ MWhm}^{-1}$, Fig. 7-10). The optimal configuration providing the maximum value of capture width ratio ε_{owc} for the aforementioned wave conditions is selected.
- (ii) *Case B*: Combined optimization of the geometry parameters (W and D) and the applied damping (K) by considering $n=11$ waves, chosen as the more energetic in the installation site (code n_I-n_{I1} as in Tab. 7-3). The selected wave cases cover ca. 70% of the available annual energy AE_{tot} . In *case B*, the objective function, *o.f.*, is the maximization of $\overline{\varepsilon_{owc}}$, defined as a weighted average of the capture width ratio obtained for each of the n waves, ε_{owcn} , with weights being the annual energy associated to each wave, AE_n (Eq. 7.12)

$$o.f. = \max_i \left(\overline{\varepsilon_{owc}} \right)_i = \max_i \left(\frac{\sum_n \varepsilon_{owc_n} AE_n}{\sum_n AE_n} \right)_i \quad \begin{array}{l} \text{n=tested wave} \\ \text{i=OWC configuration (D,W,K)} \end{array} \quad (7.12)$$

Table 7-3: Wave cases selected for the example application of the MRM in *case B* (wave height H , wave period T , annual energy AE_n , fraction of the total annual energy in the reference installation site AE_n/AE_{tot}).

<i>wave</i> ($h=25m$)	H [m]	T [s]	AE_n [MWhm ⁻¹]	AE_n/AE_{tot}
n1	1.5	6	1.4	0.07
n2	1.5	7	1.3	0.06
n3	1.5	8	1.3	0.06
n4	2	6	2.4	0.11
n5	2	7	1.2	0.06
n6	2	8	0.6	0.03
n7	2.5	6	0.6	0.03
n8	2.5	7	2.6	0.13
n9	2.5	8	0.8	0.04
n10	3	7	1.21	0.06
n11	3	8	0.71	0.03
Total fraction of AE_{tot} in the installation site:				0.68

In both *Case A* and *Case B*, a direct search approach is applied. Therefore, the range of the parameters is preliminary fixed, then the parameter space (i.e. the set of combination of the values of W , D and K) is defined by choosing a discretization step for each parameter. The *compressible MRM* (summarized in Table 7-2), is then used to evaluate ε_{owc} over the entire parameter space.

The chamber width W is varied between 7.5 m and 11.5 m, with a discretization step 0.2 m, i.e. in a range containing the optimum value of $W^* \sim 0.12$ (see *Chapter 5*) for all the considered waves (Table 7-3). The front wall draught D is varied between 3.5 and 6 m, with a discretization step 0.2 m. Values of $D < 3.5$ m are not considered, to limit the possibility of occurrence of the *inlet broaching phenomenon* for higher waves, which would result in loss of the extracted power due to sudden pressure change in the OWC chamber (see *section 5.4.1*). Values of the turbine damping K between 0.6 and 1.4 kg^{1/2}m^{-7/2} are tested, with discretization step 0.04 kg^{1/2}m^{-7/2}.

The resulting parameter space is composed of ca. 5700 combinations of W , D and K .

It has to be underlined that the range of the parameters selected for the exemplary application, would result in values of the non-dimensional model parameters, W^* , D^* , K^* , and h^* (defined as in Eqs. 7.2-7.5) within the range $h^*=1.5-3.5$, $D^*=1.8-5$, $W^*=0.08-0.2$, $K^*=20-170$. This range, as aforementioned, corresponds to that in which the optimal geometry is expected, and that used for the formulation of the *compressible MRM*. Relatively reliable predictions of the MRM could therefore be expected in this application.

For *Case A*, the application of the *compressible MRM* would result in the selection of an optimal configuration $W=8.9$ m, $D=3.5$ m, $K=0.8$ kg^{1/2}m^{-7/2}, with a capture

width ratio $\varepsilon_{owc} \sim 0.83$. For $D=3.5$ m, ε_{owc} values very close to 0.83 (i.e., $\varepsilon_{owc} = 0.83 \pm 0.01$) can be obtained with different combinations of W and K (Fig. 7-11,a) e.g. $W=8.5$ m and $K=0.84$ $\text{kg}^{1/2}\text{m}^{-7/2}$, $W=9.3$ m and $K=0.76$ $\text{kg}^{1/2}\text{m}^{-7/2}$.

A possible strategy to choose among almost equivalent alternatives in terms of ε_{owc} could be, e.g., to select the one with the lower value of W , minimizing therefore the cost of the device construction. The possible difference in the mechanical efficiency of an air turbine specifically designed to induced the selected level of damping on the OWC system should be an additional criterion to lead the choice among almost equivalent geometries in terms of ε_{owc} .

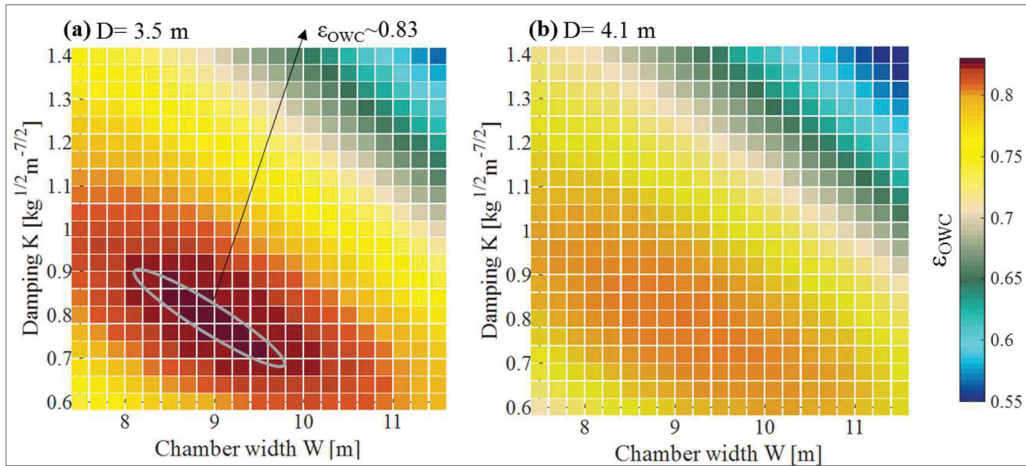


Figure 7-11: Scatter plot of the OWC capture width ratio ε_{owc} obtained with the *compressible MRM* for the example application of *Case A*: wave height $H=2.5$ m, period $T=6$ s, water depth $h=25$ m, damping $K=0.6-1.4$ $\text{kg}^{1/2}\text{m}^{-7/2}$, chamber width $W=7.5-11.5$ m and draught $D=3.5$ m (a) and 4.1 m (b).

For *Case B*, i.e. when the wave conditions n_I-n_{II} are considered (parameters as in Table 7-3), the application of the model including the air compressibility effect would result in the selection of the optimal geometry (having values of $\overline{\varepsilon_{owc}}$, defined as in Eq. 7-12, ~ 0.71) $D=3.5$ m, and equivalently: $W=8.9$ m and $K=0.84$ $\text{kg}^{1/2}\text{m}^{-7/2}$, $W=8.5$ m and $K=0.88$ $\text{kg}^{1/2}\text{m}^{-7/2}$ or $W=9.3$ m and $K=0.8$ $\text{kg}^{1/2}\text{m}^{-7/2}$ (Figure 7-12). With respect to *case A*, therefore, the optimal value of the damping K is slightly higher.

The shift towards higher values of the optimal damping K when aiming at the maximization of ε_{owc} over a range of different incident wave frequency, which is found when applying the MRM, is confirmed in the literature (Curran et al. 1997). Higher damping values are beneficial for the performance when the incident wave frequency does not correspond to the OWC resonance frequency (as is necessary the case if more than one incident wave frequency is considered, for an OWC device with fixed geometry). In other words, overdamped OWC shows a better performance over a wider range of frequencies, as already discussed in *section 5.4.3*.

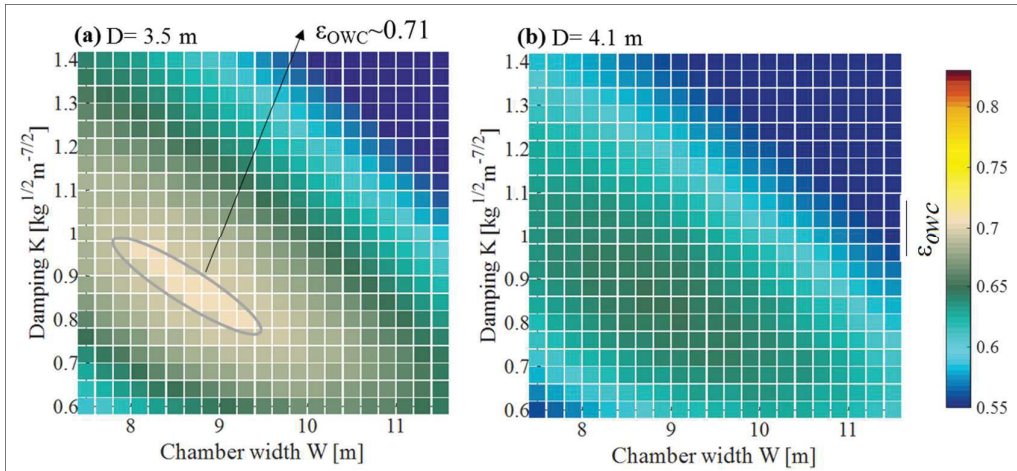


Figure 7-12: Scatter plot of the average OWC capture width ratio $\overline{\varepsilon}_{owc}$ obtained with the *compressible MRM* for the example application of *Case B*: wave heights $H=1.5-3$ m, periods $T=6-8$ s, water depth $h=25$ m, damping $K=0.6-1.4$ $\text{kg}^{1/2}\text{m}^{-7/2}$, chamber width $W=7.5-11.5$ m and draught $D=3.5$ m (a) and 4.1 m (b).

The difference in the optimal geometry selected by applying the optimization criteria of *case A* and *Case B* is quite limited. This may be due to the particular installation site chosen for the example application. For the selected waves in *Case B*, more than 50% of the total annual energy is associated with the wave period $T=7$ s, which is also the period of the wave used for the optimization in *Case A*. Higher difference between the two strategies could emerge when applying the model in installation sites characterized by a higher variation in the distribution of the annual energy among different wave periods.

As a comparison, the *incompressible MRM* was also applied to perform the example application of *Case A* and *Case B*. The *incompressible MRM* would expectedly lead to the selection of approximately the same OWC geometries as the *compressible MRM*. When using the *incompressible MRM*, however, a slight overestimation of the maximum ε_{owc} (~ 0.88 vs 0.83 , for *Case A*) and $\overline{\varepsilon}_{owc}$ (~ 0.76 vs 0.71 , for *Case B*) is obtained with respect to the *compressible MRM*.

The new *compressible MRM*, allowing to evaluate the performance of an high number of design alternatives with much less computational effort, is exemplarily applied for the optimization of an OWC for an hypothetical installation in a 25 meters water depth in Central Tuscany. Two optimization strategies are comparatively tested: *Case A*, optimization for a wave height $H=2.5$ m, period $T=7$ s; *Case B*, optimization over a range of different wave conditions (wave heights $H=1.5-3$ m, period $T=6-8$ s). The model predicts a shift towards higher values of the optimal damping K when aiming at the maximization of ε_{owc} over different wave frequencies, which is confirmed in the literature (Curran et al. 1997) and in the CFD parameter study (*Chapter 5*). Overdamped OWC, therefore, shows a better performance over a wider range of incident wave frequencies.

7.4. Summary and discussion

Based on the analysis of the results of the CFD parameter study, a new model (MRM) is proposed. The model is able to predict the OWC capture width ratio ε_{owc} given the wave parameters (wave height H and period T), the geometrical parameters of the device (chamber width in wave propagation direction, W , front wall draught, D), and the turbine damping (K). The model allows to implicitly account for the non-linear effects observed in the CFD model, including e.g. the effect of flow separation, turbulence and vortex formation.

The functional structures of the MRM are a priori imposed to reflect the physical phenomena observed in the CFD parameter study (*Chapter 5*).

The model is first formulated by multiple regression on the results of incompressible CFD simulations (resulting in the so-called *incompressible MRM*), so that it can be validated by applying it on both the results of additional incompressible CFD simulations and to the laboratory data by Crema et al. 2016. The performance of the *incompressible MRM* is quite good in predicting the OWC capture width ratio ε_{owc} (determination coefficient $R^2=0.95$) in the range of parameters used for the formulation of the model ($h^*=1.5-3.5$, $D^*=1.8-5$, $W^*=0.08-0.2$, $K^*=20-170$). It has to be underlined that this range also corresponds to that containing the optimal geometry for the OWC (see *section 5.1*). Furthermore, tentatively applying the model outside this range, an absolute error on the prediction of ε_{owc} lower than 0.2 is found, with a R^2 -value 0.82, proving the consistency of the model formulation.

After the validation of the *incompressible MRM*, a version of the model able to consider the effect of air compressibility is proposed, by correcting the results of the incompressible CFD model applying the correction factors obtained in *Chapter 6*. Thus, a model including also compressibility effects is obtained (the *compressible MRM*).

An example application of the new *compressible MRM* is given in *section 7.3*, proving how the model might be efficiently used for the purpose of design optimization of OWC devices in site-specific wave climates, allowing the comparison of a great number of design alternatives with limited computational effort.

The main limitations of the proposed MRM, and the subsequent suggestions for possible future work are as follows:

- (i) The MRM attempts to predict the OWC capture width ratio ε_{owc} , which is a multivariate function of the input parameters, and to reproduce all the relevant phenomena affecting ε_{owc} , implicitly including therefore non-linear effects. In order to achieve this objective, polynomial functions with relatively high order (≤ 3) are needed. Polynomial functions are well known to have poor extrapolatory properties; it is therefore suggested to limit the application of the model to the parameter range tested for its formulation in *this PhD research* ($h^*=1.5-3.5$, $D^*=1.8-5$, $W^*=0.08-0.2$, $K^*=20-170$). Further study might be needed to propose extensions of the MRM model to a wider range of design parameters.

- (ii) The MRM considers only the OWC device performance in regular waves; future work may, therefore, evaluate the effect of irregular waves on the selection of the optimal geometry for the OWC device and analyse possible corrections to be applied to the model formulation to also account for irregular waves.
- (iii) The MRM considers a fixed OWC device, i.e. the effect of the additional motion mode arising when adopting a floating device, and their possible impact on the geometry optimization, are not accounted for by the model. The evaluation of the possibility of correcting the model formulation to also account for floating OWCs could be a future development of the present work.

CHAPTER 8

Concluding remarks and Outlooks

8.1. General summary of the thesis

This PhD research aimed at studying the combined effect of the geometry and of the damping applied by a non-linear turbine (i.e. an impulse turbine) on performance of a fixed Oscillating Water Column (OWC) device for harvesting the wave energy. The resulting knowledge base regarding the optimal OWC geometrical parameters, specifically for moderate wave climate, such as the Mediterranean Sea, have contributed to fill one of the identified knowledge gaps. The scale effect induced by neglecting the air compressibility in modelling OWC devices is also evaluated, and correction factors for the results of incompressible numerical models and for the results from small-scale laboratory testing of OWC devices are provided, contributing to fill a further recognized knowledge gap. A new conceptual model allowing to predict the capture width ratio ε_{owc} of the OWC based on its geometrical parameters, the damping applied by the turbine and the incident wave conditions is proposed. The new conceptual model might be applied as a design supporting tool in the process of the OWC device optimization.

In *Chapter 2*, the state of the art is reviewed and analysed, the knowledge gaps are identified and the implications for the objectives and the methodology of the thesis are drawn. In *Chapter 3*, a simplified frequency domain model of the OWC device, as widely used in the literature, is implemented and applied in order to perform a preliminary evaluation of the effect of different design parameters on the performance of the OWC, thus allowing to select the most relevant parameters to be considered in *this study*. Moreover, the frequency domain model is also used to predict the range of variability the physical quantities to be measured in laboratory tests by Crema et al, 2016, permitting to employ measuring sensors particularly suited (in terms of measurement limits and accuracies). In *Chapter 4*, a Numerical Wave Tank (NWT) is used, in the Computational Fluid Dynamics (CFD) environment OpenFOAM®. Different wave generation approaches are alternatively compared, and a sensitivity analysis is performed resulting in the choice of the most appropriate setting of the NWT for simulating the OWC device. In *Chapter 5*, a three-dimensional, incompressible CFD model of the OWC device, validated with laboratory experiments

(Crema et al. 2016) is used to perform the systematic parameter study. The range of the OWC parameters to be more extensively explored by means of the CFD model is selected based on those resulting in higher capture width ratio ε_{owc} from the laboratory tests. The incompressible CFD model is used to enlarge the number of evaluated configurations in the selected range of parameters, allowing a more precise identification of the optimum. In *Chapter 6*, scale effects related to air compressibility are quantified by comparative analysis of the results of the incompressible and the compressible CFD models. For this purpose, the standard compressible VOF solver of OpenFOAM is implemented into the wave model `waves2Foam`, resulting in a new solver (`compressibleWaveFoam`). Benchmark tests are performed on the new solver to ensure its capability to reproduce properly compressible effects. In *Chapter 7* a new conceptual Multiple Regression Model (MRM) is developed. The model is able to predict the OWC capture width ratio ε_{owc} given the wave conditions, the OWC geometry and the turbine damping as input variables. The new conceptual model, once validated is then adjusted by applying the correction factors for air compressibility proposed in *Chapter 6*. The relevance of the conceptual model in the OWC optimization process is demonstrated by an example application to a selected installation site in the Mediterranean Sea (Central Tuscany area).

8.2. Summary and discussion of key results

Key findings on the effect of the OWC parameters on the capture width ratio

The analysis of the results of the parameter study using the incompressible CFD model leads to the following main conclusions:

- (i) As expected, the capture width ratio ε_{owc} is a multivariate function of the wave conditions (wave height H and relative water depth kh), the geometrical parameters of the OWC (chamber width W and draught D) and of the turbine applied damping K . An optimization of the OWC can be achieved only through a combined consideration of all aforementioned parameters.
- (ii) A value of the damping K_{opt} allowing to maximize the OWC capture width ratio ε_{owc} can univocally be determined for each OWC geometry (front wall draught D and chamber width W) and relative water depth kh . *Underdamping* ($K < K_{opt}$) reduces ε_{owc} much more than *overdamping* ($K > K_{opt}$). K_{opt} is strongly dependent on both the chamber width W (K_{opt} increases when W decreases) and the relative water depth kh (assuming minimum values around resonance conditions), even if the effect of the latter is much higher. For relative water depth $kh=1.5-3.15$, the optimal value of the relative damping $KBW/\rho_a^{1/2}$ (B =chamber length transversal to wave propagation direction, ρ_a =air density) varies between 70 and 110. For $KBW/\rho_a^{1/2}=20-170$, the damping K has a crucial effect on the device capture width ratio ε_{owc} , inducing variations up to 0.3 in ε_{owc} .

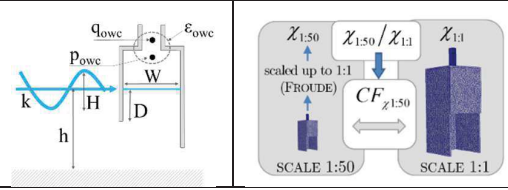
- (iii) The front wall draught D has a fundamental effect on the capture width ratio ε_{owc} , since it affects both the resonance frequency of the device and wave-induced pressure acting on the OWC. In the tested range of relative front wall draught D/H ($=1.75$ - 3.75) and kh ($=1.53$ - 3.15), it can generally be observed that increasing D may result in a decrease of the capture width ratio ε_{owc} up to 0.4.
- (iv) Maximum values of ε_{owc} are obtained for relative chamber width $W/\lambda \sim 0.12$. The decreasing rate for $W/\lambda < 0.12$ is slightly higher than for $W/\lambda > 0.12$, possibly related to non-linear effects due to different energy losses induced by flow separation under progressive waves of different length. Increasing W/λ from 0.08 to 0.12 may result in an increase of ε_{owc} up to 0.2. Therefore, relative chamber width W/λ represents one of the governing parameters for the optimization of the device design.

For the OWC considered in this *PhD research*, having the peculiarity of being detached from the sea bottom and asymmetric in the length of the front and back walls (with fixed relative back wall draught $G/h=0.6$), a maximum capture width ratio $\varepsilon_{owc}=0.87$ is found for $W/\lambda=0.12$, $D/H=1.75$, $KBW/p_a^{1/2}=70$, $H/h=0.08$ and $kh=2.07$ with constant water depth $h=0.5$ m.

Key findings on scale effects due to air compressibility

The scale effects due to air compressibility between model scale 1:50 and full scale 1:1 is analysed in terms of the non-dimensional parameter Γ (Table. 8-1), which accounts for both the level of air compression in the OWC chamber and the incident wave conditions (wave height H , wave number k and water depth h). The effect of neglecting the air compressibility results in an overestimation up to about 15% for the relative air pressure p_{owc} and the air volume flux q_{owc} , but less than 10% for the capture width ratio ε_{owc} (for $\Gamma=0.4$ - 1.0). This overestimation increases with increasing Γ (i.e. with increasing level of the pressure in the air chamber). Air compressibility effects are remarkably higher (about 20% on p_{owc} , and q_{owc}) in the *inhalation phase* (airflow from turbine to chamber with $p_{owc}<0$) than in the *exhalation phase* (airflow from chamber to turbine with $p_{owc}>0$).

Table 8-1: Summary of the proposed correction factors (CF) for the pressure oscillation amplitude in the OWC air chamber Δp_{owc} , the volume air flow oscillation amplitude Δq_{owc} the capture width ratio ε_{owc} for model scale 1:50.

	<i>parameter</i>	$CF_{1:50}$	R^2
	Δp_{owc}	$0.147\Gamma^2 + 1$	0.95
Δq_{owc}	$0.13\Gamma^2 + 0.11\Gamma + 1$	0.97	
ε_{owc}	$0.083\Gamma^2 + 1$	0.87	
$\Gamma = \Delta p_{owc1:50} / \left(\gamma H \frac{\cosh k(h-D)}{\cosh(kh)} \right) \quad CF_{\chi_{1:50}} = \chi_{1:50} / \chi_{1:1} \text{ with } \chi = \Delta p_{owc}, \Delta q_{owc} \text{ and } \varepsilon_{owc}$			

This might be physically related to the higher air velocity inside the OWC air chamber during *inhalation*, resulting in higher values of *Mach number* (Ma) and thus in more compressible flow conditions. Correction factors for the pressure inside the OWC chamber p_{owc} , the air flow rate q_{owc} and the OWC capture width ratio ε_{owc} obtained experimentally or numerically from a 1:50 OWC model, were proposed, and are summarized in Table 8-1.

Simulations with the compressible CFD code at model scales 1:25, 1:10 and 1:5 showed that scale effects due to air compressibility for OWC models are reduced at relatively large model scales, however at scale 1:5 such scale effects might still be relevant (resulting in an over prediction of the device capture with ratio up to 5% for $F=1$). Moreover, the comparative analysis of the results at different model scales showed that the magnitude of scale effects related to air compressibility is governed by the values of *Mach number* (Ma) in the OWC air chamber. This suggests that, by adopting Ma as the governing variable and by increasing the number of model scales N to be comparatively analysed and the number of tests performed at each model scale N , it might be possible to obtain a more generic formula to evaluate the scale effects due to air compressibility, valid for all scales.

New prediction formulae for the OWC pneumatic capture width ratio

A new Multiple Regression Model (MRM) is proposed, simple and computationally less demanding, able to predict the OWC capture width ratio given the wave conditions (wave height H and period T), the geometry of the device (chamber width in wave propagation direction, W , front wall draught, D), and the turbine damping (K). The model is based on dimensional analysis and multiple regression approach. The functional structures of the model are a priori imposed to reflect the physical phenomena observed in the CFD parameter study, thus trying to overcome one of the main drawbacks of common regression models (i.e. non-causality). The new model thus allows to account for the non-linear effects observed in the CFD parameter study, thus including e.g. the implicitly effect of flow separation and vortex at the submerged lip of the OWC. The overall structure of the proposed MRM, and the associated non-dimensional parameters, are summarized in Fig. 8-1.

Comparing both the incompressible CFD simulations and laboratory tests by Crema et al., 2016, the performance of the *MRM* in predicting the OWC capture width ratio ε_{owc} are quite satisfactory. The absolute error on ε_{owc} is lower than 0.1, and the determination coefficient is $R^2=0.95$ for the range of parameters used for the formulation of the model ($h^*=1.5-3.5$, $D^*=1.8-5$, $W^*=0.08-0.2$, $K^*=20-170$, parameters as in Fig. 8-1).

It has to be underlined that the aforementioned range of parameters used for the formulation of the model also corresponds to the range where the highest capture width ratio is located, as resulting from laboratory tests by Crema et al., 2016. Therefore, the application of the new MRM within this range is consistent with the objective of *this PhD research*, i.e. to provide a tool to be used in the process of OWC design optimization, specifically for a moderate wave climate.

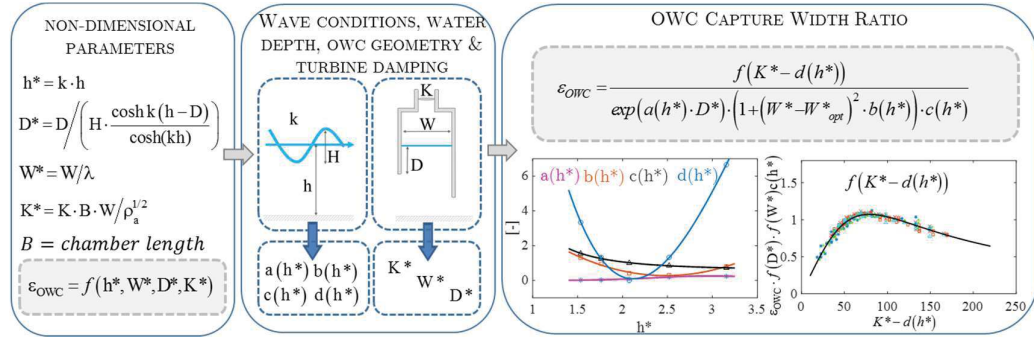


Figure 8-1: Non-dimensional parameters of the new MRM and overall structure of the model.

Even if the model is applied on a wider range of parameters ($h^*=1.2-3.5$, $D^*=2.25-40$, $W^*=0.04-0.3$, $K^*=80-800$), an absolute error on the prediction of ϵ_{owc} lower than 0.2 (with a determination coefficient $R^2=0.82$) is found with respect to the laboratory data by Crema et al. 2016, thus proving the consistency of the proposed model formulation. After the validation, the new MRM was adjusted by applying the proposed correction factors for air compressibility.

The example application of the new MRM for a hypothetical installation of the OWC device in Central Tuscany showed that the model might be efficiently used for the design optimization of OWC devices, allowing the comparison of a great number of design alternatives without excessive computational efforts.

The main limitations of the new MRM are outlined as follows: (i) the model is able to include implicitly non-linear effects (e.g. due to viscous loss, turbulence and flow separation at the OWC submerged front wall lip). Only the effects observed within the range of parameters used for the model formulation ($h^*=1.5-3.5$, $D^*=1.8-5$, $W^*=0.08-0.2$, $K^*=20-170$) might be reproduced by the new MRM. The validity of the model should be therefore cautiously limited to that range; (ii) the model is only valid for a fixed OWC device, i.e. effect induced by the additional degrees of freedom of a floating device are not accounted for; (iii) the model was developed with reference to regular waves only, therefore adjustment for irregular waves might be required. The validation of the model with a full-scale 1:1 case would also be required, in order to ensure that it can be properly applied at full scale.

8.3. Outlooks

The results of *this PhD research* could be the base for future research aimed at developing air turbines particularly suited for OWC devices to install in moderate wave climate. Knowing the damping value the turbine should apply on the OWC system while maintaining relatively high mechanical conversion efficiency is indeed fundamental, since the air turbine generally constitutes the element with the lowest efficiency in OWC systems (Falcão & Henriques 2016).

Future research might be required to overcome some specific limitations of the results

of *this PhD research*. Particularly, regarding the results of the air compressibility scale effect:

- (i) Benchmarks on the new solver compressibleWaveFoam proved its capability to reproduce accurately compressible effect (some of the benchmarks might, indeed, be representative of prototype scale due to the large dimensions of the considered geometries). However, a validation of the compressible model of the OWC at scale 1:1, on an equivalent system from both the dynamic and thermodynamic points of view, is required to confirm the results obtained at scale 1:1.
- (ii) In the overall *PhD research*, the air turbine is introduced conceptually by an induced damping idealised by vents in the OWC chamber cover. This assumption is appropriate to determine the optimal damping the air turbine should apply on the OWC chamber. However, regarding the evaluation of air compressibility effects, it should be noted that an air turbine at prototype scale may induce significant change in the specific entropy in the flow, due to viscous losses (Falcão & Henriques, 2014). The possible impact on the proposed correction factors should be further investigated in future research. For this purpose, a CFD compressible model which simulates the air turbine more accurately could be applied, e.g. with actuator disk (Réthoré et al. 2014).
- (iii) Future research might increase the number of model scales N to be comparatively analysed and the number of tests to be performed at each model scale N , and thus possibly derive a more generic formula to evaluate air compressibility scale effects, valid for all scales, by considering the *Mach number* Ma in the OWC air chamber as the governing variable.

Future research regarding the new MRM might be particularly focused on:

- (iv) The MRM considers a fixed OWC device under regular waves, i.e. the effect on the selection of the optimal geometry of the OWC device of the additional motion modes arising in a floating device, are not accounted for by the model. The evaluation of the possibility of correcting the model formulation to also account for floating OWC could be a future development of the present work. Moreover, adjustments/modifications for irregular waves will also be required.
- (v) The MRM is formulated, and cautiously valid, for the range of parameters $h^*=1.5-3.5$, $D^*=1.8-5$, $W^*=0.08-0.2$, $K^*=20-170$ (even if fairly good agreement with laboratory tests was found in the wider range $h^*=1.2-3.5$, $D^*=2.25-40$, $W^*=0.04-0.3$, $K^*=80-800$). To further extend the applicability of the model outside this range, future research might be needed to propose correction and/or modifications to the model.

References

- Arena, F., Romolo, A., Malara, G. & Ascanelli, A., 2013. On Design and Building of a U-OWC Wave Energy Converter in the Mediterranean Sea: A Case Study. In *Proceeding of 32nd International Conference on Ocean, Offshore and Arctic Engineering*. Nantes, France: ASME, p. 8.
- Babarit, A., 2015. A database of capture width ratio of wave energy converters. *Renewable Energy*, 80, pp.610–628.
- Bagnold, R.A., 1939. Interim report on wave-pressure research. *Journal of the Institution of Civil Engineers*, 12, pp.200–226.
- Berberović, E., van Hinsberg, N., Jakirlić, S., Roisman, I. & Tropea, C., 2009. Drop impact onto a liquid layer of finite thickness: Dynamics of the cavity evolution. *Physical Review E*, 79(E), p.15.
- Boake, C.B., Whittaker, T.J.T., Folley, M. & Ellen, H., 2002. Overview and Initial Operational Experience of the LIMPET Wave Energy Plant. In *Proceedings of the 12th International Offshore and Polar Engineering Conference*. Kitakyushu, Japan, p. 9.
- Bogaert, H., Léonard, S., Brosset, L. & Kaminski, M.L., 2009. Sloshing and scaling : results from the Sloskel project, Proceedings of the 19th International Offshore and Polar Engineering Conference, Osaka, Japan, ISOPE.
- Brackbill, J.U., 1992. A continuum method for Modeling Surface Tension. *Journal of Computational Physics*, 100, pp.335–354.
- Braeunig, J., Brosset, L., Dias, F. & Ghidaglia, J., 2009. Phenomenological Study of Liquid Impacts through 2D Compressible Two-fluid Numerical Simulations Some facts. *Proceedings of the 19th International Offshore and Polar Engineering Conference*, Osaka, Japan, ISOPE.
- Bredmose, H., Peregrine, D.H. & Bullock, G.N., 2009. Violent breaking wave impacts. Part 2: modelling the effect of air. *Journal of Fluid Mechanics*, 641, p.389.
- Brendmo, A., Falnes, J. & Lillebekken, P.M., 1996. Linear modelling of OWC including viscous loss. *Applied Ocean Research*, 18, pp.65–75.
- Brito-Melo, A., Gato, L.M. & Sarmiento, A.J.N., 2002. Analysis of Wells turbine design parameters by numerical simulation of the OWC performance. *Ocean Engineering*, 29(12), pp.1463–1477.
- Brito-Melo, A., Hofmann, T., Sarmiento, A.J.N.A. & Clément, A.H., 2001. Numerical Modelling of OWC-Shoreline Devices Including the Effect of Surrounding Coastline and Non-flat Bottom. *International Journal of Offshore and Polar Engineering*, 11(2).
- Brosset, L. & Dias, F., 2009. On the effect of phase transition on impact pressures due to sloshing, *Proceedings of the 19th International Offshore and Polar Engineering*

- Conference*, Osaka, Japan, ISOPE.
- Camporeale, S.M. & Filianoti, P., 2007. A linearized model of the OWC devices with additional vertical ducts. *Proceedings of the 7th European Wave and Tidal Energy Conference*. Porto, Portugal.
- Carballo, R. & Iglesias, G., 2012. A methodology to determine the power performance of wave energy converters at a particular coastal location. *Energy Conversion and Management*, 61, pp.8–18.
- Chai, X. & Mahesh, K., 2010. Dynamic-equation model for large-eddy simulation of compressible flows. *Journal of Fluid Mechanics*, 699, pp.385–413.
- Clément, A.H., 1997. Dynamic Nonlinear Response of OWC Wave Energy Devices. *International Journal of Offshore and Polar Engineering*, 7(02).
- Cole, R., 1948. *Underwater explosions*, Princeton University Press.
- Corsini, S., Franco, L., Inghilesi, R. & Piscopia, R., 2004. *Italian Wave Atlas - Atlante delle Onde nei mari italiani*, Rome: APAT - University of Roma Tre (in Italian).
- Cottet, G.-H. & Maitre, E., 2004. A level-set formulation of immersed boundary methods for fluid–structure interaction problems. *Comptes Rendus Mathématique*, 338(7), pp.581–586.
- Crema, I., Cappietti, L. & Oumeraci, H., 2016. *Report_4.2 - Phase I: Fixed OWC Model*, Internal Report -Florence University, TU Braunschweig.
- Crema, I., Simonetti, I., Cappietti, L. & Oumeraci, H., 2015. Laboratory experiments on Oscillating Water Column Wave Energy Converters integrated in a Very Large Floating Structure. In *11th Wave and Tidal Energy Conference, EWTEC2015*. p. 8.
- Cruz, J., 2009. *Ocean Wave Energy - Current Status and future perspectives*, Springer Series in Green Energy and Technology.
- Curran, R., Stewart, T.P. & Whittaker, T.J.T., 1997. Design synthesis of oscillating water column wave energy converters: performance matching. *Proceedings of the Institution of Mechanical Engineers, Part A: Journal of Power and Energy*, 211(6), pp.489–505.
- Delauré, Y.M.C. & Lewis, a., 2003. 3D hydrodynamic modelling of fixed oscillating water column wave power plant by a boundary element methods. *Ocean Engineering*, 30(3), pp.309–330.
- Deshpande, S.S., Anumolu, L. & Trujillo, M.F., 2012. Evaluating the performance of the two-phase flow solver interFoam. *Computational Science & Discovery*, 5(1), p.36.
- Dias F, B.L., 2010. Comparative Numerical study: description of the calculation case. In *Proceedings of the 20th International Offshore and Polar Engineering Conference, Beijing, China, ISOPE*.

- Elhanafi, A., Fleming, A., Macfarlane, G. & Leong, Z., 2016a. Numerical energy balance analysis for an onshore oscillating water column–wave energy converter. *Energy*, 116, pp.539–557.
- Elhanafi, A., Fleming, A., Macfarlane, G. & Leong, Z., 2016b. Numerical hydrodynamic analysis of an offshore stationary–floating oscillating water column–wave energy converter using CFD. *International Journal of Naval Architecture and Ocean Engineering*.
- Elhanafi, A., Fleming, A., Macfarlane, G. & Leong, Z., 2016c. Underwater geometrical impact on the hydrodynamic performance of an offshore oscillating water column–wave energy converter. *Renewable Energy*.
- Elhanafi, A., Macfarlane, G., Fleming, A. & Leong, Z., 2017. Scaling and air compressibility effects on a three-dimensional offshore stationary OWC wave energy converter. *Applied Energy*, 189, pp.1–20.
- Evans, D. V., 1981. Power From Water Waves. *Annual Review of Fluid Mechanics*, 13(1), pp.157–187.
- Evans, D. V., 1978. The Oscillating Water Column Wave-energy Device. *IMA Journal of Applied Mathematics*, 22(4), pp.423–433.
- Evans, D. V., 1982. Wave-power absorption by systems of oscillating surface pressure distributions. *Journal of Fluid Mechanics*, 114(1), p.481.
- Evans, D. V. & Porter, R., 1997. Efficient Calculation of Hydrodynamic Properties of OWC-Type Devices. *Journal of Offshore Mechanics and Arctic Engineering*, 119(4), p.210.
- Evans, D. V. & Porter, R., 1995. Hydrodynamic characteristics of an oscillating water column device. *Appl Ocean Res*, 17, pp.155 – 163.
- Falcão, A.F. de O., 2002a. Control of an oscillating-water-column wave power plant for maximum energy production. *Applied Ocean Research*, 24, pp.73–82.
- Falcão, A.F. de O., 2004. First-Generation Wave Power Plants: Current Status and R&D Requirements. *Journal of Offshore Mechanics and Arctic Engineering*, 126(4), p.384.
- Falcão, A.F. de O., 2004. Stochastic modelling in wave power-equipment optimization: maximum energy production versus maximum profit. *Ocean Engineering*, 31(11–12), pp.1407–1421.
- Falcão, A.F. de O., 2010. Wave energy utilization: A review of the technologies. *Renewable and Sustainable Energy Reviews*, 14(3), pp.899–918.
- Falcão, A.F. de O., 2002b. Wave-power absorption by a periodic linear array of oscillating water columns. *Ocean Engineering*, 29(10), pp.1163–1186.
- Falcão, A.F. de O., Gato, L.M.C. & Nunes, E.P.A.S., 2013a. A novel radial self-rectifying air turbine for use in wave energy converters. *Renewable Energy*, 50,

- pp.289–298.
- Falcão, A.F. de O., Gato, L.M.C. & Nunes, E.P.A.S., 2013b. A novel radial self-rectifying air turbine for use in wave energy converters. Part 2. Results from model testing. *Renewable Energy*, 53, pp.159–164.
- Falcão, A.F. de O. & Henriques, J.C.C., 2014. Model-prototype similarity of oscillating-water-column wave energy converters. *International Journal of Marine Energy*, 6(September 2015), pp.18–34.
- Falcão, A.F. de O. & Henriques, J.C.C., 2016. Oscillating-water-column wave energy converters and air turbines: A review. *Renewable Energy*, 85, pp.1391–1424.
- Falcão, A.F. de O., Henriques, J.C.C. & Cândido, J.J., 2012. Dynamics and optimization of the OWC spar buoy wave energy converter. *Renewable Energy*, 48, pp.369–381.
- Falcão, A.F. de O., Henriques, J.C.C., Gato, L.M.C. & Gomes, R.P.F., 2014. Air turbine choice and optimization for floating oscillating-water-column wave energy converter. *Ocean Engineering*, 75, pp.148–156.
- Falcão, A.F. de O., Henriques, J.C.C., Gato, L.M.C. & Gomes, R.P.F., 2013. Air turbine choice and optimization for spar-buoy oscillating-water-column wave energy converter. In *10th European Wave and Tidal Energy Conference*. Aalborg, Denmark, p. 9.
- Falcão, A.F. de O. & Justino, P.A.P., 1999. OWC wave energy devices with air flow control. *Ocean Engineering*, 26, pp.1275–1295.
- Falcão, A.F. de O. & Justino, P.A.P., 1995. OWC wave energy conversion with valve-constrained flow. In *Proceedings of the 2nd European Wave Power Conference*. Lisbon, pp. 187–194.
- Falcão, A.F. de O. & Rodrigues, R.J.A., 2002. Stochastic modelling of OWC wave power plant performance. *Applied Ocean Research*, 24(2), pp.59–71.
- Falcão, A.F. de O. & Sarmiento, A.J.N.A., 1980. Wave generation by a periodic surface-pressure and its application to wave-energy extraction. In *15th International Conference on theoretic and applied mechanics*. Toronto.
- Falnes, J., 2007. A review of wave-energy extraction. *Marine Structures*, 20(0951), pp.185–201.
- Falnes, J., 2002. *Ocean Waves and Oscillating Systems*, Cambridge University Press.
- Falnes, J. & McIver, P., 1985. Surface wave interactions with systems of oscillating bodies and pressure distributions. *Applied Ocean Research*, 7, pp.225–235.
- Filianoti, P. & Camporeale, S.M., 2008. A linearized model for estimating the performance of submerged resonant wave energy converters. *Renewable Energy*, 33(4), pp.631–641.

- Freeman, K., Dai, M. & Sutton, R., 2014. Control strategies for oscillating water column wave energy converters. *Underwater Technology*, 32(1), pp.3–13.
- Gato, L.M.C., Eça, L.R.C. & Falcão, A.F. de O., 1991. Performance of the Wells Turbine With Variable Pitch Rotor Blades. *Journal of Energy Resources Technology*, 113(3), p.141.
- Gato, L.M.C. & Falcão, A.F. de O., 1988. Aerodynamics of the wells turbine. *International Journal of Mechanical Sciences*, 30(6), pp.383–395.
- Gato, L.M.C. & Falcão, A.F. de O., 1984. On the Theory of the Wells Turbine. *Journal of Engineering for Gas Turbines and Power*, 106(3), p.628.
- Geuzaine, C., 2009. Gmsh: a three-dimensional finite element mesh generator with built-in pre- and post-processing facilities. *International Journal for Numerical Methods in Engineering* (18), pp.1–24.
- Goda, Y., 2010. *Random Seas and Design of Maritime Structures*, 3rd Edition, Singapore: World Scientific.
- Goda, Y. & Suzuki, Y., 1976. Estimation of incident and reflected waves in random wave experiments. In *Proc. 15th Int.Conf. Coastal Engeneerig*. Hawaii, pp. 828–845.
- Gomes, R.P.F., Henriques, J.C.C., Gato, L.M.C. & Falcão, a. F.O., 2012. Hydrodynamic optimization of an axisymmetric floating oscillating water column for wave energy conversion. *Renewable Energy*, 44, pp.328–339.
- Gomes, R.P.F., Henriques, J.C.C., Gato, L.M.C. & Falcão, A.F. de O., 2011. Design of a Floating Oscillating Water Column for Wave Energy Conversion. In *Proceedings of the 9th European Wave Energy And Tidal Energy Conference*. Southampton, UK.
- Gouaud, F., Rey, V., Piazzola, J., Hooff, R. Van & Van Hooff, R., 2010. Experimental study of the hydrodynamic performance of an onshore wave power device in the presence of an underwater mound. *Coastal Engineering*, 57(11-12), pp.996–1005.
- Guilcher, P.M., Brosset, L., Couty, N. & Touzé, D. Le, 2009. Simulations of breaking wave impacts on a rigid wall at two different scales with a two phase fluid compressible SPH model. In *Proceedings of the 20th International Offshore and Polar Engineering Conference*, Beijing, China, ISOPE .
- Guillard, H. & Viozat, C., 1999. On the behaviour of upwind schemes in the low Mach number limit. *Computers & Fluids*, 28(1), pp.63–86.
- Hasselmann, D.E., Dunckel, M., Ewing, J.A., Hasselmann, D.E., Dunckel, M. & Ewing, J.A., 1980. Directional Wave Spectra Observed during JONSWAP 1973. *Phys. Oceanogr.*
- Hasselmann, K., Barnett, T.P., Bouws, E., Carlson, H., Cartwright, D.E., Enke, K., Ewing, J.A., Gienapp, H., Hasselmann, D.E., Kruseman, P., Meerburg, A.,

- Müller, P., Olbers, D.J., Richter, K., Sell, W. & Walden, H., 1973. Measurement of wind-wave growth and swell decay during the Joint North Sea Wave Project (JONSWAP). *Deutsch. Hydrogr. Z*, 12(Suppl., A8), p.95.
- He, F., Li, M. & Huang, Z., 2016. An Experimental Study of Pile-Supported OWC-Type Breakwaters: Energy Extraction and Vortex-Induced Energy Loss. *Energies*, 9(7), p.540.
- Hiramoto, A., 1978. The theoretical analysis of an air turbine generation system. *International Symposium on Wave and Tidal Energy*.
- Hirt, C. & Nichols, B., 1981. Volume of fluid (VOF) method for the dynamics of free boundaries. *Journal of Computational Physics*, 39(1), pp.201–225.
- Issa, R., 1986. Solution of the implicitly discretised fluid flow equations by operator-splitting. *Journal of Computational Physics*, 62(1), pp.40–65.
- Iturrioz, A., 2013. Experimental and numerical development of a floating multi-chamber OWC device. In *10th European Wave and Tidal Energy Conference*. Aalborg, Denmark, p. 10.
- Iturrioz, A., Guanche, R., Armesto, J. a., Alves, M. a., Vidal, C. & Losada, I.J., 2014. Time-domain modeling of a fixed detached oscillating water column towards a floating multi-chamber device. *Ocean Engineering*, 76, pp.65–74.
- Iturrioz, A., Guanche, R., Lara, J.L., Vidal, C. & Losada, I.J., 2015. Validation of OpenFOAM® for Oscillating Water Column three-dimensional modeling. *Ocean Engineering*, 107, pp.222–236.
- Jacobsen, N.G., Fuhrman, D.R. & Fredsøe, J., 2012. A wave generation toolbox for the open-source CFD library: OpenFoam r. *International Journal for numerical methods in fluids*, 70, pp.1073–1088.
- Jasak, H., 1996. *Error Analysis and Estimation for the Finite Volume Method with Applications to Fluid Flows*. University of London.
- Jasak, H. & Tukovi, Z., 2007. Automatic Mesh Motion for the Unstructured Finite Volume Method. *Transaction of FAMENA*, 30(2), p.30.
- Jasak, H. & Tukovi, Z., 2010. Dynamic Mesh Handling in OpenFOAM applied to Fluid Structure Interaction simulations. In *5th European Conference on Computational Fluid Dynamics*. Lisbon, Portugal, p. 19.
- Jefferys, R. & Whittaker, T., 1986. Latching Control of an Oscillating Water Column Device with Air Compressibility. In *Hydrodynamics of Ocean Wave-Energy Utilization*. Berlin, Heidelberg: Springer Berlin Heidelberg, pp. 281–291.
- Josset, C. & Clément, a. H., 2007. A time-domain numerical simulator for oscillating water column wave power plants. *Renewable Energy*, 32(8), pp.1379–1402.
- Kamath, A., Bihs, H. & Arntsen, Ø.A., 2015. Numerical investigations of the hydrodynamics of an oscillating water column device. *Ocean Engineering*, 102,

pp.40–50.

- Karami, V., Ketabdari, J. & Akhtari, A.K., 2012. Numerical Modeling of Oscillating Water Column Wave Energy Convertor. *International Journal of Advanced renewable energy research*, 1(4), pp.196–206.
- Lee, C.H., Newman, J.N. & Nielsen, F.G., 1996. Wave Interactions With an Oscillating Water Column. In *The Sixth International Offshore and Polar Engineering Conference*. Los Angeles, California, USA: International Society of Offshore and Polar Engineers.
- Van Leer, B., 1979. Towards the ultimate conservative difference scheme. *Journal of Computational Physics*, 32, pp.101–136.
- Li, Y. & Yu, Y.-H., 2012. A synthesis of numerical methods for modeling wave energy converter-point absorbers. *Renewable and Sustainable Energy Reviews*, 16(6), pp.4352–4364.
- Liberti, L., Carillo, A. & Sannino, G., 2013. *Wave energy resource assessment in the Mediterranean, the Italian perspective*,
- Lopes, M.F.P., Hals, J., Gomes, R.P.F., Moan, T., Gato, L.M.C. & Falcão, A.F. d. O., 2009. Experimental and numerical investigation of non-predictive phase-control strategies for a point-absorbing wave energy converter. *Ocean Engineering*, 36(5), pp.386–402..
- Lopez, I., Pereiras, B., Castro, F. & Iglesias, G., 2016. Holistic performance analysis and turbine-induced damping for an OWC wave energy converter. *Renewable Energy*, 85, pp.1155–1163.
- Lopez, I., Pereiras, B., Castro, F. & Iglesias, G., 2014. Optimisation of turbine-induced damping for an OWC wave energy converter using a RANS-VOF numerical model. *Applied Energy*, 127, pp.105–114.
- Lovas, S., Mei, C.C. & Liu, Y., 2010. Oscillating water column at a coastal corner for wave power extraction. *Applied Ocean Research*, 32(3), pp.267–283.
- Luo, Y., Nader, J.R., Cooper, P. & Zhu, S.P., 2014. Nonlinear 2D analysis of the efficiency of fixed Oscillating Water Column wave energy converters. *Renewable Energy*, 64, pp.255–265.
- Lupieri, G., Puzzer, T., Contento, G., Donatini, L. & Cappiotti, L., 2015. Numerical and Experimental investigation on the wave-wave interaction in breaking and non-breaking focusing waves. In *18th International Conference on Ships and Shipping Research*. Lecco, Italy, pp. 185–195.
- Ma, Q.W., 1995. Nonlinear analysis on hydrodynamic performance of oscillating water column wave energy device with a lateral opening. In *Proceedings of the 14th International Conference on Offshore Mechanics and Arctic Engineering*. Copenhagen, Denmark: American Society of Mechanical Engineers, New York, NY (United States).

- Ma, Z.H., Causon, D.M., Qian, L., Mingham, C.G., Gu, H.B., Ferrer, P.M. & A, P.R.S., 2014. A compressible multiphase flow model for violent aerated wave impact problems A compressible multiphase flow model for violent aerated wave impact problems. *Proceedings of the Royal Society A*, (470).
- Maeda, H., Kinoshita, T., Masuda, K. & Kato, W., 1985. Fundamental Research on Oscillating Water Column Wave Power Absorbers. *Journal of Energy Resources Technology*, 107(1), p.81.
- El Marjani, a., Castro Ruiz, F., Rodriguez, M. a. & Parra Santos, M.T., 2008. Numerical modelling in wave energy conversion systems. *Energy*, 33(8), pp.1246–1253.
- Martín, M.P., Piomelli, U. & Candler, G. V., 2000. Subgrid-Scale Models for Compressible Large-Eddy Simulations. *Theoretical and Computational Fluid Dynamics*, 13(5), pp.361–376.
- Martins-Rivas, H. & Mei, C.C., 2009. Wave power extraction from an oscillating water column at the tip of a breakwater ´. *Journal of Fluid Mechanics*, 626, pp.395–414.
- Mavrakos, S. a. & Konispoliatis, D.N., 2012. Hydrodynamics of a Free Floating Vertical Axisymmetric Oscillating Water Column Device. *Journal of Applied Mathematics*, 2012, pp.1–27.
- Méhauté, B., 1976. *An Introduction to Hydrodynamics and Water Waves*, Berlin, Heidelberg: Springer Berlin Heidelberg.
- Mork, G., Barstow, S., Kabuth, A. & Pontes, T.M., 2010. Assessing the global wave energy potential. In *29th International Conference on Ocean, Offshore Mechanics and Arctic Engineering*. Shanghai, China, p. 8.
- Morrison, I.G. & Greated, C.A., 1992. Oscillating Water Column Modelling. *Coastal Engineering Proceedings*, 23.
- Morris-Thomas, M.T., Irvin, R.J. & Thiagarajan, K.P., 2007. An Investigation Into the Hydrodynamic Efficiency of an Oscillating Water Column. *Journal of Offshore Mechanics and Arctic Engineering*, 129(4), p.273.
- Moukalled, F., Mangani, L., Darwish, M., 2016. *The Finitie Volume Method in Computational Fluid Dynamics, An Advanced Introduction with OpenFOAM and Matlab*, Springer International Publishing Switzerland 2016.
- Murrone, A. & Guillard, H., 2008. Behavior of upwind scheme in the low Mach number limit: III. Preconditioned dissipation for a five equation two phase model. *Computers and Fluids* (37), pp: 1209-1224.
- Nader, J.-R., Zhu, S.-P., Cooper, P. & Stappenbelt, B., 2012. A finite-element study of the efficiency of arrays of oscillating water column wave energy converters. *Ocean Engineering*, 43, pp.72–81.

References

- Nunes, G., Valério, D., Beirão, P. & Sá da Costa, J., 2011. Modelling and control of a wave energy converter. *Renewable Energy*, 36(7), pp.1913–1921.
- Paixão Conde, J.M. & Gato, L.M.C., 2008. Numerical study of the air-flow in an oscillating water column wave energy converter. *Renewable Energy*, 33(12), pp.2637–2644.
- Patankar, S. & Spalding, D., 1972. A calculation procedure for heat, mass and momentum transfer in three-dimensional parabolic flows. *International Journal of Heat and Mass Transfer*, 15(10), pp.1787–1806.
- Pecher, A., 2012. *Performance evaluation of wave energy converters*. Aalborg: Department of Civil Engineering, Aalborg University. (DCE Thesis; No. 38).
- Perdigão, J. & Sarmento, A., 2003. Overall-efficiency optimisation in OWC devices. *Applied Ocean Research*, 25(3), pp.157–166.
- Pereiras, B., López, I., Castro, F. & Iglesias, G., 2015. Non-dimensional analysis for matching an impulse turbine to an OWC (oscillating water column) with an optimum energy transfer. *Energy*, 87, pp.481–489.
- Plumerault, L., Astruc, D., Villedieu, P. & Maron, P., 2012. A numerical model for aerated-water wave breaking. pp.1851–1871, *International Journal for Numerical methods in Fluids*, 69, pp: 1851–1871.
- Raghunathan, S., Tan, C.P. & Wells, N.A.J., 1982. Theory and performance of a Wells turbine. *Journal of Energy*, 6(2), pp.157–160.
- Réthoré, P.-E., van der Laan, P., Troldborg, N., Zahle, F. & Sørensen, N.N., 2014. Verification and validation of an actuator disc model. *Wind Energy*, 17(6), pp.919–937..
- Rezanejad, K., Bhattacharjee, J. & Guedes Soares, C., 2015. Analytical and numerical study of dual-chamber oscillating water columns on stepped bottom. *Renewable Energy*, 75, pp.272–282.
- Ricci, P., 2012. *Modelling, Optimization and Control of Wave Energy Point adsorbers*. Universidade Tecnica de Lisboa, Instituto Superior Tecnico. Ph.D. thesis.
- Ricci, P., Saulnier, J.-B., Falcão, A.F. de O. & Pontes, M.T., 2008. Time-Domain Models and Wave Energy Converters Performance Assessment. In *Proceedings of the 27th Offshore Mechanics and Arctic Engineering Conference Symposium on Offshore Renewable Energy*. Estoril, Portugal, pp. 699–708.
- Robinson, R.W., 1982. *The effects of geometry-wave field interactions o the performance of oscillating water column wave energy converters*. Queens University, Belfast.
- Roller, S. & Munz, C.-D., 2000. A low Mach number scheme based on multi-scale asymptotics. *Computing and Visualization in Science*, 3(1-2), pp.85–91.
- Rusche, H., 2002. *Computational Fluid Dynamics of Dispersed Two-Phase Flows at*

- High Phase Fractions*. Imperial College of Science, Technology & Medicine, PhD Thesis.
- Sarmiento, A., Brito-Melo, A. & Neumann, F., 2006. Result from sea trials in the OWC european Energy plant at Pico, Azores. In *invited paper for WREC-IX, Proceedings WREC IX*.
- Sarmiento, A.J.N.A., 1993. Model tests optimization of an OWC wave power plant. *Int. J. Offshore Polar Eng.*, 3, pp.66–72.
- Sarmiento, A.J.N.A., 1992. Wave flume experiments on two-dimensional oscillating water column wave energy devices. *Experiments in Fluids*, 12(4), pp.286–292.
- Sarmiento, A.J.N.A. & Falcão, A.F. de O., 1985. Wave generation by an oscillating surface-pressure and its application in wave-energy extraction. *Journal of Fluid Mechanics*, 150, pp.467–485.
- Sarpkaya, T. & Isaacson, M., 1981. *Mechanics of wave forces on offshore structures* V. N. Reinhold, ed., New York.
- Senturk, U. & Ozdamar, A., 2011. Modelling the Interaction Between Water Waves and the Oscillating water column wave energy device. *Mathematical and Computational Applications*, 16(3), pp.630–640.
- Şentürk, U. & Özdamar, A., 2012. Wave energy extraction by an oscillating water column with a gap on the fully submerged front wall. *Applied Ocean Research*, 37, pp.174–182.
- Setoguchi, T., Santhakumar, S., Maeda, H., Takao, M. & Kaneko, K., 2001. A review of impulse turbines for wave energy conversion. *Renewable Energy*, 23, pp.261–292.
- Setoguchi, T., Santhakumar, S., Takao, M., Kim, T.H. & Kaneko, K., 2003. A modified Wells turbine for wave energy conversion. *Renewable Energy*, 28(1), pp.79–91.
- Shaaban, S. & Abdel Hafiz, A., 2012. Effect of duct geometry on Wells turbine performance. *Energy Conversion and Management*, 61, pp.51–58.
- Sheng, W., Alcorn, R. & Lewis, A., 2013. On thermodynamics in the primary power conversion of oscillating water column wave energy converters. *Journal of Renewable and Sustainable Energy*, 5(2).
- Sheng, W., Lewis, T. & Alcorn, R., 2012. On wave energy extraction of oscillating water column device. In *4th International Conference on Ocean Energy*,. Dublin, Ireland, p. 9.
- Sheng, W., Thiebaut, F., Babuchon, M., Brooks, J., Lewis, A. & Alcorn, R., 2013. Investigation to air compressibility of oscillating water column wave energy converters. In *32nd International Conference on Ocean, Offshore and Arctic Engineering*. Nantes, France, pp. 1–10.

- Simonetti, I., Cappietti, L., ElSafti, H. & Oumeraci, H., 2015. Numerical Modelling of Fixed Oscillating Water Column Wave Energy Conversion Devices: Toward Geometry Hydraulic Optimization. *Proceedings of the ASME 2015 34th International Conference on Ocean, Offshore and Arctic Engineering*.
- Simonetti, I., Cappietti, L., Safti, H. El & Oumeraci, H., 2015. 3D numerical modelling of oscillating water column wave energy conversion devices : current knowledge and OpenFOAM [®] implementation. In C. Guedes Soares, ed. *1st International Conference on Renewable Energies Offshore - RENEW2014, At Lisbon, Portugal*. Taylor & Francis, pp. 497–504.
- Stappenbelt, B. & Cooper, P., 2010. Optimisation of a floating oscillating water column wave energy converter. In *Annual Bulletin of the Australian Institute of High Energetic Materials*. Beijing, China, pp. 34–45.
- Strati, F.M., Malara, G. & Arena, F., 2016. Performance optimization of a U-Oscillating-Water-Column wave energy harvester. *Renewable Energy*, 99, pp.1019–1028.
- Suzuki, M., Washio, Y. & Kuboki, T., 2005. Characteristics of Floating Type Wave Power Generating System With Oscillating Water Column. In *The Fifteenth International Offshore and Polar Engineering Conference*. Seoul, Korea: International Society of Offshore and Polar Engineers.
- Sweby, P.K., 1984. High Resolution Schemes Using Flux Limiters for Hyperbolic Conservation Laws. *SIAM Journal of Numerical Analysis*, 21(5), pp.995–1011.
- Sykes, R.K., Lewis, A.W. & Thomas, G.P., 2011. Predicting Hydrodynamic Pressure in Fixed and Floating OWC Using a Piston Model. In *9th European Wave and Tidal Energy Conference*. Southampton, UK, p. 10.
- Takao, M., Kinoue, Y., Setoguchi, T., Obayashi, T. & Kaneko, K., 2000. Impulse Turbine with Self-pitch-controlled Guide Vanes for Wave Power Conversion (Effect of Guide Vane Geometry on the Performance). *International Journal of Rotating Machinery*, 6(5), pp.355–362.
- Takao, M. & Setoguchi, T., 2012. Air turbines for wave energy conversion. *International Journal of Rotating Machinery*, 2012.
- Thakker, A., Takao, M., Setoguchi, T. & Dhanasekaran, T.S., 2003. Effects of Compressibility on the Performance of a Wave-Energy Conversion Device with an Impulse Turbine Using a Numerical Simulation Technique. *The International Journal of Rotating Machinery*, 9(6), pp.443–450.
- Thiruvencatasamy, K. & Neelamani, S., 1997. On the efficiency of wave energy caissons in array. *Applied Ocean Research*, 19(1), pp.61–72.
- Torre-Enciso, Y., Ortubia, I., Aguilera, L.I.L. De & Marqués, J., 2009. Mutriku Wave Power Plant : from the thinking out to the reality. In *8th European Wave and*

- Tidal Energy Conference*. Uppsala, Sweden, pp. 319–329.
- Torresi, M., Camporeale, S.M. & Pascazio, G., 2009. Detailed CFD Analysis of the Steady Flow in a Wells Turbine Under Incipient and Deep Stall Conditions. *Journal of Fluids Engineering*, 131.
- Torresi, M., Camporeale, S.M., Pascazio, G. & Fortunato, B., 2004. Fluid dynamic analysis of the solidity of a wells turbine. In *59° Congresso annuale ATI*. Genova, p. 12.
- Torresi, M., Camporeale, S.M., Strippoli, P.D. & Pascazio, G., 2008. Accurate numerical simulation of a high solidity Wells turbine. *Renewable Energy*, 33(4), pp.735–747.
- Tryggvason, G., Scardovelli, R. & Zaleski, S., 2011. *Direct Numerical Simulations of Gas-Liquid Multiphase Flows*, Cambridge : Cambridge University Press.
- Ubbink, O., 1997. *Numerical prediction of two fluid systems with sharp interfaces*. University of London.
- Vannucchi, V., 2012. *Wave energy harvesting in the Mediterranean Sea*. University of Florence.
- Vannucchi, V. & Cappiotti, L., 2013. Wave Energy Estimation In Four Italian Nearshore Areas. In ASME, ed. *Proceedings of the ASME 32nd International Conference on Ocean, Offshore and Arctic Engineering OMAE2013*. Nantes, France.
- Villers, E., 2006. *The Potential of Large Eddy Simulation for the Modeling of Wall Bounded Flows Eugene de Villiers*.
- Wang, W. & Huang, R.X., 2004. Wind Energy Input to the Surface Waves. *Journal of Physical Oceanography*, 34, pp.1276–1280.
- Watts, K.C., Hassan, K.M., Sarwal, S.N., Alexander, H.C. & Graham, J.W., 1985. Non-linear analysis of a non-vertical walled OWC ocean wave energy converter. In *5th Offshore Mechanics and Arctic Engineering Symposium*. Dallas, Texas.
- Weber, J.W., 2007. Representation of non-linear aero-thermodynamic effects during small scale physical modelling of OWC WECs. In *Proc. 7th European Wave Tidal Energy Conference, Porto, Portugal*.
- Webster, M.F., Keshtiban, I.J. & Belblidia, F., 2004. Computation of weakly-compressible highly-viscous liquid flows. *Engineering Computations*, 21(7), pp.777–804.
- Wehausen, J. V, 1971. The Motion of Floating Bodies. *Annual Review of Fluid Mechanics*, 3(1), pp.237–268. Available at: <http://www.annualreviews.org/doi/abs/10.1146/annurev.fl.03.010171.001321> [Accessed June 7, 2016].
- Yalin, S.M., 1971. *Theory of Hydraulic Models* M. C. E. Hydraulics, ed.

References

- Yeung, R.W., 1981. Added mass and damping of a vertical cylinder in finite-depth waters. *Applied Ocean Research*, 3(3), pp.119–133.
- Yeung, R.W., 1982. Numerical Methods in Free-Surface Flows. *Annual Review of Fluid Mechanics*, 14(1), pp.395–442.
- Zhang, Y., Zou, Q.-P. & Greaves, D., 2012. Air–water two-phase flow modelling of hydrodynamic performance of an oscillating water column device. *Renewable Energy*, 41, pp.159–170.